Evaluating Hyperspectral Imagery for Mapping the Surface Symptoms of Dryland Salinity

by

Anna Dutkiewicz

Thesis submitted in fulfilment of the requirements for the degree of

Doctor of Philosophy

Discipline of Soil and Land Systems

School of Earth and Environmental Sciences

The University of Adelaide

July 2006

TABLE OF CONTENTS

LIST OF FIGURES

LIST OF TABLES

ABSTRACT

Airborne hyperspectral imagery has the potential to overcome the spectral and spatial resolution limitations of multispectral satellite imagery for monitoring salinity at both regional and farm scales. In particular, saline areas that have good cover of salt tolerant plants are difficult to map with multispectral satellite imagery. Hyperspectral imagery may provide a more reliable salinity mapping method because of its potential to discriminate halophytic plant cover from non-halophytes.

HyMap and CASI airborne imagery (at 3m ground resolution) and Hyperion satellite imagery (at 30 resolution) were acquired over a 140 sq km dryland agricultural area in South Australia, which exhibits severe symptoms of salinity, including extensive patches of the perennial halophytic shrub samphire *(Halosarcia pergranulata)*, sea barley grass *(Hordeum marinum)* and salt encrusted pans. The HyMap and Hyperion imagery were acquired in the dry season (March and February respectively) to maximise soil and perennial vegetation mapping. The optimum time of year to map sea barley grass, an annual species, was investigated through spectral discrimination analysis.

Multiple reflectance spectra were collected of sea barley grass and other annual grasses with an ASD Fieldspec Pro spectrometer during the September spring flush and in November during late senescence. Comparing spectra of different species in November attempted to capture the spectral differences between the late senescing sea barley grass and other annual grasses. Broad NIR and SWIR regions were identified where sea barley grass differs significantly from other species in November during late senescence. The sea barley grass was therefore shown to have the potential to be discriminated and mapped with hyperspectral imagery at this time and as a result the CASI survey was commission for November. Other salinity symptoms were characterised by collecting single field and laboratory spectra for comparison to image derived spectra in order to provide certainty about the landscape components that were to be mapped.

Endmembers spectra associated with saltpans and samphire patches were extracted from the imagery using automated endmember generation procedures or selected regions of interest and used in subsequent partial unmixing. Spectral subsets were evaluated for their ability to optimise salinity maps. The saltpan spectra contained absorption features consistent with montmorillonite and gypsum. A single gypsum endmember from one

image strip successfully mapped saltpans across multiple images strips using the 1750 nm absorption feature as the input to matched filter unmixing. The individual spectra of green and red samphire are dominated by photosynthetic vegetation characteristics. The spectra of green samphire, often seen with red tips, exhibit peaks in both green and red wavebands whereas the red samphire spectra only contain a significant reflectance peak in the visible red wavelength region.

For samphire, Mixture Tuned Matched Filtering using image spectra, containing all wavelength regions, from known samphire patches produced the most satisfactory mapping. Output salinity maps were validated at over 100 random sites. The HyMap salinity maps produced the most accurate results compared to CASI and Hyperion.

HyMap successfully mapped highly saline areas with a good cover of samphire vegetation at Point Sturt without the use of multitemporal imagery or ancillary data such as topography or PIRSA soil attribute maps. CASI and Hyperion successfully mapped saltpan, however, their samphire maps showed a poor agreement with field data. These results suggest that perennial vegetation mapping requires all three visible, NIR and SWIR wavelength regions because the SWIR region contains important spectral properties related to halophytic adaptations. Furthermore, the unconvincing results of the CASI sea barley grass maps suggests that the optimal sensor for mapping both soil and vegetation salinity symptoms are airborne sensors with high spatial and spectral resolution, that incorporate the 450 to 1450 nm wavelength range, such as HyMap.

This study has demonstrated that readily available software and image analysis techniques are capable of mapping indicators of varying levels of salinity. With the ability to map symptoms across multiple image strips, airborne hyperspectral imagery has the potential for mapping larger areas covering sizeable dryland agriculture catchments, closer in extent to single satellite images. This study has illustrated the advantage of the hyperspectral imagery over traditional soil mapping based on aerial photography interpretation such as the NLWRA Salinity 2000 and the PIRSA soil landscape unit maps. The HyMap salinity maps not only improved mapping of saline areas covered with samphire but also provided salinity maps that varied spatially within saline polygons.

DECLARATION

This work contains no material which has been accepted for the award of any other degree or diploma in any university or other tertiary institution and, to the best of my knowledge and belief, contains no material previously published or written by another person, except where due reference has been made in the text.

I give consent to this copy of my thesis being available for loan and photocopying.

Signed:……. Date:……..

Anna Dutkiewicz

DEDICATION

This thesis is dedicated to my entire family: to my mother Joan, for her infinite humanity, my father Wladyslaw who taught me that life is about the passionate pursuit of what you believe in, to my brother Michal for his love of the natural world and creative enthusiasm, my brother Adam for not settling on mediocrity in life, my sisters Ursula for her inspiration to believe in yourself and Cecilia, who taught me patience, forgiveness and personal strength. Thanks to Aislinn for giving me so much joy and being so understanding, and to Brian for his generosity, support and encouragement.

ACKNOWLEDGEMENTS

Thanks to my supervisors Megan Lewis, Bertram Ostendorf (University of Adelaide) and Chris Henschke (PIRSA Rural Solutions) for constant advice and support,

Cooperative Research Centre for Plant-Based Management of Dryland Salinity for their financial support, training, conference and networking opportunities to meet with fellow CRC students and researchers throughout Australia,

Bruce Allnutt, Mike South, Vince Falzon from the Point Sturt Landcare Group and all the other landowners who allowed me to access their properties.

I would like to thank the following people for assistance in the field: my fellow students David Summers and Sean Mahoney, Wilhelm Windhorst (Kiel University), Colin Rivers (University of Adelaide), Mui Lay (University of California, Davis),

Thanks also for the support from my Spatial Information Group colleagues: David Summers, Sean Mahoney, Dorothy Turner, David Mitchell, Claire Trelibs, Reza Jafari, Lyndon Zimmerman, Allana Grech, Ben Kaethner, Neville Grossman, Christina Gabrovsek, David Gerner.

I would like to thank the following people and agencies for supplying me with information, data or equipment training:

Peter Cocks from HyVista Corporation for HyMap survey, Steve Ranson from Steve Ranson and Associates for CASI survey, Richard Cresswell from CSIRO (formerly of Bureau of Rural Sciences) for Hyperion data,

Melissa Quigley and Peter Mason (CSIRO), Mark Thomas (CSIRO formerly from PIRSA), Laurie Chisholm (University of Woolongong) and Geoff Taylor (University of NSW) for assistance with the ASD Fieldspec Pro, Ian Lau (CSIRO, formerly University of Adelaide),

PIRSA Rural Solutions consultants Terry Evans (in conjunction with Southcorp Wines for assistance with EM38 survey), Hugh Longbottom, Trevor Dooley for my education on salinity, Craig Liddicoat and Peter Ciganovic for hydrological information.

Mark Raven (for XRD analysis) and Rob Fitzpatrick and Richard Merry (CSIRO Land and Water) for their expertise on saline soils,

David Maschmedt and Steve Barnett from Department of Water, Land, Biodiversity and Conservation (DWLBC, SA),

James Cameron and David Hart (DEH, SA),

Stephen Fildes (Flinders University),

Linton Johnson and David Szkup (Bureau of Meteorology),

Environmental and Geographic Information (DEH) and the Alexandrina Council for cadastral data, and Penny Balcock (PIRSA, Spatial Information Services) for geological data.

PUBLICATIONS

Refereed Publications

A. Dutkiewicz and M. Lewis, 2004, Can sea barley grass be mapped with remote sensing imagery? In *Proceedings of Salinity Solutions: Working with Science and Society Conference*, Bendigo, Victoria, August 2004.

A. Dutkiewicz, M. Lewis, B. Ostendorf, 2003, Evaluation of hyperspectral imagery for mapping the symptoms of dryland salinity, In *Proceedings of Spatial Sciences Coalition Conference*, Canberra, ACT, Sept 2003.

Other Publications

A. Dutkiewicz and M. Lewis, 2004, Spectral discrimination of sea barley grass and the implications for mapping salinity with hyperspectral imagery, In *Proceedings of Australian Remote Sensing and Photogrammetry Conference* (ARSPC), Fremantle, WA, October, 2004

1 INTRODUCTION

Human induced salinity is an expanding problem in southern Australia and in many arid and semi-arid regions of the world, including the great plains of North America, Africa, South America, China, India and the Middle East (Ghassemi *et al.*, 1995). Dryland salinity is recognised as a major land degradation problem in Australia (PIMSEC, 1999; Webb, 2000) particularly in productive agricultural regions.

Research groups and catchment managers are becoming aware of the need for improved remote sensing technologies for baseline mapping and ongoing monitoring of salt affected areas. The National Dryland Salinity Program stressed the importance of "greatly improved methods of using remotely sensed data to map and monitor the risk of dryland salinity" (NDSP, 2000). The Australian Dryland Salinity Assessment 2000 Technical Report also recognised the benefits of the increasing availability of improved satellite and other remote sensing methods (Webb, 2000). Clearly, there is a need for broad-scale, consistent salinity mapping methods. The implementation of monitoring and evaluation strategies is necessary to "ensure we have appropriate data on streamflow and quality, groundwater depth and quality, vegetation cover and salinised land areas" (1999).

Therefore, improved remote sensing technologies have an important role to play in mapping and monitoring dryland salinity. Spies and Woodgate (2004) recently compiled a technical report for the National Dryland Salinity Program (NDSP) in Australia, assessing various remote sensing technologies for their applicability to mapping dryland salinity in Australia. Several remote sensing methods such as aerial photography, multispectral satellites and airborne geophysics, have already contributed to the ongoing search for knowledge regarding the surface and subsurface extent of dryland salinity. The NDSP report noted that the spatial scales of airborne hyperspectral imagery are suitable for both paddock and regional level mapping and would provide a superior performance to multispectral satellites for natural resource management. The report concluded that hyperspectral imagery has the potential to not only improve the accuracy of mapping the current areas affected by dryland salinity but also to assist in monitoring salinity spread at either regional scales or fine scales over targeted high value agricultural areas.

This research investigates the potential of a more recent remote sensing technology, hyperspectral imagery, to map the surface expressions of dryland salinity.

1.1 The problem of dryland salinity

Dryland salinity refers to human induced salinity in non-irrigated areas. In Australia, the major salt affected areas of concern are situated in southwestern Western Australia and the Murray Darling Basin. Vast quantities of naturally occurring salts reside in the soils and regolith underlying most of Australia's productive agricultural land. The regolith salt mainly originates from sea spray carried inland and deposited on the land as rainfall and dust over thousands of years (George *et al.*, 1998; Herzeg *et al.*, 2001). The source of salt in the Murray Basin groundwaters has evolved from a combination of marine fallout and continentally derived solutes and evapo-transpiration over tens of thousands of years of relatively arid environmental conditions (Herzeg *et al.*, 2001).

Dryland salinity is caused by widespread land clearing post-European settlement. Broad scale clearing of indigenous eucalypt forests, woodland and savannah scrubland has increased the amount of water infiltrating to the groundwater system. Australian native trees and plants are very efficient at using soil water. Their roots draw water from deep in the ground and they use water all year round so that very little infiltrating rainwater finds its way through to the groundwater system. Native vegetation has been replaced by shallow-rooted annual crops and pasture that use less water and for only part of the year. The excess incoming rainfall either runs off into streams and rivers, or more importantly, infiltrates below the root zone and accumulates as groundwater, a process known as groundwater recharge. As the groundwater level rises, it dissolves the benign salt stored in the soil profile and brings it or close to the surface or discharge at the surface.

In Australia, major impacts of dryland salinity include damage to agricultural areas, salinisation of rivers and loss of land and aquatic habitats which reduces biodiversity (Webb, 2000).

1.2 The surface symptoms of dryland salinity

Dryland salinity discharge sites can be recognised through a range of surface symptoms relating to vegetation, soils and position in the landscape. Three stages of saline discharge have been defined (Chaturvedi *et al.*, 1983). The primary stage involves surfacing water (waterlogging), the intermediary stage is declining plant condition and

the introduction of salt tolerant plant species or halophytes and the final process is the annihilation of all vegetation and the development of permanent salt water or dry salt deposits on the surface. Dryland salinity is most often associated with low-lying areas such as flats, catchment drainage lines, lake margins, stream banks and land depressions (Department of Primary Industries, 2004). In addition, saline discharge can occur at the base of hills where there is a change in surface gradient to a gentler slope (break in slope).

Waterlogging refers to surface layers of the soil profile becoming permanently or periodically saturated with rising saline groundwater (Maschmedt, 2000), which can result initially in increased vegetation cover. Permanent moist soils or free surface water often indicates a groundwater discharge site, particularly in summer when most crops and pasture have dried out. Saline seeps are areas where highly saline groundwater discharges to the land surface and this groundwater may be naturally saline or may have mobilised salt stores deeper within the soil profile. Free water with electrical conductivity measuring above 5 dS/m in winter is most likely to be groundwater (Department of Primary Industries, 2004).In Australia, salt affected soils are classified as saline, sodic and alkaline soils (Chhabra, 1996); the latter two soil types are not associated with dryland salinity. Saline soils are defined by the levels of salt ion concentration mainly Cl^-, SO_4^{2-}, Ca^{2+}, Na^+, Mg^{2+} and to a lesser degree HCO_3^-. In Australia, NaCl is the most common salt found in soils of arid to subhumid regions (Fitzpatrick *et al.*, 2003; Isbell *et al.*, 1983) and in some regions saline soils are also composed of sulfate salts, such as $NaSO_4$, MgSO4, and $CaSO_4$ (gypsum) (Fitzpatrick *et al.*, 2003; Isbell *et al.*, 1983). Levels of salt ion concentrations or soil salinity can be determined by measuring the electrical conductivity either of a solution of soil and water ($EC_{1:5}$) or with ground-based geophysics electrical conductivity instruments. Salinity at the land surface can be broadly divided into 7 classes: nonsaline (less than 2 dS/m); moderately low (2-4 dS/m); moderate (4-8 dS/m); moderately high (8-16 dS/m); high (16-32 dS/m); very high and extreme salting (greater than 32 dS/m) (Maschmedt, 2000).

Soil salt accumulation impairs plant growth by reducing water availability to the plants. Mild salinity creates stressful conditions for many plants (Larcher, 1980) and induces plant symptoms such as 1) yellowing of leaves of crops and pasture (chlorosis) and drying before the growing season has ended; 2) slow growth rate and stunting of leaves;

3) whole plant growth rate decline; 4) reduced number of plants; 5) greater susceptibility to disease and 6) decreased seed germination and viability (Department of Primary Industries, 2004; (Larcher, 1980). These indicators become quite noticeable as the salinity spreads and patchy areas of discolouration or dieback appear in the fields of crops or pasture. The deteriorating crops and pasture can be replaced by halophytes, one of the most conspicuous indicators of salinity. Halophytic plants have adapted to saline soils by developing distinctive leaf, stem and root structures that either regulate salt ion uptake, eliminate and dilute saline water, or allow the plant to tolerate salt accumulation.

In Australia, common halophytic plants associated with mild salinity include sea barley grass, swamp couch and wimmera rye grass (Department of Primary Industries, 2004). As salinity increases to moderate levels (8-16 dS/m), these halophytes are progressively replaced by species such as salt grass, ruby saltbush, ice plant and spiny rush (Department of Primary Industries, 2004). Ultimately, when severe levels of salting are attained (greater than 16 dS/m), the only species remaining are highly tolerant plants such as beaded glasswort, samphire and rounded noon flower (Department of Primary Industries, 2004). These easily recognisable halophytes are stunted bushes, often reddish in colour with semi-succulent leaves. Plants develop tolerance to salinity by diluting salts ions in distended cells (succulence) or compartmentalising salt in plant structures such as the leaf vacuoles (Larcher, 1980). Succulence is a property of numerous halophytes caused by high concentrations of soil chloride ions. As the salts are drawn into the plant during growing season, the salt concentration can be considerably reduced if excess water can been drawn simultaneously. Samphires and other plants adapted to severely saline areas are typically found in the lowest parts of the landscape (Barrett-Lennard, 2003). Halophytic species often exhibit zonation, growing in homogeneous patches associated with favourable soil conditions and topographic features (Barrett-Lennard, 2003). Zonation of halophytic vegetation over sizable areas means that these species are ideal candidates for mapping with remote sensing imagery.

The final extreme stage in the salinisation process is the development of highly concentrated saline seeps. Plant damage is so severe that no vegetation, including halophytes, can be sustained. At this point, soil becomes exposed and prone to erosion. Stock can even exacerbate soil exposure by preferentially occupying the wet, cool, salty

discharge sites. On bare ground where saline seeps persist, surface water can readily evaporate, leaving behind an obvious white stain of salt crystals or salt crust. In arid regions these crystalline crusts mainly contain NaCl (Chhabra, 1996). At these severe levels of salinity (greater than 32 dS/m), no plants can tolerate the conditions and a permanent saltpan will result.

Different salinity symptoms are associated with varying levels of salinity as well as changing hydrogeological provinces. In the winter dominant rainfall regions of southern Australia, particularly in Western Australia and the Upper South East (USE) of South Australia, waterlogging is of primary concern. In these cropping areas, salinity mapping surveys have reported a range of other salinity symptoms, such as exposed salt-affected ground, marginally saline areas with a good cover of halophytic vegetation (Furby, 1995; Furby, 1998; Furby, 1999). Adjacent to the USE are the western margins of the Murray Basin where discharge from regional aquifers produce severe regional dryland salinity problems. In the coastal plains of South Australia, salinas with high salinity levels occur up to 150 km inland (Warren, 1982), sometimes associated with extensive samphire flats. The salinas are easily recognisable as broad flattish areas low in the landscape that exhibit symptoms such as vegetation death, salt accumulation on the surface and soil erosion. Similar salinity levels occur in some parts of the eastern Mallee in Victoria, where groundwater salinity levels are similar to sea water (Coram *et al.*, 2000). In this region, lowlying shallow ephemeral lakes and wetlands have concentrated through evaporation to form salinas (Coram *et al.*, 2000).

Groundwater salinity generally decreases from the western reaches of the Murray Darling Basin to the eastern basin margins and into the NSW and Victoria uplands (Coram *et al.*, 2000). Victoria reports a variety of symptoms with more severe salinity occurring in the west and lower slopes of the ranges of NSW and Victoria and in Central Victoria. In the uplands of eastern Australia, levels of salinity are generally low or moderate and in the steeper uplands large areas of salinisation seldom occur (Coram *et al.*, 2000). These areas are more likely to exhibit less severe symptoms of salinity such as salt tolerant grasses.

1.3 Conventional mapping and monitoring dryland salinity

Unambiguous knowledge as to the distribution and quantity of recharge and discharge is necessary for the implementation of dryland salinity management plans, particularly in

the worst affected agricultural districts. Data gathering about how these processes vary spatially across the landscape and how they change over time is time consuming and expensive (SCARM, 2000).

For over a decade, studies have assessed multispectral remote sensing imagery for mapping areas affected by dryland salinity, particularly in Australia, because traditional farm surveys failed to "provide maps of where the salinity is, where it is spreading to or the rate at which it is spreading" (Evans *et al.*, 1996). Current remote sensing methods include optical systems, such as aerial photography and satellite imagery, and more recently airborne electromagnetics and improved optical hyperspectral sensors. The satellite borne Landsat Thematic Mapper has been considered the most appropriate cost effective method for mapping and monitoring dryland salinity at regional or catchment scales, whereas aerial photography is the most accurate method at farm scale (Webb and Price, 1994).

1.3.1 Aerial photography

Aerial photographs are interpreted by comparing observed colour, fine details and tonal changes to other relevant expert groundbased knowledge such as geology, geomorphology, soils and landuse (Ferdowsian, 1994). Typical aerial photography mapping is at a medium (1:20,000 to 1:80,000) or fine scales (1:4,000 to 1:20,000).

Aerial photographs were utilised by the National Land and Water Audit in NSW and SA to supplement groundwater data to produce landscape maps of dryland salinity (Webb, 2000). The highly regarded Soil Landscape Unit maps in South Australia were also based on aerial photographic interpretation in conjunction with extensive field soil sampling (Maschmedt, 2000). Salinity mapping from aerial photographs involves the detection of visible salt on the land surface or the identification of surrogate landcovers such as vegetation and surface water that infer salinity (Spies and Woodgate, 2004). Mapping might also entail detecting landforms related to salinisation landscape processes. Areas that have distinctive soil and landscape characteristics are portrayed as homogeneous mapping units on conventional maps or polygons in GIS (digital geographical system) databases. This mapping convention usually acknowledges that the mapping units do not portray spatial variability of soils at the scale of mapping. In addition, it does not allow for mapping of gradational or transitional zones of soil variation.

Although photo interpretation is an important aid to salinity mapping, Hick and Russell (1988) point out that aerial photography is technically restricted by the lack of "geometric control and photosensitivity" and the limited spectral coverage beyond visible wavelengths. Conventional aerial photography generally requires time consuming and costly visual interpretation for mapping which is not well suited to digital analysis and more automated mapping approaches. Recent development in Australia is the introduction of aerial digital cameras, although no significant salinity mapping projects have been reported (Spies and Woodgate, 2004).

1.3.2 Geophysical mapping of subsurface salinity

There are many geophysical methods available for geological and hydrogeological investigation, including gravity, magnetics, electromagnetic and radiometrics. The most important geophysical methods for subsurface salinity mapping are groundbased or airborne electromagnetics.

Electromagnetics methods measure the electrical conductivity of soils and regolith. High conductivity is usually associated with electrolytic dissolved salts in moisture-filled pore spaces. Saline groundwater is highly conductive whereas dry salt is non-conductive. However, careful interpretation is required because various studies have found some clay types to also have high conductivity (2001).

Though geophysics has an important role to play in mapping aspects of subsurface salinity, the National Airborne Geophysics Project has also named other crucial datasets. These datasets include topography, orthophotos, hydrological data, multi-spectral data (e.g. Landsat satellites, airborne multi-spectral and thermal scanners), soil maps and geophysical data. However, the report acknowledged that many datasets are not readily available or are not at the scale or resolution needed.

1.3.3 Multispectral remote sensing of surface expressions of salinity

The first Landsat multispectral satellite was launched in 1972 for the specific purpose of broad-scale repetitive observation of land areas on the surface of the earth to discriminate dominant landcover types of vegetation soil and water (Campbell, 1996). Since earth-orbiting satellites periodically pass over the same region at regular intervals, new data time is recorded each time so that changes in land use and condition can be monitored.

The Landsat TM wavelength bands coincide with the visible, near infrared (NIR) and shortwave (SWIR) regions in the electromagnetic spectrum. These bands were chosen to optimise discrimination of common landcovers for landuse mapping, general vegetation inventories and geological studies (Jensen, 2000). The particular value of these wavebands is water penetration, discrimination of vegetation types, differentiation of clouds, snow and ice and identification of certain hydrothermally altered rocks. The visible and NIR bands maximise leaf reflectance related to leaf pigmentation, leaf canopy and structure and moisture content.

Early on, classification methods and vegetation indices were developed for monitoring the environment and change in landuse patterns. Vegetation indices sensitive to vegetation condition were also developed to extract and model plant biophysical variables associated with vegetation health, such as green biomass and the related leaf area index (LAI) [1]. Jensen (2000) credits Rouse *et al* (1974) with the development of the widely used Normalised Difference Vegetation Index or NDVI, which has been commonly applied to multitemporal satellite data to map general changes in vegetation.

Over the last two decades, several studies have assessed multispectral satellite imagery for mapping and monitoring surface salinity with mixed results (Hick and Russell, 1988; Wheaton *et al*., 1992); Mougenot *et al*, 1993; (Evans and Caccetta, 2000; Evans *et al*., 1996; Furby *et al*., 1998; Furby *et al*., 1995; Kiiveri and Caccetta, 1998; Metternicht and Gonzalez, 2000) Howari, 2003; Metternicht and Zinck, 2003). Landsat TM imagery incorporating the thermal band proved useful in discriminating white surface expressions of salt from bright sandy soils because both soils are indistinguishable in the visible and near infrared wavelengths (Metternicht and Zinck, 1997; Verma *et al*., 1994). Separation of vegetated saline from non-saline sites can be achieved by comparing satellite images from dry season images to images taken at the time of maximum vegetation growth (sometimes referred to as “spring flush”) (Hick and Russell, 1988; Rao *et al*., 1991). During the spring flush, there is maximum vegetation growth at the non-saline sites, then as the dry season progresses, the

[1] Vegetation indices have been well summarised by Jensen, J.R., 2000. Remote sensing of the environment: An earth resource perspective. Prentice-Hall Series in Geographic Information Science. Prentice Hall, Upper Saddle River, N. J.

vegetation dries out. This phenological change in vegetation may not be apparent at saline sites; instead, vegetation can be limited all year round.

Integration of satellite imagery with other datasets has also improved mapping accuracy (Caccetta *et al*., 2000; Evans and Caccetta, 2000; Evans *et al*., 1996; Furby *et al*., 1998; Furby *et al*., 1995; Kiiveri and Caccetta, 1998; Thomas, 2001). Kirkby (1992) recognised the scope for integration of datasets such as digital elevation models (DEM), soil type, geology and groundwater within the GIS framework. For example, Evans *et al* (1996) integrated digital elevation data with Landsat imagery using a decision tree classifier, to produce successful classification maps of several landcover classes such as bare salt scalds, bare soil, water, remnant vegetation, crops and pasture.

Multispectral satellite imagery is currently regarded as the preferred low cost broad scale mapping method because of its ability to map extreme surface expressions of salinity. The main advantages of satellite imagery are the synoptic views of large areas and the repeated acquisition at intervals of a few weeks (Gunn *et al.*, 1988). However, multispectral data has limited diagnostic capabilities because it lacks fine scale spatial information (compared to aerial photography) and spectral information (Kruse, 1998). The major limitations of direct mapping of salt affected soils with multispectral imagery occur where saline soils are covered with salt-tolerant vegetation (Furby *et al* 1995; Howari, 2003) and where there is no evidence of salt crust (Howari, 2003). Furby *et al.* (1995) also noted that non-saline exposed soils were often confused with bare, severely salt affected areas. Maximum likelihood classification was then able to accurately map spectrally distinct bare saline affected areas and halophytes, but, marginally saline areas with salt tolerant grasses and weeds were mapped with less accuracy and were often spectrally confused with heavily grazed pastures or low productivity non saline pastures (Wheaton *et al*., 1992). Most studies have attempted to overcome the spectral and spatial limitations of the imagery by combining multitemporal imagery and ancillary data, such as soils and terrain data.

Fraser and Joseph (1998) suggest that Landsat spectral resolution is inadequate because the difference between the spectra of saline land, stubble and waterlogged land was “not significant enough to allow spectral separation”. Furthermore, they concluded that the broadband spectral response of saline soil is extremely variable, with only extreme expressions of surface salt, such as large salt scalds, exhibiting spectral uniformity. In addition, the absence of narrow bands in the ranges of 700-730 nm, 730-760 nm and

900-1100 nm limits the ability to discriminate plant species and plant health (Hick and Russell, 1988).

Research groups and catchment managers are becoming aware of the need for improved remote sensing technologies for baseline mapping and ongoing monitoring of salt affected areas (NDSP, 2004). The NAGP Report recommended investments in R&D to optimise technology to "improve the performance of radiometrics and hyperspectral remote sensing techniques for the definition of soils and their mineralogical, physical and chemical properties". Thomas (2001) concluded that emerging remote sensing technologies would not only increase current dryland salinity extent mapping capabilities, but also improve salinity prediction. These new technologies include imagery acquired by the satellite borne ASTER sensor, RADAR-derived digital elevation models (DEM), airborne geophysics and high resolution hyperspectral remote sensing.

1.4 The advantage of high spectral resolution imagery

Hyperspectral remote sensing began in the 1980s with the development of AIS (Airborne Imaging System) and the NASA Airborne Visible-InfraRed Imaging Spectrometer (AVIRIS). Hyperspectral remote sensing instruments are a major advance in remote sensing capabilities because they offer a significant increase in the number of spectral bands compared to multispectral instruments. Multispectral sensors "drastically under sample the information content available from a reflectance spectrum" (Kruse, 1998) by acquiring data in only a few spectral bands, each up to several hundred nanometers wide. In contrast, hyperspectral or imaging spectrometers sample 100-200 or more bands at fine intervals, generally less than 20 nm wide. The large number of contiguous fine resolution bands produce almost continuous spectral response curves.

Hyperspectral imagery has the unique combination of high spectral resolution and the ability to be calibrated to absolute reflectance, so that direct comparisons can be made to field and laboratory spectra. Laboratory and field spectrometers directly measure the radiation reflected from materials as continuous response curves in the visible, near infrared (NIR) and shortwave infrared (SWIR) wavelengths. This continuous spectral response curve is referred to as the spectral signature.

In order to evaluate hyperspectral imagery for mapping dryland salinity, it is necessary to firstly understand the spectral properties of soils and vegetation and how salinity influences their spectral response.

1.4.1 Spectral response of plants

The overall spectral reflectance of plant canopies is a function of the total leaf area exposed to the sensor, an absorption coefficient, a scattering coefficient and the background reflectivity (Knipling, 1970). Therefore the canopy spectral response can be a mixture of reflectivity and absorption from photosynthetically active green leaves and branches, shadows and background soil. However, it is the spectral response of leaves that dominate the reflectance spectra of green plant canopies.

The spectral response of green leaves is a function of chlorophyll and other pigments, various biochemicals, internal leaf structure and leaf water content[2]. The surface of the leaf is largely translucent to solar radiation, whereas the underlying layers containing pigments absorbs radiation. The absorption properties of chlorophyll, carotenes and xanthophyll pigments produce the general low reflectivity in the visible part of the spectrum between 400 and 700 nm (Gates *et al.*, 1965). In this wavelength region, the main spectral features of green leaves are the chlorophyll a and b absorption in the blue and red wavelengths and a characteristic peak in green wavelengths (of 525-605 nm). Consequently, the visible part of the spectrum is important for discriminating between plant species (Elvidge, 1990).

Typically, the continuous laboratory spectral signature of healthy photosynthetically active green leaves has significantly higher reflectance in the NIR, associated with leaf cellular structure, and beyond 1300 nm reflectance is dominated by broad water absorption features (Gates *et al.*, 1965); Knipling, 1970, Gausman, 1973). The rapid increase in reflectance between the visible red and NIR wavelengths around 700 nm is known as the red-edge. The spectral structure within the NIR region is shaped by strong water absorption features and associated “lobes” at 900, 1080 and 1270 nm (Elvidge, 1990).

---

[2] A comprehensive table of published absorption features of plant spectra has been compiled by Lewis and Jooste Lewis, M. and Jooste, V., 1999. Identification of vegetation signatures in AMS imagery., Unpublished report to the Anglo American Corporation.

In the short wave infrared (SWIR) region beyond 1300 nm, the overall shape of green leaf spectra is mainly influenced by water. Green leaf spectra are dominated by broad water absorptions centred at 1460 and 1950 nm, which generally "mask' finer lignin, cellulose, tannin, pectin and plant wax absorption minima seen in dry plant material (Elvidge, 1990). Cellulose and lignin absorption features are combinations and overtones of fundamental absorptions in the thermal infrared. Elvidge lists the cellulose features centred at 1220, 1480, 1930, 2100, 2280, 2340 and 2480 nm, and lignin absorptions which occur at 1450, 1680 and 1930 nm, a broad absorption region centred at 2090 nm and SWIR absorptions at 2270, 2330, 2380 and 2500 nm.

1.4.2 Effects of stress and senescence on plant spectral response

Spectral changes in stressed leaves can be seen principally in the visible and VNIR regions spanning 400-800 nm (Carter and Miller, 1994; Elvidge, 1990; Hick and Russell, 1988; Knipling, 1970; Wang *et al.*, 2001). During early senescence, the red-edge, around 700 to 800 nm, shifts to shorter wavelengths and the NIR "leading edge" collapses (Elvidge, 1990).

Advanced senescence or chlorosis (i.e. yellow to red brown leaves) is symptomatic of extreme changes in leaf pigments (Elvidge, 1990; Knipling, 1970). Reduced radiation absorption by deteriorating chlorophyll produces a simultaneous increase in reflectance in visible green and red wavelengths (Carter and Miller, 1994; Knipling, 1970)). Gausman and Allen (1973) discussed the significant contribution of decreased leaf water content in the yellow (non dried) leaf spectra to increased reflectance in the 750-1300 nm range. Other studies also recognise the value of examining spectral structure in the SWIR region for detecting plant chlorosis (Elvidge, 1990; Hick and Russell, 1988).

1.4.3 Spectral variation between plant groups and species

Spectral differences between plant types are difficult to detect, because most plants have essentially the same biochemical constituents. Furthermore, most pigments, biochemical and structural components have relatively broad and often overlapping absorption features (Elvidge, 1990), unlike the fine, distinctive absorptions of minerals. Therefore, spectral variations between plant types are mainly based on relative differences in reflectance across broad spectral bands (Lewis, 2001). However, there are also considerable relative differences in reflectance within plant groups, due variation in

structure, growth stage, health and composition. Unfortunately, the spectral variability between species may be less than the range of variability within species (Price, 1994).

Despite these difficulties, early studies identified variations in reflectance spectra between plant groups, and even to some extent between species (Gates *et al*., 1965; Gausman and Allen, 1973; Knipling, 1970). Generally, plant pigment variation between groups can be observed in the visible part of reflectance spectra, whereas variations in cell structure and water content are expressed in the NIR and SWIR regions. Differences in these regions contribute to plant group discrimination (Elvidge, 1990; Gates *et al*., 1965; Lewis, 2001; Lewis, 2002; Sampson *et al.*, 1998). Specifically, desert succulents reflect substantially more radiation in the visible and NIR regions than mesophytes (Gates *et al*., 1965). The visible part of the spectrum associated with chlorophyll absorption and the bands associated with the "red-edge" region, were also found to be the key regions for maximum discrimination of grass species in the African rangelands (Schmidt and Skidmore, 2001). For discriminating groups of Australian arid zone plants, the most influential spectral regions are the infrared (beyond 740 nm), the chlorophyll absorption band centred at 680 nm, the green and other visible wavebands (Lewis, 2001).

In the SWIR region, Elvidge demonstrated that the broad water features prominent in the reflectance spectra of fresh leaves mask many fine cellulose and lignin absorption features in plants of mesic environments. These fine fetures become evident in the spectra of dried plant material. These biochemical absorptions may be more readily observed in the spectra of plants adapted to arid environments, because of specialised leaf tissue structure, such as leaf thickening and sometimes reduced leaf water content (Lewis *et al.*, 2000).

Therefore, spectral discrimination of halophytic species may also be possible because of their distinctive leaf and stem structure adaptations. Lewis *et al* (2000) observed that semi-succulent foliage of salt tolerant chenopod shrubs display subdued VNIR reflectance and multiple SWIR absorption features that can be attributed to waxy cuticle leaf coating. Dehaan and Taylor (2002B) found the spectral signature of samphire (*Halosarcia pergranulata*) to be characterised by two peaks at 555 nm and 624 nm due to accessory pigments and a distinctive slope to the infrared reflectance plateau between 1250 and 1400 nm. Furthermore, the variable depth of the NIR water absorption features in conjunction with the height of the associated "lobes" at 900, 1080 and 1270

nm are also important structures for plant species differentiation (Elvidge, 1990) such as halophytes (Dehaan and Taylor, 2002B).

Discriminating plant groups such as halophytes is showing promise, particularly for plants with spectral features in the SWIR. However, difficulties arise from the highly variable nature of foliage reflectance due to leaf angle, crown structure and nonphotosynthetic vegetation, all of which may impede discrimination and must be considered during spectral analysis (Cochrane, 2000).

1.4.4 Spectral characteristics of soils

The spectral signature of soils is a function of soil texture (particle size) and surface roughness, soil moisture content, organic matter content and mineral constituents such as iron oxide and clay content (Ben-Dor *et al.*, 1999), particularly in the wavelength range 1300-2400 nm (Baumgardner *et al*., 1985; Hick and Russell, 1990).

Mineral constituents such as iron oxides and clay groups have more easily recognisable features. The major characteristics of soil reflectance curves are strong water absorption bands at 1450 and 1950 nm and occasionally at 970, 1200 and 1770nm (Baumgardner *et al*., 1985). Strong absorption bands are due to bound water, specifically hydroxyl ions. Clay minerals generate strong water absorption features due to their hygroscopic properties. The spectra of kaolinite soils contain an hydroxyl feature around 1400 nm, coinciding with the 1450 nm water feature, and an asymmetric doublet hydroxyl feature around 2200 nm (Goetz *et al.*, 1985).

The properties of saline soils which most influence their reflectance spectra are salt minerals, poor soil structure, low organic matter, low microbial activity and free or crystal lattice bound water (Ben-Dor, 1999). However, the complexity of soil properties makes spectral identification of soil saline minerals problematic (Csillag *et al.*, 1993), compounded by the fact that one of the most common salts, halite, has an essentially featureless spectrum in the optical wavelengths (Crowley, 1993).

Nevertheless, some studies have investigated spectral properties of salt crusts, identifying distinctive spectral features relating to numerous evaporite minerals (Crowley, 1993). Saline crusts, formed by sustained evaporation of near surface groundwater, are combinations of evaporite minerals. The saline crusts have been found to exhibit fine diagnostic absorption features, particularly in the SWIR region, corresponding to overtones of fundamental vibrations of hydrogen bonded structural

water molecules and other ions such as carbonate and nitrate (Crowley, 1993). Saline crusts are combinations of evaporite minerals and have various diagnostic absorption features in the SWIR region (Crowley, 1993). Drake concluded that anhydrous chloride and sulphate minerals such as halite and anhydrite, possess very similar high albedo spectra in addition to the ubiquitous water absorption features near the 1450 and 1950 nm (Drake, 1995).

More recently, some spectral features of irrigation induced saline soils have been identified by Dehaan and Taylor (2002B). However they acknowledge, like Csillag, that precise determination of soil composition through spectral analysis was difficult, particularly the surface salt efflorescence, which is highly sensitive to variations in watertable height. Saline soils were found to have a pronounced reflectance high, or shoulder, from around 800 nm to 1300 nm, with the slope of this ramp decreasing as salinity increases. Dehaan and Taylor (2002B) also reported that increasing salinity could be inferred from the reduced intensity of the 2200 nm hydroxyl feature and a reflection high at 800 nm. However, reduction in the clay feature could be associated with increasing moisture.

1.5 The potential of hyperspectral imagery to map dryland salinity

Many field and laboratory studies have demonstrated the existence of spectral characteristics associated with salinity symptoms, such as plant stress (namely chlorosis and reduced plant growth), halophytic plant species, soil moisture, saline mineralogy and salt scalds. When interpreting remotely sensed images, it is assumed that differences exist between the spectral signature of different types of soils and vegetation and between healthy vigorously growing vegetation and stressed plants and that these differences can be observed and assessed (Gates *et al*., 1965). Distinctive spectral features associated with different landscape components can be extracted and used to produce image maps showing the location and abundance of each component. High spectral resolution imagery, therefore, makes possible greater discrimination between landscape features, vegetation groups and species, and more precise crop health evaluations.

By exploiting the distinctive spectral characteristics of soil and vegetation, high spectral resolution airborne imagery has mainly been applied to surface geological mapping (for details of AVIRIS geological mapping case studies see Kruse (1998)). However, its

capabilities are being extended to map soil minerals and properties (Palacios-Orueta and Ustin, ; Ryan and Lewis, 2001), vegetation types (Chewings *et al.*, 2000; Lewis, 2002; Lewis *et al.*, 2000; McGwire *et al.*, 2000; Roberts *et al.*, 1993) and coastal areas (Dekker and Bukata, 2002; Green *et al.*, 1998; Silvestri *et al.*, 2002; Underwood *et al.*, 2003).

Hyperspectral data has the potential for detecting subtle changes in plant pigments sensitive to stress (Gamon *et al.*, 1993). Wavebands associated with pigment sensitivity are commonly used in narrow band vegetation indices, developed by field or laboratory spectral studies. Gamon *et al.* (1993) applied NDVI to AVIRIS data and concluded that structurally based indices are able to capture seasonal and spatial patterns in canopy greenness and therefore plant productivity. A leaf scale water stress model based on NIR, green, red and SWIR waveband indices was successfully applied to HyMap imagery to map variations moisture stress in eucalypts (Chisholm, 2001).

Other than plant stress, the presence of halophytic plant species is an obvious symptom of saline soils. Some initial success was achieved in the Lewis *et al.* (1999) study which isolated chenopod shrubs, such as halophytic saltbush, from Airborne Multispectral Scanner data.

A significant recent study by Dehaan and Taylor (2002A) assessed hyperspectral imagery for mapping irrigation-induced salinity. Image-derived spectra (endmembers) were successfully equated with several halophytic species. Image endmembers with twin reflectance peaks in the visible red and distinctive slope between 1250 and 1400 nm were identified as either samphire, which under saline conditions appears red, or the purple/red halophyte sea blite. Distinctive absorption features at 2080 and 1720 nm also identified halophytic grasses. In image-derived spectra, the authors also found that the presence of evaporite minerals, such halite and bassenite, could be inferred from a prominent shoulder at 800 nm, and variations in hydrate absorption features at 900 and 1150 nm. They concluded that airborne hyperspectral data could differentiate saline from non-saline bare ground (due to ploughing for example), which is a significant advance over earlier sensors.

1.6 Conclusion

By exploiting the distinctive spectral characteristics of soil and vegetation, high spectral resolution airborne imagery has proved a powerful tool for geological and land cover

mapping. Preliminary studies have also applied hyperspectral imagery to mapping soil and vegetation indicators of irrigation-induced salinity (Dehaan and Taylor, 2002A; Taylor, 2001; Whiting and Ustin, 1999), although the resultant maps were not statistically assessed for accuracy. The fine spectral and spatial resolution of airborne hyperspectral imagery may allow for discrimination of salt tolerant plants and certain properties related to saline soils. To evaluate the capabilities of hyperspectral imagery for mapping dryland salinity, studies need to be carried out in affected regions with variable terrains, soils and landcovers and using hyperspectral imagery with different spectral and spatial specifications.

1.7 Research aims

Given the magnitude of the dryland salinity problem in Australia and the limitations of current remote sensing methods, the overall aim of this study was to determine whether hyperspectral imagery can be used to improve the mapping and monitoring of surface symptoms of dryland salinity. The study used a South Australian site within the Murray-Darling Basin to characterise the reflectance properties of surface salinity symptoms and evaluate the suitability of several forms of hyperspectral imagery for mapping them at catchment scales.

Specifically, the project objectives were to

1. Characterise how dryland salinity was expressed in the landscape and determine those salinity symptoms were spectrally and spatially suited to mapping with hyperspectral imagery;
2. Identify the optimum time of year for mapping each target symptom, especially areas with a good cover of salt tolerant vegetation.
3. Compare and evaluate the suitability of different spectral and spatial resolutions of airborne and hyperspectral imagery for mapping selected dryland salinity symptoms;
4. Compare image-derived maps of salinity symptoms with conventional soil and salinity mapping and multispectral image mapping; and
5. Develop an efficient and consistent processing procedure for mapping symptoms of salinity at regional and catchment scales.

1.8 Significance

This research responds to the recent calls from the National Dryland Salinity Program for improved remote sensing methods for baseline mapping and ongoing monitoring of dryland salinity. Hyperspectral imagery has the potential to address the problem of underestimating the extent of salt affected land because the high spectral and spatial resolution imagery may allow for mapping of salt affected land with a good cover of vegetation. This study explores that potential by evaluating several forms of hyperspectral imagery, each with differing spatial and spectral resolutions, and collected at different times of year, for their suitability for mapping dryland salinity symptoms.

While studies to date have applied hyperspectral imagery to the mapping of soil and vegetation indicators of irrigation induced salinity at specific sites (Dehaan and Taylor 2002B), this study evaluates hyperspectral imagery for mapping salinity across broader landscapes where dryland agriculture is the predominant landuse. Dryland salinity affects larger areas and a wider range of landscape contexts than irrigation induced salinity. The study area is part of the Lower Murray region and has large areas of salt affected land that are contributing to the increasing salinity of the Murray River and Lake Alexandria and is an increasing threat to agriculture. The Lower Murray region has been identified as a "priority region" by the National Action Plan for Salinity and Water Quality[3].

Mapping farms, catchments and regions necessitates the use of extensive sets of airborne hyperspectral imagery to cover these broad areas of interest. These extensive datasets pose a challenge which require the development of suitable radiometric and geometric image calibration methods as well as techniques for consistent image analysis and mapping. In meeting these methodological challenges, this research places emphasis on the use of readily available image analysis and mapping techniques to provide catchment managers with an accessible alternative to conventional salinity mapping based on aerial photography interpretation and multispectral satellite imagery.

[3] Priority region map is available from the National Action Plan for Salinity and Water Quality (NAP) website [http://www.napswq.gov.au/priority-regions.html]

1.9 Thesis outline

Chapter 1 has provided an introduction to the problem of dryland salinity and reviewed the literature on remote sensing methods for salinity mapping and the capabilities of hyperspectral imagery. The aims and significance of this research have also been explained.

In Chapter 2, the hydrogeology and history of landuse at the study site are described in order to explain the occurrence of dryland salinity in the region. Current salinity maps from the region are also reviewed. Soil analyses are presented to demonstrate the levels of salinity at some salt affected sites. Finally, the results of field observations and measurements are presented, leading to the identification of salinity symptoms that have suitable spatial distribution for remote sensing mapping.

Chapter 3 reports the spectral characterisation of these salinity symptoms in order to establish which symptoms had spectrally distinguishing properties and were therefore suited to mapping with hyperspectral imagery. This chapter also presents methods used for collecting multiple field and laboratory spectra of various grass species at different times of year. Statistical comparisons were performed in order to determine the optimum time of year to map sea barley grass, an important early indicator of salinity.

Chapters 4, 5 and 6 detail the mapping of the chosen salinity symptoms with HyMap multiple airborne image swaths, Hyperion satellite imagery and CASI multiple swaths respectively. Image feature extraction mapping procedures were devised to optimise salinity mapping for each hyperspectral dataset, and field data was used to assess the accuracy of the mapping.

Chapter 7 reports comparisons of the resultant hyperspectral salinity maps to previous salinity maps of the study site. The final Chapter reviews the results from each section and summarises the key findings of this research.

2 CHARACTERISING SALINITY AT POINT STURT

2.1 Introduction and aims

The initial research stage aimed to characterise salinity at the study site, Point Sturt in South Australia, by examining local salinity maps and landuse history in the area. The next stage involved field observations and soil sample analysis. Fieldwork entailed identifying salinity symptoms and collecting and analysing soil samples to measure salinity levels. Field observations aimed to determine which salinity symptoms were spatially suited to mapping with remote sensing imagery and to identify the optimum time of year for mapping each target symptom, especially areas with a good cover of salt tolerant vegetation.

2.2 Study Site

Point Sturt is situated 70 km southeast of Adelaide on the eastern side of the southern Mt Lofty Ranges in South Australia (Figure 2-1). Point Sturt Peninsula juts into Lake Alexandrina, near the mouth of the Murray River and is part of the Murray-Darling Basin catchment. The peninsula and the lake are part of the Murray River coastal plain.

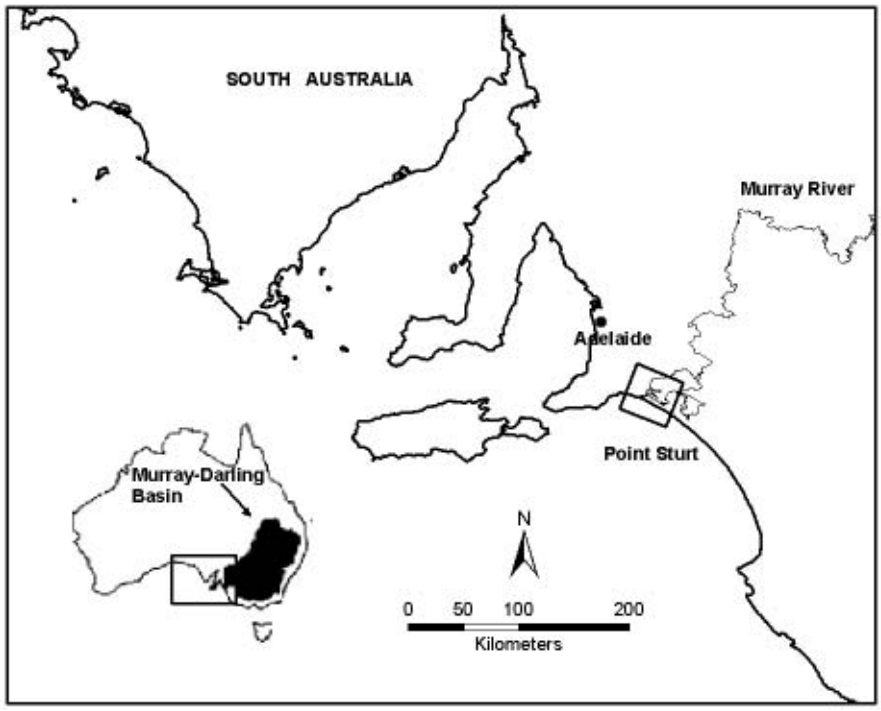

Figure 2-1 Point Sturt Peninsula is located at the mouth of the Murray River in South Australia

2.2.1 Climate

The area has a Mediterranean climate with cool, wet winters (June to August) and warm, dry summers (December to February) (Figure 2-2). The peninsula is predominately a dryland farming region with a mean annual rainfall of approximately 425 mm.

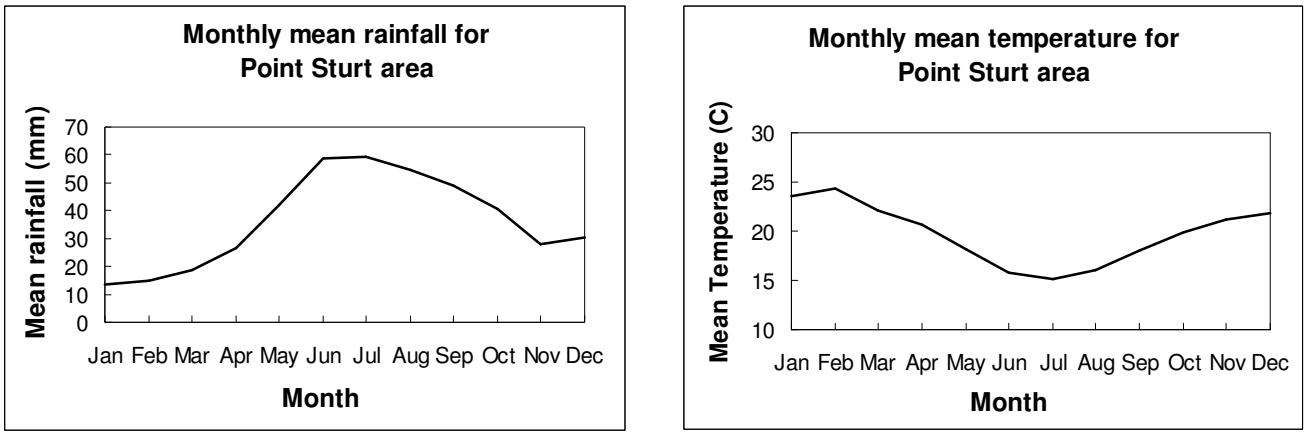

Figure 2-2 Monthly mean rainfall (top) and temperature (bottom) from 1989 to 2003 (from Hindmarsh Island immediately south of Point Sturt). Data from the Bureau of Meteorology [http://www.bom.gov.au/]

2.2.2 Landscape and hydrogeology

Point Sturt is part of the Murray-Darling Basin depression, which has filled with Quaternary and Tertiary sediments. The salt stores in the sediments have accumulated primarily originate from rainfall and aeolian deposition of airborne marine salts, which have been concentrated through evaporation over tens of thousands of years of relative aridity (Herzeg *et al.*, 2001). The peninsula itself is part of an ancient coastal dune range (Thomas, 2001). Interdunal salt lakes originated during the Holocene when sea-water fed groundwater lakes formed in the permeable Quaternary beach-dune system (Warren, 1982).

The area can be divided into two definable hydrogeological regions based on two main regional aquifer systems (Figure 2-3), the deeper regional confined limestone aquifer in the east and the upper watertable clay aquifer in the west (Dooley and Henschke, 1999). The eastern area is dominated by sandy soils overlaying rocky calcrete containing the limestone aquifer system. The calcrete rises to the highest point, 29 metres, at the far eastern end of the peninsula. In the west, the dominant soil types include sands, loams and calcareous soils of variable depths overlaying sedimentary clays that host the

separate regional clay aquifer. The main clay aquifer flow terminates into coastal and central lowlying areas in preference to Lake Alexandrina (Dooley and Henschke, 1999). In these low-lying areas, there is highly saline groundwater due to strong evaporative discharge. These areas are associated with dryland salinity symptoms, such as waterlogging, saline discharge sites, saltpans and hyper-saline lakes; some of these extreme saline areas are thought to be naturally occurring primary salinity (Thomas, 2001). Of concern are the increasing saltloads in the swales and flats on the peninsula that directly feed into the Lake Alexandrina (Dooley and Henschke, 1999).

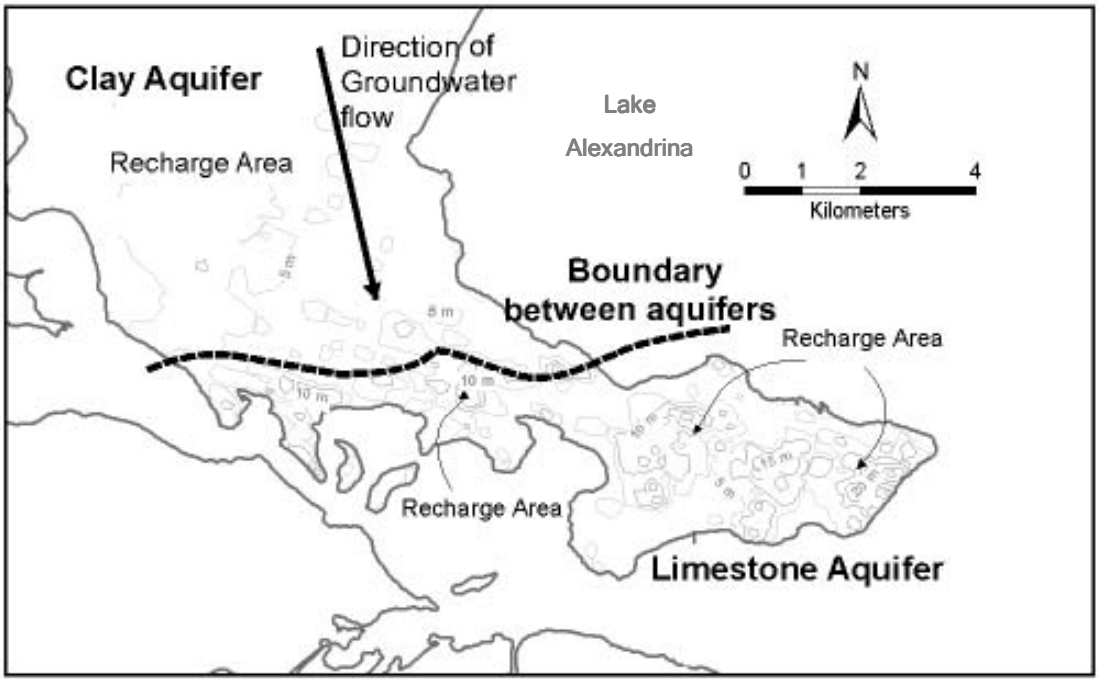

Figure 2-3 Hydrogeological map of Point Sturt Peninsula showing the boundary between the clay and limestone aquifers (dashed line), major recharge areas (after Henschke (2000)) and elevation contours.

2.2.3 History

Since the time of European settlement in the 1800s, extensive land clearing has contributed to aquifer recharge. By 1956 the entire peninsula was cleared but large tracts of less dense remnant vegetation still persisted in the west (Figure 2-4). The early settlers noticed the sharp contrast between the fertile, grassy, open country of the Angas-Bremer plains in the north and the thickly wooded mallee scrub which grew on a variety of high limestone content soils (Faull, 1981). The native halophytic vegetation

around the lake was samphire, sea barley grass[4] and saltwater couch (Faull, 1981). On the peninsula, the dense mallee scrub gave way to low woodland formation in which she-oaks and melaleucas were common.

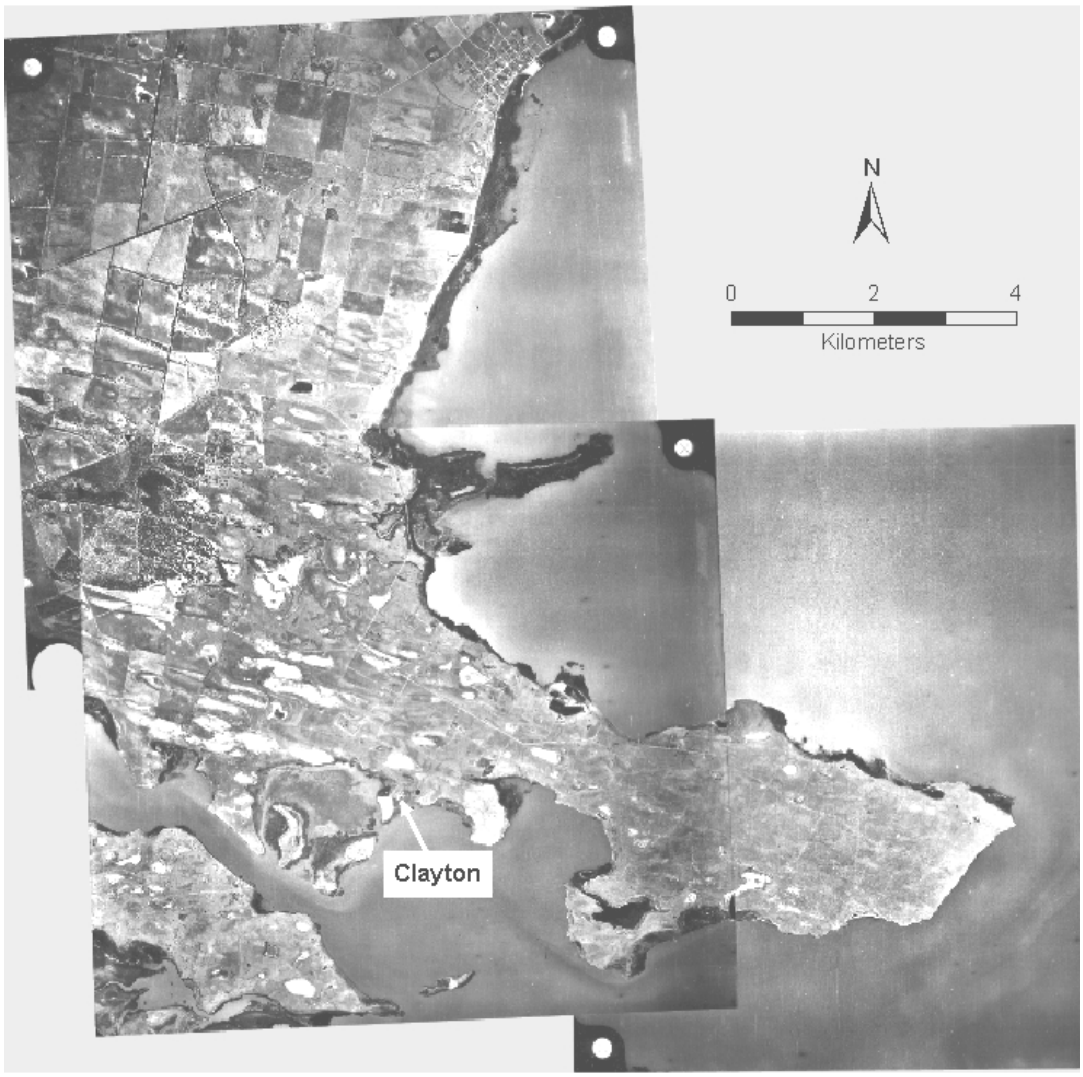

Figure 2-4 Mosaic of three aerial photographs taken in 1956 of Point Sturt (courtesy of Department of Environment and Heritage, Mapland, South Australia). The land had been extensively cleared by this time. At the time there were significant areas of remnant vegetation in the west and little vegetation on the bare dune ridges just north of the site where the township of Clayton later developed. White exposed soils are visible throughout the peninsula

2.2.4 Present landuse and vegetation

Today, annual grasses and pastures cover most of the study site, with mixed agriculture of grazing and cropping in the west and predominately grazing in the east. However,

[4] Faull designates sea barley grass as a native halophyte, however in Flora of South Australia Part IV (Jessop, 1986) defines sea barley grass as an introduced species.

small patches of remnant native vegetation still persist throughout the area, mainly on the dunes in the west and some riparian wetlands thrive in coastal areas (Michalski, 2000).

Much of the lowlands are at risk from rising watertables (Dooley and Henschke, 1999), which are recharged from three main sites (Michalski, 2000). The Point Sturt management plan developed strategies to reduce recharge whilst supporting the economic viability of the local farmers (Michalski, 2000).

2.2.5 PIRSA soil maps

During the 1990's, an inventory of the land and soil resources of South Australia's agricultural districts was undertaken to produce a base-line database of soil attribute maps using the geographic information system (GIS) technology (Maschmedt, 2000; PIRSA Land Information, 2001B). The PIRSA soil landscape units (SLU) maps were compiled by extrapolating and interpolating data from air photo interpretation, field observations and recordings, laboratory analysis, stratigraphy, expert knowledge and existing mapping data.

The inventory includes a range of soil and landscape attributes which are linked to each soil landscape unit (SLU) or mapping polygon with hard boundaries that represent transition zones (PIRSA Land Information, 2001B). Each attribute has some significance for agricultural use or management. Interpretive boundaries were mapped from 1:40,000 colour aerial photography and mapped onto 1:50,000 or 1:100,000 base depending on the agricultural district. Photographic information was also supplemented with soil data from over 24,000 field sites. Soil mapping in the Point Sturt region was predominately carried out at a scale of 1:50 000[5]. Maschmedt recognises there are limitations in the mapping system as the "criteria used to define the classes are based on observation and experience only, and not on experimental work".

The attribute *salinity induced by rising watertables* (SALT_COM) accounts for dryland salinity but does not distinguish secondary and primary salinity (Maschmedt, 2000). This salinity attribute is assigned seven classes depending on the level of salinity of the landscape as a whole (Table 2-1) and the extent of land affected by highly saline

[5] The border between the 1:50,000 and 1:100,000 maps occurs at the eastern tip of the Point Sturt Peninsula. This border corresponds to the boundary between South Australian map sheets.

seepage (Table 2-2). The landscape units with assigned salinity levels can be represented as a GIS map (Figure 2-5).

Table 2-1 PIRSA soil landscape unit description of salinity levels. Sea barley grass would be mainly expected to occur in the moderate to moderately high salinity level areas and samphire and saltpans in the very high to extreme areas (after Maschmedt, 2000).

Salinity level	Vegetative indicators	EC (dS/m)
Low	No evidence of salt effects	<2 (surface) <4 (subsoil)
Moderately low	Subsoil salinity	<4 (surface) 4-8 (subsoil)
Moderate	Halophytic species such as sea barley grass are usually evident	4-8 (surface) 8-16 (subsoil)
Moderately high	Halophytes are common - sea barley grass, curly rye grass and salt water couch	8-16 (surface) 16-32 (subsoil)
High	Land dominated by halophytes with bare areas. Samphire & ice plant evident	16-32 (surface) >32 (subsoil)
Very high	Supports only samphire, swamp tea-tree or similar halophytes	>32 (surface)
Extreme	Bare salt encrusted surface	>32 (surface)

Table 2-2 PIRSA soil landscape unit attribute that refers to *salinity induced by watertable* levels. This attribute is designated 7 salinity classes A-G, where A is assigned to soil polygons with negligible salinity and G is assigned to extremely saline polygons (After PIRSA, 2001). Descriptions of salinity levels, from negligible to extreme, are shown in Table 1.

Class	Nature of watertable induced salinity
A	Negligible
B	Slight salinity, or less than 2% of land affected by highly saline seepage
C	Moderate salinity, or 2 - 10% of land affected by highly saline seepage
D	Moderately high salinity, or 10 - 30% of land affected by highly saline seepage
E	Moderately high to high salinity, or 30 - 50% of land affected by highly saline seepage
F	High salinity. More than 50% of land affected by highly saline seepage
G	Very high to extreme salinity
X	Not applicable

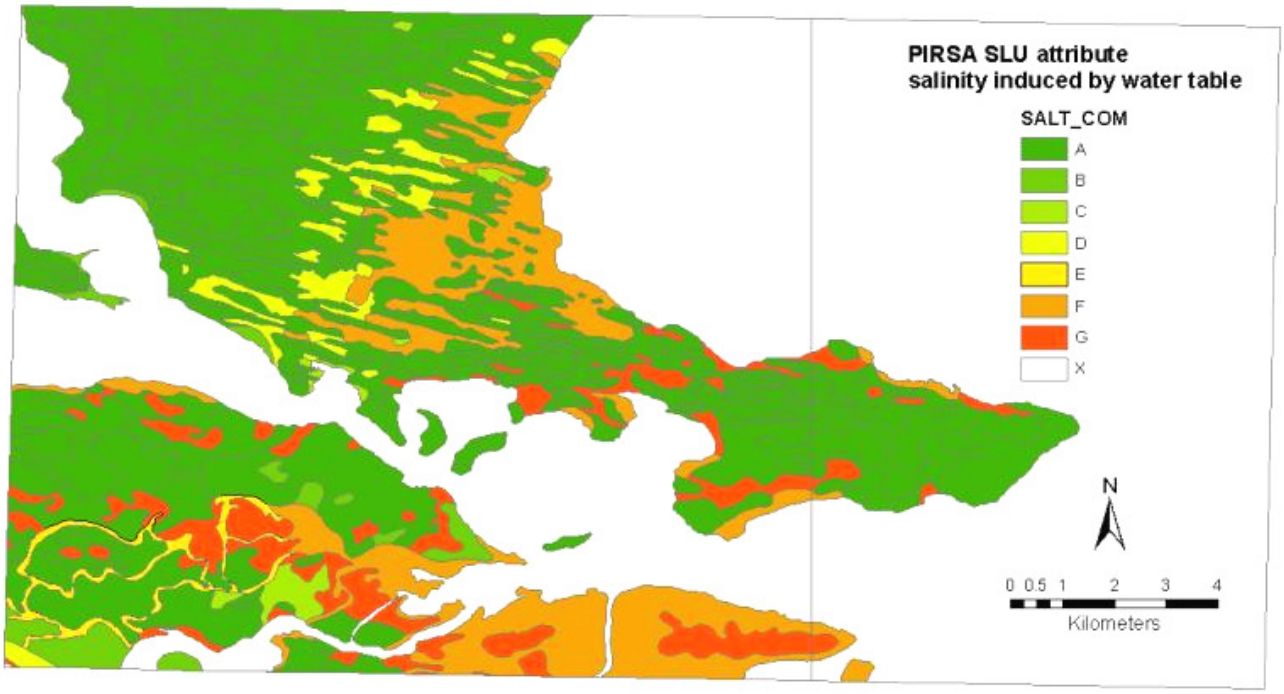

Figure 2-5 PIRSA salinity induced by watertable map showing salinity classes associated with each soil landscape unit. Note that Class E (moderately high to high salinity) was is not represented on the Point Sturt Peninsula.

The main saline discharge sites assigned moderate, high and extreme salinity levels (Classes C, D, F & G) are located along the coastal areas and across the central region where the clay aquifer flow terminates (Saline Class E is not represented on the peninsula). Salinity decreases inland away from the peninsula.

2.2.6 National Land and Water Resources salinity map

The National Land and Water Resources Audit was the first rigorous scientific attempt to present a national perspective of salinity in Australia (Webb, 2000). The Audit recognised that dryland salinity management requires knowledge of the extent and impacts of dryland salinity and therefore compiled an overview of the extent, current status and risks of dryland salinity in Australia. State by state comparisons were not considered because the methods, scale and reliability of data underpinning the state assessments were varied. Estimates from Western Australia, South Australia and New South Wales were considered the most reliable (Webb, 2000).

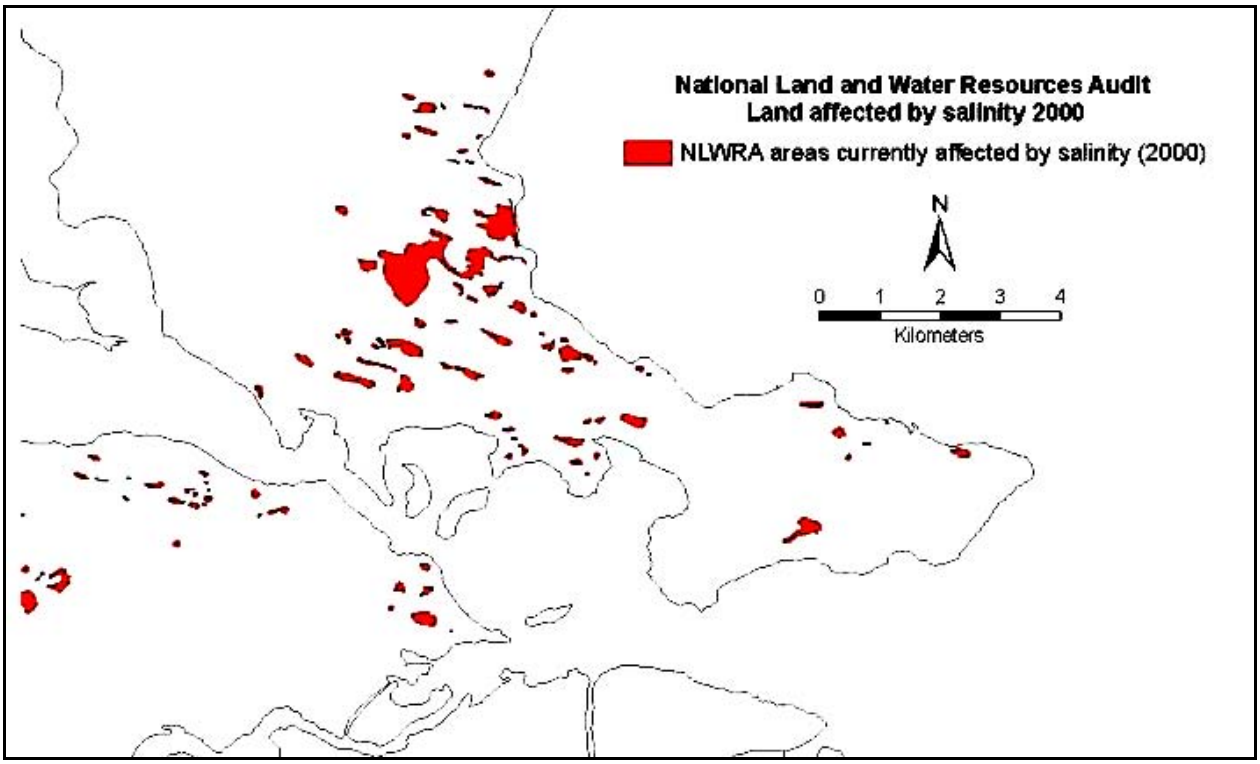

Figure 2-6 The National Land and Water Resources Audit extent of land affected by salinity in 2000 (Salinity 2000) was obtained from the Australian Natural Resources Atlas [http://audit.ea.gov.au/anra/atlas_home.cfm].

2.2.7 Landsat ETM dryland salinity maps

Recent studies have mapped dryland salinity in the Point Sturt area (Figure 2-7) based on Landsat ETM imagery and spatial data integration (Clarke, 2000; Thomas, 2001). The Thomas study in 2001 evaluated Landsat imagery for mapping dryland salinity as part of the South Australian Land Condition Monitoring Project. Salinity mapping involving vegetation indices, classification techniques and multitemporal Landsat data proved inadequate for discriminating saline from other exposed soils with the Landsat imagery alone. Ultimately *severely saline areas* were mapped through integration of Landsat imagery with selected information from the PIRSA soils database (described in section 2.2.5). The Landsat-based study found that the most suitable procedure to discriminate saline areas from other degraded areas was a combination of unsupervised classification, the thermal band from a summer image, NDVI analyses and depth to watertable information from the PIRSA soils database.

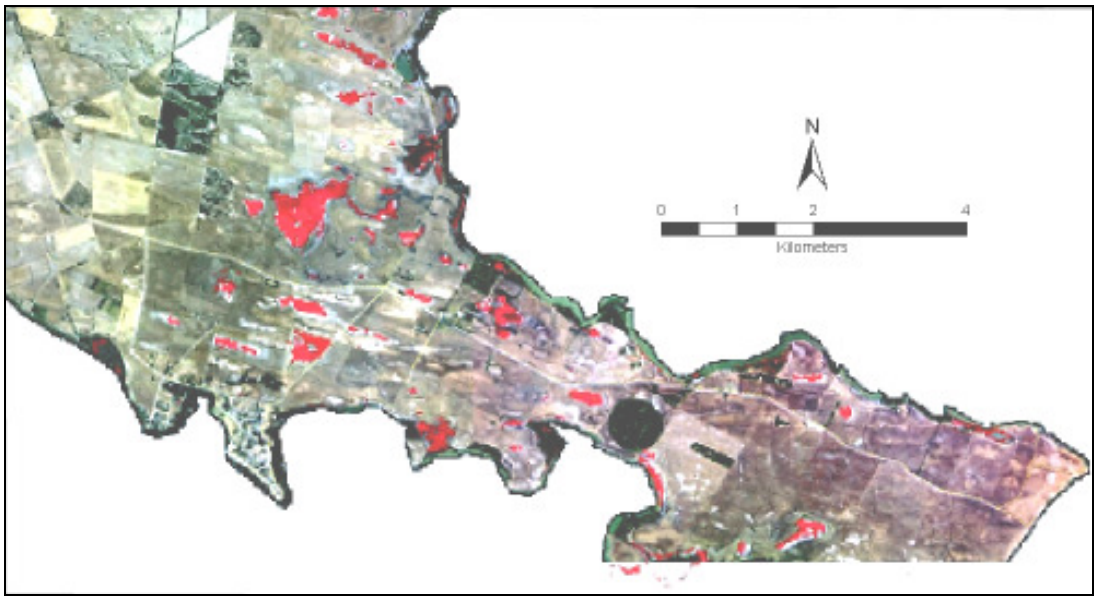

Figure 2-7 Map of *severely saline areas* (red) based on Landsat ETM imagery and spatial modelling (Thomas, 2001).

2.3 Field methods

2.3.1 Identifying surface expressions of salinity

Soil and vegetation salinity symptoms that extended over sizeable homogeneous areas were identified as suitable for mapping. These areas were required to span an area covered by several hyperspectral image pixels to allow for global positioning system unit (GPS) and georegistration errors, so suitable symptoms needed to cover a minimum of 10 x10 m (in the case of high spatial resolution airborne imagery used in this study, the ground resolution is 3 m).

Point Sturt landscape is dominated by annual dryland pastures. The region is interspersed with remnant native vegetation, predominately mallee, and irrigated pastures, which are intersected by unsealed roads of exposed calcrete. The mallee vegetation stands are often sparse revealing exposed sandy mallee soils. Soils are also exposed in roadside quarries and on sand dune ridges. The location and extent of some of these areas were recorded with a global positioning system unit (GPS) offering 1-2 m accuracy, and photographs taken. These sites were visited during different seasons in 2003 and 2004 to observe changes in vegetation and soil moisture in order to understand how salinity is expressed in the landscape. This knowledge was used to help make decisions regarding optimal times of year to acquire hyperspectral imagery for mapping different salinity symptoms.

2.3.2 Soil sampling

Soil sample sites were selected according to two criteria. Firstly, sites were located within the two aquifer systems. Most of the sites were associated with the major discharge region where the clay aquifer terminates at the interface with the limestone aquifer (Sites A, AA and F). Site B was located along the southern coast and is associated with the limestone aquifer. Secondly, sample sites were also selected on the basis of accessibility to properties because access to some parts of the study area was limited due to landuse. The main study sites contained a representative range of salinity symptoms in the area (Figure 2-8).

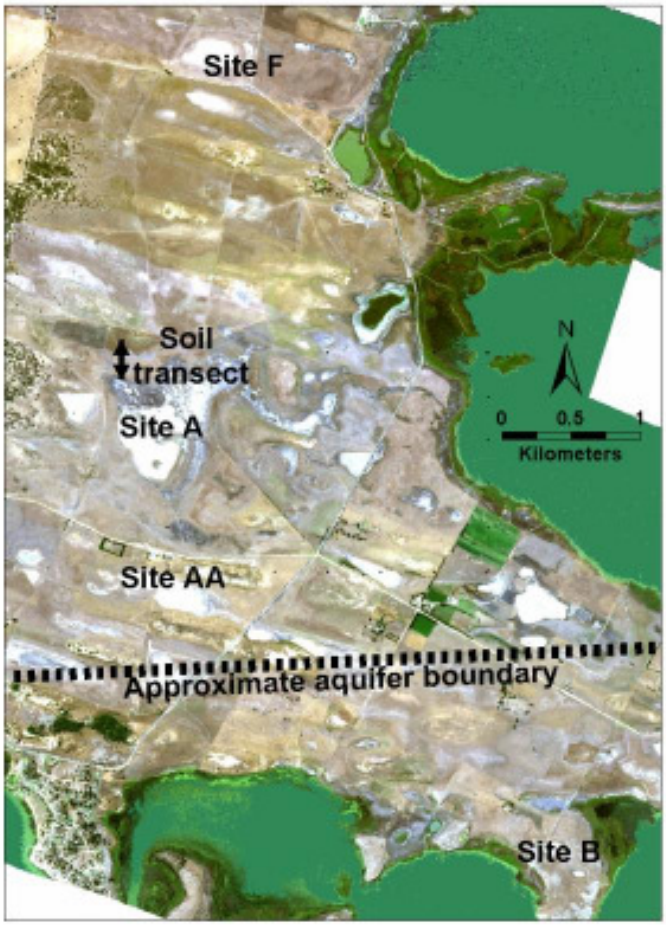

Figure 2-8 Map of showing 4 main saline sites. The clay aquifer discharges at Sites A, AA and F whereas the limestone aquifer discharges at Site B.

Three surface soil samples were collected from the main Site A saltpan and one sample collected from Site B for comparison. At the Site A saltpan, soil samples were also collected at 10 cm depth intervals from the one soil pit (Site A1) and two soil cores (Sites A2 and A3) in order to investigate subsurface soil horizons, watertable levels and

fluctuations. The subsurface measurements of salinity have no direct relationship to the remote sensing imagery but provide an understanding of the vertical distribution of salinity through the soil profile. Soil samples were analysed in the laboratory to determine salinity levels ($EC_{1:5}$), pH and soil mineralogy through X-Ray Diffraction analysis (XRD). Knowing the geographical coordinates of each site allowed for direct comparisons between soil analysis, field spectral measurements and spectral information derived from georegistered hyperspectral imagery.

Surface soils were also sampled from 14 sites at 20 m intervals along a transect, extending out from the edge of the Site A saltpan, in order to demonstrate the relationship between decreasing soil salinity levels and changes in vegetation (Figure 2-9). The first transect sample was located in very wet black soil within a patch of dense samphire, the next sample was collected 10m away, to the north, in the sea barley grass and the remainder were sampled every 20 m, terminating on a low rise over 200 m away where no halophytic grasses were evident.

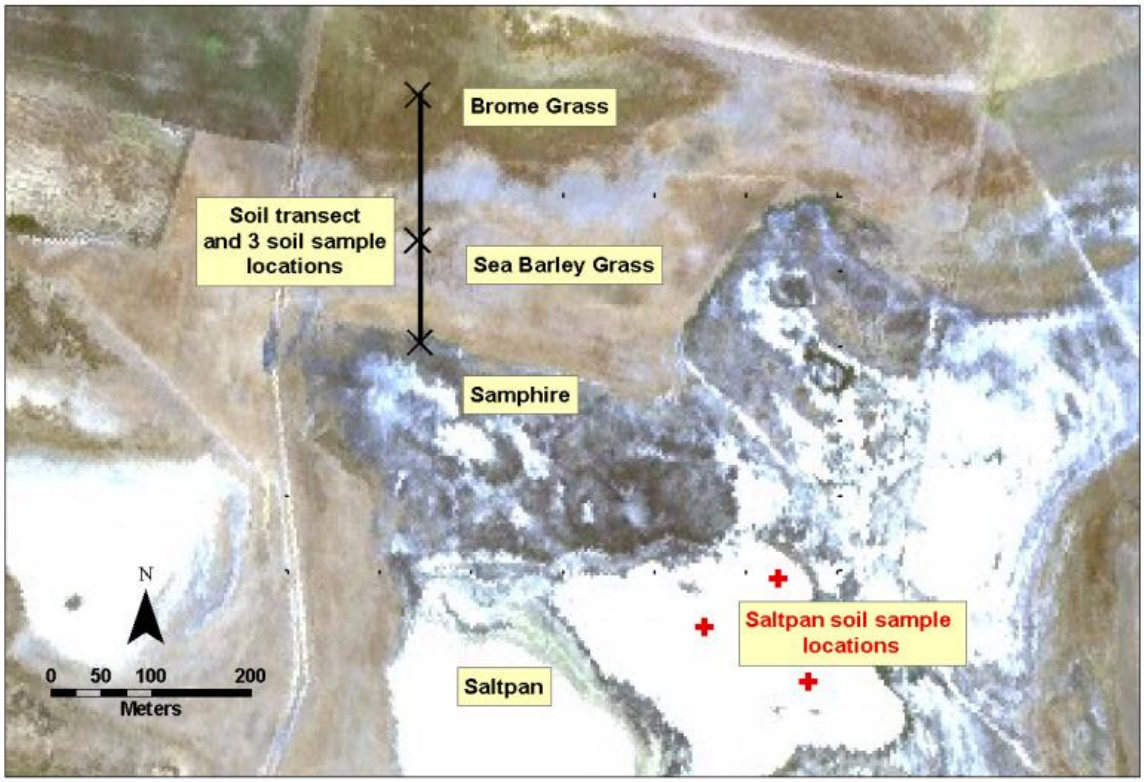

Figure 2-9 Detail of Site A showing GPS locations where surface and depth soil samples (red) were collected. The soil transect (black) extended north from the samphire, across the sea barley grass and terminating on a rise covered with non-halophytic grass.

2.3.3 Salinity and soil water content

Soil samples were analysed to determine the level of salinity and soil water content at salt affected sites. The soil water content may give an indication of the level of waterlogging from shallow groundwater. The level of soil salinity was determined by measuring the electrical conductivity of a solution of soil and water in a ratio of 1 part soil and 5 parts deionised water ($EC_{1:5}$). The solutions were shaken for 1 hour before measuring.

Soil water content is defined as the mass of water relative to the mass of dry soil particles, often referred to as the gravimetric water content, is given by

$$\theta_m = \frac{\text{mass of soil water}}{\text{mass of dry soil}} = \frac{(\text{mass of wet soil}) - (\text{mass of oven dried soil})}{\text{mass oven dry soil}}$$

In the field, soil samples were sealed in double plastic bags to preserve the soil water for transport to the soil laboratory. Soil samples were weighed before and after oven drying for 24 hrs at 105^o C.

2.3.4 Soil mineralogy

XRD analysis was also performed on 11 samples (3 samples from the saltpan surface, 5 saltpan samples at different depths and 3 surface samples along the soil transect) to determine soil mineralogy pertaining to salinity and enabled comparisons with the minerals identified from spectral analysis of field and image spectra. XRD analysers are instruments used to identify minerals and crystalline compounds. The principle is based on passing high-energy X-rays through ground soil samples and the resulting diffraction pattern (which occurs in accordance to Braggs Law) is related to crystal interplanar spacings (Sumner, 2000). No two minerals have exactly the same distances between planes of atoms. The diffracted beam from different minerals produces high-count rates or peaks at different diffraction angles. Peaks occurring at known angles can identify mineral compounds.

XRD patterns were recorded with a Philips PW1800 microprocessor-controlled diffractometer using Cobalt Kα radiation. Because of financial restraints, only a limited number of samples were analysed. The samples were ground in an agate mortar and pestle before being lightly pressed into aluminium sample holders for insertion into the

XRD analyser. Diffraction patterns were recorded in steps of 0.05° 2θ with a 1 second counting time per step.

Each mineral identified in the results was assigned approximate percentage of total mineral content of the sample. A mineral content of 60% was defined as dominant, 20-60% as sub-dominant, 5-20% as minor and less that 5% was defined as trace.

A limited number of samples were investigated with XRD analysis, including surface saltpan samples at three locations at the Site A and one at Site B. From the soil pit at Site A1, analysis was also performed on soils extracted at 10 cm depth intervals. Three surface samples were also analysed from the 14 surface samples collected at 20 m intervals along the soil transect.

2.4 Results

A range of salinity symptoms was observed throughout the Point Sturt Peninsula. The symptoms indicated a range of salinity levels, from moderate (marine couch and dead trees), high (exposed soils and samphire) through to extreme salinity (saltpans) (Figure 2-10). Salinity symptoms corresponding to varying levels of salinity were best observed at different times of the year.

January to March corresponded to the driest months in which dry saltpans, exposed soils and perennial vegetation, including perennial halophytes were easily identified among a background of dry grass (Figure 2-10). Mild to moderate salinity indicated by a good cover of salt tolerant annual vegetation, such as sea barley grass, was best observed in wetter months because annual grasses could be more readily identified from their distinctive seed heads. At the height of the wet season in August, saltpans and coastal vegetation were inundated with water (pronounced waterlogging).

2.4.1 Saline soils

Three surface soil samples from Site A saltpan (Figure 2-9) were fine grained, sandy clay, mid grey with a fine thin creamy-white crust, particularly at the pan edges, also with evidence of pale fibrous plant material and small shells. Just below the dry surface the soil was very moist. In contrast, the saltpan at site B was covered with a coarse thick white salt crust underlain by black wet mud. Chemical and XRD analysis confirmed the extreme salinity of both sites, the EC levels of the crust at Site B was 10 times greater than Site A (Table 2-1). Both saltpans contained evaporite minerals halite and gypsum.

The presence of gypsum is unsurprising because large Holocene gypsum deposits are common along the South Australian coastline (Warren, 1982). The white crust at Site B appeared to be crystalline halite because of the cubic structure of the large crystals.

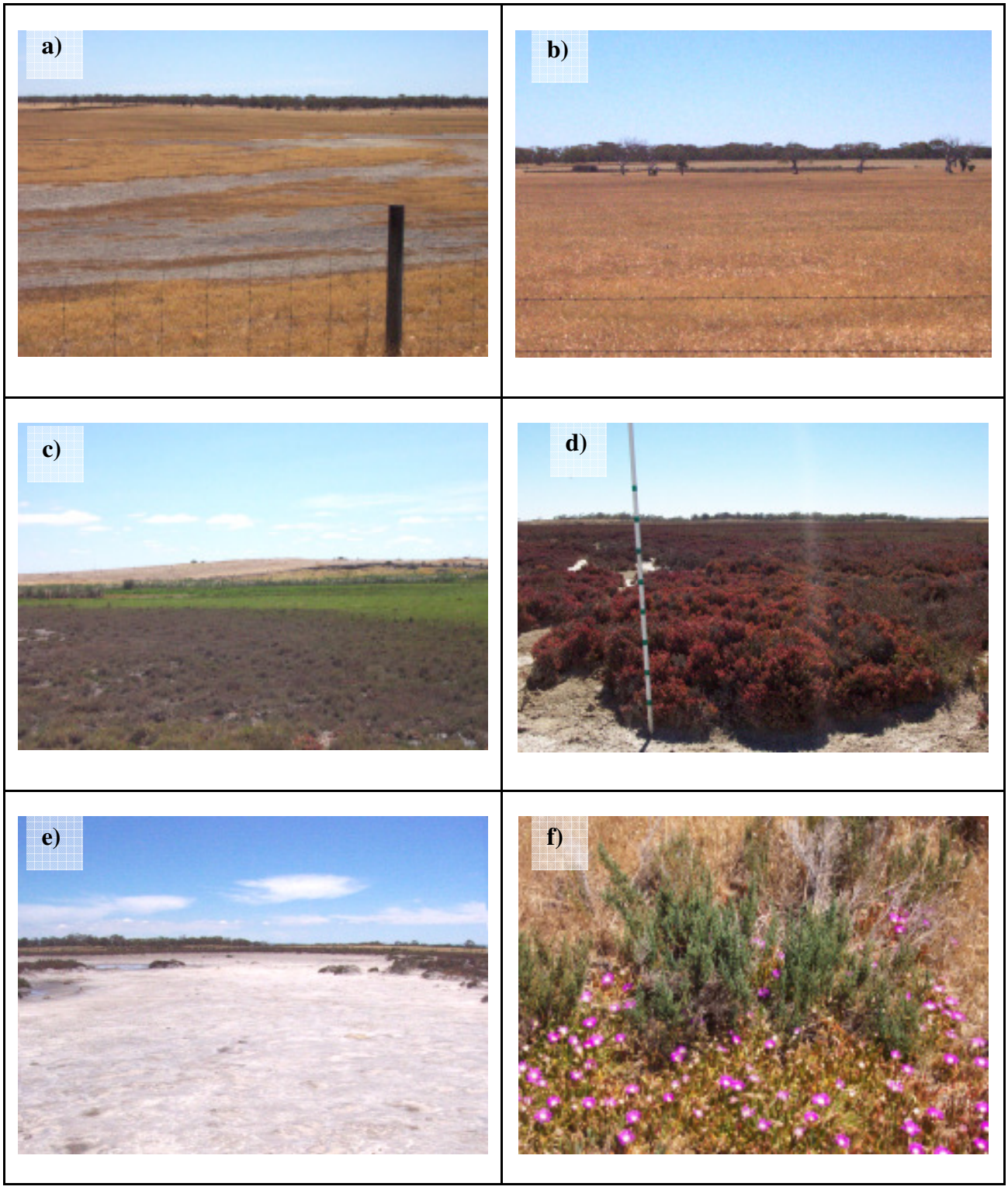

Figure 2-10 Symptoms of high to extreme salinity at Point Sturt during the dry season: a) plant dieback; b) dead trees; c) samphire *(Halosarcia pergranulata),* and marine couch grass (*Sporobolus virginicus*); d) red phase samphire; e) saltpan at Site A and f) pigface *(Carpobrotus glaucescens)*

Table 2-3 Analysis of three surface soil samples from the main saltpans at Site A and B. The surface layer of crystals at Site B is halite.

Sample Site	Depth	Description	pH	$EC_{1:5}$ (dS/m)	XRD Mineralogical Composition
Site A1 Saltpan	**Surface**	Saltpan crust, grey soil, undecomposed organic matter	9.3	28.1	Dominant halite, sub-dominant gypsum, minor calcite, trace quartz, kaolin and possible smectite (montmorillonite)
Site A2 Saltpan	**Surface**	Saltpan crust, fine creamy white crystal, grey soil	9.3	14.9	Dominant quartz, sub-dominant halite, trace gypsum, albite (Na feldspar) and orthoclase (K feldspar)
Site B Saltpan	**Surface**	Saltpan crust, cubic white crystals	9.0	159.0	Dominant halite, trace gypsum and quartz

At saltpan Site A1, the soil pit profile was clearly separated into two clay rich layers, the surface grey layer and the lower red layer indicating high iron oxide content (Figure 2-11a and b). $EC_{1:5}$ and pH values decrease with depth (Table 2-4). The high EC values at the surface were consistent with high salinity resulting from sustained evaporation of surface groundwater. The surface EC values approach the 14 dS/m samphire tolerance level.

Figure 2-11 a) Saltpan soil pit (Site A1) showing the leached upper horizon grading to iron oxide dominated lower horizon at 30 cm and b) the downward view illustrates the shallow groundwater seeping into the pit at a depth of 60 cm, shortly after digging was completed.

In the soil pit (Site A1), XRD analysis identified subdominant/minor gypsum and gypsum traces were found in all other soil samples at different depths B (Table 2-4). The EC and pH measurements indicate extremely saline, alkaline soil. The higher values at the surface and the presence of evaporite minerals are indicative of evaporative processes that have concentrated groundwater salts to form evaporite mineral deposits.

Table 2-4 Soil analysis of samples collected at 10 cm depths from saltpan at Site A. The pH and EC measurements indicate extremely saline, alkaline soil. The higher values at the surface indicated the surface evaporative concentration of the groundwater salts. The XRD results confirm the presence of the evaporite minerals halite and gypsum.

Depth Profile A1 (Site A soil pit)				
Depth (cm)	**Description**	**pH**	**$EC_{1:5}$ dS/m**	**XRD Qualitative Analysis**
0-10	Saltpan layer - mid grey	8.29	35.5	Dominant quartz, minor halite, gypsum, smectite, trace kaolin and calcite
10-20	Saltpan layer - light grey	8.89	17.5	Dominant quartz, minor halite, possible ankerite (Fe dolomite), Mg-calcite, trace gypsum, kaolin, calcite, albite, orthoclase, aragonite and mica (illite)
20-30	Saltpan layer - light red/brown	8.29	12.5	Dominant quartz, minor halite, gypsum, Mg-calcite, trace kaolin, calcite, possible ankerite, albite, orthoclase and mica
30-40	Saltpan layer - mid red/brown	8.18	14.0	Dominant quartz, minor gypsum, Mg-calcite, possible smectite, trace halite, kaolin, possible ankerite, albite, mica
40-50	Saltpan layer - mid red/brown + large crystals	8	13.0	Dominant quartz, minor halite and gypsum, kaolin, Mg-calcite, possible smectite, trace albite and mica

Soils were also sampled at regular depth intervals at two other saltpan locations (Table 2-5). These samples showed reduced salinity levels compared to the main soil pit but still rate as high to extreme, with the highest values again in the surface layer.

Table 2-5 Soil analyses at 10 cm depths from 2 other sample sites on the main Site A saltpan. These soils also show the increased salinity at the surface due to evaporation. No XRD analysis was performed.

Depth profile A2 (Site A)			Depth profile A3 (Site 3)		
Depth (cm)	**pH**	**$EC_{1:5}$ (dS/m)**	**Depth (cm)**	**pH**	**$EC_{1:5}$ (dS/m)**
0-10	8.5	15.80	0-10	8.74	29.00
10-20	8.62	7.70	10-20	8.73	17.80
20-30	8.69	6.80	20-30	8.36	20.20
30-40	8.76	4.00	30-40	8.36	27.20
40-50	8.33	5.80	40-50	8.71	21.90

At Site A, there was a change in soil salinity along the soil transect (Figure 2-9) that extended north from edge of the saltpan. Away from the edge, clay content, soil water and EC values decreased as the proportion of sand increased (Table 2-6 and Figure 2-12). As soil salinity decreases so does the soil water content, which indicates that there is waterlogging by saline discharge at the pan edge. In the soil transect samples with highest EC values, XRD analysis shows that soil is dominated by clay (smectite) and also contains minor amounts of saline minerals halite and gypsum (Table 2-6). The clay dominant soils at the pan edge indicate that the clay aquifer is near the surface. Midway along the transect, evaporite minerals and clay are absent but quartz dominates indicating a more sandy soil.

Table 2-6 Soil analysis from three soil transect samples. Soil water EC and pH all decrease at increasing distance from the samphire-sea barley grass interface. The XRD analysis shows the change from clay to sandy soils along the transect. Soil analysis results for all transect soil samples are shown in Figure 2-12.

Distance from saltpan (m)	Depth	Description	Gravimetric water content (θ_m)	pH	$EC_{1:5}$ (dS/m)	XRD Mineralogical Composition
0	**Surface**	Black soil, high clay	50.0	8.02	10.00	Dominant smectite, minor gypsum, quartz, kaolin, trace halite, albite, Mg-calcite, mica
110	**Surface**	Very dark grey soil, increasing sand	18.8	5.9	0.19	Dominant quartz, trace kaolin, albite, orthoclase and mica
250	**Surface**	Brown sandy soil	6.2	6.4	0.07	Dominant quartz, trace albite and orthoclase

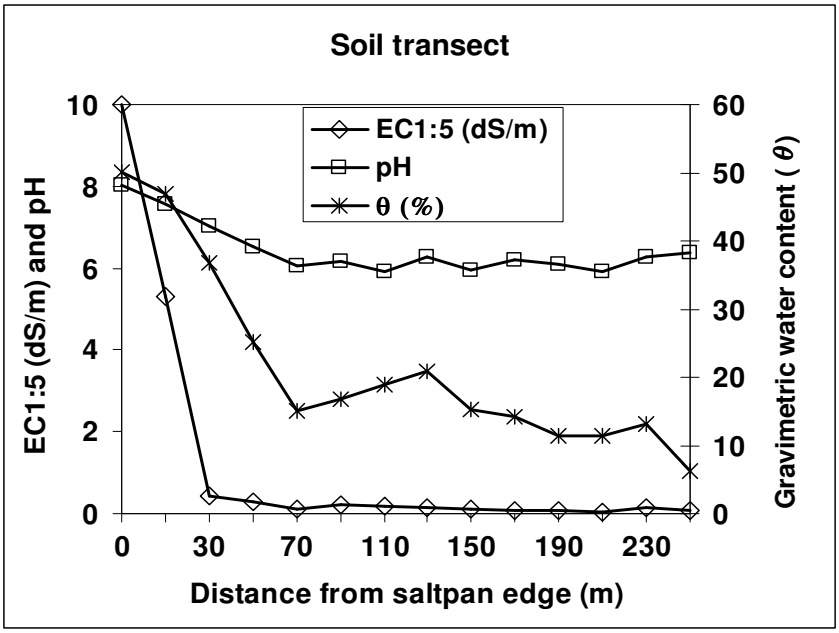

Figure 2-12 Soil analysis along transect extending out from saltpan at Site A. EC values, soil moisture and pH decreased away from the samphire-sea barley grass interface (0 m) indicating the change from high salinity to non-saline soils.

2.4.2 Vegetation symptoms of salinity

Saline areas with a good cover of vegetation were evident at Point Sturt. Perennial and annual halophytes that indicate varying levels of salinity were best observed at different times of year.

In the dry season, perennial halophytes were easily identified amongst a background of dry grass (Figure 2-10 c and d). Vast dense samphire patches usually were easily recognisable surrounding saltpans (Figure 2-10 e). Samphire is a low, dense, succulent, native shrub with numerous woody stems and short, segmented branchlets made up of small succulent beaded leaves. The shrub can appear green or change to red in highly saline areas, tolerating soils with $EC_{1:5}$ values greater than 16 dS/m (Department of Primary Industries, 2004) and survives partial inundation for several months over winter (Barrett-Lennard, 2003). Saltpans surrounded by samphire were characteristic of the main study areas Site A, in the central lowlying clay aquifer discharge site, and along the coast at Site B.

In summer and early autumn, annual halophytic grasses could not be readily be identified because few seed heads remained on the senesced plants. September, October and November were the best months to observe annual grasses because at this time of

year seed heads were well formed. During these wetter months, sea barley grass *(Critesion marinum* also known as *Hordeum marinum)* was observed to be a dominant halophytic plant species other than samphire in the area (Figure 2-13*)*. Sea barley grass is an introduced annual grass species found growing in a range of soils and can tolerate moderately saline soils, with $EC_{1:5}$ values ranging from 4 to over 16 dS/m (Department of Primary Industries, 2004; Maschmedt, 2000; Maschmedt, 2001; van Gool and Moore, 1998). By September, sea barley grass had reached maximum growth phase. Sea barley grass and brome grass *(Bromus* sp.*)* were easily identifiable.

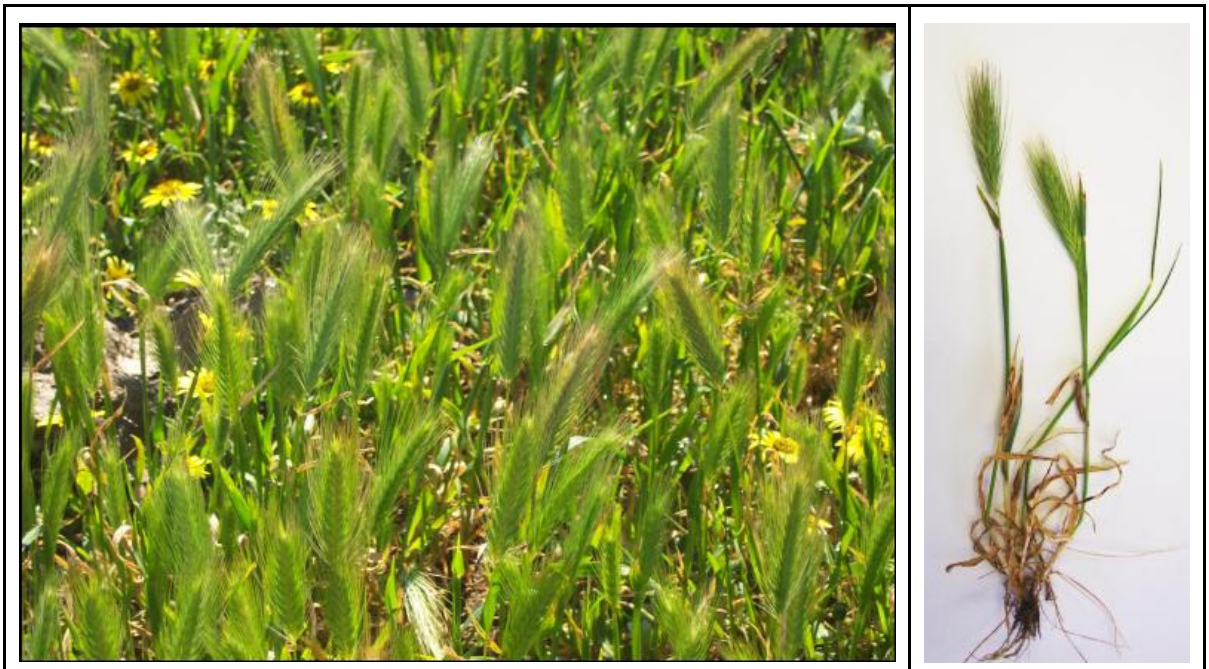

Figure 2-13 Dense large zones (left) of sea barley grass (Critesion marinum) with well developed seed heads (right) were evident during spring (September 2004)

Different halophytic species are indicators of different levels of soil salinity. The change in species and corresponding change in salinity levels was observed at Site A. Here there was a change in soil salinity along the soil transect (Figure 2-9) that extended north from the edge of the main saltpan. At the pan edge, samphire was the only halophyte growing in waterlogged black soil with an EC value of 10 dS/m (Table 2-1).

The high salinity and water content at this location is likely to be due to shallow groundwater. Away from the samphire edge, as soil salinity and soil water content decrease there is a corresponding change in plant species. Just 10 m away, sea barley grass dominates where salinity falls to 5.3 dS/m (moderately saline). As salinity levels

decrease further, sea barley grass is replaced by non-halophytic grass such as brome grass *(Bromus* sp.*)* and silver grass *(Vulpia* sp.*).*

Through November as the seasonal rains abated, a larger variety of halophytic annual grass species could be identified and were observed to be in various stages of senescence. By the end of November, homogenous patches of sea barley grass appeared to be greener than other senescing grasses at the main study area (Sites A, AA, B and Site F in the north). Sea barley grass appeared greener than other grasses toward the end of November because it occupied the low-lying, wetter soils (Hugh Longbottom, Rural Solutions, SA, pers. comm.). The various stages of senescence could be clearly seen at Site AA (Figure 2-14). Here symptoms of moderate salinity levels included bare patchy ground, sea barley grass and curly rye grass *(Parapholis incurva).* The site was surrounded by non-halophytic species such as brome grass *(Bromus* sp.*)*, silver grass *(Vulpia* sp.*)* and wheat *(Triticum* sp.*)*. In midwinter (early August), sea barley grass and other annual grasses were found to be immature with underdeveloped seed heads. Sea barley grass plants were sparsely distributed and therefore unsuitable for remote mapping at this time of year.

Figure 2-14 Moderately saline area at Site AA (November 2003). Green sea barley grass (a) and curly rye grass (b) have colonised the lowlying saline soil. Silver grass and brome grass (c and d) surround the pan. Close-up images of the 4 major grass species are inset.

Zonation of sea barley grass was particularly evident in moderately saline areas where it grew in dense homogeneous patches. Therefore in terms of spatial distribution, the optimum time of year to map sea barley grass would be from September to November before drying off. In terms of spectral information, it appeared that November would be

the preferred time of year to discriminate later senescing sea barley grass from non-halophytic grasses. During the spring flush and senescence many areas containing halophytic and non-halophytic grasses had been grazed, leaving little plant material for discrimination.

Other vegetation salinity symptoms observed throughout the landscape included small patches of pigface and sparse curly rye grass, one large coastal stretch of marine couch and isolated dead trees associated with a low lying area in the north (Figure 2-10). During spring in September, there was no evidence of decline in crop vigour due to salinity in the few irrigated pastures.

2.5 Conclusion

In the central groundwater discharge area, measured $EC_{1:5}$ values were greater than 20 dS/m within the bare saltpans, confirming the extreme salinity of the site. XRD analysis determined that the main evaporite minerals in the saltpans and saline soils were halite and gypsum. Similarly, Site B saltpan was found to contain dominant halite and a trace of gypsum. Calcite and clay minerals were found to be minor constituents in most of the soil samples. Adjacent the saltpans, changes in soil salinity were associated with corresponding changes in plant species. The abrupt transition from samphire to sea barley grass was associated with a sharp drop in $EC_{1:5}$ values from 10 dS/m, at the pan edge, to 5.3 dS/m just 10 m away. .

Site visits established that the dominant halophytic plants growing in these areas were samphire *(Halosarcia pergranulata)* and sea barley grass *(Critesion marinum)*. Table 2-7 summarises the salinity symptoms at Point Sturt. Saltpans and samphire were suitable candidates for remote mapping in the dry season because of their spatial distribution and their contrasting appearance to dry grass background. Adjacent to the extremely saline areas at Point Sturt, sea barley grass, an important early indicator of salinity, was also observed to grow in large homogeneous areas.

In high to extreme saline areas at Point Sturt, halitic and gypsic saltpans, exposed soils due to plant dieback and samphire were selected as the best salinity candidates for hyperspectral mapping during the dry season. In moderately salt affected areas, sea barley grass is the best annual halophytic species to map during “spring flush” (September) or senescence (November).

Table 2-7 Summary of salinity symptoms at Point Sturt and their suitability for mapping with hyperspectral imagery

Salinity Level	Salinity symptom	Distribution	Suitability for mapping with remote sensing
Extreme salinity	Waterlogging	Surface water on saltpans	Possible surface water – for subsurface use radar
	Salt encrusted pans	Most pans are dry during summer field visits	Possible spectral features due to minerals & soil colour
	Coastal mud flats and pans	Coastal large	Possible spectral features due to minerals & soil colour
High to very high	Samphire	Large extent around most salt pans - green and red phase	Dense patches and perennial, not very green, SWIR features
	Pigface	Only patchy small areas <1m^2	Not suitable
	Bare patchy ground	Bare patches in field approx 1-3m wide over 1 hectare	Good extent, dry surface
	Dead trees	Individual trees have spatial extent	Not suitable
Moderate salinity	Crop stress	None evident at 3 irrigated sites	Not suitable
	Sea barley grass	In summer, difficult to identify, good cover in spring. In November appears greener than non-halophytes	Good distribution but not suited when dry, best time may be “spring flush” or during senescence
	Marine couch	Large dense zone but only one site	Only one patch observed not for widespread mapping
	Curly rye grass	Sparse at one site	Not suitable

Although a set of vegetation indicators have been identified at Point Sturt, these same species may not be reliable indicators in other regions. Perennial halophytes are good indicators for mapping during the dry season, although it is worth noting that in some salt affected catchments, perennials such as saltbush are increasingly being introduced for stock grazing and to assist in ameliorating saline land (Barrett-Lennard, 2003) and may therefore be mapped as salt affected land. Furthermore, grazing of halophytic grasses, as occurred at Point Sturt, can reduce the ability to discriminate indicator species with remote sensing. Finally, single symptoms such as sea barley grass are not always a definitive indicator of salinity: a combination of several symptoms provides a more reliable diagnosis (Department of Primary Industries, 2004; NSW Department of Natural Resources, 2005).

3 SPECTRAL CHARACTERISATION OF SALINITY

3.1 Introduction and aims

Of fundamental importance to hyperspectral salinity mapping is an understanding of the spectral characteristics of soil and vegetation salinity symptoms. Hyperspectral imagery may allow for discrimination of salt tolerant plants and certain properties related to saline soils. Hyperspectral sensors have the potential to map saline areas with good cover of salt tolerant species that are difficult to map with multispectral satellite imagery (Furby *et al*., 1998; Furby *et al*., 1995; Wheaton *et al*., 1992).

Overall spectral shape and discrete absorption features (particularly in the SWIR) are important in explaining soil properties (Ben-Dor *et al*., 1999). Even though halite has an essentially featureless spectrum (Hunt *et al.,* 1971) some studies have been successful in identifying spectral features pertaining to saline soil mineralogy. Some spectral properties of irrigation induced saline soils have been identified by Dehaan and Taylor (2002B). Dehaan and Taylor reported that increasing salinity could be inferred from the reduced intensity of the 2200 nm hydroxyl feature, a reflection high at 800 nm and features at 980 and 1180 nm. Therefore saline soil mapping could be based on distinguishing either spectral shape or well-defined saline mineral absorption features.

To successfully map vegetation salinity symptoms their reflectance must differ from that of the surrounding vegetation. To ascertain whether different species have the potential to be discriminated and mapped with hyperspectral imagery, comparisons can be made between field or laboratory acquired reflectance spectra of the target species and surrounding vegetation (Schmidt and Skidmore, 2001; Schmidt and Skidmore, 2003). The reflectance spectra of plants adapted to arid or saline environments may contain distinguishing biochemical absorptions (Lewis *et al*., 2000). The spectra of salt tolerant shrubs contain traces of leaf coating, cellulose and lignin absorptions in the VNIR and SWIR regions. The visible and NIR regions are also important due to accessory pigments and leaf structures (Dehaan and Taylor, 2002B). Therefore, high spectral resolution imagery has the potential to discriminate halophytic vegetation from non-halophytes because they have spectral properties associated with adaptations to saline environments.

Schmidt and Skidmore (2001) found that field spectra of various African grass species showed significant statistical difference over the red part of the visible spectrum and in

the region of 1300 nm. Thenkabail (2004) studied reflectance spectra from shrubs, grasses, weeds, and agricultural crop species and recommended 22 narrow bands in the visible, NIR and SWIR to discriminate different types of vegetation. The narrow visible wavebands at 655 and 675 nm may vary significantly due to changes in leaf area index (LAI), biomass, nitrogen, soil background, canopy structure, cultivars types and moisture and were therefore the most sensitive to contrasts between vegetation and soil.

Early signs of plant stress were associated with a shift in the red edge to shorter wavelengths (Elvidge, 1990). During late senescence, spectral changes would be expected in the NIR and SWIR regions. In these wavelength regions spectral differences are due to changes in moisture, biomass and plant structure (Elvidge, 1990; Gates *et al*., 1965; Knipling, 1970; Schmidt and Skidmore, 2001; Thenkabail *et al*., 2004). Therefore from these previous studies, it appears that most spectral regions have a role to play in discriminating between plant species, particularly those in variable stages of senescence. Furby (1998) indicated that the low accuracies of multispectral salinity maps could be improved by exploiting seasonal differences between crops and halophytic species.

In the previous chapter, samphire, saltpans and sea barley grass were identified as the most suitable candidates for mapping with remote sensing imagery. This section aimed to determine which salinity symptoms were spectrally suited to mapping with hyperspectral imagery and to identify the optimum time of year for mapping each target symptom, especially areas with a good cover of salt tolerant vegetation. Of particular interest was sea barley grass *(Critesium marinum)* because it is often the first salt tolerant plant species to colonise soils with developing salinity and, in conjunction with other salinity symptoms, is a useful indicator of moderately salt affected soils in agricultural areas. Statistical comparisons between the reflectance spectra of sea barley grass and other species aimed to determine whether the species has the potential to be discriminated and mapped with hyperspectral imagery.

3.2 Methods

Field and laboratory reflectance spectra were collected from a representative range of soil and vegetation landcovers and salinity symptoms. The spectra of salinity symptoms were collected from previously identified salt affected study sites at Point Sturt and at different times of year. A range of soil and vegetation spectra were collected initially to

identify distinguishing spectral characteristics of soil and vegetation salinity symptoms. In addition, a selection of grass spectra were collected at different times of year to evaluate whether sea barley grass could be distinguished from other annual grasses.

3.2.1 Spectral collection sites

Soil and vegetation spectra were collected at previously identified study sites located in the major discharge region where the clay aquifer terminates (Sites A, AA and F) and at Site B along the southern coast. At each site, spectra were collected from a representative range of nonsaline landcovers and salinity symptoms, including samphire, sea barley grass and saltpans. Locations of ground-sampling sites were taken with a differential GPS, offering better than 5-metre accuracy.

3.2.2 Time of year

Different salinity symptoms were best observed at different times of the year (Chapter 2). In high to extreme saline areas, saltpans and samphire were selected as the best salinity candidates for hyperspectral mapping during the dry season. Therefore, spectra of saltpans and vegetation, including samphire were collected in February (2003). In moderately salt affected areas, the optimum time of year to map sea barley grass was determined to be either “spring flush” (September) or senescence (November), when sea barley grass appeared greener than other grasses because it occupies the low-lying, wetter soils. Therefore, multiple spectra of annual grasses were collected in September and in November to statistically compare the spectra of sea barley grass to other annual grasses.

3.2.3 Collection of soil and vegetation spectra

Field and laboratory spectra were collected with the portable Analytical Spectral Devices (ASD) FieldSpec Pro spectrometer (Figure 3-1). The instrument internally combines three spectrometers to cover the visible and near infrared (VISNIR) and two shortwave infrared (SWIR) wavelength regions, which provides a full range of 350 to 2500 nm with 1 nm spectral sampling.

Soil spectral measurements were taken of soil samples that were collected from saltpans at Site A and Site B and transported to the laboratory for salinity measurements and XRD analysis. The soils were air-dried for at least 24 hours prior to taking spectral measurements because drier soils maximise the depth of soil mineral absorption features

(Lobell and Asner, 2002). Because oven-drying may alter the mineralogy of some salts and clays (Dehaan and Taylor, 2002B), air-drying was therefore considered the best method for removing soil moisture whilst preserving major absorption features that were diagnostic of dominant soil minerals.

Plant spectra were collected at two different scales: 1) plot scale in the field (Figure 3-1) and (Figure 3-2) and 2) foliage scale in the laboratory under controlled conditions (Figure 3-3). Plot-scale spectral measurements were acquired at 10 cm above patches of the grasses and recorded reflectance from a plot of approximately 5 cm in diameter (Figure 3-2). For foliage scale spectral measurements, fresh plant samples were harvested and immediately stored in sealed plastic bags, placed in insulated ice-cooled containers for transportation, such that the laboratory spectral measurements were completed within 3 hours of collecting the fresh plants samples (Figure 3-3). The foliage scale spectral measurements were acquired with a low intensity light source to minimise plant wilting (Figure 3-3).

Figure 3-1 Collecting spectra in the field with the portable spectrometer

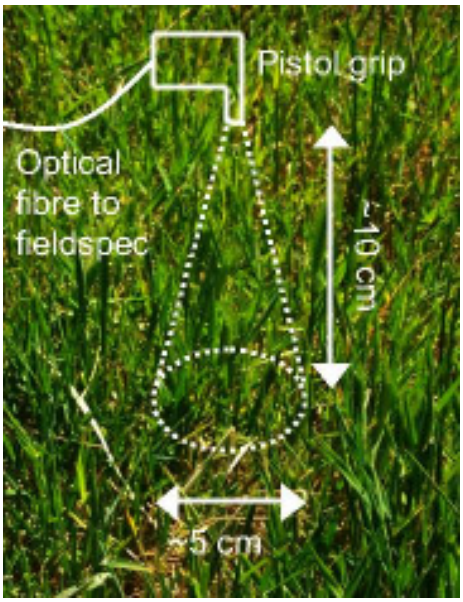

Figure 3-2 Schematic diagram of the field of view (~5cm) of the spectrometer

Figure 3-3 Method for collecting spectra from soil and plant samples in the laboratory

In September, i*n situ* plot scale reflectance spectra and fresh samples were collected of sea barley grass and brome grass *(Bromus* sp.*)* (Table 3-1). At the time of senescence in November, more species were readily identifiable because seed heads had matured. Field and laboratory spectra were collected of sea barley grass and curly rye grass *(Parapholis incurva)*, and non-halophytic senescing plants brome grass and silver grass *(Vulpia* sp.*)* and wheat *(Triticum* sp.*)* (Table 3-2).

Table 3-1 Species and number of samples of spectra collected in September (spring flush). Some samples were not analysed because of excessive noise *

Plant Species	**Number of *in situ* field spectra**	**Number of laboratory spectra**
Sea Barley Grass (*Critesium marinum)*	14 *(not used)**	8
Brome Grass *(Bromus* sp.*)*	11 *(not used)**	11

Table 3-2 Species and number of samples of spectra collected in November. The field spectra of wheat were not used because insufficient good quality spectra were collected*

Plant Species	**Number of *in situ* field spectra**	**Number of laboratory spectra**
Sea Barley Grass (*Critesium marinum*)	35	61
Brome Grass *(Bromus* sp.*)*	25	18
Silver Grass *(Vulpia* sp.*)*	12	-
Curly Rye Grass *(Parapholis incurva)*	15	20
Wheat *(Triticum* sp.*)*	3 *(not used)**	21

Some field spectra contained noisy regions particularly in the SWIR. Therefore, processing of some spectra was required to reduce noise. For each target material, forty

spectra were collected at 1-second intervals. These forty spectra were averaged and the bands with the highest standard deviation, corresponding to the three regions where the individual spectrometers joined, were removed. The averaged spectra were also smoothed in Spectra Solve (Lastek Pty. Ltd.) using the Savitzky-Golay least squares algorithm, which was superior to the Box-Smoothing method for preserving the depth and shape of absorption features (Savitsky and Golay, 1964).

3.2.4 Statistical analysis

In order to determine whether sea barley grass has the potential to be mapped with hyperspectral imagery, the spectra of sea barley grass were statistically compared to other grass species in September and in November. A standard series of two-group t-tests were performed to test the hypothesis that there is no significant difference between the mean of sea barley grass and other grass species. Specifically, at each wavelength the t-test compared the set of sea barley grass spectra to the spectra of a different species to determine whether the mean reflectance values were significantly different from each other in any wavelength region. For computational efficiency, statistical comparison was only performed at every second wavelength.

The means of two species were considered significantly different if their t-values were greater than the critical t-value equivalent to probabilities of less than 0.05. T-values were calculated assuming pooled variance (rather than separate variance) because the numbers of spectral samples were different for each species group and their variances were unequal. Unequal variances at each wavelength were verified by means of standard F-statistic tests.

3.3 Results and discussion

3.3.1 Spectral characteristics of saline soils

The individual spectra from the main saltpan at Site A were characterised by broad water absorption features at 1450 and 1950 nm. The spectra contain a steep visible ramp, a broad shoulder near 800 nm, distinct doublet absorption feature with peaks centred at 2200 and 2270 nm, a single 1755 nm feature and a triple feature at near 1500 nm (Figure 3-4). Inferring soil mineral content from the 2200 nm absorption feature is problematic because both gypsum and clay spectra contain features in this region. The diagnostic gypsum features were emphasised in continuum-removed soil spectra, where

each spectra is normalised using a continuum defined by local spectral maxima (Better Solutions Consulting, 1999). The conspicuous feature at 1755 nm and the triple feature were shown to be consistent with USGS spectral library gypsum spectra (Figure 3-5). XRD analysis (Chapter 2) confirmed the dominant presence of halite, quartz and gypsum. The USGS spectra of both halite and quartz were essentially featureless with high albedo at all wavelengths so were difficult to detect spectrally, although, increasing salinity may be inferred from the reduction of intensity of the 2200 nm hydroxyl feature and precipitation of halite may be related to a reflection high at 800 nm.

The spectrum collected from the coarse thick white salt crust Site B was characterised by a brighter flatter visible/NIR region, and shallow absorption features at 2200 nm and 1755 nm (Figure 3-4). The 1755 nm feature suggests the presence of gypsum but the shallow nature of both features indicates low gypsum content. The shallow features together with the bright flat visible/NIR slope compared to the other saltpan spectra, may suggest crystalline halite. The spectra from site A and B do not show any significant iron oxide absorption at 870 nm, consistent with the lack of red hues in the soil colour. Some samples display slight concavity between 600-700 nm, which may be indicative of small traces of iron oxide or more likely to be residual vegetation pigment, such as chlorophyll (at 664 nm).

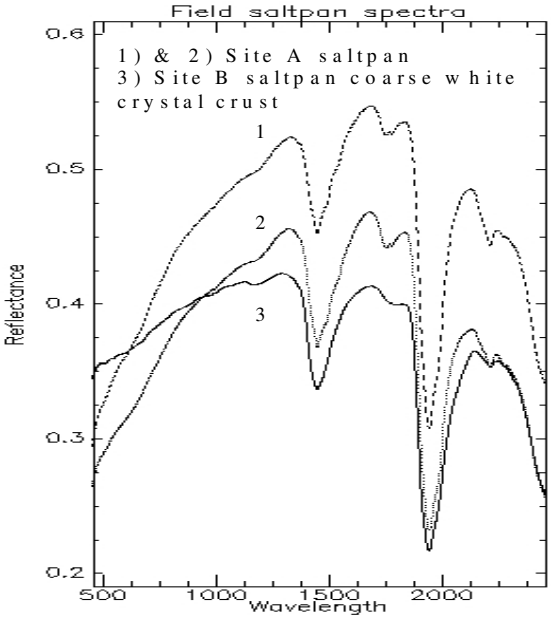

Figure 3-4 Comparison of salt crust spectra from Site A and Site B

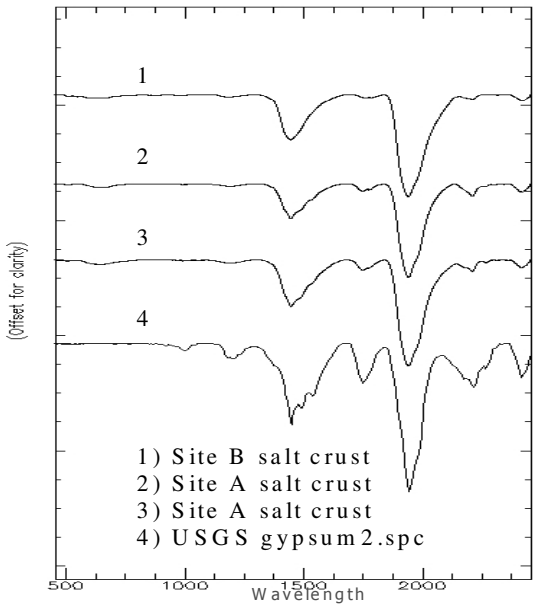

Figure 3-5 Continuum removed salt crust spectra from Site A, Site B and USGS gypsum spectra.

3.3.2 Spectral characteristics of perennial species

The individual spectra of samphire were collected from representative green and red plants at the saline study sites (Figure 3-6, Figure 3-7 and Figure 3-8). The samphire spectra contain discontinuities because wavelength regions that were overly affected by noisy artefacts (950 nm region, where the spectrometer sensors overlap, and the two water absorption regions at 1400 and 1900 nm) were not displayed. The plant spectra were dominated by photosynthetic vegetation characteristics such as the chlorophyll absorption, a red edge increase and a high NIR plateau containing deep water absorption features.

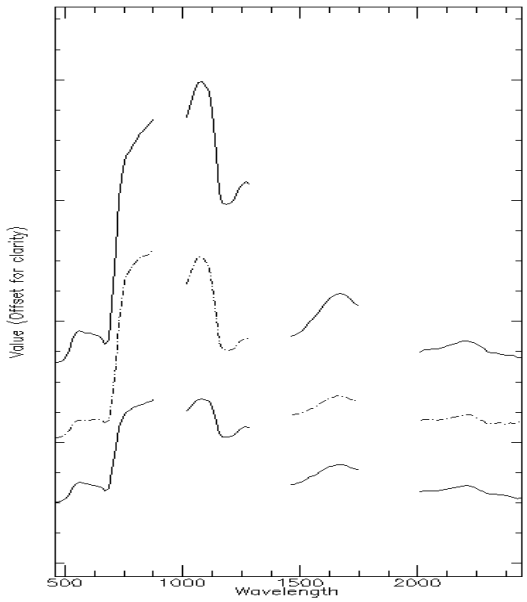

Figure 3-6 Field spectra of green samphire

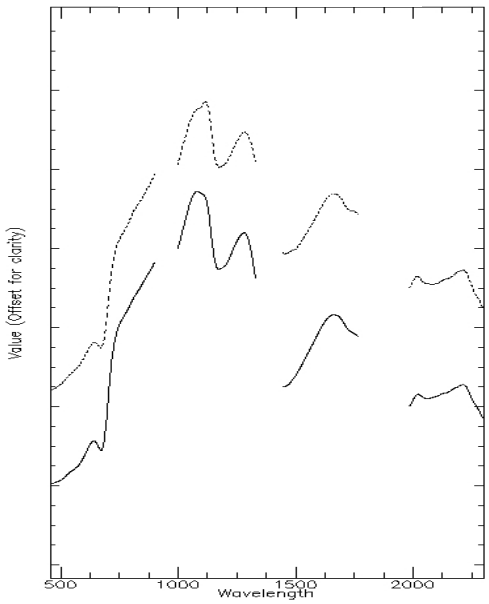

Figure 3-7 Field spectra of red samphire

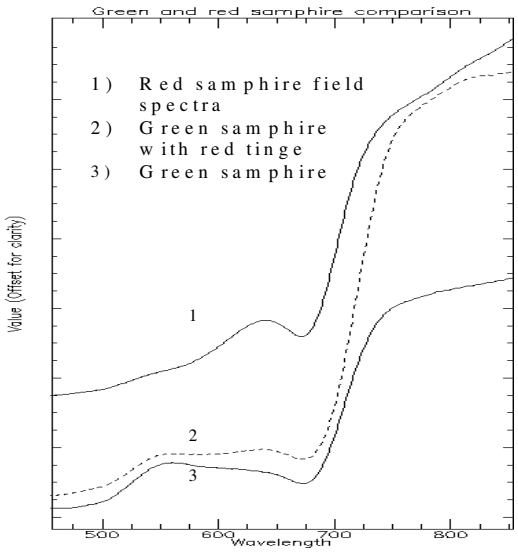

Figure 3-8 Detail showing green and red samphire reflectance peaks

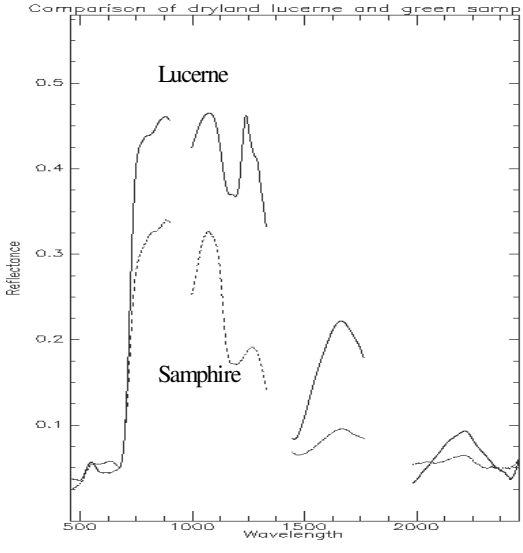

Figure 3-9 Comparison of dryland lucerne and samphire spectra

The spectra of green samphire, often seen with red tips, exhibit peaks in both green and red wavebands and not surprisingly red samphire spectra contain a significant reflectance peak in the visible red wavelength region (Dehaan and Taylor, 2002B). Samphire spectra have additional features of note, including a sloping red edge shoulder and cellulose-lignin features at 2100 nm and 2300 nm, possibly due to stalks or leaf wax coating (Elvidge, 1990; Lewis *et al*., 2000). The sloping red edge is most prominent in the red phase spectra. Spectral features beyond 2300 nm were not considered because they were likely to be overly affected by instrument noise and spectral smoothing.

The spectrum of dryland lucerne differs from samphire spectra in the visible/NIR and in the SWIR regions (Figure 3-9). Dryland lucerne spectra have a deeper chlorophyll absorption, higher NIR plateau and featureless SWIR.

3.3.3 Statistical comparisons of grass species

The laboratory spectra of sea barley grass and brome grass were collected at the time of "spring flush" (September). The mean spectra of both species appear similar at this time of year (Figure 3-10). The spectra are characterised by typical green vegetation features such as chlorophyll absorption at 680 nm (less well defined in the field spectra) and a steep rise in reflectance around 700 nm (the red edge).

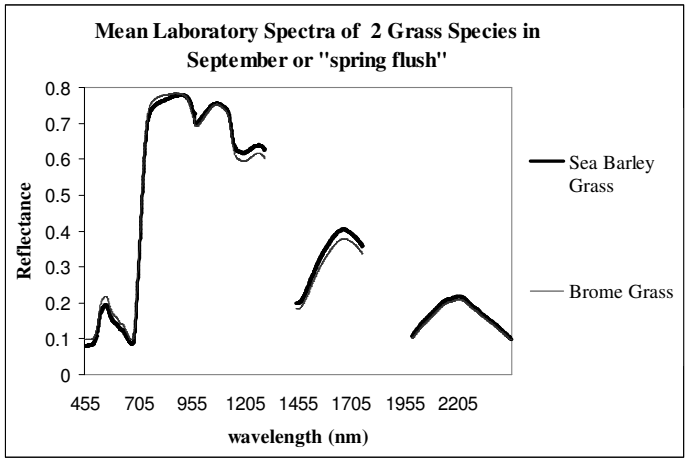

Figure 3-10 Mean spectra of sea barley grass and brome grass at the time of maximum growth or "spring flush" (September)

The standard t-test results showed there were no significant differences (t-values < t-critical) between the mean spectra of sea barley grass and brome grass at any wavelengths (Figure 3-11).

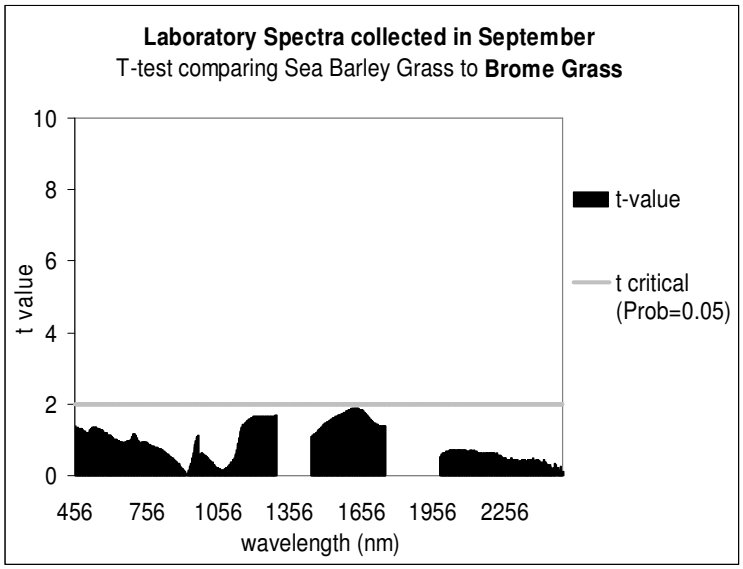

Figure 3-11 "Spring flush" t values by wavelength for pairs of comparisons between mean spectra of sea barley grass and brome grass. There is no significant difference at any wavelengths

The field and laboratory mean spectra of sea barley grass were compared to mean spectra of four other plant species, collected in November (Figure 3-12). The most obvious difference between the field and laboratory spectra is the difference in overall brightness or albedo. The lower field reflectance can be attributed to the reflectance including a mix of background soils and shadow (Kipling, 1970) and to differences in illumination source. The background soil, together with the presence of more dry plant material in the field, may also account for the subtle SWIR structures in the spectra of brome and sea barley grass (Figure 3-12).

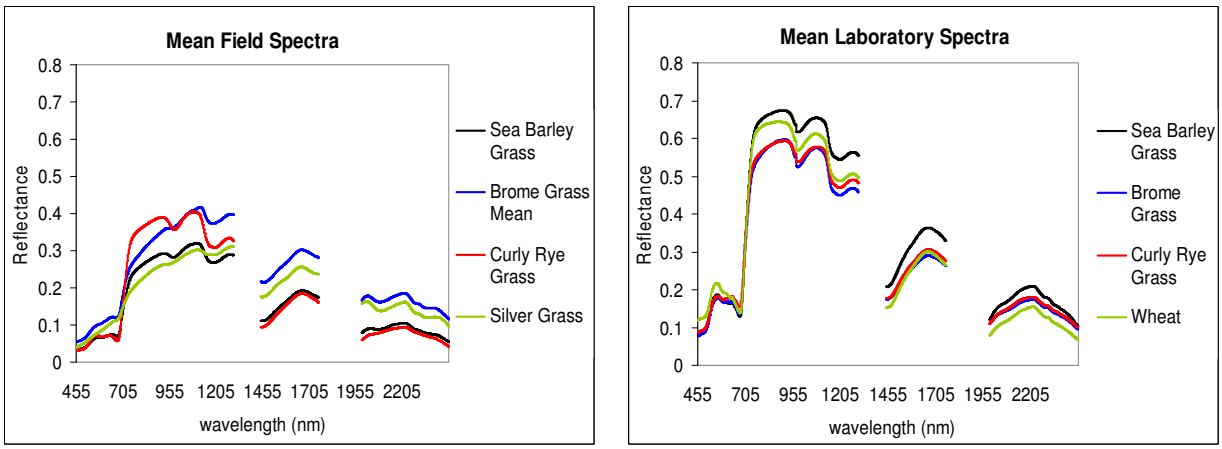

Figure 3-12 Mean spectra acquired at the time of senescence (November) of four grass species: a) field spectra; b) laboratory spectra

Results of statistical comparison between sea barley grass and other plant reflectance are shown in Figure 3-13. There are broad wavelength regions where sea barley grass differs from other species in both field and laboratory spectra. The field and laboratory spectra of sea barley grass consistently demonstrated significant differences (t-values > t-critical) from other plant species in both the NIR and SWIR regions.

In November, the reflectance of sea barley grass was significantly different from every other species in the region from 1170-1298 nm, for both field and laboratory acquired spectra. The green (560 nm) and red (680 nm) part of the visible spectrum was also found to be significantly different when comparing field-acquired spectra, but comparisons of laboratory spectra failed to identify this region as significant. The narrow red edge region near 700 nm is the only region with no significance for any species pairs. The red edge is where significant differences are expected to occur between early senescing and non-senescing vegetation (Elvidge, 1990). However, there are two possibilities to explain the lack of spectral difference in the red edge region. Either senescence had advanced in all species such that the red shift had already occurred, or that the t-test could not find a significant difference between the means because of spectral variation within species.

The importance of the NIR and SWIR regions for discriminating plants at various stages of senescence is consistent with known spectral changes that occur in plants as they reach the end of their growing season. Internal biochemical and structural changes result in distinct spectral modifications in the NIR, notably the collapse of the NIR shoulder and increase reflectance in the SWIR (Elvidge, 1990). In the November field spectra (Figure 3-12 a), spectral differences can be seen in these regions when comparing the greener halophytic grasses to the non salt-tolerant species. The mean spectra of non-halophytes (brome and silver grass) have collapsed NIR shoulder and higher reflectance in the SWIR, where fine spectral features related to dry plant materials such as cellulose and lignin are becoming evident. On the other hand, halophytic grasses have higher NIR reflectance for both field and laboratory acquired spectra (Figure 3-12 a and b respectively). The expected changes in the visible and SWIR reflectance are not as evident in the laboratory mean spectra, which suggests that in the field other factors influence reflectance including the presence of more dry plant material, background soils and shadow (Kipling, 1970).

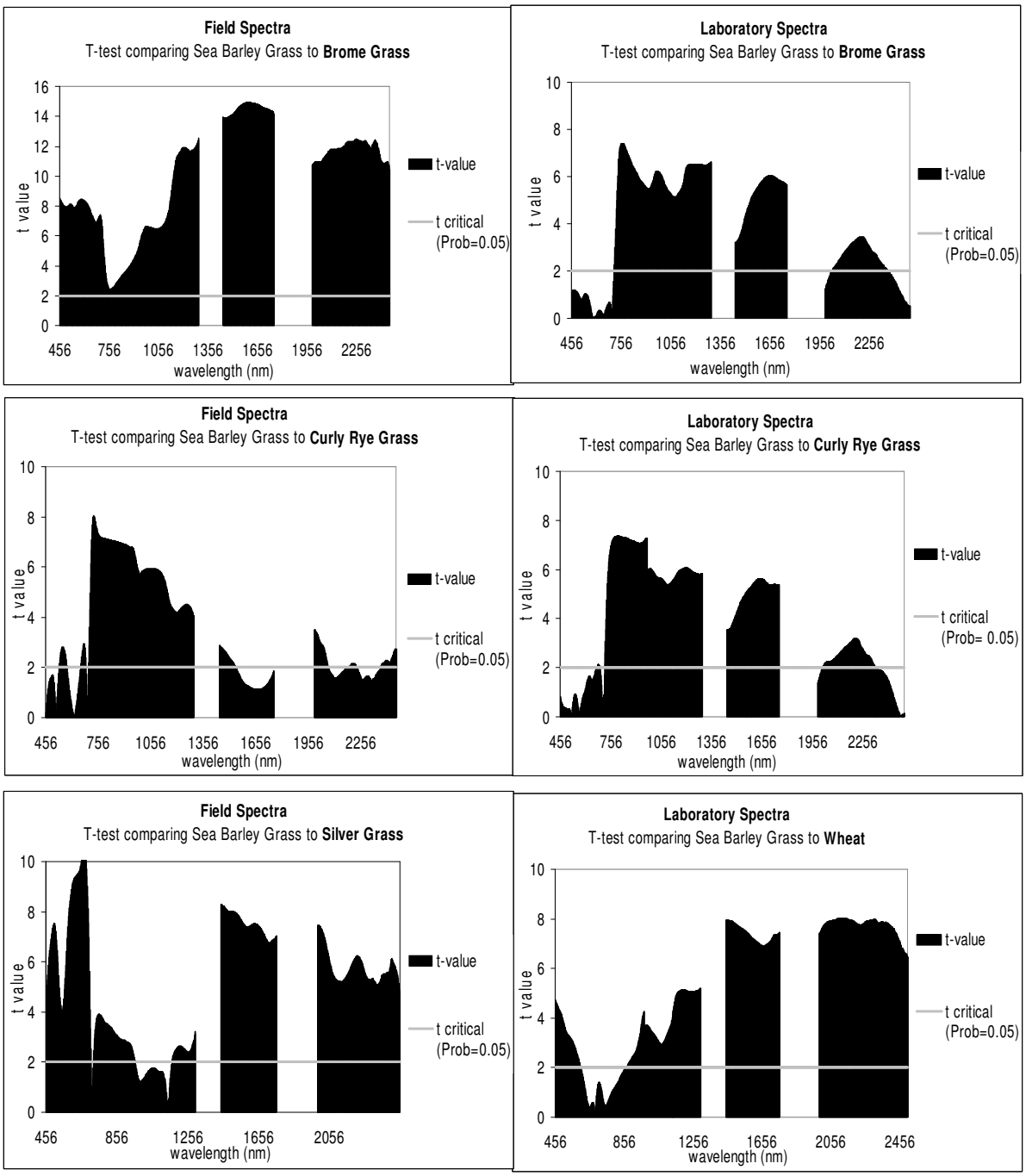

Figure 3-13 T-values by wavelength comparing the mean spectra of sea barley grass to non-halophytic grass species. The spectra differ significantly where t>t critical, equivalent to a probability=0.05. There are consistently significant differences at most wavelengths except at the red edge around 700 nm.

The significance of the 1170-1298 nm region and the absence of significant differences in the red edge, corroborates the results of Schmidt and Skidmore (2001 and 2003), who found that the narrow region around 1300nm and the red part of the visible region to be the most important wavelengths for species separation and the red edge to be the least important. The t-tests inability to identify significant differences in this region suggest

that for senescing species there is a larger variation in "greenness" within each species than between species, particularly sea barley grass because the spectra were acquired from all three field sites.

3.4 Conclusion

At Point Sturt, distinguishing spectral characteristics were found in both soil and vegetation symptoms of salinity, including sea barley grass, samphire and extremely saline soils.

The spectra of saltpan soils contain spectral features consistent with gypsum such as the broad absorption feature at 2200 nm, a single 1755 nm feature and a triple feature near 1500 nm. The presence of gypsum was also confirmed by XRD analysis (see results presented in Chapter 2). The spectra of the coarse thick white salt crust collected at Site B are characterised by a brighter flatter visible/NIR region, and shallow absorption features at 2200 nm and 1755 nm (Figure 3-4). The 1755 nm feature suggests the presence of gypsum but the shallow nature of both features indicate low gypsum content. XRD analysis confirmed the crystal crust to be halite.

The individual spectra of green and red samphire are dominated by photosynthetic vegetation characteristics such as the chlorophyll absorption, a red edge and NIR plateau containing deep water absorption features. The spectra of green samphire, often seen with red tips, exhibit peaks in both green and red wavebands and not surprisingly red samphire spectra contain a significant reflectance peak in the visible red wavelength region (Dehaan and Taylor, 2002B). Samphire spectra have additional features of note, including a sloping red edge shoulder and cellulose-lignin features at 2100 nm and 2300 nm, possibly due to stalks or waxy cuticle coating the succulent beaded leaves (Elvidge, 1990; Lewis *et al*., 2000).

Late in the dry season, saline soils at Point Sturt contained less moisture. The lack of surface moisture meant that spectral features pertaining to soil properties could be maximised in field spectral measurements (Lobell and Asner, 2002). Therefore, late in the dry season is an ideal time to exploit the soil and saltpan spectral characteristics for hyperspectral salinity mapping. Furthermore, the dry season appears to be a suitable time of year to distinguish homogenous patches of samphire from the senesced annual grasses, which dominate the landscape, and native mallee vegetation. However at this

time, fewer halophytic species are available to map because annual grasses have senesced and are indistinguishable on the ground.

November appears to be as the optimum month in this environment to exploit spectral differences between the variable rates of senescence between halophytic grasses and other annual species. Multiple reflectance spectra were collected of sea barley grass and other annual plant species such as curly rye grass, silver grass, brome grass and wheat, during spring and senescence in September 2004 and November 2003. The 2-group t-test results show that there were no significant differences between sea barley grass and brome grass during "spring flush". However during senescence, there were broad wavelength regions where sea barley grass differs significantly from other species for both field and laboratory spectra. Broad visible, NIR and SWIR regions were identified where sea barley grass differs significantly from other species. The red edge did not show significant differences most likely due to the considerable variation in reflectance within each senescing species, which corroborates the results of Schmidt and Skidmore (2001).

Selected dryland salinity symptoms have distinctive spectral properties, making them potentially suitable for mapping with hyperspectral imagery acquired over dryland agricultural landscapes. Plant species adapted to saline environments, highly saline soils and senescing halophytic grasses all have discriminating spectral features in the visible, NIR and SWIR wavelength regions. Sensors that incorporate all these regions include HyMap and AVIRIS airborne scanners and the Hyperion satellite-borne scanner. These sensors would therefore be suited to mapping various salinity symptoms. The CASI scanner was available to fly surveys over the study area when annuals vegetation were in the late stages of senescence (November). CASI airborne scanner operates over the NIR spectral range, a spectral region that exhibited significant spectral differences related to the varying rates of senescence of sea barley grass and non-halophytic brome grass. Analysis of CASI data may therefore be able to distinguish sea barley grass from non-halophytic grasses and was considered an appropriate sensor for mapping sea barley grass during senescence, even without the SWIR spectral region.

4 MAPPING SALINITY SYMPTOMS WITH HYMAP HYPERSPECTRAL IMAGERY

4.1 Introduction and aims

Although satellite imagery has the advantage of being able to map salinity at catchment and regional scales, its spatial and spectral resolutions are limited. These limitations may be overcome by the high spectral and spatial resolution of airborne hyperspectral imagery. Mapping over larger areas, such as those captured by single satellite scene, is problematic for hyperspectral airborne scanners due to the relatively small areas covered by narrow, high spatial resolution image swaths. Therefore, mapping significant areas with airborne imagery requires integration of data from many flight lines. If dryland salinity mapping could be readily achieved across multiple image swaths, then high spatial and high spectral resolution imagery would have the significant advantage of fine scale mapping over catchments. Improved salinity maps would provide a valuable tool for land managers and landcare groups to target amelioration plans and evaluate remediation projects, such as saltland pasture implementation (Barrett-Lennard, 2003) or necessary large-scale native revegetation programs (Pannel, 2001).

Hyperspectral analysis of single image swaths has been applied to mapping native vegetation types (Chewings *et al*., 2000; Lewis, 2002; Lewis *et al*., 2000; McGwire *et al*., 2000; Roberts *et al*., 1993) and has proven particularly valuable in geological mapping (van der Meer, 1998). Mineral mapping has involved both full spectral mixture analysis, which maps all the scene components (Kruse and Boardman, 2000; Chabrillat *et al*, 2000; Resmini *et al*, 1997) and partial unmixing methods, which targets specific compontents of interest. Various partial unmixing methods that are widely used include matched filtering (Harsanyi and Chang, 1994), Mixture Tuned Matched Filtering (Boardman 1998) and least-squares spectral band fitting (Clark *et al*, 1990). Various studies have shown that partial unmixing methods are suitable for geological mapping (Kruse *et al.*, 1999); Kruse and Boardman, 2000; Kruse *et al*, 2000; Chabrillat *et al*, 2000), mapping clay soils (Chabrillat *et al.*, 2002) and evaporite minerals (Crowley, 1993).

Recent research has focussed on evaluating different hyperspectral processing methods for soil and vegetation separation and even plant species discrimination. Most studies

have been conducted in arid and semi arid ecosystems although quantitative monitoring of vegetation in these areas is challenging due to the relatively low vegetation cover and the resulting spectral mix of exposed rock, soil and plant litter (Chen *et al.*, 1998). However, Asner *et al.* (2000) demonstrated that green foliage, wood, standing litter and bare soil had distinctive spectral properties using first derivative spectra. These distinctive spectral properties were utilised by linear unmixing, also known as spectral mixture analysis (SMA), one of the most promising hyperspectral processing methods (Sommer *et al.*, 1998) for scene component abundance mapping. SMA is a complete mixture model which assumes each pixel spectrum is a weighted linear mixture of spectral endmembers such as vegetation, soil and shadow, which can be selected either from a spectral library (field or laboratory) or by deriving end-members from the purest pixels in the image. The set of image end-members should describe all spectral variability for all pixels (Sommer (1998) refers to Adams *et al*. (1989) and Smith *et al*. (1990)). Partial unmixing methods including spectral angle mapping and mixture tuned match filtering have been applied to mapping invasive weeds (Mundt *et al*., 2005; Williams and Hunt Jr., 2002).

A study in the arid regions of central Australia found pure soil pixels were more easily extracted than pure spectral signatures of sparse trees and shrub canopies and actively growing and senescing vegetation (Chewings *et al*., 2000). SMA has also been shown to readily discriminate green vegetation, shade and soil endmembers (Roberts *et al*., 1993) and green vegetation, non-green vegetation and shade (Gamon *et al*., 1993) in AVIRIS hyperspectral data.

Further studies have successfully discriminated more subtle spectral characteristics associated with vegetation species. The importance of VNIR and SWIR features for arid plant species discrimination was emphasised by Lewis *et al* (2000). They found automated unconstrained spectral unmixing of Airborne Multispectral Scanner images in the VNIR wavelength region typically produced vegetation endmembers which correlated to field components, namely Eucalypts, other trees, relatively sparse understorey shrubs and herbs, dry plant litter and soil encrusting lichens. Lewis attributed the success of SWIR regions for vegetation discrimination to cellulose-lignin and other biochemical absorption features near 2100-2200 nm and 2310 nm, originally identified by Elvidge (1990).

Significantly, a preliminary study by Dehaan and Taylor (2002A) has specifically investigated mapping soil and vegetation indicators of irrigation-induced salinity by image analysis of a single airborne hyperspectral swath. The most successful mapping methods were found to be MTMF and spectral feature fitting, although the resultant salinity maps were not statistically assessed for accuracy.

The overall aim of this part of the study was to determine whether accurate maps could be produced of dryland salinity symptoms over larger areas covered by multiple HyMap image swaths. Mapping larger areas with high resolution airborne imagery is problematic because of the need to manage multiple image swaths. There is a general lack of information in literature regarding multiple strip processing, even though there is research being conducted in this field (*pers. comm.* Dr. Peter Hausknecht, HyVista Corporation (2005))**.** Multiple strip processing is nontrivial and requires consistent radiometric calibration across and between swaths, accurate strip georegistration and time consuming processing of large data volumes. Analysing hyperspectral data is computationally intensive, therefore the same reference spectra should be used to map symptoms across multiple strips in order to process the large data volumes efficiently. This study aimed to develop an efficient and consistent processing procedure for mapping salinity across the multiple image swaths using commercially available image processing techniques, like Dehaan and Taylor (2002A), such that if these methods proved successful, catchment managers could readily apply hyperspectral imagery to baseline salinity mapping and monitoring.

Finally, this study also aimed to assess whether the dry season was suitable for mapping dryland salinity symptoms and to develop a practical strategy to validate the salinity maps across subdivided agricultural land where a proportion of landholdings were not accessible.

4.2 HyMap imagery

The HyMap sensor (HyVista Corporation) is an airborne scanner that scans the earth's surface line by line, and records radiance over the visible NIR and SWIR wavelength regions. The HyMap sensor is mounted in a gyro-stabilised platform to minimise distortions due to aircraft pitch, roll and yaw motions. The instrument is designed to operate between 2000 to 5000 m above ground level to achieve typical ground resolution between 3 to 10 m. In-flight, the data is corrected for dark current/electronic

offsets, and converted to radiance using laboratory and on-board radiometric calibration information. The HyMap sensor delivers a good signal to noise ratio of greater than 500:1 and a spatial accuracy of 4.5 m (Cocks *et al.*, 1998).

The Point Sturt HyMap imagery was acquired on 14 March 2001. The 126 band data, at 10-20 nm spectral resolution, spanned a wavelength range from 430 to 2486 nm. The HyMap imagery consisted of 6 overlapping swaths that were obtained during parallel flights (Figure 4-1), covering an area of approximately 140 km^2 at 3m ground resolution (Figure 2). Large fields of yellow dry grass dominate the true colour composite image (Figure 1) because the data was acquired in early autumn, before the winter rains. These dry grass fields are interspersed with greener irrigated areas, dryland lucerne pasture *(Medicado sativa)*, lake fringing marshes and remnant native mallee *(Eucalyptus* sp.*)* stands. Bright areas of exposed soil, such as dry saltpans, small quarries and sand dunes are clearly visible in the centre of the image.

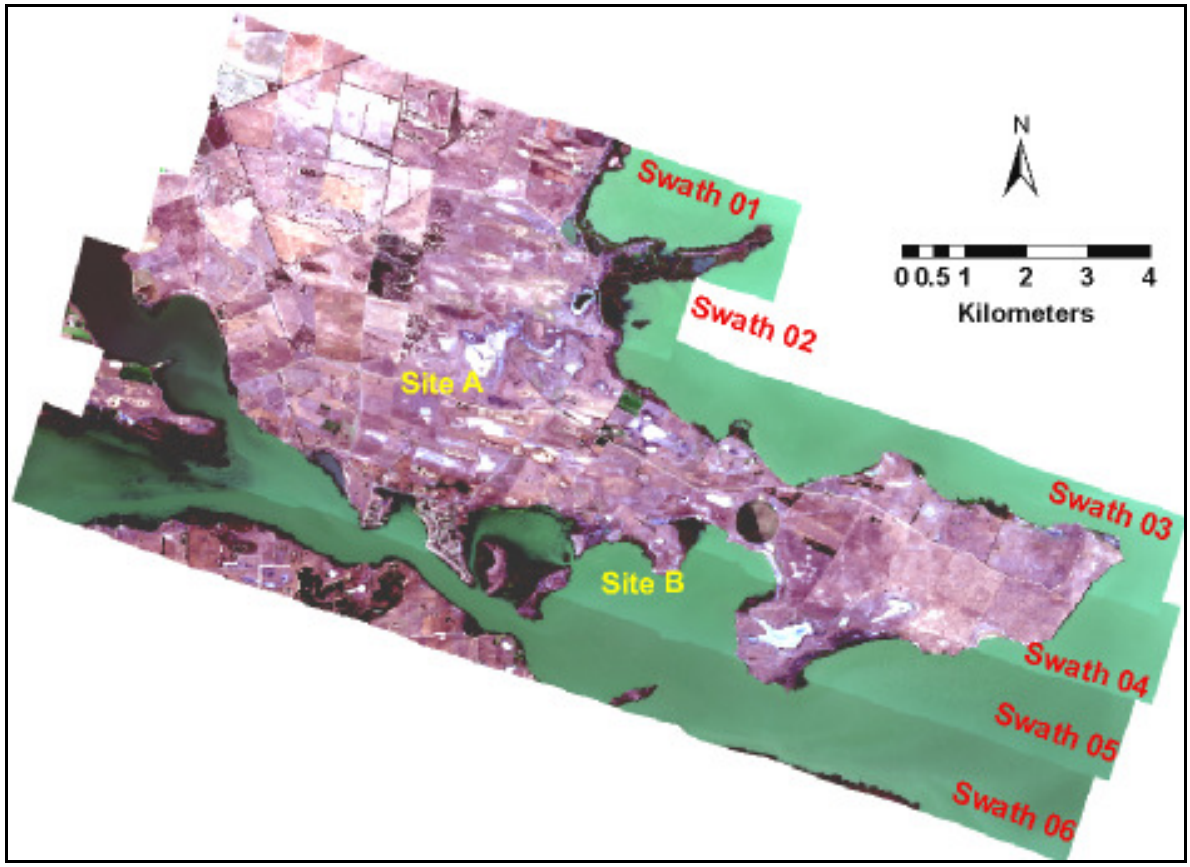

Figure 4-1 Mosaic of six parallel hyperspectral image strips displayed in true colour, covering approximately 140 km^2. The locations of study Sites A & B are also displayed.

The image strips were acquired during the dry season. Only one major rainfall event fell in the months prior to image acquisition (Figure 4-2). Highly saline soils, saltpans and samphire are most suited to mapping during the dry season, as they have spectrally distinguishing features in a background of dry grass (Chapter 2 and 3). These saline soils are often exposed and the halophytic species exhibit zonation, which means that these species are ideal candidates for mapping with remote sensing imagery. A key image analysis task entailed spectrally distinguishing the saline from non-saline sand hills and quarries and also distinguishing perennial halophytic vegetation while excluding other perennial vegetation (dryland lucerne and native vegetation) in a background of dry grass. With the absence of recent rains, image spectra associated with exposed soil would be relatively unaffected by soil moisture.

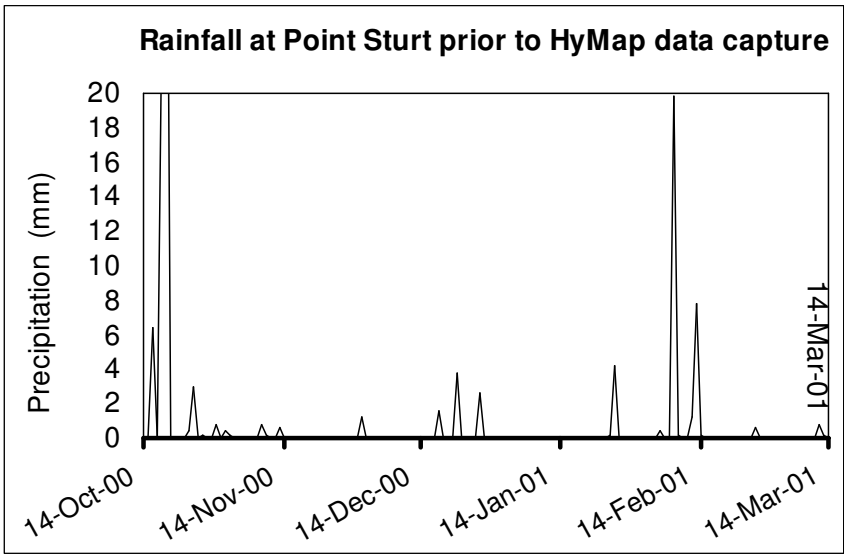

Figure 4-2 Daily rainfall prior to the acquisition of HyMap imagery on 14 March 2001. There was only one major rainfall event one month before.

4.3 Hyperspectral processing and mapping

The analysis of hyperspectral imagery provides a powerful tool for mapping different landcover types. A common mapping approach is referred to as unmixing. The basic assumption of unmixing is that in a natural landscape each pixel spectrum contains reflected radiation from a mixture of landcovers such as vegetation, dry plant material and background soil. Unmixing separates out the spectral information of these sub-pixel elements (Boardman *et al.*, 1995).

Before proceeding with unmixing, preprocessing is required to correct for environmental conditions at the time of image acquisition, and within image variation due to the acquisition configuration. The subsequent unmixing processing ultimately produces maps of target materials.

4.3.1 Preprocessing: atmospheric and cross track illumination correction

There are three approaches available for atmospheric correction of hyperspectral imagery 1) image based methods such as log-residuals 2) empirical methods, which require ground measurements, and 3) model-based correction, which require no ground data and is the most widely used. Model based software such as ACORN (Atmospheric Correction Now, ImSpec LLC) and FLAASH (Fast Line-of-sight Atmospheric Analysis of Spectral Hypercubes, RSI) converts the radiance recorded by the hyperspectral sensor to surface reflectance, thus enabling comparisons between image spectra and field or laboratory derived spectra.

Radiance to reflectance calibration involves correcting for the solar irradiance curve and solar irradiance variations, particularly variations in sun angle, and accounts for atmospheric absorptions, scattering and reflection and atmospheric path effects. These software programs are based on the MODTRAN4 algorithm, which predict atmospheric composition and effects from meteorological data, relevant to the time of image acquisition, and from water absorption bands such as 940 nm and 1100 nm. MODTRAN models follow the radiative transfer models described by Gao and Goetz (1990) as follows:

$L_{sensor}(\lambda)=L_{sun}(\lambda)\ T(\lambda)\ R(\lambda)\ \cos(\theta) + L_{path}(\lambda)$

Where

λ= wavelength

$L_{sensor}(\lambda)$=radiance at sensor

$L_{sun}(\lambda)$ = Solar radiance above atmosphere

$T(\lambda)$ = total atmospheric transmittance

$R(\lambda)$ = surface reflectance

θ =incidence angle

$L_{path}(\lambda)$ = path scattered radiance (single and multiple scattering)

However, current atmospheric correction programs do not apply the topographic ($\cos(\theta)$ term) correction because typically this information is not available. Therefore the land

surface is assumed to be horizontal with Lambertian reflectance. The end result is called "apparent reflectance", which can be converted to surface reflectance if the surface topography is known (Kruse, 2004).

ACORN atmospheric correction software was suited to HyMap data because it corrected for variations in solar irradiance and absorption by atmospheric water vapour and gases over the 350 to 2500 nm spectral range. Therefore, ACORN was used to convert HyMap data from radiance to apparent surface reflectance (ImSpec LLC, 2002).

Variations in across-swath illumination are mainly due to variations of sunlight angle and intensity that occur over the course of an airborne acquisition survey. The solar variations generally result in a systematic increase in pixel brightness, toward the edge of the image swath. If such variations are accounted for, then there may still be radiometric discontinuity between strips.

Across-track illumination effects were corrected by calculating mean brightness values for all bands in each pixel across-track and these values were then displayed as a series of curves (ENVI Software, (Better Solutions Consulting, 1999)) A polynomial function was then fitted to each of these curves to remove the across-track variation. The lake water was masked out in each of the strips to reduce the effect of low water reflectance on the strip spectral statistics. The cross-track correction was not applied to the two remaining water dominated strips because the process was found to exaggerate across track effects.

4.3.2 Hyperspectral image analysis

Further processing aimed to produce distribution maps of spectrally distinct salinity symptoms, such as samphire and saltpans, through standard hyperspectral processing techniques as described by Kruse (1999). These techniques involved data noise reduction, locating spectrally pure pixels, endmember extraction and interpretation, followed by partial unmixing mapping of salinity symptoms. Partial unmixing was selected for this study over complete linear unmixing because it is most suited to mapping selected scene components (Boardman, 1995) such as targeted salinity symptoms.

Noise reduction in hyperspectral processing is based on the *maximum noise fraction transformation*, MNF, described by (Green *et al.,*1988; Lee *et al.*, 1990)). Maximum noise fraction calculates an orthogonal set of components from a multivariate image, to

maximise signal to noise ratio, instead of maximising variance as in the case of principal component analysis (Lee *et al*., 1990). The output MNF data is a series of uncorrelated bands in terms of increasing signal-to-noise (i.e. the first component contains the maximum noise). A variant of this method is employed in ENVI (RSI Inc.) software (Bhargava *et al.*, 1999) but is called *minimum noise fraction* and is given the same acronym *MNF*. In this case the data is transformed in terms of SNR, but the components or new bands are instead organised in reverse order of decreasing SNR. In other words, the transformed data is a series of uncorrelated bands with the first band maximising signal and the last band containing maximum noise. A number of desirable bands were selected and the data transformed back into hyperspectral image space for further analysis.

From the MNF transformed data, the most spectrally pure pixels were then extracted using the "Pixel Purity Index" (PPI) (Harsanyi and Chang, 1994). PPI found the most spectrally pure pixels by repeatedly projecting n-dimensional scatter plots onto a random unit vector and selecting the extreme pixels in each projection (Boardman *et al*., 1995). Automated cluster analysis then extracted endmember spectra from the spectrally pure pixels located at the apices of the n-dimensional data clouds. After this first cut selection, manual endmember selection was performed to cull unwanted noisy endmembers and to select additional useful endmembers. The resulting endmembers were identified through interrogation with ENVI Spectral Analyst and comparison to field data. Image-derived and field spectra were compared to USGS library spectra. The USGS spectral library was suitable for mineral mapping but not suitable for vegetation mapping because it did not contain any pertinent Australian or halophytic vegetation spectra.

A partial unmixing method was sought that would minimise processing time and produce salinity symptom maps across several image swaths. The ideal method should be able to employ a single reference spectrum, either a pure endmember from one image strip or an external spectrum, to map target symptoms across multiple image strips, thereby ensuring consistency of discrimination and reducing endmember extraction processing.

Partial unmixing methods such as matched filtering and least-squares band fitting (spectral feature fitting or SSF) were suitable for mapping soils with well-defined spectral absorption features pertaining to saline minerals. Matched filtering maximises

the response of each reference spectrum pixel by pixel and minimises the response of the unknown unwanted background signatures (Harsanyi and Chang, 1994). Mixture Tuned Matched Filtering (MTMF) was described by Boardman (1998) as the superior matched filtering method. MTMF, though related to MF, has the advantage of highlighting pixels significantly different from background pixels but which do not match the reference spectra (Boardman, 1998). The MTMF, matched filtering and least-squares band fitting methods are able to use a single reference spectra to map across multiple image swaths.

Various partial unmixing mapping techniques were tested to determine the best method for mapping saltpan soils and samphire. The tests were performed on image swath that covered the main saline discharge region (swath 03) where the clay aquifer flow terminates. To determine the optimum method for mapping saltpans, three matched filtering tests were performed using reference spectra subset to include different wavelength ranges; 1) SWIR1 and SWIR2, 2) SWIR 2 only and 3) 1670-1790 nm. The SWIR1 and SWIR2 corresponded to wavelength regions that contained fine, diagnostic mineral absorption features. The wavelength range that produced the most accurate saltpan map was then compared to mapping with spectral feature fitting using the equivalent range.

Preliminary partial unmixing tests established that MF was not an ideal candidate for discriminating and mapping vegetation symptoms. MTMF has been used successfully to map non-halophytic vegetation (Williams *et al.,* 2002) and results from previous studies also showed the potential of this method for mapping halophytic vegetation (Taylor *et al.*, 2001; Dehaan and Taylor, 2002A). Therefore, even though separate processing of each strip was required to produce pure endmembers, MTMF was nonetheless selected as the method most appropriate for mapping vegetation salinity symptoms. Because MTMF technique requires MNF transformed data internal image reference spectra samphire reference spectra were either endmembers extracted from the PPI results or mean spectra extracted from regions of interest spanning known homogenous areas of particular surface salinity symptoms.

Matched filtering and mixture tuned matched filtering output maps were grey scale images, where bright pixels are an indication that the pixel spectrum is close match to the reference spectrum. For MTMF results, a ratio of the “score” image band over the “infeasibility” band was used for the final samphire maps. The grey scale output maps

were thresholded to select areas closely matching the samphire reference spectrum. The selected threshold values were based on two criteria 1) to coincide with the break of slope on the distribution histogram of brightness values and 2) *a priori* knowledge of the extent of some saline areas. Threshold values corresponded to brightness values in the 99.5 to 99.9 percentile histogram intervals. The values were conservatively chosen to underestimate rather than overestimate the extent of the mapped features.

All partial unmixing was carried out on raw image strips and the threshold maps were subsequently georeferenced using the inflight geographical lookup tables (GLTs). The georeferenced threshold maps were exported as themes into geographical information systems (GIS) software for accuracy assessment. Within GIS software (ArcMap 9.0) a neighbourhood filter was applied to smooth the edges of the mapped features in order to partly compensate for the conservative extent of the salinity symptom maps. Additional georeferencing was carried out using ground control points (GCP) to finetune the alignment of each strip for more accurate groundtruthing.

4.4 Accuracy Assessment

To assess the accuracy of the salinity maps, nearly 100 groundtruthing sites were randomly selected using GIS software. Initially, only a limited number of random sampling sites fell within saline areas, therefore further stratified random sampling was also performed to augment the samples with additional sites corresponding to saline areas. Fifty-five sites situated within the area covered by swath 03 were available for accuracy assessment of the partial unmixing soil mapping tests. The groundtruthing data for accuracy assessment were collected in March 2004.

The sampling sites were all located within a 500 m buffer from the road network to allow for visual inspection of those sites that fell inside inaccessible paddocks. Remote sampling sites could be located from the direction and distance indicated by the differential GPS. However, these inaccessible sample sites were only included if they could be clearly sighted and the presence or absence of samphire or saltpans identified with certainty. For example, expansive, upward-sloping hillsides with a uniform coverage of only dry grass were common in the area. These slopes could be unambiguously described as not containing samphire and saltpans. To take into account GPS and georegistration errors, a 7.5m radius buffer was also created around each

sampling point to approximately enclose an area equivalent to 3x3 m pixels (i.e. 9x9 metres on the ground).

The presence or absence of each salinity symptom was recorded within an approximate 7.5m radius of each GPS location. Samphire was scored as present if cover was greater than 10%. Only obvious pans and exposed soils containing extremely salt tolerant plant species, such as samphire, were labelled as saltpans. Exposed soil and the presence of sparse sea barley grass were not considered saline areas severe enough to be considered saltpans.

The error matrix method of accuracy assessment, as described by Congalton (1991), was applied to each salinity map. The samphire and saltpan maps were assessed in separate error matrices because they had been independently derived using partial unmixing. The two symptoms were not mutually exclusive classes, as in traditional thematic maps, but could both be observed at the same site. Subsequent Kappa analysis was performed to produce KHAT statistic values. The KHAT correlation value, which ranges from 0 to +1 in this case, is a measure of how well the salinity symptom map agrees with the field data (i.e. whether the maps represent results better than a random classification). Congalton (1991) assigns KHAT values into three levels where

$\hat{K} > 0.8$ represents strong agreement
$0.4 < \hat{K} < 0.8$ represents moderate agreement
$\hat{K} < 0.4$ represents poor agreement

4.5 Results and Discussion

Two image strips, encompassing the major discharge areas, proved the most successful for producing the widest range of soil and vegetation endmembers and the fewest noisy endmembers (Figure 4-3).

Soil endmembers were compared to USGS mineral spectra and field and laboratory spectra. In general, spectral characteristics identified were associated with gypsum and calcite (absorption feature centred at 2343 nm) and kaosmectites, dry grass, irrigated pasture, and water. Reduced spectral or spatial range datasets also produced samphire endmembers. The clay and gypsum spectra were primarily associated with saltpans, while the calcite spectra were associated with dirt roads characterised by exposed calcrete bedrock.

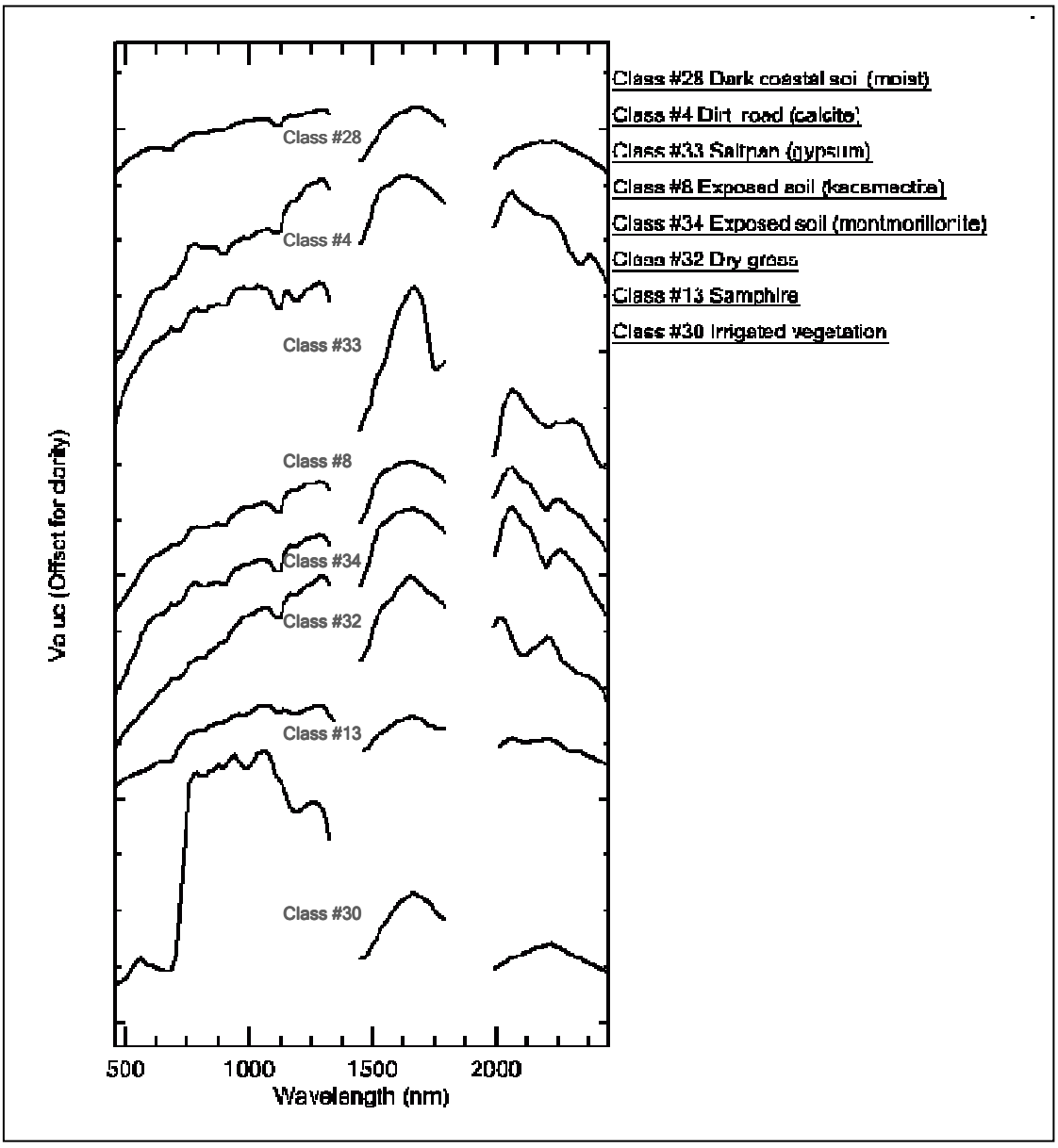

Figure 4-3 Selection of endmembers extracted from one image strip. Similar endmembers from the same landcover types (for example more irrigated and dry vegetation) were not displayed.

The samphire endmembers extracted from two strips contained the same features seen in the field spectra: the collapsed red edge shoulder; shallow chlorophyll absorption and finer cellulose-lignin features in the 2100-2200 nm range (Figure 4-4). Unfortunately, samphire endmembers were unable to be generated using automated endmember selection procedures from every image strip, even though samphire was present. Therefore samphire reference spectra had to be created from image regions of interest (ROI) that spanned known homogeneous, dense samphire patches with minimal soil exposure. Even though the ROI spectra were likely to be a mixture of samphire and

some background soil, the similarity in spectral properties between samphire endmember, field samphire spectra and ROI spectra suggested that mean spectra from each strip were suitable reference spectra for partial unmixing mapping (Figure 4.4).

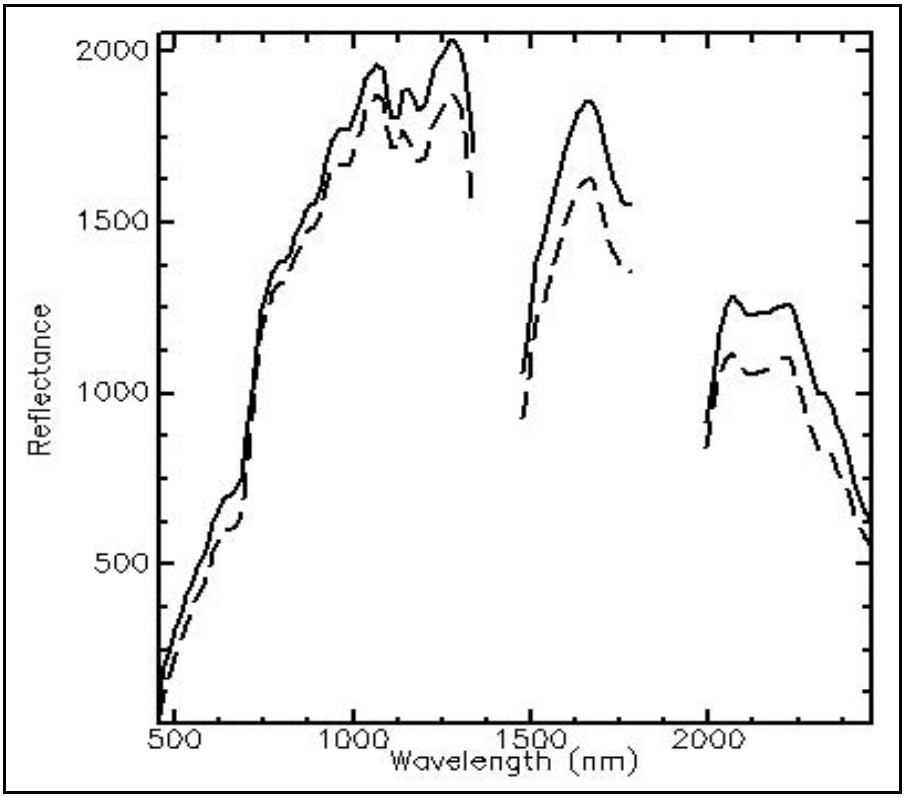

Figure 4-4 Comparison of samphire endmember (dashed) and samphire mean spectrum (solid). The ROI spectrum was generated from a region that encompassed a known samphire patch.

Samphire and saltpans, the best candidates for salinity mapping, appeared to have defining spectral characteristics. In the case of the saltpans, the conspicuous gypsum absorptions were selected as the best features to exploit in partial unmixing mapping of saltpans (Figure 4-5). The image and field saltpan spectra did not contain any distinct absorption features pertaining to saline minerals other than gypsum.

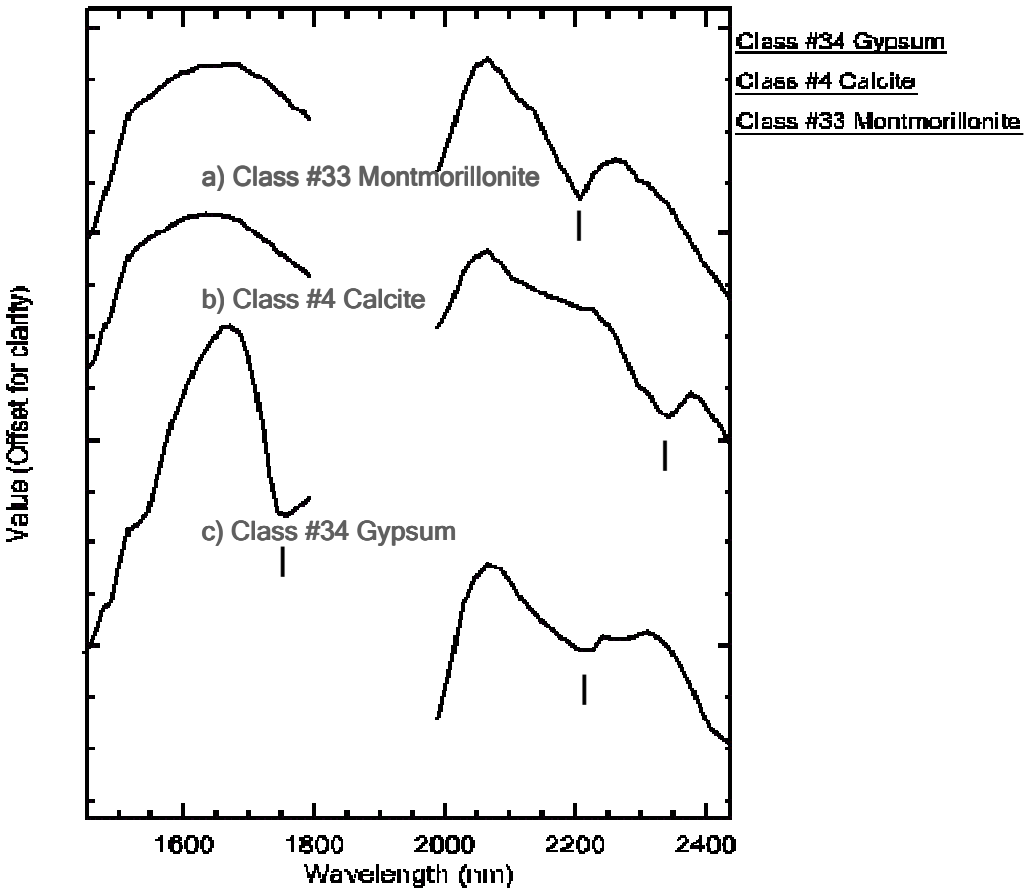

Figure 4-5 Detail of soil image-derived endmember spectra. The absorption features correspond to USGS minerals spectra of a) gypsum b) calcite 3) montmorillonite or kaosmectite

MF saltpan mapping tests using an image-derived endmember with gypsum features found that the SWIR2 region and the SWIR1 and SWIR2 regions combined produced unreliable saltpan maps. The SWIR1 and SWIR2 regions spanned both the 1750 and 2200 nm gypsum absorption features. These regions failed to map a number of saltpans and incorrectly commissioned unsealed roads and sand dunes as saltpans (Table 4-1). Mapping based on the broad 2200 nm gypsum feature (SWIR2) alone was unreliable because it coincided with the 2200 nm clay hydroxyl feature (Figure 4-5), corroborating the gypsum mapping result of Crowley (1993). MF saltpan mapping was most successful when the selected wavelength ranges of the image data and reference spectra encompassed the 1750 nm gypsum absorption feature (1670-1790 nm) (Table 4-1). Matched filtering using the 1750 nm feature successfully mapped most saltpans and the highly saline soils with some samphire cover, whilst excluding the exposed non-saline soil on vegetated dunes, dirt roads and roadside quarries. Matched filtering was

therefore selected as the preferred soil mapping method because of the results of the mapping tests and because a single reference spectrum could be used for mapping multiple image swaths.

Table 4-1 Partial unmixing mapping tests on image swath 03. Matched filtering produced the most accurate maps (KHAT=0.67) when using the gypsum 1750 nm feature.

Mapping method	Wavelength range	Type of accuracy	Map class	Accuracy	KHAT
MF	450 - 2450 nm	Producers Accuracy	Saltpan	0.43	0.29
			No Saltpan	0.85	
		Users Accuracy	Saltpan	0.50	
			No Saltpan	0.81	
	SWIR1 & SWIR2	Producers Accuracy	Saltpan	0.21	0.21
			No Saltpan	0.95	
		Users Accuracy	Saltpan	0.60	
			No Saltpan	0.78	
	SWIR2	Producers Accuracy	Saltpan	0.36	0.37
			No Saltpan	0.95	
		Users Accuracy	Saltpan	0.71	
			No Saltpan	0.81	
	1670-1790 nm	Producers Accuracy	Saltpan	0.57	0.67
			No Saltpan	1.00	
		Users Accuracy	Saltpan	1.00	
			No Saltpan	0.87	
SFF	1670-1790 nm	Producers Accuracy	Saltpan	0.57	0.54
			No Saltpan	0.93	
		Users Accuracy	Saltpan	0.73	
			No Saltpan	0.86	

MF unmixing with an endmember extracted from one strip effectively mapped saltpans in four other image strips. The georeferenced mosaic combining all image strips is shown in Figure 4-6. The bright areas indicating high gypsum abundance coincide with the location of known saltpans throughout the peninsula. The most significant area mapped is the central lowlying plain where the clay aquifer flow terminates (Site A). Here numerous bright areas coincide with the known location of saltpans and highly saline exposed soils. Other areas of high gypsum abundance correspond to coastal saltpans including the salt encrusted pan at Site B. Unmapped dark areas within saltpans are due to some remnant surface water that masks the mineral absorption features in the image spectra.

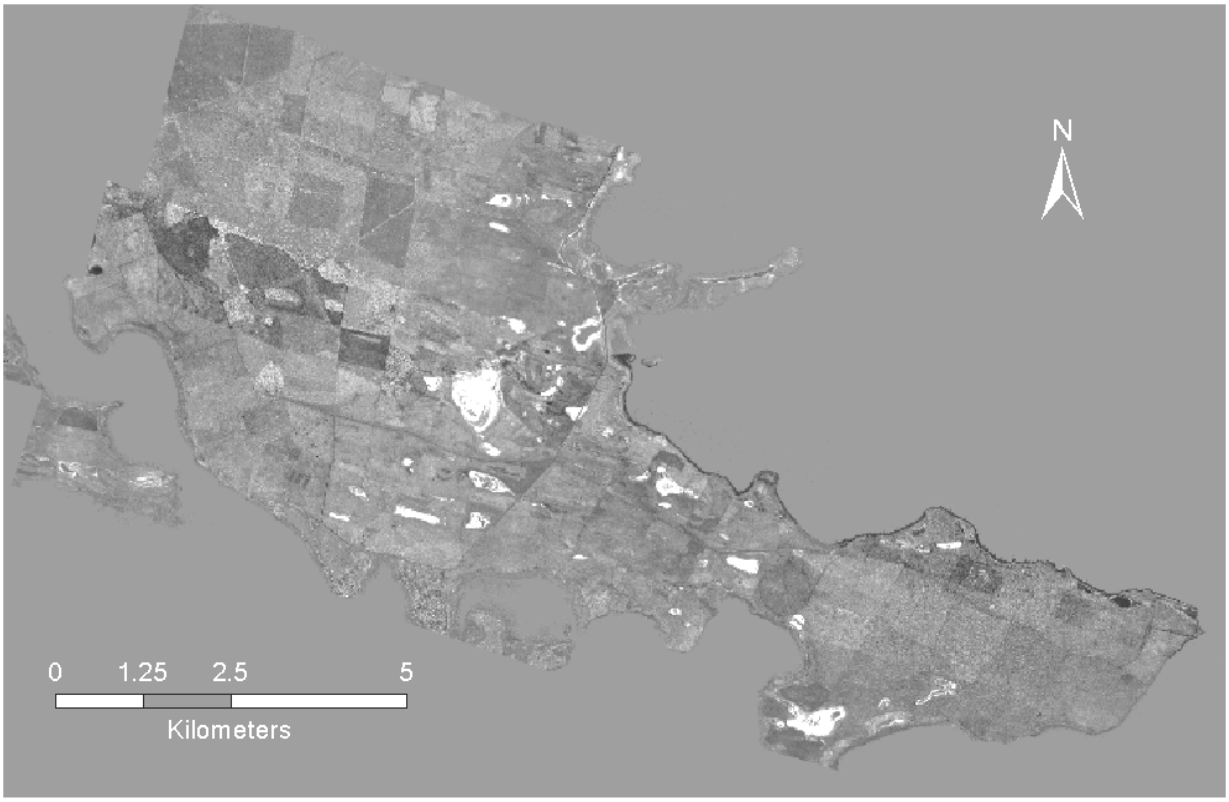

Figure 4-6 MF gypsum map where bright areas, indicating areas of high gypsum abundance, coincide with the location of known saltpans

The samphire maps produced were equivalent to maps produced with an image-extracted endmember, therefore ROI spectra generated from within each image strip were deemed suitable reference spectra for MTMF mapping. Preliminary partial unmixing tests were carried out to compare the suitability of mapping using reduced datasets over various wavelength ranges. The unmixing tests indicated that optimum data range for MTMF mapping samphire encompassed the entire visible to SWIR region (455-2500).

A ratio of the MTMF "score" image over the infeasibility image was used as the final samphire maps. The georeferenced mosaic of samphire maps, produced from four image strips, is shown in Figure 4-7. Strip 01 was not processed because no significant patches of samphire could be located in the area. The maps reveal high abundance areas of samphire surrounding the numerous saltpans and fringe some coastal areas. As expected, MTMF proved capable of discriminating areas of samphire from irrigated pasture and perennial dryland lucerne and native vegetation stands.

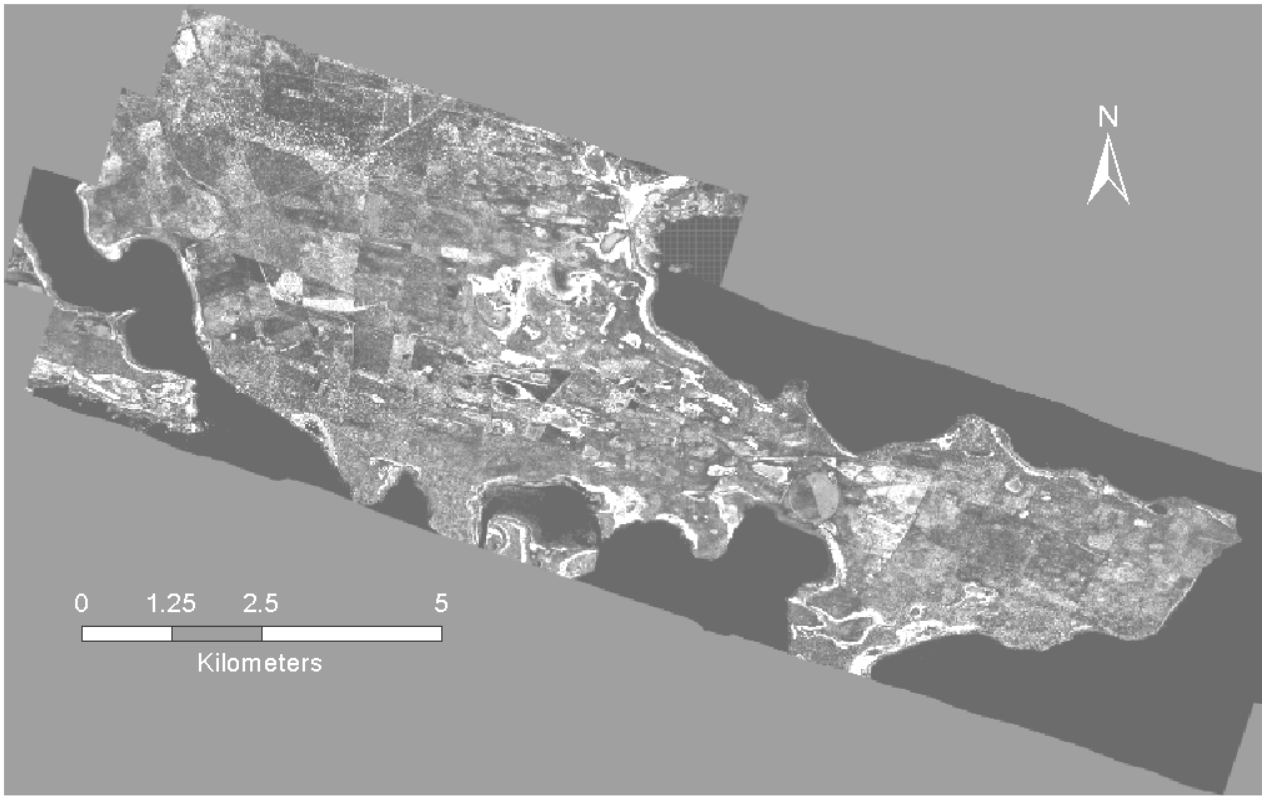

Figure 4-7 Samphire map comprising georeferenced MTMF results of 4 image strips. Bright pixels indicated areas of high abundance.

The highest MF and MTMF scores in the images were thresholded to create the salinity symptom maps. Because these high abundance areas were spatially continuous and well defined, the cutoff values could be determined through an iterative fine tuning processing to produce maps that coincide with the extent and location of known samphire patches and saltpans. The threshold values were chosen to underestimate rather than overestimate the extent of the saltpans areas. The threshold maps were exported into GIS software and a neighbourhood filter applied to smooth the mapped features (Figure 4-8).

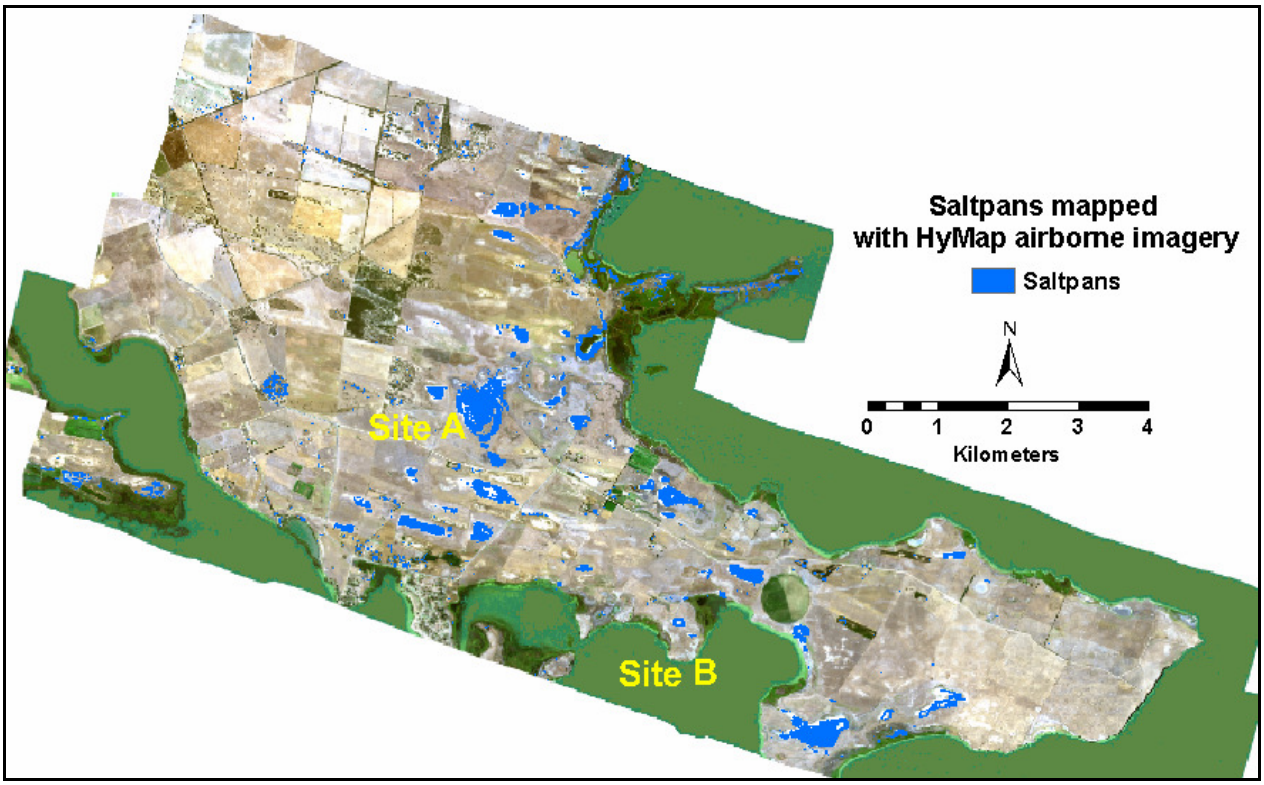

Figure 4-8 Saltpans were mapped at Site A and B with HyMap imagery. Matched filtering discriminated the highly saline soils of the saltpan from the non-saline dunes and quarries.

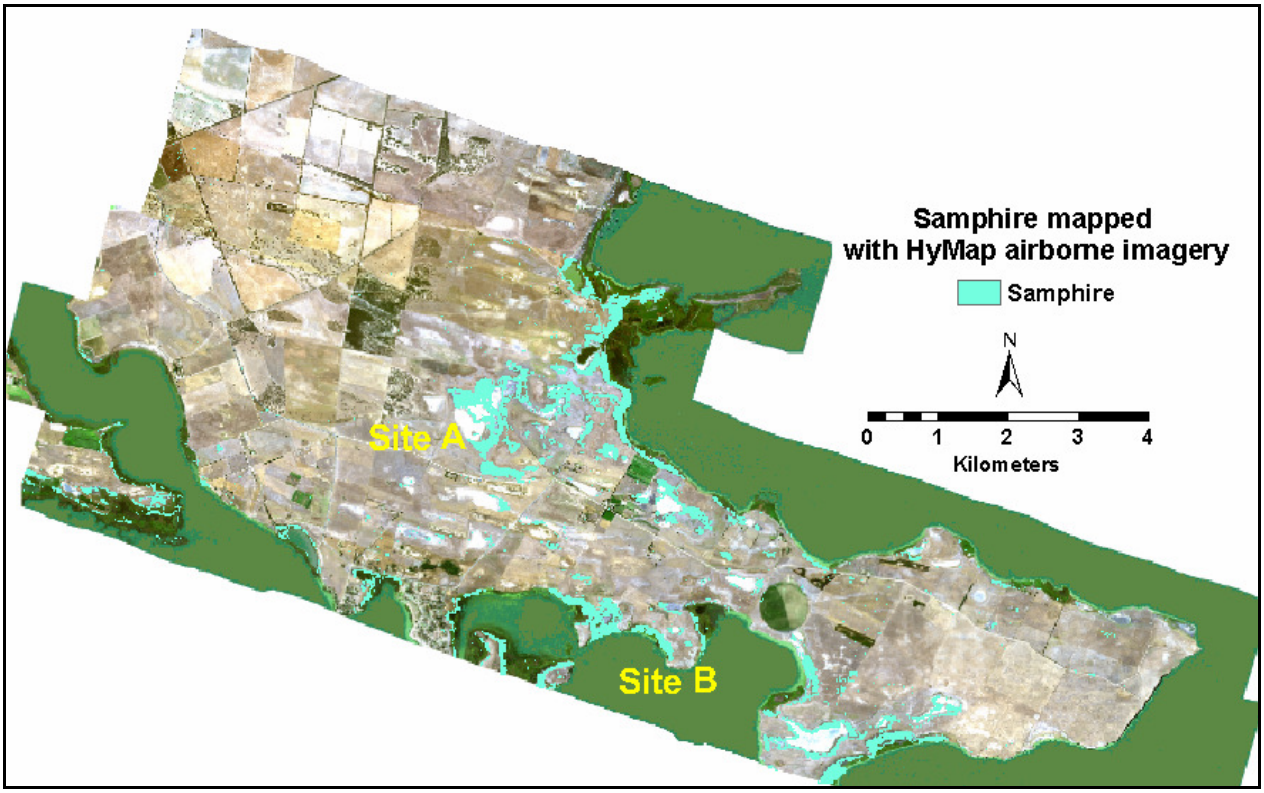

Figure 4-9 Samphire was mainly mapped along the coast and surrounding the major saltpan at Site A and in the central discharge area.

The optimum processing flow for samphire and saltpans followed the same preprocessing and standard hyperspectral image analysis procedures which produced maps for accuracy assessment (Figure 4-10). The difference between the two flows was the choice of MTMF for samphire vegetation mapping and reference spectra derived from each image swath using a priori knowledge of the location of samphire patches.

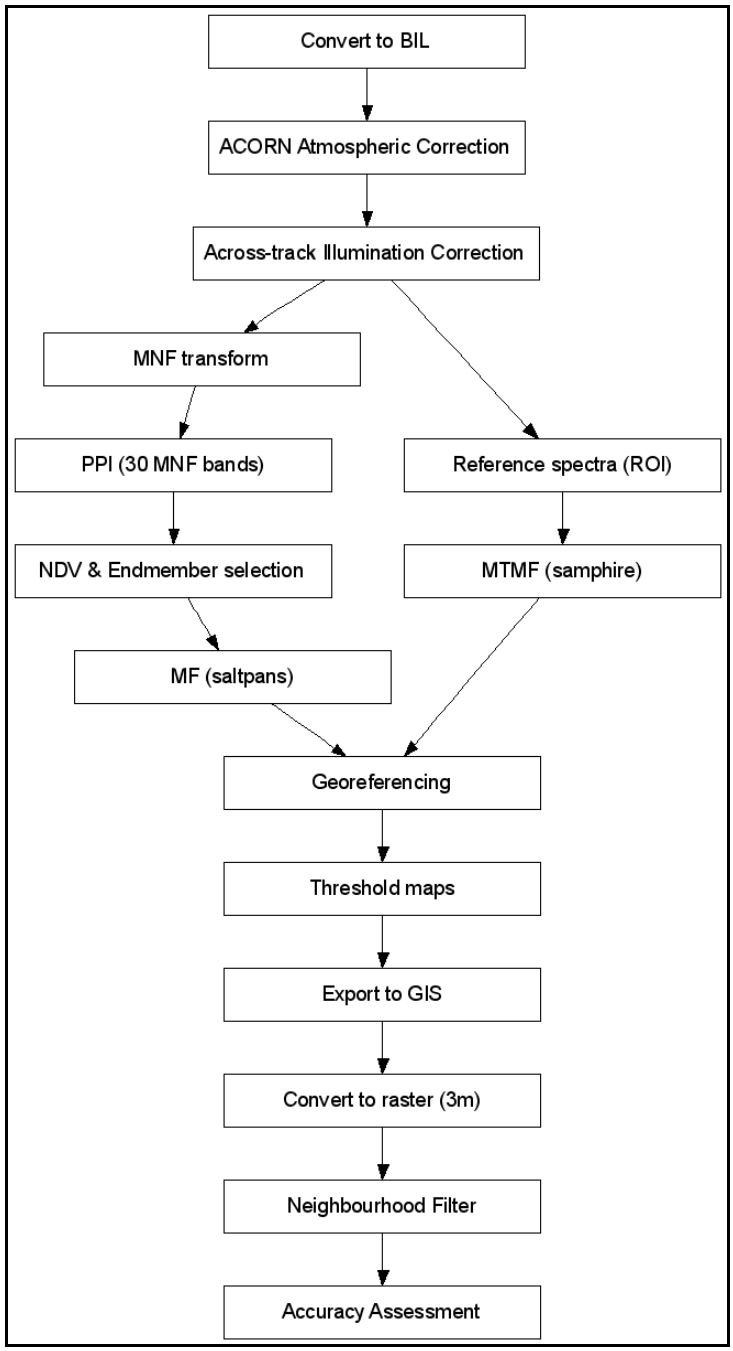

Figure 4-10 Optimum processing flow for mapping multiple HyMap image swaths

Standard error matrices were constructed for the samphire and saltpan maps (Tables 1a and 1b). Separate matrices were required for the samphire and saltpans because the two symptoms were mapped independently over a different number of hyperspectral image strips and hence utilised a different number of sampling sites. In each error matrix there are only two mutually exclusive categories: the presence or absence of a particular symptom at each field site.

Table 4-2 a) Error Matrix for the samphire map (129 sample sites over 4 image strips)

Samphire Error Matrix		Field		Total
		Present	**Absent**	
Image	**Present**	17	4	21
	Absent	12	96	108
	Total	29	100	129

Total accuracy…….88

Producer's accuracy (%)

Present…….59

Absent…….96

Users accuracy (%)

Present…….81

Absent…….89

KHAT…….0.61

Table 4.2 b) Error Matrix for the saltpan map (137 sampling sites over 5 image strips)

Saltpan Error Matrix		Field		Total
		Present	**Absent**	
Image	**Present**	17	2	19
	Absent	16	102	118
	Total	33	104	137

Total accuracy…….87

Producer's accuracy (%)

Present…….52

Absent…….98

Users accuracy (%)

Present…….89

Absent…….86

KHAT……..0.58

The overall accuracies of both samphire and saltpan maps, 88% and 87% respectively, are high and the maps show a moderate agreement with the field observations, as is evident from the calculated KHAT values of 0.61 and 0.58 respectively (Table 4-2 a and b).

Pixels within native mallee vegetation stands were sometimes mistakenly mapped as saltpans. This misclassification is most likely due to the native vegetation spectra containing shallow absorption features between 1720 and 1760 nm, coinciding with the gypsum absorption feature centred at 1750 nm. Absorption features in the 1700 nm region in the mallee vegetation are most likely due to non-green plant components like dry leaves, bark (Elvidge, 1990) and characteristics more typical of species adapted to arid environments (Elvidge, 1990; Lewis *et al*., 2000). Some errors also occur because the threshold values used to produce the maps from the MF and MTMF outputs were

chosen to underestimate rather than overestimate the extent of the saltpans areas. Decreasing the threshold values would increase the areal coverage of the actual saltpans and samphire but would evoke more errors by mapping more native vegetation. Overall, subjective fine-tuning of threshold values may improve the accuracy of maps but ideally, a generalised, objective and consistent method for optimising threshold values to produce accurate maps needs to be established. Currently, on the ground expert knowledge of one or more areas where the salinity symptoms appear is essential to enable the selection of reasonable threshold values.

4.6 Conclusion

At Point Sturt, saltpans and samphire were found to be the most spectrally distinctive dryland salinity symptoms and may therefore be suitable candidates for mapping salinity with hyperspectral imagery acquired over other dryland agricultural areas. Samphire and highly saline soils were successfully mapped across multiple image swaths from a single date airborne survey with no ancillary data. Both soil and vegetation salinity symptom maps were produced using readily available software and standard hyperspectral processing methods. Multiple swath processing was effectively dealt with through successful atmospheric correction, across track illumination correction and fine tuning georegistration to GPS locations. Matched filtering appears to be a suitable partial unmixing method to minimise the processing multiple parallel images. Finally a practical strategy was devised across to validate the salinity maps across the large study area, which included many inaccessible landholdings.

A single image derived endmember was used as reference spectrum for mapping extremely saline soils across 5 image swaths. These saline soils containing gypsum were most effectively mapped with a reduced dataset spanning the 1750 nm absorption feature. Non-saline soils such as quarries, dirt roads and sand dunes were successfully excluded. The major sources of error in mapping saltpans were firstly the omission of pixels around the saltpan fringes (threshold underestimation) and secondly errors of commission from native perennial vegetation, whose spectra contain absorption features associated with non-green plant components throughout the SWIR region. However, these encouraging results suggest that other soil minerals associated with salinity may also be mapped with hyperspectral imagery through the judicious isolation of absorption features or combinations of absorption features.

The samphire image spectra contained distinguishing properties such as a gently sloping red edge, shallow chlorophyll absorption and a subtle double reflectance peak in the visible green and red wavelengths. These features are consistent with samphire spectra collected with a narrow-band field spectroradiometer. MTMF exploited these spectral properties, successfully mapping ground validated samphire patches whilst exclusive of perennial dryland lucerne pasture and native mallee. The most successful maps were produced using the entire spectral range, suggesting the importance of the SWIR region for mapping halophytic chenopods with scleromorphic characteristics. However, unlike MF mapping, MTMF is unable to utilise one reference spectrum to map multiple strips, therefore each strip required an intrinsic spectrum to map samphire. The inability to extract samphire endmembers from every strip was addressed by extracting ROI mean spectra from known dense samphire patches.

In both salinity symptom maps, KHAT values of approximately 0.6 showed that there was a moderate agreement between the image maps and the field observations. The absence of an objective, automated procedure for threshold value selection means that threshold optimisation requires sufficient groundbased knowledge of a detailed area within each image strip.

During the dry season, soils were found to contain less surface moisture and saline seepage (Chapter 2) in dryland farming areas and drier soils maximised the depth of soil mineral absorption features (Chapter 3). Evidence of soil mineralogy can also be found in spectra derived from HyMap imagery acquired in the dry season. Furthermore, the dry season appears to be a suitable time of year to distinguish homogenous patches of samphire from the senesced annual grasses that dominate the landscape and native mallee vegetation. However, fewer halophytic species are available to map because annual grasses have senesced and are indistinguishable on the ground.

5 MAPPING SALINITY SYMPTOMS WITH HYPERION SATELLITE IMAGERY

5.1 Introduction and aims

Airborne hyperspectral acquisitions have considerable advantages over multispectral satellite missions not only because of their possible higher spatial and spectral resolution but also because the user can influence the time of acquisition and flight path orientation. However, airborne hyperspectral image processing involves increased complexity due to multiple swaths. Space-borne hyperspectral sensors have the potential to redress the spectral limitations of multispectral satellite imagery whilst having the satellite advantage of repeatability over larger areas.

The Hyperion sensor is an experimental hyperspectral instrument on the Earth-Observing 1 (EO-1) satellite, which was launched in 2000 (Pearlman *et al.*, 2001). The instrument is a pushbrooom scanner, measuring an entire row of the image and the two detector arrays simultaneously measure the complete wavelength range. The spectral resolution however is far superior to multispectral satellite imagery, with 10 nm spectral bandwidth and 242 wavebands over 400 to 2500 nm range. The wavelength range is consistent with HyMap data and ASD field spectrometers. The spatial resolution is equivalent to Landsat satellite images, with each ground resolution of approximately a 30 x 30 m.

A range of northern and southern hemisphere studies was conducted in the first years of Hyperion operation, as part of the instrument validation process (Ungar, 2002). Hyperion imagery was applied to agricultural assessment (Eckert and Kneubuhler, 2001); (Van Niel *et al.*, 2001), environmental (Cetin, 2004; Chewings *et al.*, 2002) and mineral mapping (Crowley *et al.*, 2003; Cudahy *et al.*, 2001). The Hyperion validation report for the Australia sites (Jupp and Datt, 2004) highlighted the problem with poor signal to noise (SNR) performance. In particular, there was low SNR in the visible/NIR regions, below about 500 nm and above about 900 nm, and in the two SWIR regions. The signal to noise ratio has been estimated at 50:1 in the SWIR for Hyperion, versus over 500:1 for the airborne sensors (Kruse and Boardman, 2002).

To compound the noise problem, the data beyond 2300 nm was reported to be poor, which significantly impedes the reliable detection of many useful minerals and is

therefore a major limitation for Hyperion mineral mapping applications. However, in general spectral smoothing was not recommended because it may remove finer spectral features located in noisy regions of the spectrum but which are not impossible to discern. Further difficulties were highlighted in the validation report, especially in the instrumental overlap between the arrays near 950 nm and the overlap between water vapour and CO_2 absorption near 2000 nm.

Another issue that arose during the validation phase was the problem of the variable spectral response function of each detector (a function of the centre wavelength, CWL, and full width at half maximum, FWHM) across the 256 pixels of a line. The variable CWL and FWHM, also know as the "spectral smile", resulted from the dispersion of an image slit across the two detector arrays (Jupp *et al.*, 2002). The smile effects are most significant in the VNIR and negligible in the SWIR. Prior to June 2002, the CWL and FWHM were standardised by using the values for pixel 128 (TRW method), however since then, a better response has been produced by calculating average values over all 256 pixels (ECD method) (Quigley, 2004). The main effect of the smile is to make some of the atmospheric absorption areas unstable.

Despite the inherent data noise, initial results established that Hyperion data from the SWIR spectrometer could be used to produce useful mineralogical information. Minerals such as dolomite, chlorite, and muscovite could be distinguished and mapped (Cudahy *et al*., 2001; Kruse and Boardman, 2002). At Mount Fitton, Cudahy *et al.* (2001) determined that "with appropriate pre-processing" and good environmental conditions, mineral spectral features could be identified in the SWIR. However, in the Cudahy study only a limited number of mineral endmembers were extracted using automated procedures, consequently, recognisable mineral spectral were instead extracted from regions of interest using a priori knowledge of mineral deposits.

In arid and semi-arid regions, spatially meaningful abundance maps were produced of photosynthetic vegetation (PV), non-photosynthetic vegetation (NPV) and soil (Chewings *et al*., 2002). These preliminary results were achieved using the visible and NIR wavelength regions. Broad groups of woody vegetation could be separated using vegetation indices based on the red edge features. Some spectrally distinct agricultural crops have been classified with some degree of success but the overall mapping results were disappointing (Eckert and Kneubuhler, 2001). The study pointed to major

problems being the time of year for image acquisition and the small size of the fields in the intensively farmed study area, rather than the low SNR of Hyperion data.

Therefore, even though Hyperion data is noisy, these studies indicate that hyperspectral satellite imagery is suited to mapping minerals using absorption features in the SWIR but not beyond 2300 nm. Broad vegetation groups can also be separated out such as PV, NPV, woody vegetation and even some spectrally distinct crops, if the agricultural area is not subdivided for intensive farming. The spatial resolution has the same moderate resolution as Landsat TM satellite imagery and is suited to dryland agricultural areas where the major landuse is broad scale cropping and grazing such as at Point Sturt. Asner and Heidebrecht (Asner and Heidebrecht, 2003) compared Hyperion to AVIRIS imagery for SMA mapping of deserts in Argentina and found that at 30m resolution PV for both imagery were statistically similar but Hyperion achieved lower accuracies for NPV and soil cover estimates. These lower accuracies were attributed to poor signal to noise performance in the SWIR region.

To date, no study has evaluated high spectral resolution satellite imagery for mapping dryland salinity. Following the achievement of HyMap image analysis and salinity mapping, this part of the study aimed to exploit the high spectral resolution of Hyperion imagery to map soil and vegetation symptoms of dryland salinity at Point Sturt in South Australia. In particular, image analysis aimed to discriminate saline soils from non-saline and to distinguish halophytic vegetation, like samphire, from other perennial vegetation, such as native mallee vegetation and other perennial species.

Being an experimental instrument, the fundamental challenge with processing Hyperion imagery is the high noise content in the data. Other than noise reduction methods, image analysis aimed to follow HyMap procedures to allow for direct comparisons between the output salinity symptom maps of both types of hyperspectral sensor.

5.2 Analysis of Hyperion imagery

5.2.1 Hyperion data

The EO-1 satellite has a sun synchronous orbit at an altitude of 705 km and crosses the equator at 10.01am local time, 1 minute behind Landsat ETM. The Hyperion scanner acquires imagery covering a region 7.65 km cross-track and 185 km along-track. The ground resolution is 30 x 30 m. The instrument has two spectrometers that acquire data

over two separate wavelength regions, the VNIR (400 to 1000 nm) and the SWIR (900 to 2500 nm).

The Hyperion image swath was supplied by the Bureau of Rural Sciences, Australia (Figure 5-2). The imagery was supplied as calibrated radiance Level 1B data and the VNIR and SWIR data components had been spatially co-registered. The data was acquired on 18 February 2002. The image was therefore acquired during summer, around the same dry time of year that the HyMap survey was flown (but 1 year later). Again, low rainfall was measured in the area prior to image capture (Figure 5-1).

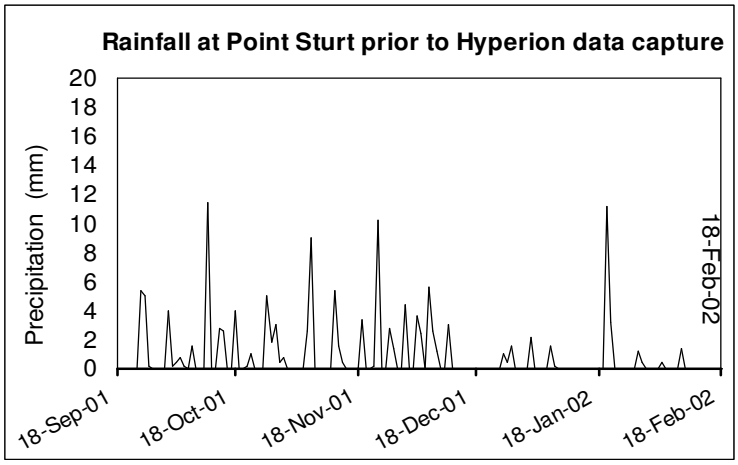

Figure 5-1 Daily rainfall prior to the acquisition of Hyperion imagery on 18 February 2002. There is only one major rainfall event one month before.

The full data strip of 93.84 km was acquired over an area well beyond the limits of the study site extending 65 km north of Point Sturt area, into the Mount Lofty Ranges. Like the HyMap imagery, the southern half of the scene covering the study site is dominated by dry vegetation, with some central bright areas corresponding to saltpans. Small areas of exposed soil such as sandhill ridges, roadside quarries and dirt roads were not clearly visible because of the coarse spatial resolution of the image. The green lake fringes are evident but there are less conspicuous green irrigated areas where compared to HyMap.

5.2.2 *Specialised image pre-processing for Hyperion imagery*

Hyperion image analysis involved preprocessing to reduce noise and atmospheric correction followed by standard hyperspectral image analysis and mapping procedures (Figure 5-5).

Hyperion data preprocessing was performed using the CSIRO's Mineral Mapping Technologies Group (MMTG) A-List Hyperspectral Processing Software, supplied as an ENVI extension. The software is a series of modules which are applied in a prescribed sequence as set out in the guidelines devised by Quigley *et al*. (2004) and in the MMTG-A processing manual (Mason, 2002). The processing sequence involves interpolating pixel data coinciding with bad sensor detector cells, normalising columns to reduce image striping and masking out remaining problem pixels for the following stages of image analysis.

The full data strip was therefore spatially subset to restrict the data to the study site (Figure 5-3). Spectral subsetting was performed to remove the first bands 1-7 and last bands 225-242 as they contained non-calibrated null values. Other bands removed were bands 8-10 (wavelengths 427-447 nm) and bands 221-224 (wavelengths 2365-2395) to ensure removal of any extra noisy bands. Other bands excluded were bands 58-78 (wavelengths 936- 1058 and 852-922) to account for the spectral overlap between the two detectors. A total of 189 bands remained (53 removed).

The data was then spatially subset to exclude the deep water region in the west prior to statistical calculations in the noise reduction procedures (Quigley, 2004). Remaining water pixels were also masked out by selecting a region of interest to cover the remaining lake water with a 5 pixel buffer zone to eradicate noisy pixels in the lake and along the lake fringes.

Figure 5-2 Hyperion raw image swath

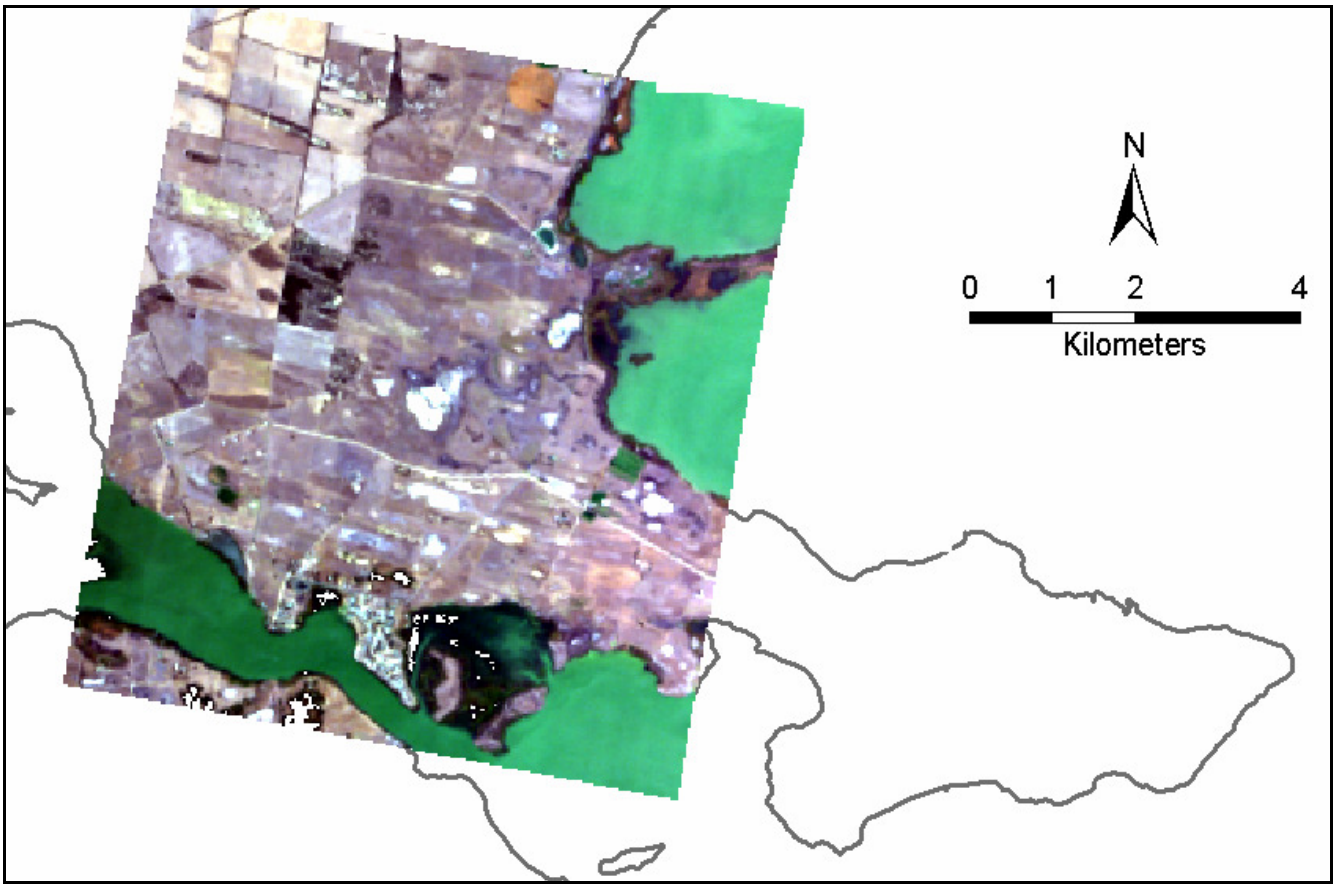

Figure 5-3 Hyperion strip spatially subset to the Point Sturt area (georegistered true colour)

The next processing steps were designed to reduce the significant noise, inherent in the Hyperion data by masking out "bad pixels" throughout the scene due to instrument anomalies (Mason, 2002). Tests showed that a Legendre Polynomial correction was not required, so only a standard deviation window (min=50, max=25001) was applied which found 22 outlier pixels in the Hindmarsh Island lake area. The mask was applied prior to the next processing steps of replacing bad cells with interpolated values from neighbouring cells. Significantly bad detector cells are identified according to standard deviation (of +/- 4 in this case) of an entire detector array-row. A small number of bad cells found, followed by visual inspection in the detector array and manual deselecting of wrongly identified good cells.

Striping is a significant problem in Hyperion imagery, caused by variations in the calibration of cells in the cross-track direction (Mason, 2002). Destriping is a less aggressive bad cell removal that calculates gain and/or offset corrections for each detector cell in the 2-dimensional detector array, the values were applied to normalise the columns in the single band image thereby reducing image striping.

Atmospheric correction was applied to the noise-reduced Hyperion scene. Although the recently developed HATCH model was designed to compensate for the inadequate CWL calculations in Hyperion, it has been shown to produce smoother reflectance spectra but still requires model development (Goetz *et al.*, 2003). In any case, with the reasonable results of ACORN attained by Quigley *et al* (2004), it was therefore selected as the preferred atmospheric correction method for Hyperion data in this study.

ACORN requires input parameters such as time of acquisition, coordinates, elevation, sensor flying height and visibility. Only the 1140 nm region was used to derive water vapour because the 940 nm channel is located within the NIR/SWIR overlap region (Quigley, 2004). All artefact suppressions were turned on to maximise noise reduction.

For quality control, the atmospherically corrected data was visually examined. The water regions were badly dealt with by ACORN, with water spectra containing extremely high amplitude noise over all channels. Overall, high levels of noise persisted in the image spectra and the undesirable CO_2 absorptions, around 2000 nm, were still evident. In general, the noise was most prominent in the NIR plateau between 900 nm and 1150 nm overlap region and the SWIR2. Random image spectra were examined to find common spectral characteristics pertaining to exposed soil and photosynthetic vegetation. Small areas of exposed soil such as sandhill ridges, roadside quarried and dirt roads were not easily located because of the coarse spatial resolution of the image. Very few mineralogical absorption features were apparent in the noisy SWIR2 region even in the large saltpans which extend over several pixels. Typical green vegetation spectra were present in irrigated areas, though they appeared particularly noisy in the NIR plateau between 900 nm and 1150 nm and the SWIR2.

To reduce the noise, the 189 band reflectance data was MNF transformed. The MNF bands with corresponding high eigenvalues (eigenvalues>3) were retained leaving 30 bands, and noisy bands rejected. The noise-reduced dataset was then ready for endmember extraction and partial unmixing. The next phase of MMTG processing involved pure pixel extraction similar to the standard ENVI PPI method except that it had the added advantage of identifying spectrally extreme “outlier” pixels that are usually undesirable man-made materials (Mason, 2002). These outlier pixels can dominate the n-dimensional visualiser data clouds and are dealt with in HypPPI by being preferentially selected in a first pass “mini-PPI”, excluded in the main processing

pass and restored in the final stage with extremely high scores, so they can be manually excluded if required.

5.2.3 Standard hyperspectral processing methods

Endmembers were extracted from HypPPI using automated cluster analysis. Visual inspection excluded noisy unusable endmembers from further analysis. The spectra were all identified by comparison with field, HyMap and USGS spectra and using detailed field based knowledge of the landcover at each pixel location.

Because the image was acquired at a similar time of year as the HyMap imagery, the same salinity symptoms were targeted for mapping with Hyperion imagery. Salinity symptoms were successfully mapped using a combination of standard hyperspectral image analysis methods. With Hyperion satellite imagery, the superior MTMF unmixing was suitable using either an endmember or ROI reference spectrum. Both types of reference spectra were examined for their suitability. For MTMF mapping, the water absorption regions were excluded from analysis (1356-1467 nm and 1800-2082 nm). The wavebands from 1971-2082 nm were excluded because they included the prominent doublet CO_2 absorption features that were not accounted for during atmospheric correction.

All MTMF mapping was then performed on the georegistered MNF data to avoid the need to georegister each partial unmixing result. Nearest neighbour resampling was used to warp the image because this method transfers values of the nearest pixel to the warped image without interpolation, thereby preserving the original pixel reflectance values.

As with the HyMap unmixing results, the MTMF “Score” band was divided by the “Infeasibility” band to produce grey scale images. High values from these images were selected using threshold values and directly exported to GIS for accuracy assessment. Again the threshold values were determined from extensive field knowledge.

No filtering was applied to the maps in GIS because of the large pixel size. Mapping accuracies employed the identical method used to assess the accuracy of the HyMap saltpan and samphire maps. Over 100 random field sites were available within the extent of the Hyperion scene. Again, standard error matrix and Kappa analyses, as described by Congalton (1991), produced KHAT statistic values.

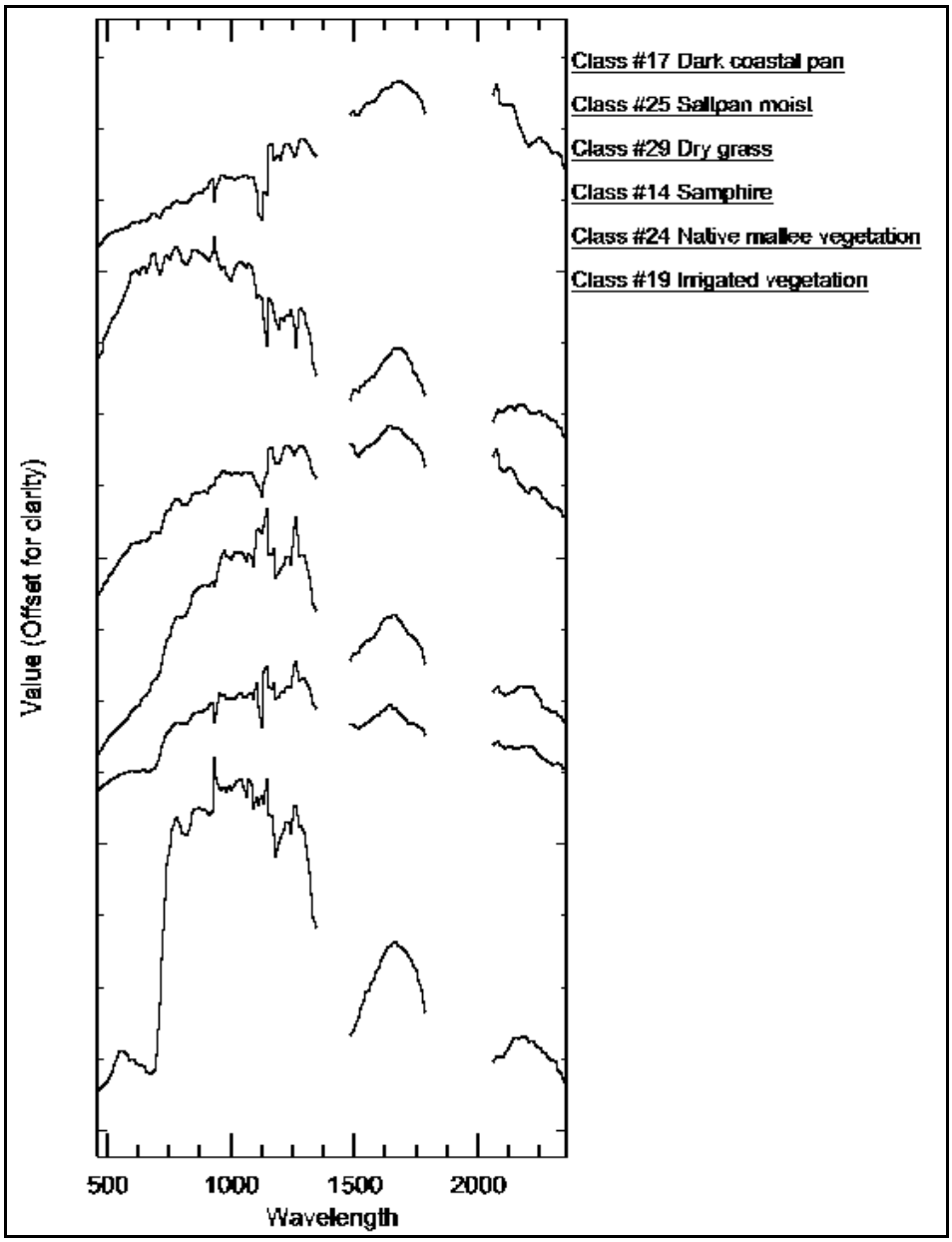

Figure 5-4 A representative selection of endmembers extracted from the Hyperion image. Noisy endmembers are not displayed

5.3 Results

Thirty-one endmembers were extracted using automated cluster analysis. Visual inspection showed that there were many noisy unusable endmembers associated with unmasked water pixels along the coastline. Subsequent manual removal of these undesirable spectra left 15 useable endmembers. Image spectra of representative landcovers are displayed in Figure 5-1. The endmembers were all identified by comparison with field, HyMap and USGS spectra and using detailed field based knowledge of the landcover at each pixel location. Seven endmembers were associated with soils but did not contain any soil diagnostic mineralogical absorption features,

except Class 17 from the dark mud pan near Site B. Class 25 and Class 14 were identified as saltpan and possible samphire endmembers respectively. No endmembers had obvious gypsum features in the SWIR at 1750 or 2200 nm.

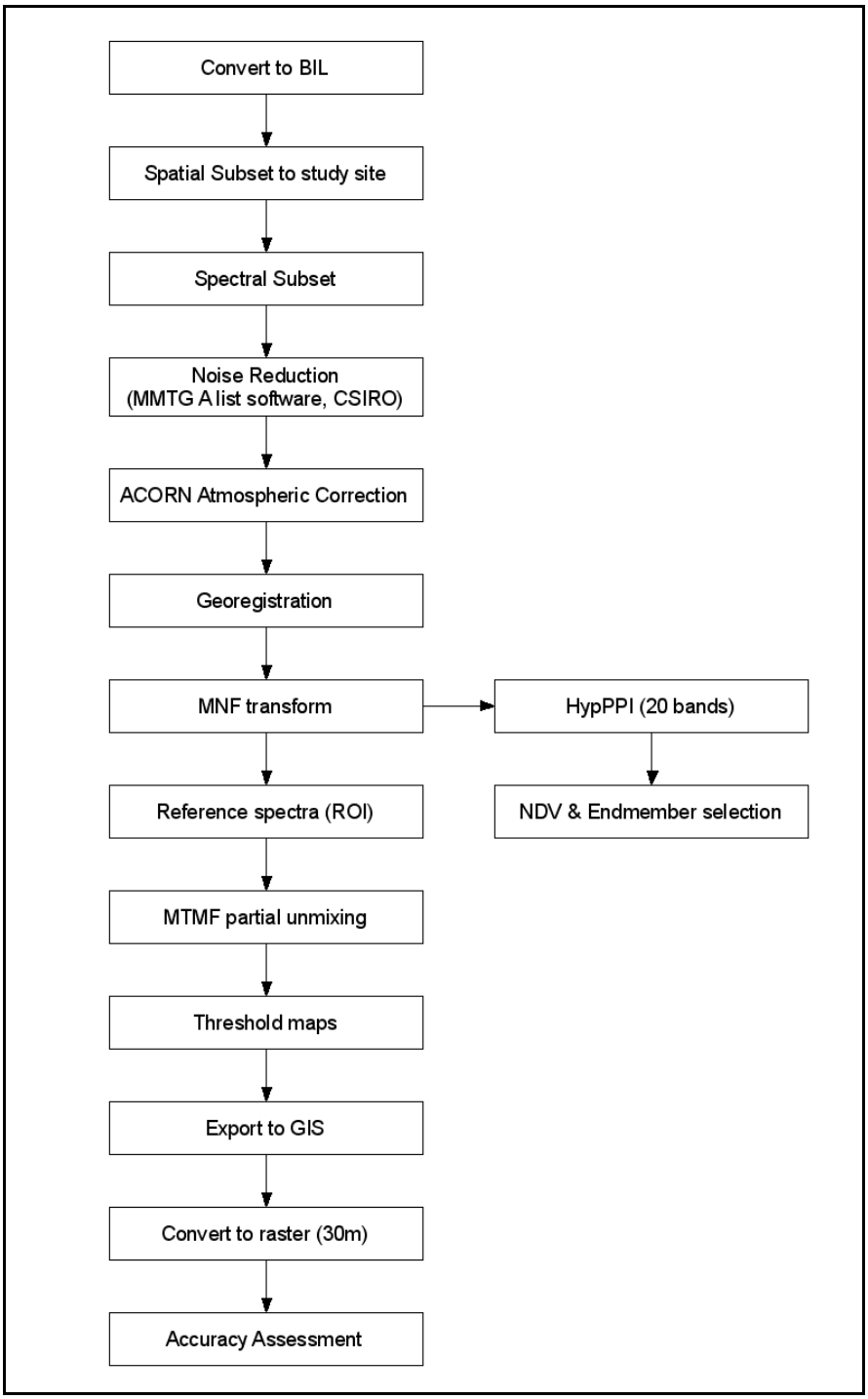

Figure 5-5 Processing flow for Hyperion data.

The endmember spectra contained substantial noise in the NIR plateau between 900 nm and 1150 nm and to a lesser degree in the SWIR2 region. The apparent uniqueness of

the endmembers was likely to be noise related rather than caused by legitimate soil or vegetation features. The SWIR2 region contained few mineralogical features and those that were observed could not be confidently attributed to soil minerals and may instead be noise artefacts. The noise is unlikely to be related to high soil water content because little rain fell in the area prior to image acquisition. Therefore, endmembers were rejected as candidates for partial unmixing mapping. With the success of samphire mapping with HyMap ROI spectra, this method was chosen as the preferred option for deriving samphire and saltpan reference spectra. The added benefit of selecting reference spectra in this manner was the reduced noise levels due to the averaging over several pixel spectra. The noise problem also seemed to substantiate the use of MTMF, the most robust partial unmixing method. The optimal image analysis flow, involves noise reduction, atmospheric correction MTMF mapping and subsequent accuracy assessment (Figure 5-5).

The samphire reference spectra originated from the dense samphire zone at Site A. The reference spectrum for saltpan mapping was not generated from the largest saltpan in the region at site A because the reflectance in the SWIR wavebands was low with few absorption features and significant noise, suggesting the presence of significant amounts of soil moisture. Instead, the reference spectrum was derived from a large pan at Site AA, just south of Site A. The soil spectra from Site AA appeared to have higher reflectance in the SWIR and less noise.

The MTMF results are displayed in Figure 5-6 and Figure 5-7. Bright areas are areas of high abundance of samphire around at the Site A discharge, along the lake coastline and at Site B in the south. Other incorrectly mapped areas of subdued brightness occur in the remnant mallee vegetation stands. The saltpans scattered throughout the discharge regions are successfully mapped. Bright areas coincide with some areas at Site A, interdunal pans in the south, exposed soils at site F, and some coastal pans. The main areas incorrectly mapped as saline soils are some exposed soil in northern fields and Clayton urban areas. As expected, the main saltpan at Site A was not mapped because of low reflectance and noise in the SWIR2 wavelength region.

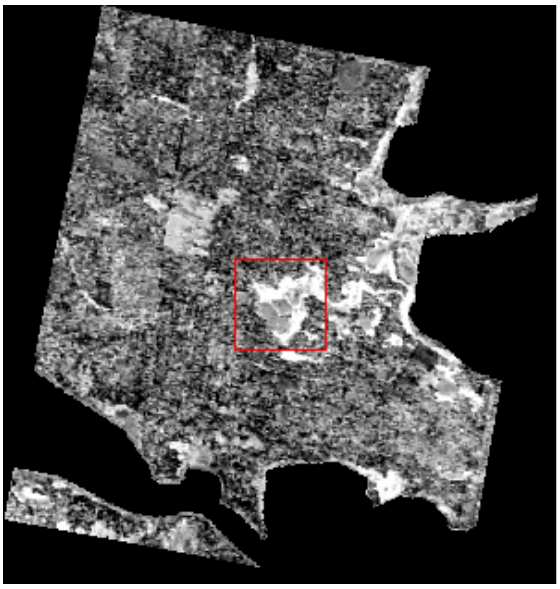

Figure 5-6 MTMF result using mean samphire reference spectrum. The samphire around the central saltpans (red square) and along the coast was successfully mapped.

Figure 5-7 MTMF result using mean saltpan reference spectrum. Bright saltpans are dispersed throughout the central and coastal discharge areas. The main Site A pan is not clearly mapped.

The final maps were produced by selecting pixels with high values above thresholds of 95.5% for samphire, and 96.5% for saltpans. In other words, threshold values were selected in order to isolate less than 5% of the total image area. The maps were imported into GIS for groundtruthing (Figure 5-8).

The overall mapping accuracies were 0.82 for samphire (a) and 0.79 for saltpans (b). Although these values appear high they are not adequate indicators of the true quality of the maps. A better indicator is the KHAT values of 0.50 and 0.38. The KHAT values reflect the fact that partial unmixing failed to map all saltpan and samphire areas. For the saltpans in particular, the most prominent omission is the large central saltpan at Site A. The main commission errors are those pixels wrongly identified as saltpans in the township of Clayton and scattered throughout dry fields. The main commission errors in the samphire maps were the misclassification of native vegetation as samphire.

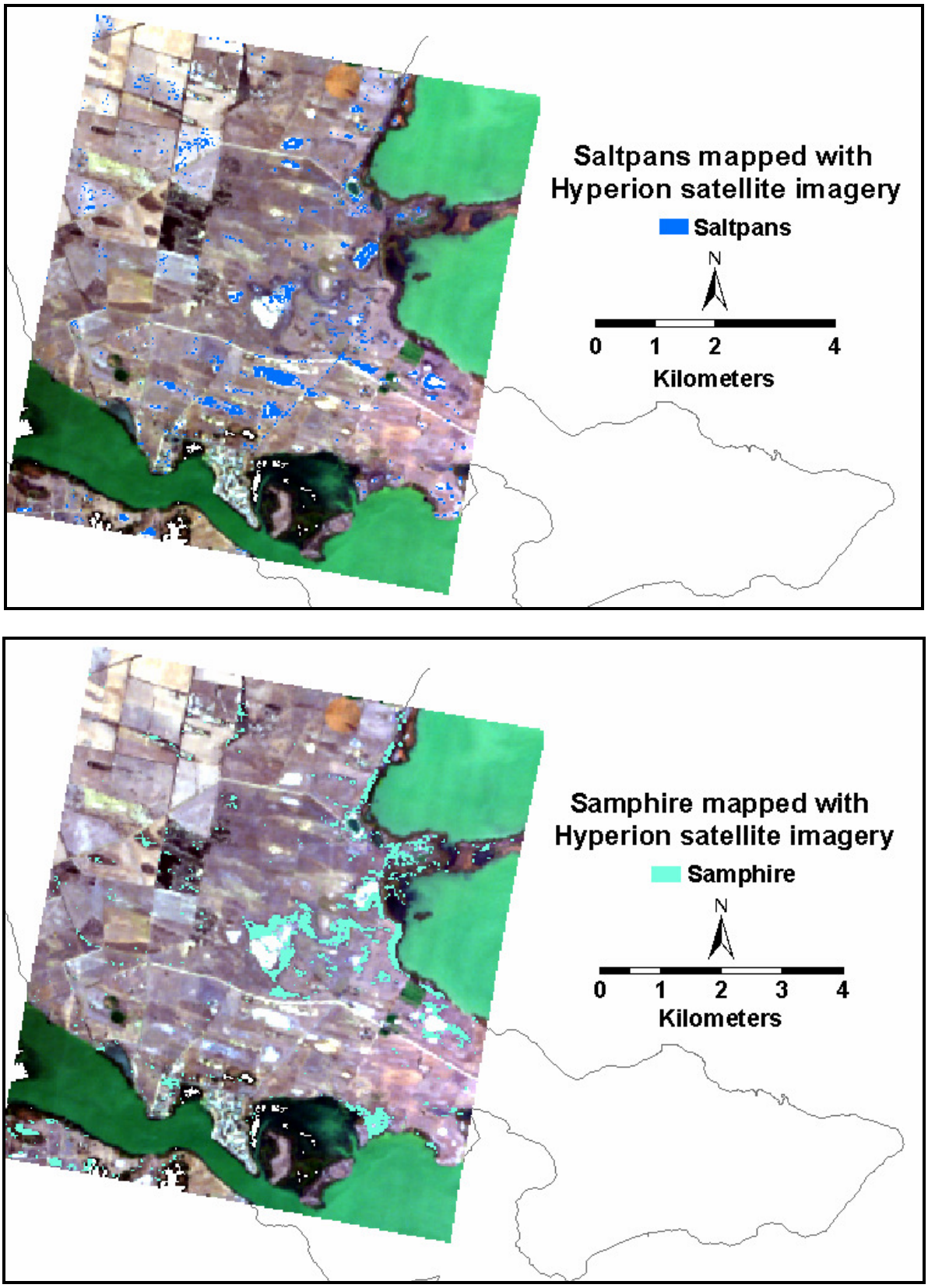

Figure 5-8 Saltpan (top) and samphire (bottom) maps are displayed in GIS layout. Several saltpans throughout the discharge regions are also successfully mapped. The central and coastal samphire areas are well defined.

Table 5a) Error Matrix for the samphire map, where a KHAT value of 0.50 show a moderate agreement with field data

Samphire Error Matrix		Field		
		Presence	Absence	Total
Image	Presence	16	8	24
	Absence	12	78	90
	Total	28	86	114

Total accuracy…….82

Producer's accuracy

Presence…….57

Absence…….91

Users accuracy

Presence…….67

Absence…….87

KHAT…….0.50

Table 5b) Error Matrix for the saltpan map, where KHAT value of 0.38 show a poor agreement with field data

Saltpan Error Matrix		Field		
		Presence	Absence	Total
Image	Presence	12	6	18
	Absence	18	78	96
	Total	30	84	114

Total accuracy…….97

Producer's accuracy

Presence…….40

Absence…….93

Users accuracy

Presence…….67

Absence…….81

KHAT…….0.38

5.4 Conclusions

Endmembers derived from the Hyperion image contained significant noise particularly in the far NIR region and lacked diagnostic absorption features in the SWIR. The spectral region around 2000 nm was excluded from mapping because an adequate atmospheric correction could not be achieved. Therefore, the samphire and saltpan maps were produced with MTMF partial unmixing using MNF-transformed ROI generated reference spectra. KHAT values of 0.50 and 0.38 were calculated for the samphire and saltpans maps respectively. Saltpan maps also showed a moderate agreement with field data but poor accuracies were achieved for samphire maps.

Hyperion salinity maps had lower accuracies compared to HyMap samphire and saltpan maps, with KHAT values of 0.61 and 0.58 respectively (Table 5-1). The low mapping accuracy of the saltpans and samphire maps was primarily due to the high level of Hyperion data noise that masked important, subtle, spectral features related to soil and vegetation. Although data noise was the primary factor adversely influencing mapping accuracy, the 30 m spatial resolution was also a contributing factor. At this ground resolution, there were more boundary and mixed pixels, adding to classification confusion (Quattrochi and Goodchild, 1997). In particular, the poor mapping accuracy of the samphire maps may be affected by data noise in the NIR and SWIR wavelength regions. The reflectance in the NIR region is related to moisture and leaf structure,

associated with succulence, and the SWIR region contains important spectral properties related to woody stalks and halophytic adaptations (Elvidge, 1990; Lewis, 2002).

Table 5-1 Comparison of Hyperion and HyMap salinity mapping accuracies. Saltpans maps from both sensors showed a moderate agreement with field data however, Hyperion samphire maps showed poor agreement compared to HyMap

Hyperspectral sensor (platform)	Salinity symptom	Accuracy (KHAT)
HyMap (airborne)	Saltpans	0.58
	Samphire	0.61
Hyperion (satellite)	Saltpans	0.50
	Samphire	0.38

The major advantage of the Hyperion imagery is the high spectral resolution that is equivalent to HyMap data. The other advantage is that the along-swath coverage is equivalent to other satellite imagery and the 7.5 km swath-width is over 5 times the width of a single airborne swath (with ground resolution of 3 m). However, the disadvantage of multispectral and Hyperion satellite imagery is the coarse ground resolution of 30 m which is equivalent to Landsat and contributes to the lower mapping accuracies.

If future high spectral resolution satellites have significantly higher SNR performance similar to airborne sensors, then the salinity mapping has enormous potential for improvement. High spectral resolution satellite imagery could successfully discriminate halophytic species that inhabit large zones encompassing several 30x30 m pixels. During the dry season, samphire is ideal candidate for mapping problematic saline areas with a good cover of perennial vegetation. At this time of year, hyperspectral imagery could also isolate spectral features relating to soil mineralogy to distinguish large areas of exposed saline soils from non-saline exposed soils. Because satellite imagery covers larger areas and has the advantage of regularly passing over the same area, hyperspectral satellites are well suited to monitoring salinity over medium sized catchments. Imagery from other times of year needs to be evaluated to determine whether halophytic annual vegetation can be mapped.

6 MAPPING SALINITY SYMPTOMS WITH CASI AIRBORNE IMAGERY

6.1 Introduction and aims

Results presented in previous chapters indicate that hyperspectral imagery is capable of mapping salinity indicators such as samphire and saltpans during the dry season. The dry season proved an ideal time to map these symptoms because the lack of soil water and the ability to discriminate perennial halophytic samphire from background of dry annual grasses. This time of year, however, is not suited to mapping other salinity symptoms, in particular, annual vegetation. Furthermore, the extensive wavelength range may not necessary for mapping those symptoms that exhibit distinctive spectral properties in the visible and NIR wavelength regions.

Sea barley grass is a widespread, important indicator of emerging salinity. Spectral discrimination analysis of laboratory and field spectra suggests that spring-summer senescence may be the optimum time of to distinguish sea barley grass from other grass species in more advanced stages of senescence (Chapter 3). The end of the "spring flush" and beginning of the dry season was selected as the optimal time of year for mapping sea barley grass with hyperspectral imagery. Sections of the visible and NIR regions proved to be significant in discriminating regions, therefore a hyperspectral imaging scanner that encompassed this wavelength region had the potential for mapping sea barley grass.

The Compact Airborne Spectrographic Imager, CASI (ITRES Research Limited) is an airborne imaging scanner that acquires hyperspectral imagery in the visible and near infrared wavelengths. CASI imagery is therefore well suited to water quality assessment because of the continuous optical wavelength range between 400 to 1000 nm and the flexibility of programmable bands (Dekker and Bukata, 2002). Studies of coastal environments and water quality have focussed on chlorophyll, turbidity, algae, suspended materials and seagrass (Thomson *et al*, 1998; Clark *et al*, 1997; Thomson *et al*. 2003; Green *et al*, 1998).

A common application of CASI imagery is vegetation mapping because the VISNIR region is associated with leaf pigments (Gates *et al*., 1965) and leaf structure (Gausman and Allen, 1973). VISNIR airborne scanners have been applied to the determination of

canopy coverage in Northern hemisphere forests (Leckie *et al*, 2005; Blackburn and Milton, 1997; Fernandes *et al*, 2004; Haboudane *et al*, 2004). Blackburn and Milton felt hyperspectral VISNIR imagery was necessary to resolve some subtle changes in canopy reflectance due to variations in leaf pigment concentration (Blackburn and Milton). CASI imagery has also been used to determine leaf chlorophyll content as a measure of crop health in precision agriculture studies (Zarco-Tejada, 2000).

Of greater relevance to this study, is the application of CASI imagery for mapping grasslands. Grassland communities in Denmark were mapped with CASI using standard classification methods (Jacobsen *et al,* 2000). Mapping degraded grasslands was also investigated using simulated spectra that emulated the wavelength range and resolution of CASI scanner (Yamano *et al*, 2003). Discrimination analysis was performed on the simulated spectra. The fourth derivative reflectance spectra around 670 nm and 720 nm were found to be effective discriminators for distinguishing grass species which were indicators of degraded areas. Schmidt and Skidmore (2001) compared the laboratory spectra of grass species in Africa to CASI image spectra. Although not stated, the imagery appeared to be collected at the time of year when the reflectance curves of the grass species had characteristics of typical green vegetation. The image spectra were extracted from pixels dominated by a specific species.

The VISNIR region has been rarely used to map soils presumably because there are few spectral features in the region pertaining to soil mineralogy. However, there have been a few studies that have mapped soils based on soil colour and its intimate relationship with iron oxide content. In VISNIR region, soil colour has been associated with soil type and soil properties such as organic matter (Ben-Dor *et al*., 1997; Palacios-Orueta and Ustin, 1998; Post *et al*., 2000), iron oxide (Ben-Dor, 2002; Ben-Dor and Banin, 1994; Palacios-Orueta and Ustin, 1998) and iron mineral content is primarily observed. Recently, the CASI-48 imager has been shown to reliably map soil rubification, or iron oxide formation, in coastal sand dunes in Israel (Ben-Dor *et al., In Press*). Skidmore *et al* (1997) used eucalypt forest as surrogate for soil properties and found that soil phosphorus and pH correlated with CASI data. Furthermore, the shape of the NIR shoulder has also been linked to salinity status of soils (Dehaan and Taylor, 2002B).

In Chapter 5, sea barley grass was found to be spectrally distinguishable from other annual grasses across broad wavelength regions because it appeared to senesce later in the season. During senescence, the VISNIR spectral region is most responsive to

changes in plant pigment content, particularly changes in chlorophyll content, and leaf structure. Grassland mapping maybe further be enhanced by the judicious choice of time of year for image acquisition.

The primary aim of CASI image analysis was to produce maps of sea barley grass. From results presented in Chapter 3, spectral analysis found November to be as the optimum month in this environment to exploit spectral differences between the variable rates of senescence of sea barley grass and other annual species. Spectral differences occur across broad spectral regions because sea barley grass stays greener longer in lowlying wetter areas than surrounding non-halophytic annual grasses. Therefore, CASI imagery acquired during spring senescence has the potential to discriminate and map sea barley grass. To evaluate the imagery further, image analysis aimed to produce samphire and saltpan maps to allow for direct comparisons to the HyMap salinity symptom maps.

6.2 CASI survey and data specifications

Plant spectral properties change over relatively short periods of time (Schmidt and Skidmore, 2002), particularly during senescence so that the time of year for image acquisition is important. In October and November 2004, a number of visits to Point Sturt confirmed that sea barley grass was still quite green at this time of year and many other non-halophytic annual grasses, such as brome and silver grass, appeared to be in more advanced stages of senescence. However, it was also noted that some crops and wild pastures also maintained a level of greenness, which could contribute to errors when mapping sea barley grass with the imagery acquired at this time. Nonetheless, mid to late November was selected as the ideal time to acquire imagery to optimise sea barley grass mapping.

The CASI-2 survey was flown on 25 November 2003. The flight paths were designed to run east-west to follow the length of the peninsula thereby minimising the number of swaths required to cover the study area. Seven parallel image swaths were acquired (Figure 6-1). The data was delivered as radiometrically corrected to at sensor radiance and geocorrected in WGS84 UTM projection, Zone 54 south. The scanner was programmed to capture the wavelength spectral range from 413 to 959 nm using 48 bands at 11.7 nm bandwidth.

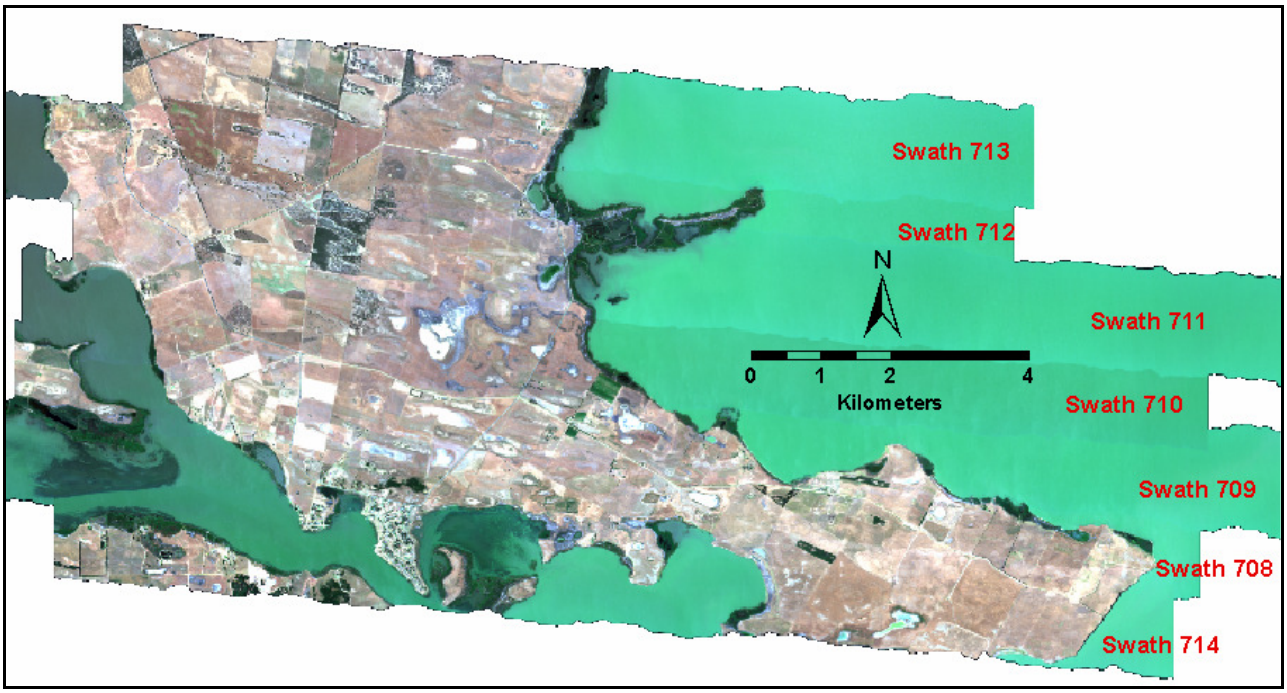

Figure 6-1 Mosaic of seven CASI image swaths

In the weeks prior to data acquisition, seasonal rains were abating which heralded the onset of senescence in the region (Figure 6-2). With the absence of recent rains, surface soil moisture would be declining and thus have a reduced effect on image spectra associated with exposed soils.

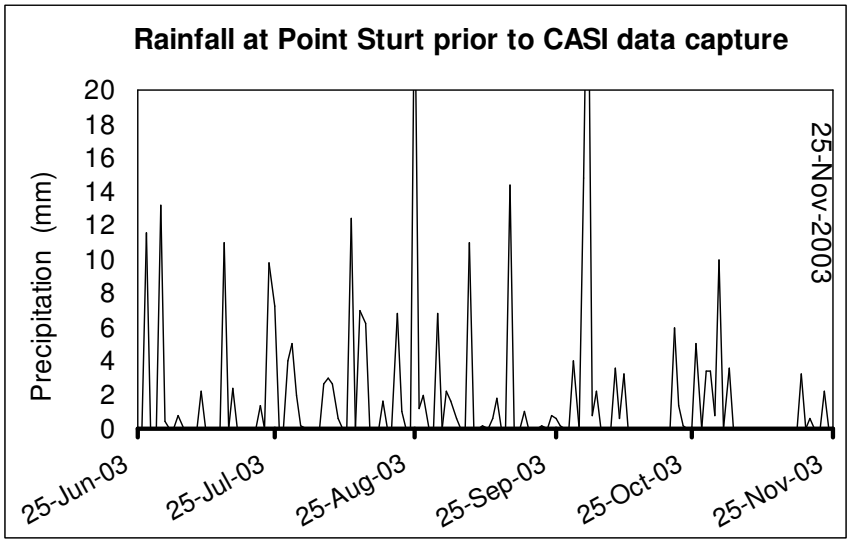

Figure 6-2 Daily rainfall six months prior to the acquisition of CASI imagery on 25 November 2003. There are fewer rainfall events in November.

6.3 CASI data pre-processing methods

The first stage in pre-processing was atmospheric correction preferably using ACORN software, which had successfully corrected the HyMap data. However, the CASI data

only extended to 959 nm, such that the image spectra did not encompass both sides of the 940 nm water vapour absorption feature (pers. com. Research Systems Inc.). In fact, ACORN tests produced output reflectance data with a steep rise in reflectance around 900nm, indicating that calculations were severely overcorrecting the data (Figure 6-3).

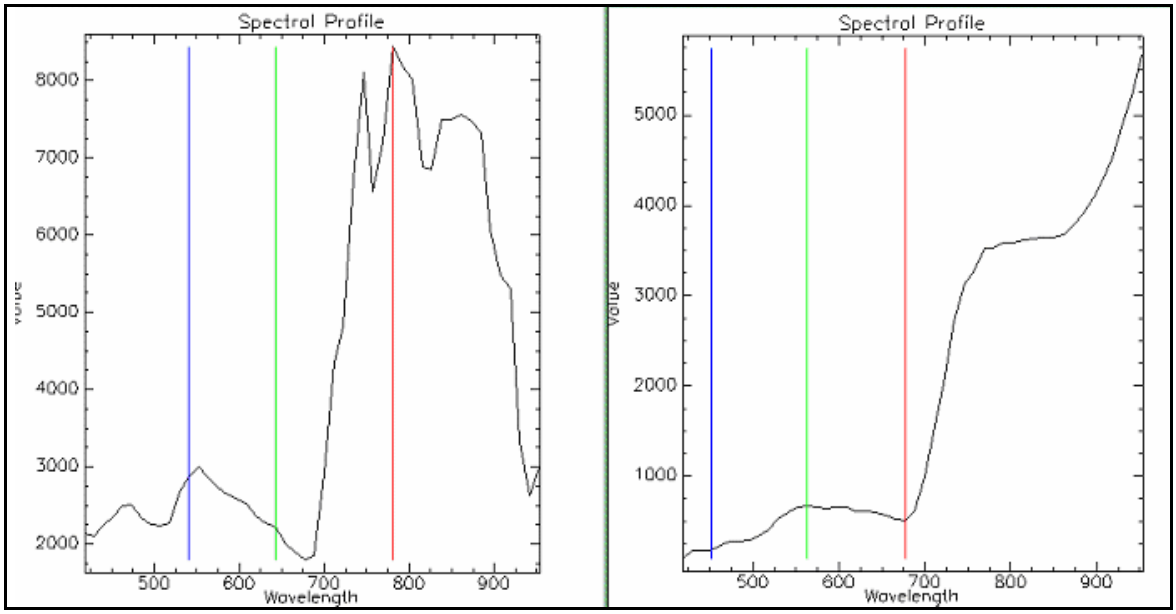

Figure 6-3 CASI image spectra before (left) and after (right) ACORN atmospheric correction. The spectrum on the right clearly shows the prominent overcorrection around 940 nm.

Both ACORN and FLAASH (Fast Line-of-sight Atmospheric Analysis of Spectral Hypercubes) algorithms are based on the MODTRAN-4 algorithms, FLAASH, with the CASI 820 nm options, seems to be more suited to atmospherically correcting CASI data (pers. com. Research Systems Inc.). FLAASH proved more successful, significantly reducing the over correction calculation around 940 nm, without eliminating it altogether (Figure 6-4). The disadvantage of FLAASH was the appearance of low amplitude spikes at 740 nm at the NIR shoulder, which could not be eliminated through spectral polishing.

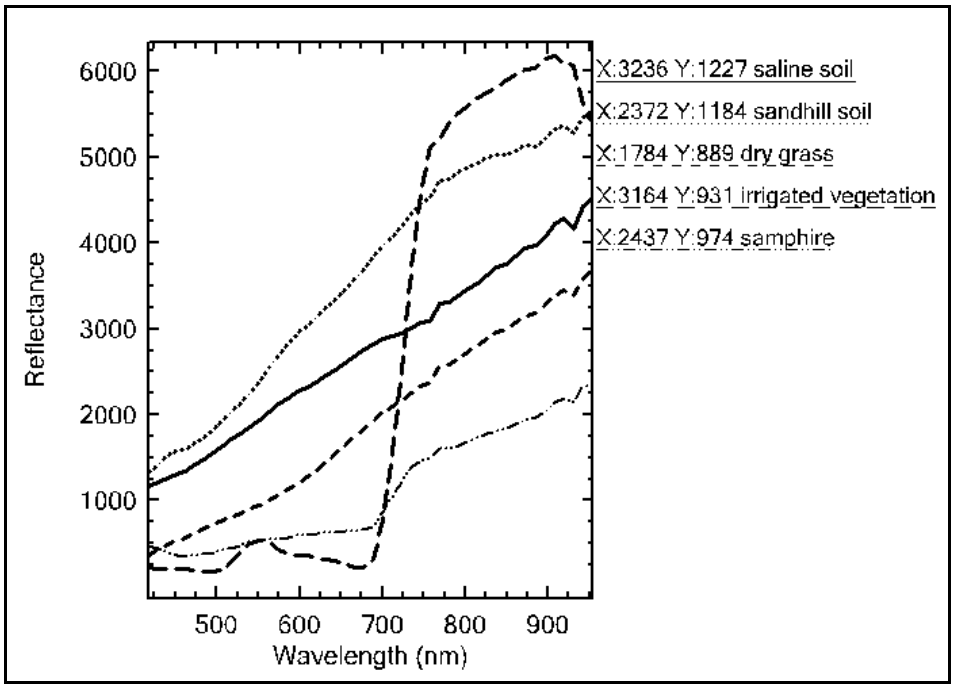

Figure 6-4 Example of CASI spectra after atmospheric correction with FLAASH. In the saline soil spectra note the small 740 nm peak and the smaller overcorrection rise around 940 nm.

In HyMap processing, across track variations in brightness could be accounted for by applying across track illumination correction to the raw image swaths. However, across track corrections could not be applied to the CASI data because the image swaths were supplied already geocorrected and with no GLT translation files. Therefore, across track illumination correction could not be used in this case. An alternate procedure was therefore required to account for the undesirable across track illumination effects that can adversely affect mapping continuity within and between image swaths.

6.4 Salinity symptom mapping with CASI imagery

All further image analysis was performed on georegistered, atmospherically corrected image swaths. Image analysis closely followed the effective HyMap mapping procedures because the partial unmixing mapping of selected salinity symptoms was already tested and proved successful. Employing similar mapping procedures also allowed for direct comparisons between CASI and HyMap salinity symptom maps.

The data was MNF transformed, noisy bands removed, pure pixels identified and endmembers extracted from these pure pixels. Noisy bands beyond MNF band 20, where the eigenvalues fell below 2.0, were removed for subsequent pure pixel extraction and partial unmixing mapping. However in each MNF dataset, some high eigenvalue bands appeared to contain the expected strong, across-track illumination

effects. Unfortunately these bands appeared to contain scene information other than just the across track effects, so removing them in further processing was considered inappropriate.

The problem was investigated using MNF transformed data from swath 708, which contained 3 bands with strong across track effects: bands 2 (dark edge effects), 3 (bright edge effects), and noisy band 17 (less pronounced edge darkening). These three bands were removed and an inverse-MNF image produced. Image spectra from the inverse image with 3 MNF bands removed contained a comparatively higher reflectance around the chlorophyll absorption features then image spectra with no MNF bands removed (Figure 6-5). Evidently removing both MNF bands 2 and 3 with high eigenvalues discarded too much valuable spectral information between 600 and 700 nm pertaining to vegetation (Figure 6-5). Similarly, an inverse-MNF was performed that excluded MNF bands 2 and 17 but retaining MNF band 3. In this case, the inverse MNF scene had undesirable bright edge effects consistent with the bright edges of the removed MNF band 3.

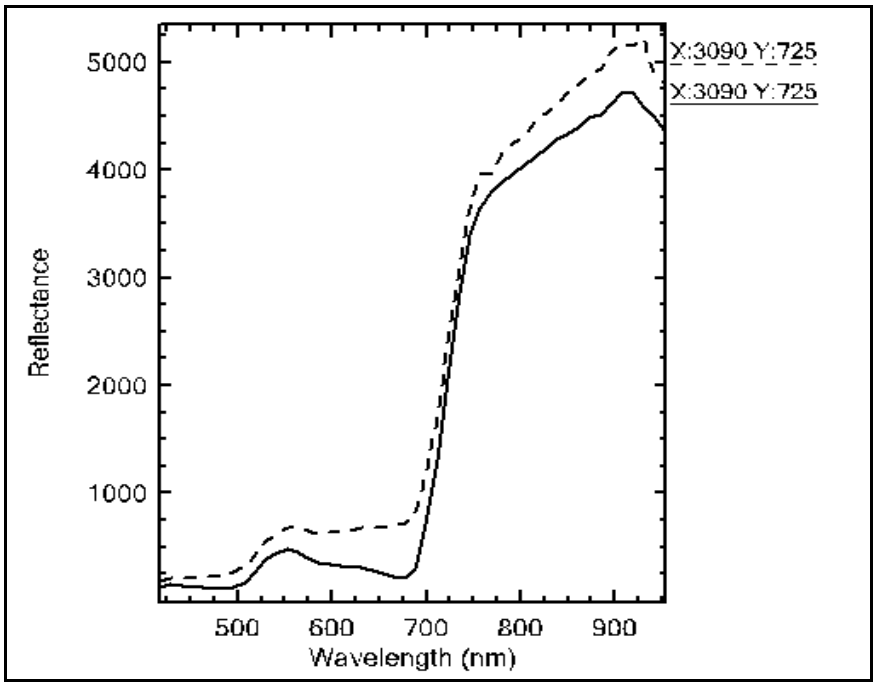

Figure 6-5 Two irrigated vegetation spectra 1) inverse-MNF spectra with MNF bands 2&5 excluded showing the increase in red reflectance (dotted) and 2) inverse-MNF spectra with no across track illumination bands removed (solid line)

Therefore, no ideal options were available for correcting across track illumination effects. Either high eigenvalue bands could be removed to reduce the across track effect or the bands could be removed which would reduce the effectiveness of mapping across

image swaths. Ultimately a compromise solution was to remove MNF band 2 because it contained the most pronounced across track effects.

6.4.1 Endmember extraction

Again, endmembers were sought to use as reference spectra for partial unmixing mapping. A total of 20 MNF bands (excluding band 2) were input in to PPI and endmembers were then extracted. The endmembers extracted were similar to those derived from the HyMap imagery and were again dominated by unwanted spectra associated with manmade structures. In general, the desirable endmembers extracted from each image strip included soils, saltpans and green vegetation spectra.

6.4.2 Partial unmixing mapping of sea barley grass and samphire

No sea barley grass endmembers were identified and samphire spectra were only extracted from only two image strips. MTMF mapping was conducted using mean reference spectra derived from a region of known sea barley grass and samphire in each mage swath.

The location of sea barley grass patches were recorded with GPS during a number of field trips in August, October and November, when the sea barley grass field spectra were collected. These sea barley sites were then located in the CASI image swaths and image reference spectra collected for partial unmixing mapping.

For samphire maps, the reference spectra were, wherever possible, taken from the same sites as the HyMap samphire regions. Some sites on the edge of CASI strips were not used because mapping biased the edges. Again, samphire was not mapped in the northern most swath because no samphire patches had been found in this area.

6.4.3 Saltpan partial unmixing mapping methods

Most saltpan endmembers contained noisy data between 650-750 nm or were mixed spectra with vegetation and water characteristics. The endmember selected for MF mapping was Class 7 extracted from swath 710 (Figure 6-6). Class 7 was a smooth bright spectrum that was associated with a large saltpan at Site A.

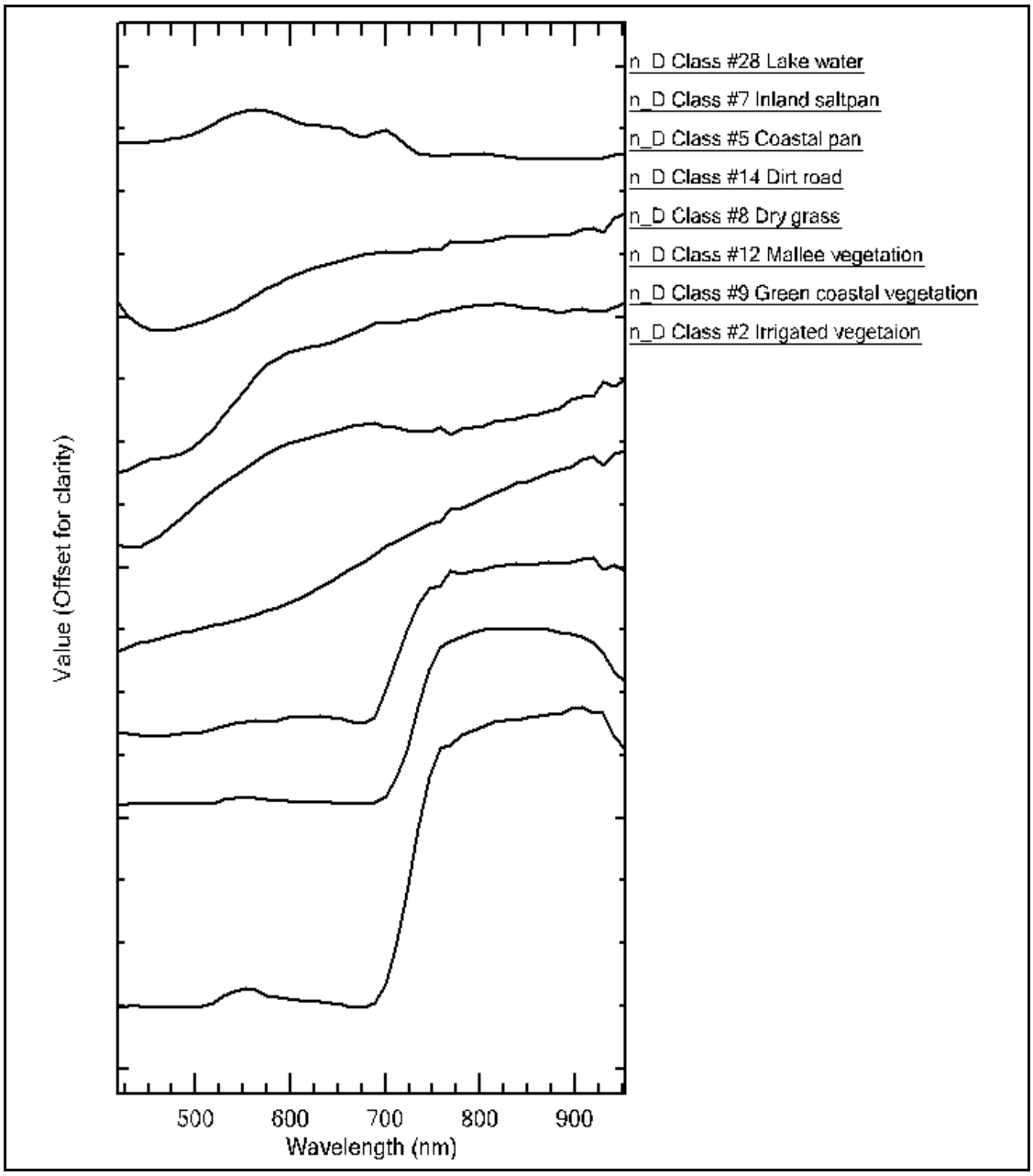

Figure 6-6 Endmember spectra from swath 710

Saltpans were also mapped with MTMF for comparison to the MF maps. Matched filtering unmixing was attempted to map across multiple image strips using a single image-derived reference spectrum. This approach was unable to separate saltpans from dirt roads and exposed sandy soil in other strips. To improve saltpan mapping an alternate strategy was needed, therefore it was decided to produce maps with the MTMF method that had proved more successful in vegetation mapping (samphire). To derive image reference spectra, groundbased knowledge was used to select regions of interest that corresponded to saltpans in each of the image swaths. This targeted reference

extraction process was preferable to image derived endmembers because many pixel spectra in saltpans were noisy or had low reflectance indicating the presence of water.

A ratio of the MTMF "score" band over the infeasibility band produced grey scale images from which thresholds were applied to create salinity symptom maps. For consistency among image swaths, a threshold value was selected that corresponded to the 99th percentile in each image histogram. The 99% thresholds value was considered appropriate because they were comparable to the HyMap map thresholds.

6.5 Accuracy Assessment

The saltpan, samphire and sea barely grass threshold maps were exported as themes into geographical information systems software for accuracy assessment. Within GIS software (ArcMap 9) a neighbourhood filter was applied to smooth the mapped features.

6.5.1 Samphire and saltpan maps

Over 100 random field sites were available for groundtruthing the salinity maps. The samphire maps required fewer sites because the northern-most swath was not mapped. Standard error matrix and Kappa analyses, as described by Congalton (1991), produced KHAT statistic values.

6.5.2 Sea barley grass maps

Unfortunately, the accuracy assessment method devised for HyMap maps could not be applied to the sea barley grass maps. There were few field sites where the occurrence of sea barley grass had been documented because groundtruthing was completed in February/March to coincide with the season when the HyMap survey was flown. At this time late in the dry season, the seed heads of annual grass had dispersed making grass species impossible to identify.

The sea barley grass maps were statistically compared to the saline and nonsaline landscaped units in the PIRSA soil maps to establish whether these moderately saline areas were distributed within previously defined salt affected zones. The PIRSA maps were considered suitable data to perform a more generalised form of map validation because expert knowledge involved interpreting aerial photographs and soil soluble salt levels (electrical conductivity measurement) (Maschmedt, 2000; Maschmedt, 2001).

The *salinity induced by watertable* attribute (described in Chapter 2) was divided into saline and nonsaline classes (Table 6-1). Within GIS software, zonal statistics calculated the percentage area of sea barley grass pixels mapped in saline and nonsaline areas.

Table 6-1 PIRSA SLU attribute "salinity induced by watertable" is assigned 8 classes A-G (after (PIRSA, 2001A)).

***Salinity induced by watertable* class**	**Salinity level**
A	Nonsaline (negligible salinity)
B C D E F G	Saline (slight to extreme salinity)

6.6 Results of partial unmixing mapping

Samphire, saltpans and sea barley grass were mapped with partial unmixing of CASI hyperspectral imagery. The optimum processing flow for sea barley grass, samphire and saltpans followed the HyMap preprocessing and hyperspectral image analysis procedures (Figure 6-7) using reference spectra derived from each image swath using a priori knowledge of the location of samphire patches.

Partial unmixing successfully mapped the highly saline soils where in saltpans and highly saline exposed soils where samphire dominated. The saltpans and samphire were predominately mapped in well-defined patches in the central and coastal saline discharge areas. Sea barley grass was mapped in less well defined patches but is predominately associated with the saltpan and samphire mapped areas (Figure 6-8). However, the sea barley grass maps are more sparsely distributed, and are particularly evident along the interface between image swaths.

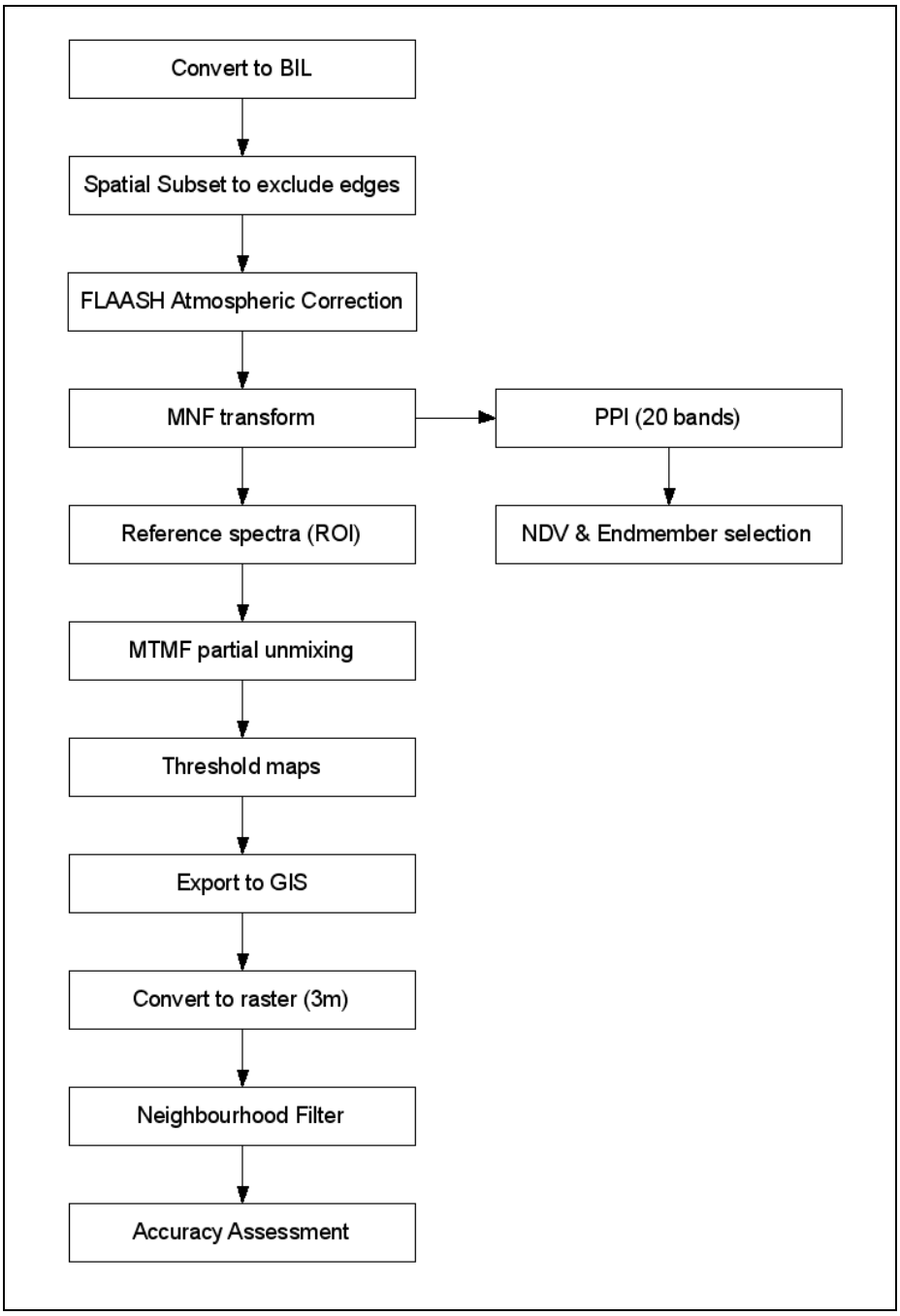

Figure 6-7 Salinity symptom mapping flow

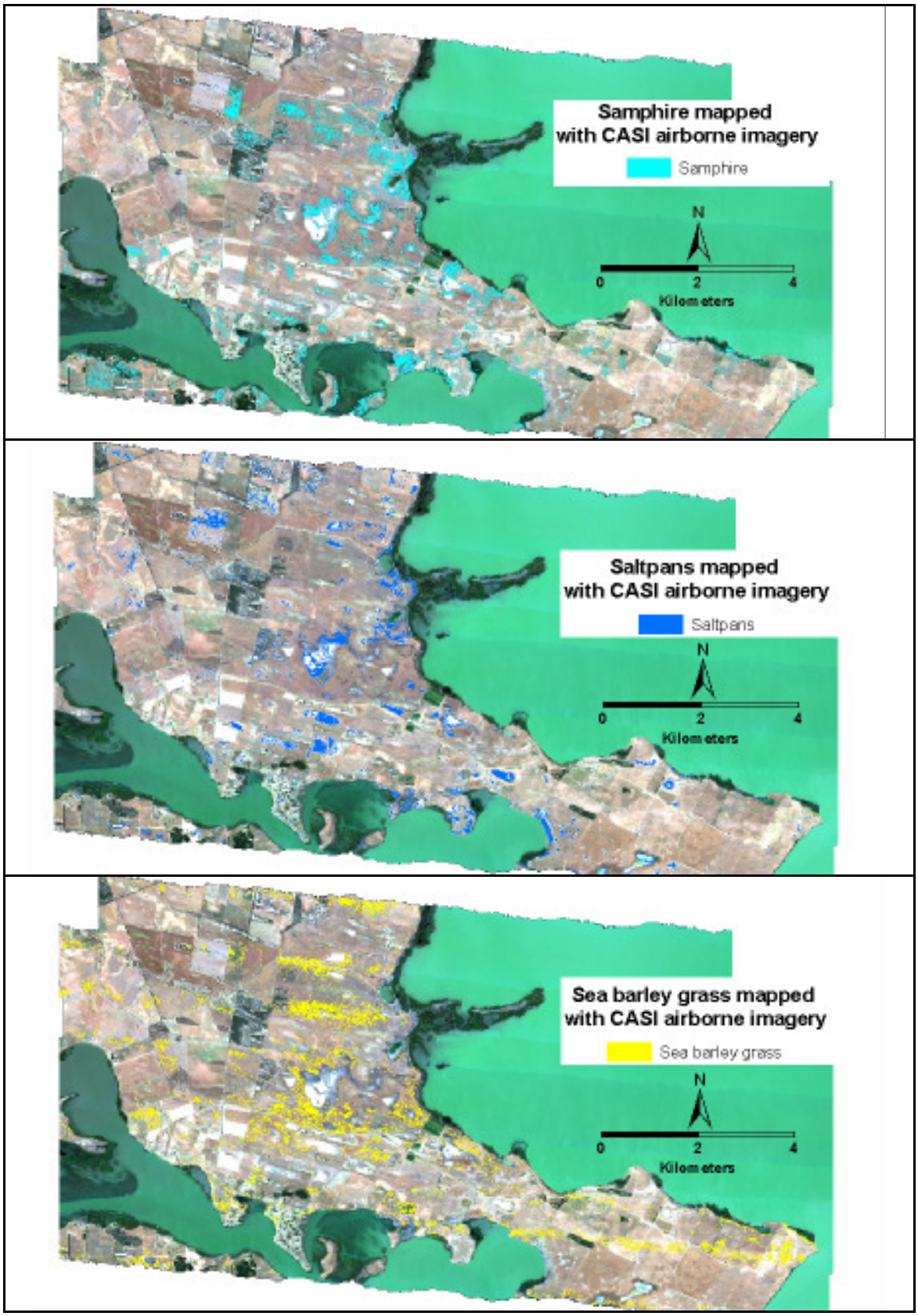

Figure 6-8 CASI salinity symptoms map at Point Sturt. Many mapped saltpans (blue) and samphire (cyan) were confined to the central and coastal saline areas. Sea barley grass (yellow) mapped areas were more sparsely distributed adjacent saline areas.

KHAT values showed that the samphire and saltpan maps were in moderate agreement with field data. The KHAT values for the samphire and saltpan maps were 0.48 and 0.51 respectively (Table 6-2 and Table 6-3). The saltpan maps showed a slightly higher agreement with the field data than the samphire maps. The main sources of errors in the saltpans and samphire maps were errors of omission where only 14 out of 29 samphire field sites and 17 out of 33 saltpan sites were mapped. These field sites were generally mixed sites with a proportion of samphire cover and exposed soil.

Table 6-2) Error Matrix for the samphire map (133 sample sites over 6 image swaths)

Samphire Error Matrix		Field		
		Presence	**Absence**	**Total**
Image	**Presence**	14	6	19
	Absence	15	98	113
	Total	29	104	133

Total accuracy 0.84

Producer's accuracy (Omission error)

Present…….0.48

Absent…….0.94

Users accuracy (Commission error)

Present…….0.70

Absent…….0.87

KHAT…….0.48

Table 6-3) Error Matrix for the saltpan map (138 sample sites over 7 image swaths)

Saltpan Error Matrix		Field		
		Presence	**Absence**	**Total**
Image	**Presence**	17	6	23
	Absence	16	99	115
	Total	33	105	138

Total accuracy 0.84

Producer's accuracy (Omission error)

Present…….0.52

Absent…….0.94

Users accuracy (Commission error)

Present…….0.74

Absent…….0.86

KHAT…….0.51

Salinity symptoms mapped with CASI imagery are overlain with the PIRSA soil landscape unit polygons. Partial unmixing successfully mapped samphire and saltpans in the designated saline soil landscape units.

Zonal statistics confirms that more sea barley grass appeared to be mapped in the nonsaline western slopes and high ground on the peninsula compared to saltpan and samphire maps. A higher percentage of sea barley grass (4.8%) was mapped in nonsaline areas compared to the samphire (2.7%) and saltpan (1.6%) maps (Figure 6-10). The PIRSA designated nonsaline areas are associated with the western slopes and the higher ground on the peninsula in the east.

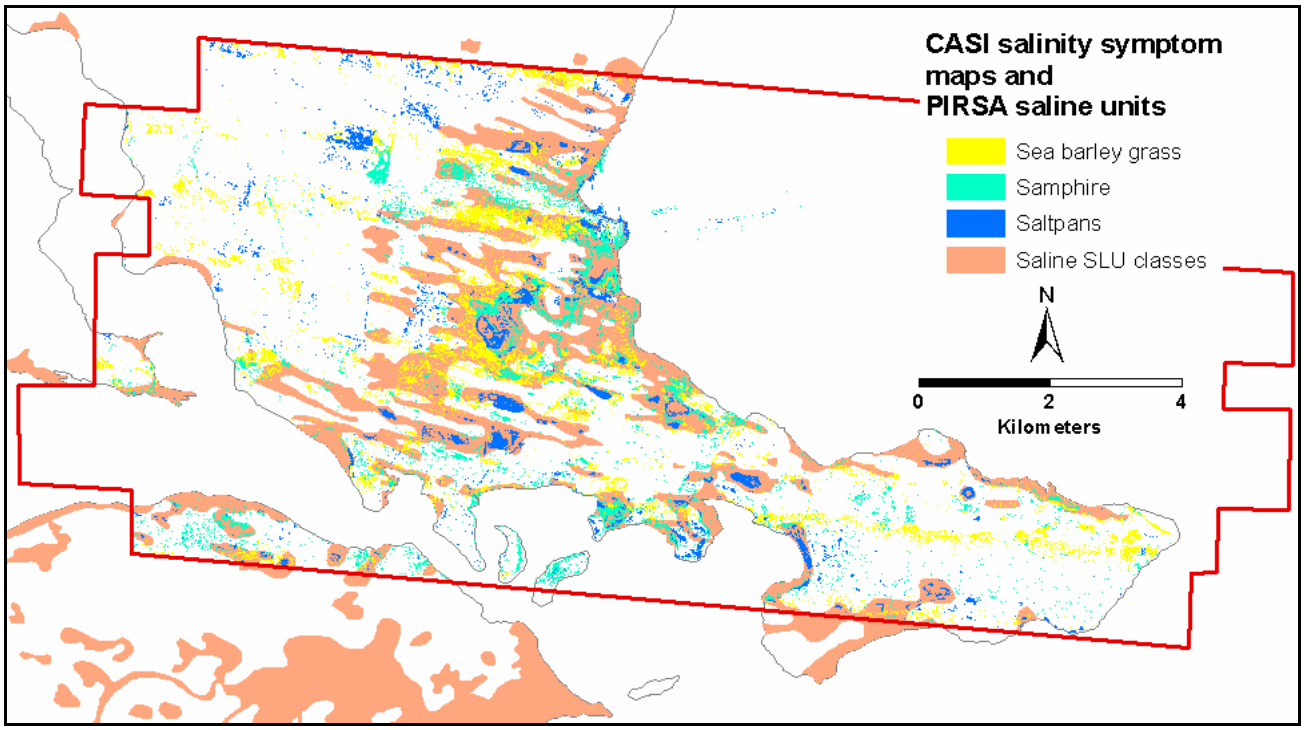

Figure 6-9 Detail of salinity symptom maps overlain with the PIRSA SLU polygons. The black dotted line shows a discontinuity in mapping saltpans across 2 image swaths

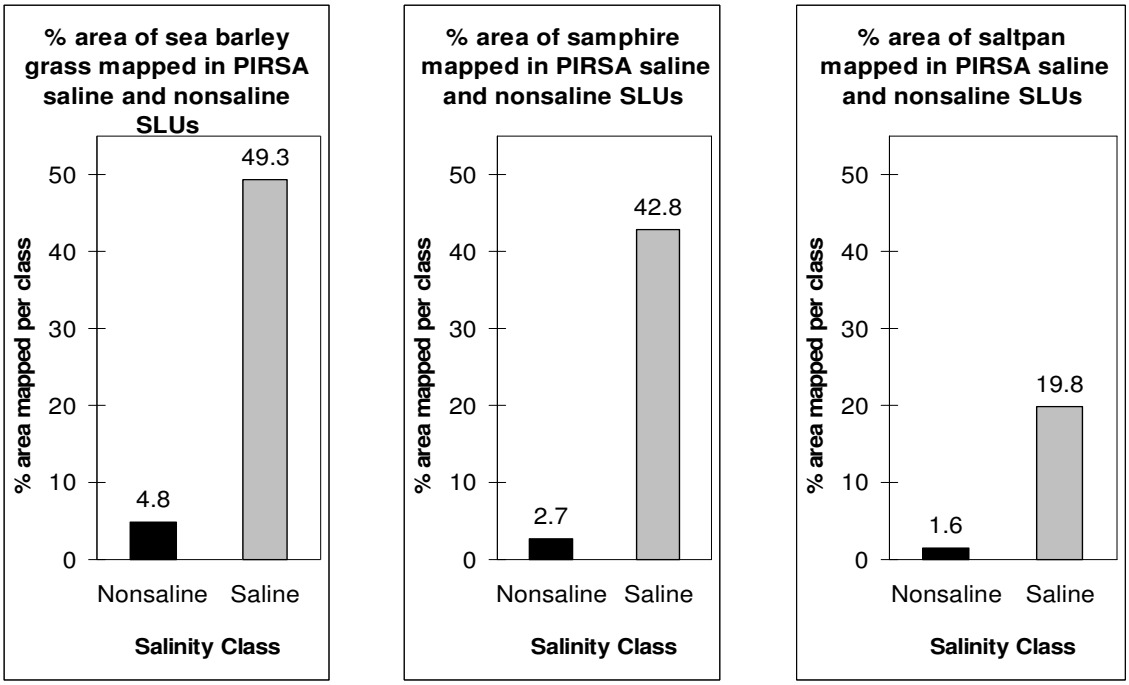

Figure 6-10 Zonal statistics showing the % area of sea barley grass, samphire and saltpans mapped in nonsaline and saline areas defined in the PIRSA SLU maps

6.7 Discussion and Conclusions

CASI imagery was acquired during November in order to distinguish late-senescing sea barley grass, a dominant halophytic plant species at Point Sturt, from a background of other annual non-halophytic grasses. Image analysis not only produced maps of sea barley grass but also samphire and saltpans for comparisons to similar maps produced from other forms of imagery.

Analysis of the CASI imagery followed the processing flow devised for mapping salinity symptoms with HyMap imagery. One major modification to the CASI flow was the replacement of ACORN with FLAASH atmospheric correction because ACORN could not use the 820 nm feature for calculating water vapour corrections. Another difference was the removal of MNF band 2 to account for across track illumination affects. The mosaicked maps contain stronger evidence of discontinuities across swath boundaries than HyMap, which suggests that residual across track effects were still present. The final difference was the choice of mixture tuned matched filtering over matched filtering for mapping soils. MF was unable to distinguish saline soils from non-saline soils when mapping across multiple image strips with a single image endmember.

Zonal statistics showed that higher proportion of sea barley grass was mapped in nonsaline areas compared to the samphire and saltpan maps. The comparatively higher proportion of sea barley grass in these non-saline areas suggests that the sea barley grass mapping was less reliable than saltpan and samphire mapping with CASI imagery. The better accuracy of the samphire and saltpan maps is reflected in the KHAT values of 0.48 and 0.51 respectively, both values indicate a moderate agreement with field data.

The main source of errors in the samphire and saltpan maps was the omission of field sites with samphire cover and exposed background soil. These omission errors suggest that significant differences in reflectance over the visible near infrared region alone may not be able to distinguish samphire from other vegetation.

The main error in the sea barley grass maps is associated with the similarity in spectra between senescing sea barley grass and other grasses and pastures in the area. Sea barley grass stays greener longer in lowlying wetter areas, however other plant species in nonsaline areas may also senesce at different rates depending on position in the landscape, spatially varying soil moisture and individual species response to these conditions. Near surface water would vary from year to year depending on climatic

conditions and, to an extent, changes in landuse, such as irrigation, cropping and grazing practices. Because the rate of senescence is dependent on these environmental conditions, it is difficult to identify a precise time that would maximise sea barley grass mapping from year to year.

The saltpans were mapped at the same accuracy as the HyMap maps. This is perhaps an unexpected result because the CASI spectra of saline soils do not contain well-defined absorption features in the visible near infrared wavelength region pertaining to mineralogy. Therefore, the most significant distinguishing characteristic of saline soil was related to spectral shape. The presence of halite and low organic matter produces high albedo in saline soils (Ben-Dor *et al*., 1997; Drake, 1995). However *in situ* saline soils at Point Sturt were affected by soil moisture, which produces lower spectral response (Lobell and Asner, 2002). Therefore, the distinguishing feature of CASI image spectra was lower albedo and the shape of the visible near infrared wavelength region, as identified by Dehaan and Taylor (2002B).

The limited wavelength range of 418–953 nm also had repercussions for allowing successful atmospheric corrections. When commissioning the surveys, it is important to ensure the wavelength range encompasses both sides of the 940 nm water absorption feature from 870-1020 nm. An improved range may result in less noise and no over correction around 940 nm.

Ultimately, CASI image analysis produced samphire and saltpan maps that showed moderate agreement with field data. However, samphire maps had a lower mapping accuracy compared to HyMap (KHAT value of 0.61). This lower accuracy and the difficulties in mapping sea barley grass suggests that the CASI imagery has a reduced capability for mapping vegetation symptoms of salinity, particularly those species that contain spectrally distinguishing characteristics in the SWIR. More precise vegetation mapping may require the SWIR regions as indicated in the spectral discrimination analysis and HyMap samphire mapping.

7 COMPARISON OF HYPERSPECTRAL AND CONVENTIONAL SALINITY MAPS

7.1 Introduction and aims

Ground validated samphire and saltpan maps were produced from unmixing HyMap multiple airborne image swaths (Chapter 4), Hyperion satellite imagery (Chapter 5) and CASI multiple swaths (Chapter 6). Moderately saline areas were also mapped by unmixing CASI imagery using senescing sea barley grass reference spectra, although these maps were not validated with ground data. HyMap image analysis produced the most accurate salinity maps compared to the other hyperspectral imagery.

In this chapter, the hyperspectral salinity maps are compared to previous Point Sturt salinity maps that were introduced in Chapter 2. Previous salinity maps include conventional maps based on aerial photography interpretation, such as the National Land and Water Resources Audit (NLWRA) salinity maps from 2000 and the PIRSA *salinity induced by watertable* attribute map, and the map of *severely saline areas* based on Landsat ETM imagery (Thomas, 2001). These comparisons aimed to assess the benefits and limitations of each method for mapping salinity.

7.2 Methods

The PIRSA *salinity induced by watertable* maps were compiled by assigning classes to each soil landscape unit according to a combination of the levels of salinity of the landscape as a whole, and the extent of land affected by highly saline seepage (Maschmedt, 2000). Saline seepage occurs where saline groundwaters rise near to the land surface (Maschmedt, 2000) and highly saline seepage is assumed to refer to seepages with high salinity levels over 16 dS/m (Table 2.1). SLU polygons were defined on the basis of a range of soil and landscape attributes.

Within GIS software, zonal statistics calculated the area of samphire, saltpan and sea barley grass mapped per SLU salinity class. In the zonal statistic plots, salinity classes associated with each class were labelled simply “slight” through to “extreme” for convenience (Table 6-1). Sea barley grass was expected to occur in moderate to highly saline areas (Classes C to E) (Table 6-1). Samphire was expected to occur in high to extreme levels of salinity (classes F and G) whereas saltpans were expected to be associated with extremely saline areas (Class G) (Table 6-1).

Table 7-1 Expected salinity symptoms associated with each PIRSA SLU "salinity induced by watertable" class (after (PIRSA, 2001A) and Maschmedt, 2001). Sea barley grass would be mainly expected to occur in moderate to high levels of salinity and samphire in the high to extreme areas (Classes F and G). *Class E was not represented at Point Sturt.

Salinity	Name of salinity levels	Dominant salinity symptoms expected in
A	None	None
B	Slight	Negligible
C	Moderate	Sea barley grass
D	Moderately high	Sea barley grass
E *	Moderately high to high	Sea barley grass, samphire and bare areas
F	High	Samphire and bare areas
G	Very high to extreme	Samphire, bare areas and salt encrusted

The National Land and Water Resources Audit mapped the extent of dryland salinity in SA (Salinity 2000 maps) by identifying seeps, scalds and other indicators of salt affected areas from aerial photographs[6] (Barnett, 2000). These maps were also qualitatively compared to the HyMap saltpan and samphire maps by overlaying them in a GIS program.

The Land Condition Monitoring study (2001) mapped *severely saline areas* in the Point Sturt area based on Landsat ETM imagery and spatial data integration (Thomas, 2001). In this chapter, the *severely saline areas* map is compared to the HyMap saltpan and samphire maps. The Landsat based map was initially georeferenced to the HyMap mosaic (presented in Chapter 4) before importation into GIS software. The severely saline area maps was then overlain with the HyMap saltpan and samphire themes.

7.3 Results

7.3.1 Comparison to PIRSA salinity maps

The SLUs with saline attributes have been overlain with salinity maps produced from HyMap multiple airborne image swaths, Hyperion satellite imagery and CASI multiple swaths (Figure 7-1 a, b and c). The hyperspectral salinity maps predominately coincide with SLUs assigned saline classes in the central discharge region and along the coastal areas. As expected, the samphire and saltpan areas are mainly associated with high

[6] The dates of the aerial photographs used in mapping were not specified in the South Australian NLWRA report.

(class F) to extreme (class G) saline areas. The CASI and Hyperion salinity maps are associated with more non-saline SLUs than the HyMap.

Zonal statistical analysis quantifies these observations. For each hyperspectral dataset, zonal statistics plots show that symptoms of different salinity levels were, in general, mapped in the appropriate SLU salinity class. For each hyperspectral dataset, samphire and saltpans were predominately mapped in high to extreme SLUs (Classes F and G) (Figure 7-2, Figure 7-3 and Figure 7-4).

The HyMap plot (Figure 7-2) shows that samphire and saltpans were mapped in 21.5% of the high salinity SLUs (class F) and 13.7% of the very high to extreme salinity SLUs (class G). Zonal statistics appear to corroborate the high accuracy of the HyMap salinity maps because the lowest proportion of samphire and saltpans are in the nonsaline areas. The Hyperion plots (Figure 7-3) shows that samphire and saltpans were mapped in 26% of the high saline class (class F) and 24.8% of the very high to extremely saline class (class G). More saltpans and samphire were mapped in the high and low saline classes compared to HyMap.

The CASI zonal statistics plot (Figure 7-4) show that samphire and saltpans were mapped in 20.6% of the highly saline areas and 15.9% of the very high to extremely saline areas, similar proportions to HyMap. The highest proportion of sea barley grass was mapped in the moderately saline class. Sea barley grass is expected in classes assigned moderate to high levels of salinity (C to F, but Class E is not represented at Point Sturt) but perhaps over a reduced area in the higher classes because of the higher proportion of land affected by highly saline seepage. A comparatively higher proportion of sea barley grass (4.9%) was mapped in the non-saline class (western slopes and high ground on the eastern tip). These areas were observed to be non-saline during field visits, which suggests that non-saline landcovers were incorrectly mapped as sea barley grass.

Detail of the SLU maps with overlaid saltpan and samphire maps is displayed in Figure 7-5. This area is the main discharge zone at the interface between the clay and limestone aquifer system. In this region, the saline SLUs are mainly assigned saline classes associated with moderate (classes C and D), high (class F) to extreme levels of salinity (class G) and a percentage of the land affected by highly saline seepages. In this mapping representation, soil is treated as being homogeneous within each unit.

In contrast, the fine spatial resolution of the HyMap salinity maps takes into account the spatial heterogeneity of soils within the saline SLUs, as image analysis successfully mapped highly saline (samphire) and extremely saline (saltpans) soils. These high-resolution raster based salinity maps provide a more realistic representation of the variability of soil salinity by mapping the areas that actually display the highest salinities, rather than the SLUs that contain the higher salinities.

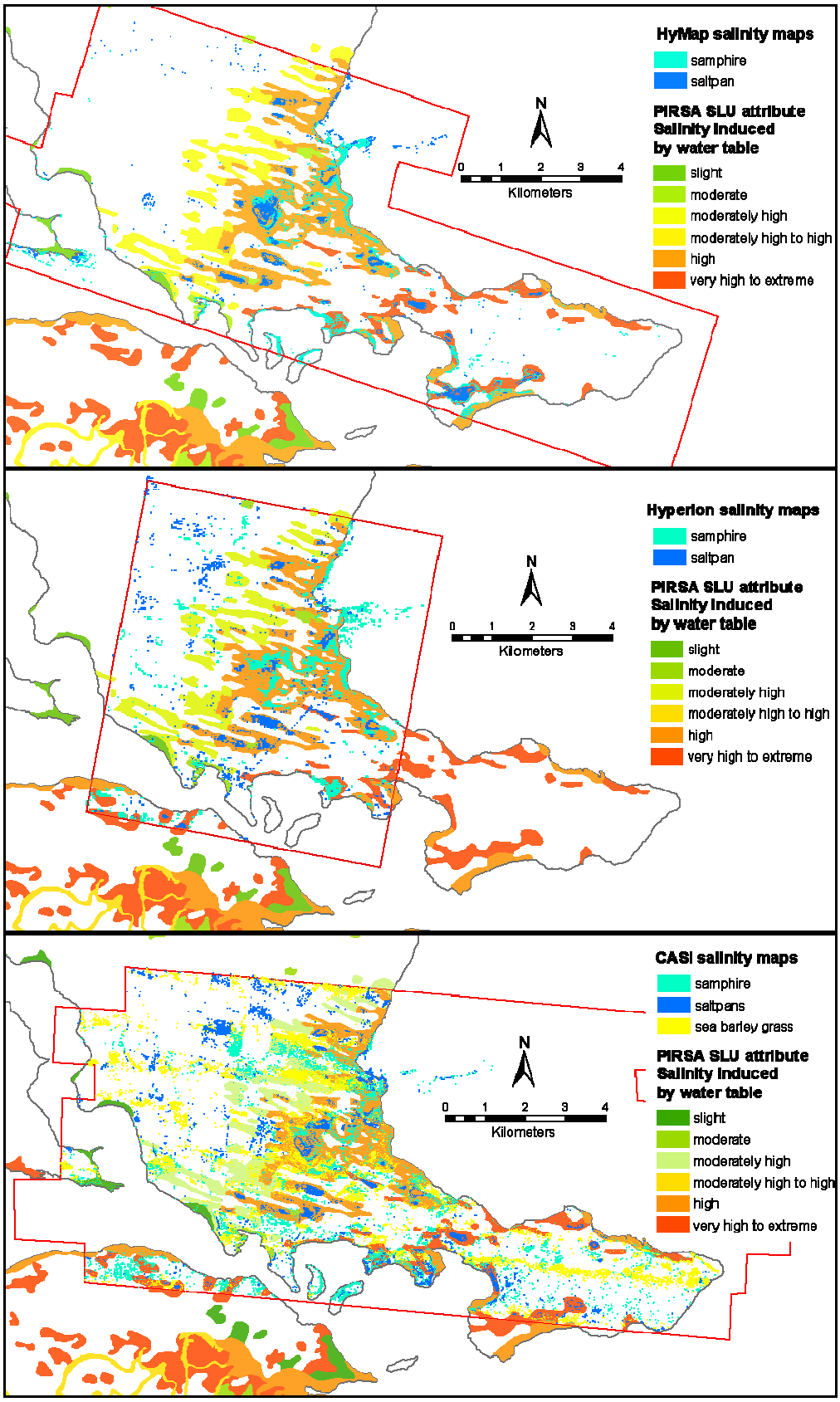

Figure 7-1 PIRSA salt affected areas overlaid with the salinity maps produced from a) HyMap, b) Hyperion and c) CASI hyperspectral data (with image extent outlined in red).

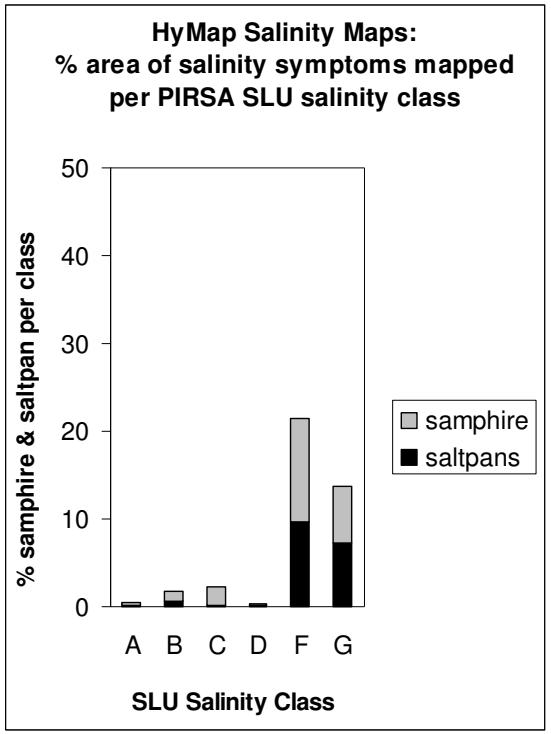

Figure 7-2 HyMap: Samphire and saltpans were mapped in 21.5% of the high salinity SLUs (class F) and 13.7% of the very high to extreme salinity SLUs (class G).

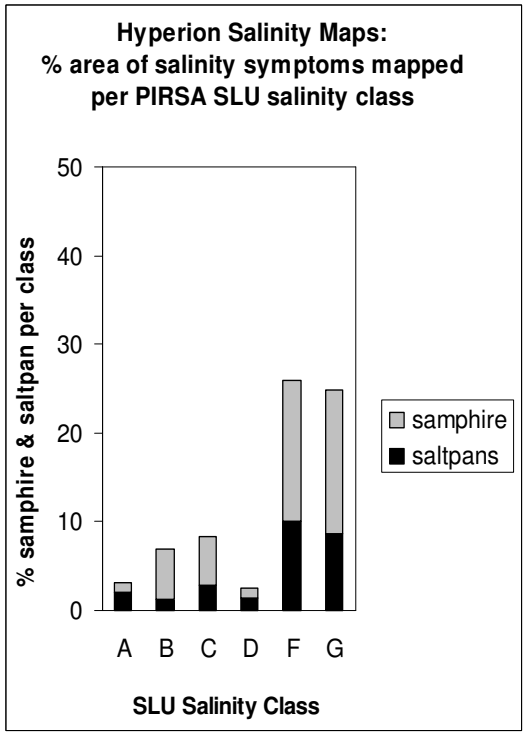

Figure 7-3 Hyperion: samphire and saltpans were mapped in 26% of the high saline areas (SLUs class F) and 24.8% of the very high to extremely saline (SLUs class G). More saltpans and samphire were mapped in low saline SLUs compared to HyMap

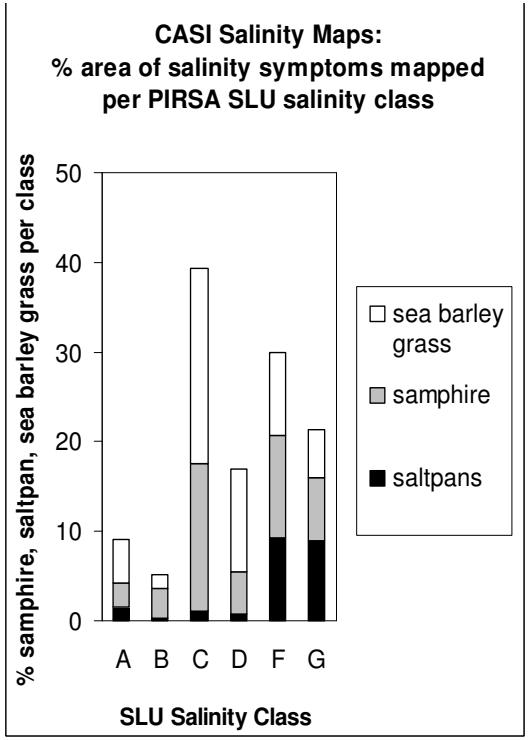

Figure 7-4 CASI: samphire and saltpans were mapped in 20.6% of the highly saline areas and 15.9% of the very high to extremely saline areas. The highest proportion of sea barley grass was mapped in moderately saline areas. A high proportion of sea barley grass was also mapped in non-saline areas.

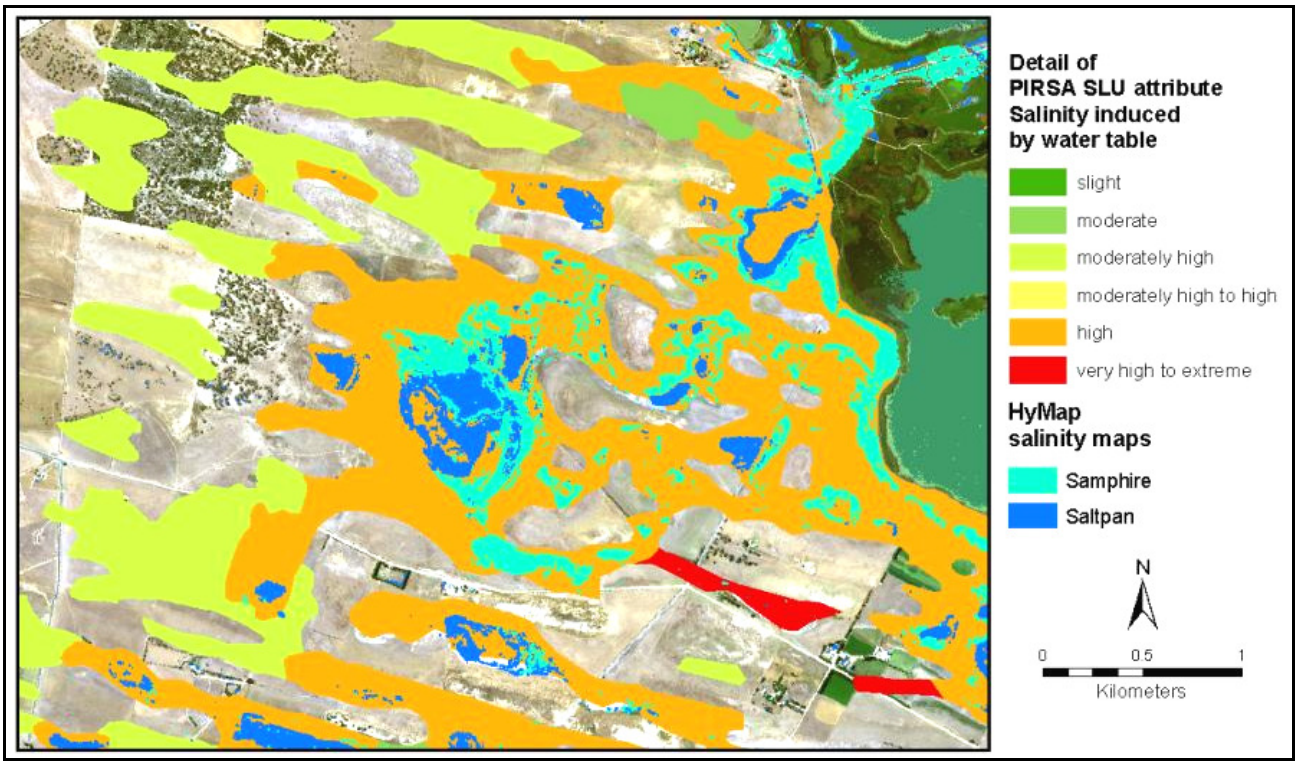

Figure 7-5 Detail of HyMap salinity symptom (Site A) overlaid with PIRSA Soils Landscape Units attribute of salinity induced by watertable

7.3.2 Comparison to NLWRA dryland salinity map

The differences between the NLWRA Salinity 2000 maps and the HyMap salinity symptom maps are illustrated in Figure 7-6. Both mapping approaches were able to map exposed saline soils, although a number of saltpans were not identified in the HyMap maps. The spectra of unmapped pans were most likely either adversely affected by surface moisture or lacked well-defined gypsum absorption features because their surface soils were instead dominated by halite. However, more saltpans identified by fieldwork were mapped in the Salinity 2000 maps. Partial unmixing of HyMap data was able to map samphire growing along the northeast and southern coasts. These areas were not delineated through by the aerial photograph interpretation. Therefore, unmixing of HyMap data was more successfully able to map saline land with a good cover of samphire vegetation.

Detail of the HyMap and Salinity 2000 maps is displayed in Figure 7-7. The HyMap maps depict the spatial variability of salinity within the Salinity 2000 boundaries by mapping high salinity (samphire) and extremely saline soils (saltpans) pixel by pixel, to provide a more realistic representation of soil variability rather than delineating units that contain saline areas.

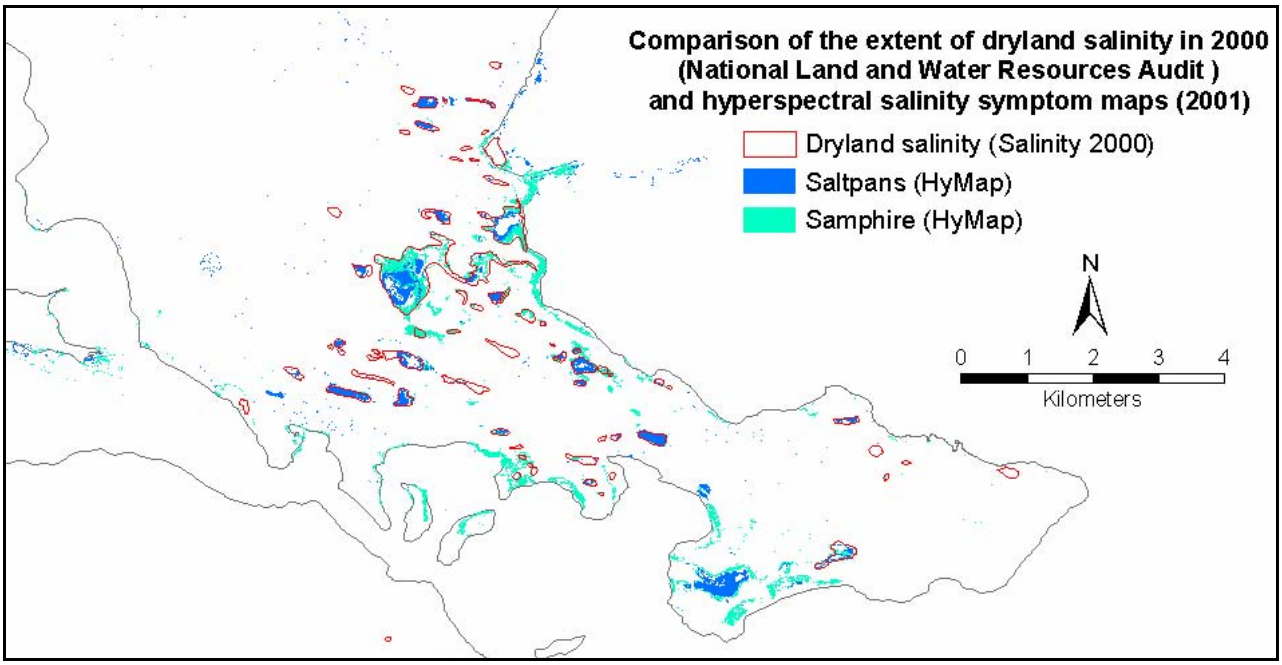

Figure 7-6 NLWRA dryland salinity 2000 map overlain with the HyMap samphire and saltpans maps.

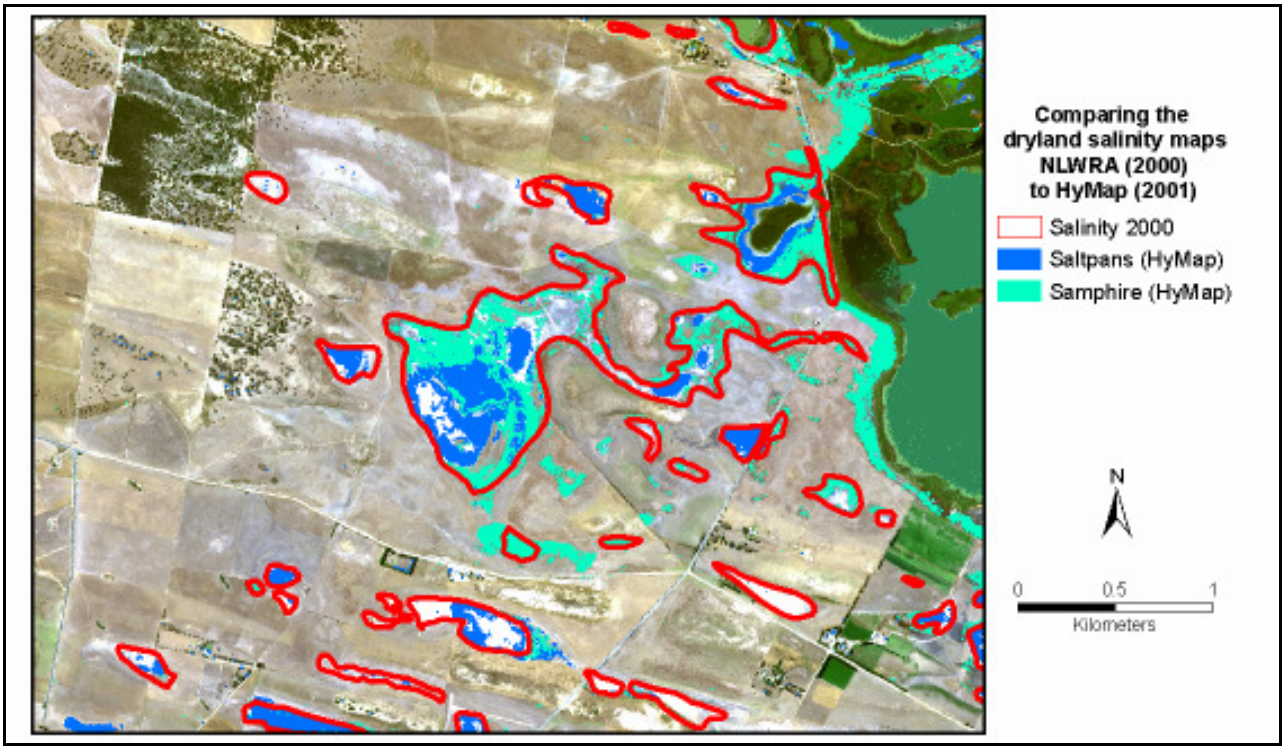

Figure 7-7 Detail of the NLWRA dryland salinity 2000 map and the HyMap salinity maps overlying the true colour HyMap image. The HyMap image analysis was better able to map saline land with a good cover of samphire vegetation along the central and southern coasts.

7.3.3 Comparison to Landsat based salinity maps

The Landsat based map of *severely saline areas* (Thomas, 2001) predominately identified areas of exposed saline soils associated with the central and coastal discharge zones (Figure 2-7). The map was produced through image analysis of multitemporal

Landsat imagery with the success of the maps being partially attributed to the integration of watertable information from the PIRSA soil landscape units map. The Landsat-based salinity maps are compared to the HyMap samphire and saltpan maps in Figure 2-7b. The HyMap saltpan map has mapped similar extent of exposed soils in saline areas and has successfully excluded nonsaline exposed soils in fields, quarries and on sand dunes.

The main difference between the Landsat based and HyMap salinity maps was the increased extent of highly saline areas mapped. HyMap image analysis successfully mapped salt affected areas with a good cover of samphire vegetation particularly along the eastern central lake fringe and along the southern coast. A key advantage of HyMap image mapping was the use of single date imagery compared to Landsat-based mapping, which required multitemporal data combined with information from the PIRSA SLU attribute maps that were mainly based on extensive aerial photo interpretation and the expert knowledge of experienced field operators.

7.4 Conclusion

Saline classes from the PIRSA soil maps were compared to salinity maps produced from HyMap multiple airborne image swaths, Hyperion satellite imagery and CASI multiple swaths. Overall the trends in the zonal statistics plots were as anticipated for the three salinity symptoms. The hyperspectral samphire and saltpan maps, which are indicators of highly saline and extremely saline soils respectively, mainly coincided with SLUs assigned saline classes in the central discharge region and along the coastal areas. As expected, the samphire and saltpan areas are mainly associated with high (class F) to extreme (class G) saline areas. The CASI and Hyperion salinity maps are associated with more non-saline SLUs than the HyMap.

As expected, zonal statistics showed that the highest proportion of sea barley grass was mapped in the moderately saline class. The least saline classes, A and B, contained the lowest proportion of land mapped as sea barley grass, although, the comparatively higher proportion of sea barley grass in the non-saline class suggests that a significant area of non-saline landcover was incorrectly mapped as sea barley grass.

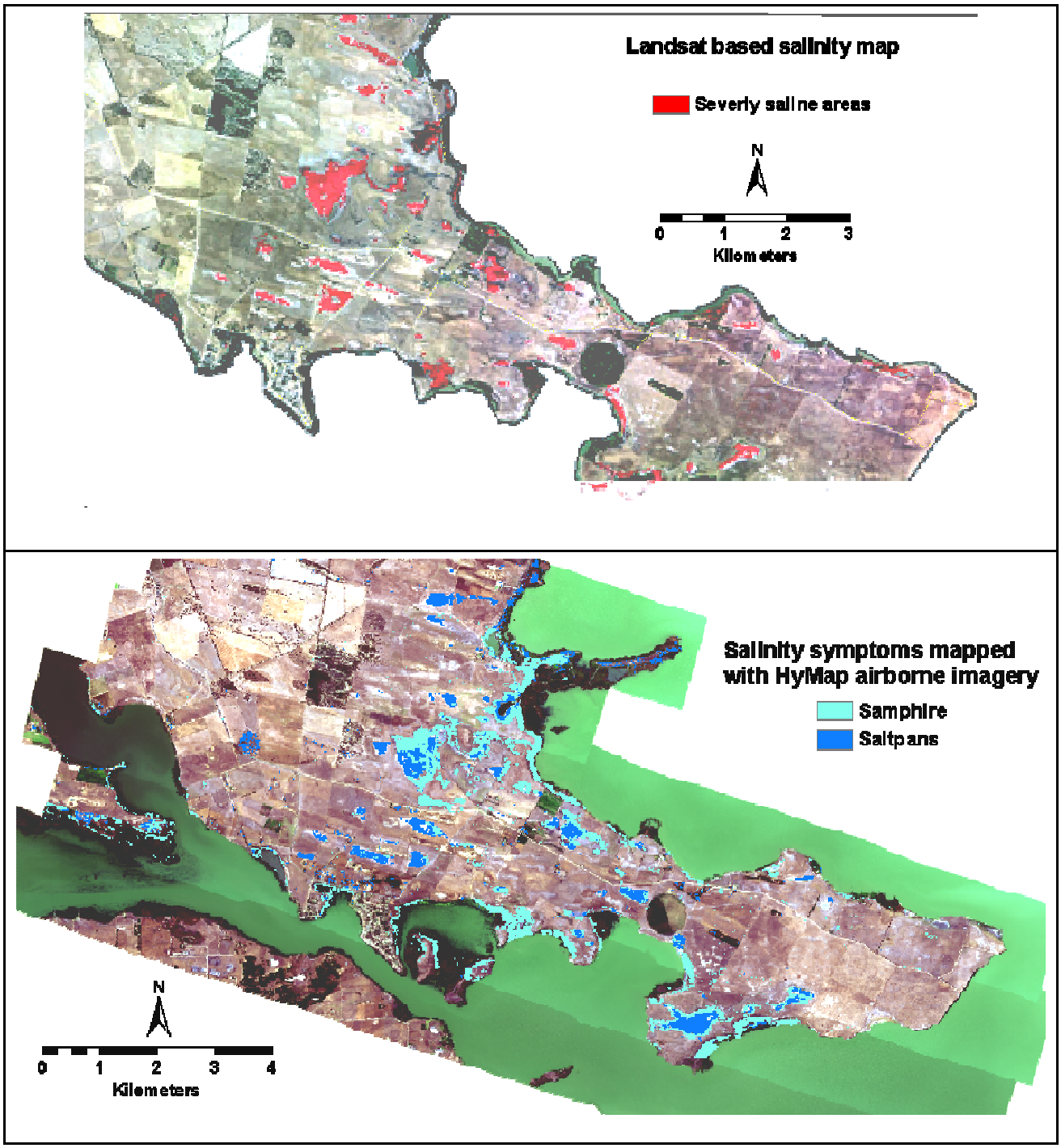

Figure 7-8 a) Map of *severely saline areas* (red) based on Landsat ETM imagery (source (Thomas, 2001) previously presented in Chapter 2) b) compared to the HyMap saltpan and samphire maps (bottom).

Compared to the NLWRA dryland salinity maps, the most obvious improvement in the HyMap maps is the ability to map samphire areas along the central and southern coasts that could not be mapped from aerial photograph interpretation. The HyMap salinity mapping has the advantage over aerial photograph interpretation because the high-resolution spectral information in the visible, NIR and SWIR regions, allows for

discriminating samphire vegetation, a common indicator of highly saline soil. However, the increase in spectral information has not provided an improved ability to map exposed saline soils, in the Point Sturt area.

The combination of the HyMap samphire and saltpan maps has also provided an improvement to the problem of mapping saline areas with multispectral satellite imagery. HyMap image mapping has the significant advantage of using only single date imagery compared to Landsat-based mapping which required multitemporal data in combination with external PIRSA soils data that was derived from extensive aerial photo interpretation and the expert knowledge of experienced field operators.

Overall, the advantage of the hyperspectral imagery is not only the higher spatial resolution but also higher spectral resolution which allows for mapping areas with a good cover of vegetation, in this case, highly saline areas covered with the salinity indicator species samphire. HyMap image analysis successfully mapped highly saline (samphire) and extremely saline (saltpans) soils within homogeneous soil units. Salinity maps produced from hyperspectral airborne imagery have the advantage of being fine resolution raster based maps that depict salinity as varying spatially within discrete boundary soil polygons of conventional mapping. The fine spatial resolution of these hyperspectral salinity maps provides a more realistic representation of the variability of high to extremely salt affected land at a farm scale. These maps are capable of enhancing currently available soil maps and allow salinity management programs to be more precisely targeted in the landscape. The HyMap samphire and saltpan maps would also provide suitable input data to the more recent digital soil mapping models that are using various forms of raster data to improve soil mapping.

8 DISCUSSION AND CONCLUSION

Given the magnitude of the dryland salinity problem in Australia and the limitations of current remote sensing methods, this study aimed to determine whether hyperspectral image analysis has the capability to improve the mapping of surface symptoms of dryland salinity. Improved mapping would primarily mean the ability to map saline areas with a good cover of vegetation (Furby 1995; Howari, 2003) and to distinguish exposed saline soils from non-saline soils, without the need to integrate ancillary soil and terrain data.

In particular, this study aimed to evaluate hyperspectral imagery with differing spectral and spatial resolutions for their ability to map surface symptoms of salinity. In the case of airborne hyperspectral sensors, HyMap and CASI, an important objective was to deal with the nontrivial problem of processing multiple image swaths, such that an efficient and consistent analysis procedure was developed for mapping symptoms of salinity across broad areas. Space-borne hyperspectral imagery has the potential to redress the spectral limitations of multispectral satellite imagery while having the satellite advantage of frequent repetition over larger study areas. In the case of the Hyperion imagery, a principal objective was to reduce noise levels to maximise salinity symptom mapping for comparison to airborne sensors.

As a precursor to mapping salinity, this study initially aimed to identify salinity symptoms that were spatially and spectrally suited to mapping with hyperspectral imagery and to identify the optimal time of year to map each salinity symptom, especially saline areas supporting dense halophytic vegetation cover.

8.1 Review of results

8.1.1 Surface symptoms of dryland salinity selected for mapping with hyperspectral imagery

Fieldwork identified salinity symptoms that were homogeneous over significant areas and were spatially suitable for mapping with remote sensing imagery. The symptoms that satisfied these spatial and spectral requirements were saltpans, samphire *(Halosarcia pergranulata)* and sea barley grass *(Critesion marinum).* Saltpans are indicators of extreme saline areas. Samphire is a common indicator of high to very high

salinity, whereas sea barley grass dominates moderate to moderately high levels of salinity.

The field spectra of saltpan soils contained spectral features consistent with gypsum such as a broad absorption feature at 2200 nm, a single 1755 nm feature and a triple feature near 1500 nm. XRD analysis of the dried salt crusts from the central discharge area identified dominant halite and quartz with sub-dominant gypsum. The spectra of the coarse, thick, white salt crust, from the southern coastal pan, were characterised by a brighter and flatter visible/NIR region, and shallow absorption features at 2200 nm and 1755 nm. The 1755 nm feature suggested the presence of gypsum at Site B but the shallow nature of both features indicated low gypsum content. XRD analysis confirmed the crystal crust to be halite.

The individual spectra of green and red samphire were dominated by photosynthetic vegetation characteristics such as chlorophyll absorption, a red edge and NIR plateau containing deep water absorption features. Like those reported by Dehaan and Taylor (2002B), the spectra of green samphire, often seen with red tips, were found to contain peaks in both green and red wavebands and, not surprisingly, red samphire spectra contained a significant reflectance peak in the visible red wavelength region. Samphire spectra have additional features of note, including a sloping red edge shoulder and cellulose-lignin features at 2100 nm and 2300 nm, possibly due to woody tissue or saline adaptations such as waxy leaf coating and succulent leaves (Elvidge, 1990; Lewis *et al*., 2000).

Samphire and extremely saline soils associated with saltpans were selected as the best salinity symptoms for mapping with hyperspectral imagery because of their spatial distribution and distinguishing spectral features.

8.1.2 Optimum time of year for mapping

Late in the dry season appeared to be the optimum time of year to exploit the spectral differences between saline soils and non-saline soils and between samphire and the background dry grasses that dominate the landscape. At this time of year, soil moisture is at a minimum, which means that spectral features pertaining to soil properties could be maximised (Lobell and Asner, 2002) for partial unmixing mapping. Even though the dry season was a suitable time of year to distinguish perennial halophytic vegetation,

there were fewer halophytic species available to map at this time because all annual vegetation had senesced and appeared indistinguishable on the ground.

In moderately salt affected areas, sea barley grass was the dominant halophytic species. The optimum time of year to map sea barley grass was expected to occur between "spring flush" (September) or senescence (November) because during this period because annual grasses were readily identifiable from the mature seed heads and grew in extensive, dense, homogeneous zones. Results showed that there were no significant differences between the spectra of sea barley grass and brome grass during "spring flush", however, during senescence, sea barley grass differed significantly from other annual species across broad visible, NIR and SWIR wavelength regions. The red edge reflectance did not appear to be significantly different between senescing species, which corroborates the results of Schmidt and Skidmore (2001) but contradicts the findings of Thenkabail *et al.* (2000 and 2004). Therefore, late November was identified as the optimum time to exploit spectral differences between the varying rates of senescence of sea barley grass and other annual species.

8.1.3 Comparison of different hyperspectral imagery

Senescing halophytic grasses and plant species adapted to saline environments, highly saline soils had distinguishing spectral features in the visible, NIR and SWIR wavelength regions. These vegetation symptoms of salinity grew in dense homogeneous patches, making them suitable for mapping with hyperspectral imagery. Imagery from three hyperspectral sensors of differing spectral and spatial resolutions were compared for their ability to map these salinity symptoms (Table 8-1). HyMap and Hyperion sensors incorporate the visible, NIR and SWIR wavelength regions and were most suited to mapping soil and vegetation symptoms of salinity. HyMap airborne imagery and Hyperion imagery was acquired during the dry season, which was suitable for mapping dryland salinity symptoms of samphire and saline soils.

The CASI airborne sensor was an appropriate sensor for mapping sea barley grass, because the spectral range spanned the visible and NIR regions which are important for plant discrimination. In fact, discrimination analysis showed that throughout this wavelength region, field spectra of sea barley grass exhibited significant differences from non-halophytic grasses.

Table 8-1 Hyperspectral imagery was acquired from 3 different sensors: 2 airborne and one satellite instrument. The HyMap and Hyperion data was captured during the dry season and the CASI imagery was captured during spring senescence.

Hyperspectral sensor (platform)	Spatial resolution	Spectral resolution	Spectral range	Date of capture	Season description
HyMap (airborne)	3 m	10-20 nm	450 - 2500 nm	14 March 2001	End of dry season
Hyperion (satellite)	30 m	2 nm	450 - 2500 nm	18 February 2002	Mid dry season
CASI (airborne)	3 m	10-15 nm	450 960 nm	25 November 2003	End of spring senescence

8.1.4 Analysis of multiple image swaths

To deal with analysis of multiple swaths of airborne image data, an efficient and consistent processing procedure was sought for mapping salinity symptoms. Commercially available image processing techniques were employed such if these methods proved successful, catchment managers could readily apply hyperspectral imagery to baseline salinity mapping and monitoring.

Multiple-swath calibration of HyMap and CASI data was effectively dealt with through MODTRAN based atmospheric correction (ACORN and FLAASH) and fine-tuning georegistration to GPS locations. In HyMap data, systematic variations in across track illumination were corrected using standard polynomial correction function. For CASI pre-georegistered swaths, variations in across track brightness were accounted for by removing strongly affected MNF bands.

Partial unmixing tests found matched filtering to be the optimal partial unmixing method because it not only produced accurate maps but also minimised processing of multiple swaths. A single image-derived endmember could be used as reference spectrum for mapping extremely saline soils across five image swaths. Those saline soils containing gypsum were most effectively mapped with a reduced dataset spanning the 1750 nm absorption feature. Non-saline soils such as quarries, unsurfaced roads and sand dunes were successfully excluded. However, matched filtering was not suitable for vegetation mapping.

MTMF exploited the spectral properties of samphire successfully by mapping ground validated samphire patches whilst excluding perennial dryland lucerne pasture and

native mallee. The most successful maps were produced using the entire spectral range (450-2500 nm), suggesting the importance of the SWIR region for mapping halophytic chenopods with scleromorphic characteristics. However, unlike MF mapping, MTMF is unable to utilise one reference spectrum to map multiple strips, and therefore each strip required an intrinsic spectrum to map samphire.

Endmembers pertaining to halophytic vegetation were not readily extracted from each image swath through the well-known pure pixel extraction procedure (Kruse, 1999). The ability to extract a variety of vegetation endmembers is limited because of the similarity between the spectra of different halophytic species and different senescing vegetation. Spectral discrimination analysis suggests that spectral differences between plants are based on relative differences in reflectance across broad spectral bands rather than well-defined diagnostic absorption features (Lewis, 2001). A more reliable method for deriving vegetation reference spectra requires locating dense homogenous or "pure" patches of the target vegetation. This is a relevant strategy for halophytic vegetation because these species exhibit zonation based on their preferred soil conditions and topographic features (Barrett-Lennard, 2003).

Samphire and extremely saline soils associated with saltpans were successfully mapped across multiple image swaths from a single date airborne survey with no ancillary data. Both soil and vegetation salinity symptom maps were produced using readily available software and standard hyperspectral processing methods. Analysis of the CASI imagery followed the processing flow devised for mapping salinity symptoms with HyMap imagery. One major modification to the HyMap flow was the replacement of ACORN with FLAASH atmospheric correction because ACORN could not use the 820 nm feature for calculating water vapour corrections. The other main difference was the choice of mixture tuned matched filtering over matched filtering for mapping soils with CASI data. MF was unable to distinguish saline soils from non-saline soils when mapping across multiple image strips with a single image endmember.

The mosaicked CASI maps contained stronger evidence of discontinuities across swath boundaries than HyMap. The between strip differences may be due to residual variations in brightness across each CASI image swath.

8.1.5 Mapping salinity with Hyperion satellite imagery

The high spectral resolution of Hyperion imagery is comparable to HyMap and the 30 m ground resolution of the sensor is equivalent to Landsat. The advantage of a Hyperion scene is that although the along-swath coverage that is equivalent to other satellite imagery, the 7.5 km swath-width is over 5 times the width of a single airborne swath (with ground resolution of 3 m). However, the Hyperion scanner is only an experimental instrument and as such it has image quality problems associated with poor signal to noise ratio. Endmembers derived from the Hyperion image contained significant noise particularly in the far NIR region and lacked diagnostic absorption features in the SWIR. The spectral region around 2000 nm was excluded from mapping because ACORN was unable to adequately correct for atmospheric CO_2 absorption features. To maximise samphire and saltpan mapping, the superior MTMF partial unmixing was used with a MNF transformed ROI-generated reference spectrum.

8.1.6 Mapping accuracies

HyMap image analysis produced the most accurate samphire and saltpan maps compared to CASI and Hyperion imagery (Table 8-2). In HyMap saltpans and samphire maps, KHAT values of approximately 0.6 showed that there was a moderate agreement between the image maps and the field observations (Table 8-2). One of the major sources of error in mapping saltpans with HyMap imagery were errors of commission from native perennial vegetation, whose spectra contain absorption features associated with non-green plant components throughout the SWIR region (Elvidge, 1990). The absence of an objective, automated procedure for threshold value selection means that threshold optimisation requires sufficient groundbased knowledge of a detailed area within each image strip.

Hyperion saltpans and samphire maps produced KHAT values of 0.50 and 0.38 respectively (Table 8-2). The low mapping accuracy of the saltpans maps may be due to the high level of Hyperion data noise and therefore the lack of diagnostic soil mineral absorption features in the SWIR. The low mapping accuracy of the samphire maps may also be affected by data noise. Samphire mapping may also need the entire SWIR wavelength region because this region contains important spectral properties related to halophytic adaptations (Elvidge, 1990; Lewis, 2002). The coarser spatial resolution is also a contributing factor to the lower accuracy because coarser resolution reduces the

number of pure pixels. For small saltpans and patches of samphire (less than a few pixels wide) every pixel is a mixed boundary pixel.

In CASI mapping, the saltpan maps showed a higher agreement with the field data than the samphire maps. Saltpans maps produced a KHAT value of 0.51, a comparable accuracy to HyMap maps, whereas samphire maps only managed a KHAT value of 0.48 (Table 8-2). The higher saltpan accuracy is an unexpected result because CASI wavelengths incorporates the visible and near infrared wavelength regions that do not contain well-defined absorption features pertaining to soil mineralogy. The ability of CASI image analysis to map extremely saline soils effectively could instead be due to high albedo or the shape of the NIR shoulder (Dehaan and Taylor, 2002A and 2002B).

When compared with previous soil landscape unit salinity mapping (PIRSA, 2001A), the CASI derived saltpan, samphire and sea barley grass maps showed distributions as expected. The lowest proportion of saltpans was mapped in the non-saline Class A compared to samphire and sea barley grass, which also reflects the higher saltpan mapping accuracy. The highest proportion of sea barley grass was mapped in Class C and Class D, which are characterised by moderate levels of salinity. A high proportion of sea barley grass in the non-saline class A could indicate that a significant area of non-saline landcover was incorrectly mapped as sea barley grass. The main error in the CASI sea barley grass maps may be due to the similarity in spectra between senescing sea barley grass and non-halophytic senescing vegetation in non-saline areas such as hillsides. The allocation of sea barley grass pixels into known non-saline SLUs may also point to the need for the SWIR to improve discrimination of species in different stages of senescence. The importance of the SWIR region was also highlighted in the results of spectral discrimination analysis (Chapter 3), which found significant spectral differences occur across broad spectral regions in the visible, NIR and SWIR simultaneously.

The main source of errors in the CASI samphire maps was large number of field sites with samphire cover that were left unmapped. These sites were generally mixed sites, containing a combination of samphire and soil. This result suggests that significant differences in the VISNIR region alone do not contain enough spectral information to distinguish samphire from other vegetation. The allocation of sea barley grass pixels into known non-saline SLUs may also point to the need for the SWIR to improve discrimination of species in different stages of senescence.

Table 8-2 Summary of salinity symptoms mapped with HyMap, CASI and Hyperion imagery. Salinity levels are based on PIRSA classifications.

Hyperspectral sensor (platform)	Salinity symptom	Time of year	Important spectral characteristics for partial unmixing mapping	Accuracy (KHAT)	Salinity level
HyMap (airborne)	Extremely saline soils	Dry season	VIS features due to soil colour & SWIR features due to saline soil minerals	0.58	Extreme
	Samphire	Dry season	VISNIR features due to plant pigments, leaf structure & SWIR features due to woody tissue and saline adaptations	0.61	High to very high
Hyperion (satellite)	Extremely saline soils	Dry season	VIS features due to soil colour & SWIR features due to saline soil minerals	0.50	Extreme
	Samphire	Dry season	VISNIR features due to plant pigments, leaf structure & SWIR features due to woody tissue and saline adaptations	0.38	High to very high
CASI (airborne)	Extremely saline soils	Dry season	VIS features due to soil colour & NIR shoulder due to salinity status	0.51 Zonal statistics	Extreme
	Samphire	Dry season	VIS features due to plant pigments & NIR slope due to leaf structure	0.48 Zonal statistics	High to very high
	Sea barley grass	Senescence	VIS and NIR features due to senescence	Zonal statistics	Moderate

The highest KHAT values and therefore highest mapping accuracies were achieved with HyMap imagery. To assess whether the differences in mapping accuracies between sensors were statistically significant, the KHAT values and variances were used to calculate standard pairwise Z-statistics (Congalton, 1998). Six pairwise Z-statistics were calculated, HyMap-Hyperion, HyMap-CASI and Hyperion-CASI for each salinity symptom. For pairwise comparisons, Z-statistic values of less than 1.96 indicate that the error matrices are not significantly different. The Z-statistics value were less than 1.96 for all of the pairwise comparisons, indicating that the samphire and saltpan distributions maped by MyMap, Hyperion and CASI were effectively equivalent (Table 8-3). However at this time, HyMap has the greatest potential for mapping a wider

variety of salinity symptoms because of the combination of good SNR and comprehensive wavelength range that incorporates the visible, NIR and SWIR regions.

Table 8-3 Pairwise Z-statistic comparison of HyMap, CASI and Hyperion imagery.

Pairwise comparison	Z-statistic (samphire maps)	Z-statistic (saltpan maps)
HyMap-Hyperion	0.79	1.54
HyMap-CASI	0.98	0.56
Hyperion-CASI	0.18	1.00

8.1.7 Optimum processing procedure for vegetation and soil symptoms of salinity

On the basis of the findings of this research, the optimal sensors for mapping both soil and vegetation salinity symptoms are airborne sensors with high spatial and spectral resolutions that incorporate the 450 to 1450 nm wavelength range. For vegetation mapping, the optimal image processing flow (Figure 8-1a) utilised reference spectra extracted from known ‘pure’ areas on the ground. The soil mapping flow (Figure 8-1b) optimised processing efficiency by using a single reference spectrum and matched filtering to reduce the amount of multiple swath processing.

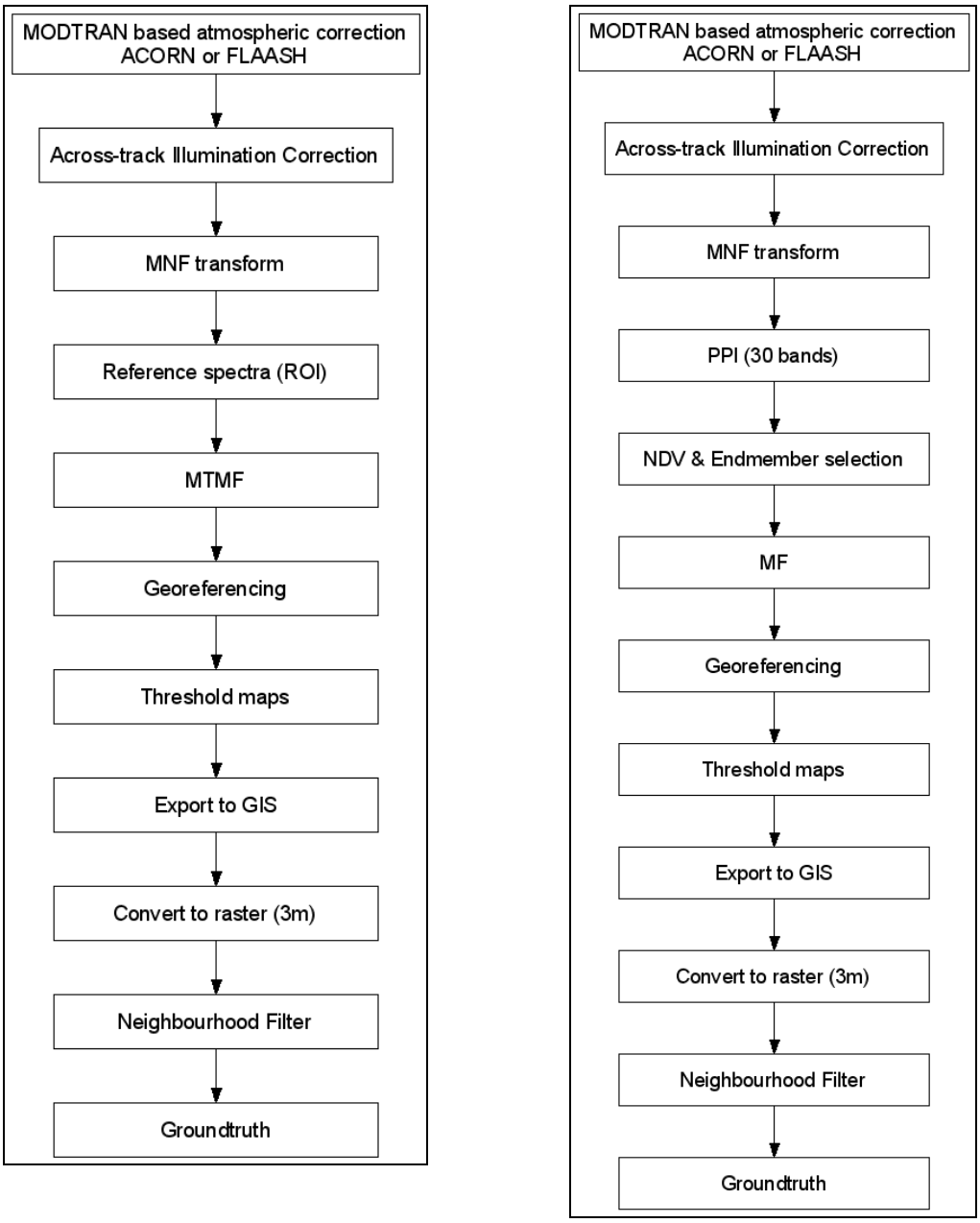

Figure 8-1 Comparing the optimum processing flow for mapping vegetation (a) and soil (b) symptoms of dryland salinity.

8.2 Limitations

The poor performance of vegetation mapping with CASI and Hyperion data may be attributed to the need to include SWIR regions as identified in the spectral discrimination analysis and HyMap samphire mapping. For CASI imagery, another contributing factor was the limited wavelength range available for atmospheric corrections that resulted in over corrected data in the 940 nm region. When commissioning the CASI surveys, the optimum wavelength range should encompass both sides of the 940 nm water absorption feature from 870-1000 nm. An improved wavelength range may result in less noise and no over-correction of image spectra in

this region. For Hyperion data, the most significant contributing factor to poor mapping performance was the noise inherent in the data.

The most accurate maps were produced for symptoms of higher levels of salinity, although, there is potential for mapping areas that exhibit lower salinity levels where halophytic grasses dominate. However in these more marginal saline areas, the mapping of halophytic grasses appeared less accurate, which may be because discrimination and mapping was based on subtle spectral differences related to phenological changes. In addition, grazing by livestock limited the ability to discriminate salt-tolerant pasture grasses at certain time of the year, a factor that may hinder hyperspectral mapping in other grazing regions.

8.3 Significance of findings

This study assessed different forms of hyperspectral data and image analysis techniques for mapping salinity in a dryland agricultural region in South Australia. The Point Sturt area contained soil and vegetation symptoms of different levels of salinity that were spectrally and spatially appropriate for mapping with hyperspectral imagery. Sea barley grass *(Critesion marinum)*, samphire *(Halosarcia pergranulata)* and saltpans were indicators of moderate, high and extreme levels of salinity respectively.

8.3.1 Optimal time of year for mapping salinity

An important aspect of this research was identification of the optimal time of year to map salinity symptoms through field observations and spectral discrimination of field and laboratory spectra. The dry season is the optimal time of year to map saltpans and perennial vegetation, including perennial halophytes such as samphire, because a contrasting background of dry annual grasses surrounds these symptoms. At this time, samphire spectra maintain distinguishing spectral properties related to photosynthetic characteristics and arid adaptations. At this time of year, extremely saline soils can also be mapped by extracting spectral features unencumbered by the adverse effects of soil moisture (Lobell and Asner, 2002). Isolating spectral features pertaining to saline mineralogy allows for the discrimination of exposed saline soils from non-saline exposed soils.

A key finding was determination of optimum time of year to map sea barley grass, an important vegetation indicator of emerging salinity and established moderately saline land. At Point Sturt, sea barley grass appeared greener than other grasses toward the end

of senescence because it occupies the low-lying, wetter soils. Therefore, late senescence is the optimum growth stage to exploit spectral differences between the varying rates of senescence between sea barley grass and other annual species because sea barley grass differed significantly from other annual species across broad wavelength ranges in the visible, NIR and SWIR.

8.3.2 Image analysis and multiple swath mapping

Both soil and vegetation salinity symptom maps were mapped across multiple airborne image swaths using readily available software. Standard hyperspectral processing methods for HyMap included MODTRAN based atmospheric correction, polynomial correction of across track illumination effects and fine-tuning georegistration to GPS locations. For CASI pre-georegistered swaths, variations in across track brightness were accounted for by removing strongly affected MNF bands although this method proved less successful. A standard processing flow was devised for each type of hyperspectral data.

8.3.3 Comparison of different sensors

HyMap image analysis produced the most accurate samphire and saltpan maps (highest KHAT values) compared to CASI and Hyperion imagery. Although Z-statistics showed that HyMap, Hyperion and CASI imagery produce equivalent samphire and saltpan maps, at this time, HyMap has the greatest potential for mapping a wider variety of salinity symptoms because of the combination of low noise and comprehensive wavelength range that incorporates the VISNIR and SWIR regions. CASI data is restricted to the VISNIR and Hyperion data has poor SNR beyond 1000 nm and into the SWIR. In fact, few SWIR features were evident in the Hyperion data, even after preprocessing to reduce noise. The Hyperion saltpan maps had the lowest KHAT value of less than 0.4 which indicates a poor agreement to field data. CASI and Hyperion saltpan maps also showed a moderate agreement with field data but poorer accuracies for samphire maps. These results suggest that samphire mapping requires all three visible, NIR and SWIR wavelength regions because the SWIR region contains important spectral properties related to halophytic adaptations (Elvidge, 1990; Lewis, 2002).

The same conclusion may also be inferred from the results of mapping sea barley grass with CASI imagery. Zonal statistics indicated that CASI image analysis mainly mapped

senescing sea barley grass in soil landscape units assigned moderate to high levels of salinity, although, a comparatively higher proportion of sea barley grass was mapped in the non-saline classes. The presence of these three waveband regions allows for discrimination of not only saline soils but also saline land with a good cover of samphire vegetation. In the case of the Hyperion imagery, the coarse spatial resolution is a contributing factor to the lower mapping accuracies.

8.3.4 Mapping saline areas with vegetation cover

Mapping saline areas with a good cover of saline vegetation has been problematic for multispectral imagery because of the inability to discriminate salt-tolerant vegetation from other vegetation (Furby 1995; Howari, 2003). HyMap successfully mapped highly saline areas supporting dense samphire vegetation at Point Sturt because of the image's high spatial and spectral resolution, without the use of multitemporal imagery or ancillary data such as topography or PIRSA soil attribute maps (Clarke, 2000; Thomas, 2001). The difficulty of mapping areas with vegetation cover is also evident in the visual comparison within GIS software of the HyMap salinity symptom maps to the NLWRA Salinity 2000 maps. The aerial photography and Landsat based salinity maps were unable to delineate extensive areas with samphire cover.

The CASI sea barley grass maps provided a less conclusive result regarding mapping moderately affected saline areas, although, the optimal time to map sea barley grass was found to be late November, when annual plant senesce. Results of this research suggest that mapping sea barley grass can be improved by using hyperspectral imagery that incorporates the visible, NIR and most importantly, the SWIR.

8.3.5 Improvements on conventional salinity mapping

The HyMap exposed saline soils maps were comparable to the NLWRA polygon based Salinity 2000 map and the Landsat based *severely saline areas*. However, this study has illustrated the advantage of the hyperspectral image analysis over these traditional soil maps. The HyMap salinity maps not only improved mapping of saline areas covered with samphire but also provided salinity maps that varied spatially within the Salinity 2000 and the PIRSA soil landscape unit polygons. Like multispectral satellite imagery, hyperspectral imagery maps have the advantage of using raster format and are therefore able to depict spatial variations in salinity on a pixel-by-pixel basis rather than as a homogenous mapping unit that changes in attributes across a discrete boundary. The 3

m ground resolution of the airborne hyperspectral data also has the advantage of providing salinity maps suitable for use at a farm or paddock scale. Therefore, hyperspectral maps provides a more detailed, realistic record of the occurrence of highly salt affected land.

8.4 Implications of hyperspectral salinity mapping

Hyperspectral imagery has the spectral and spatial resolution capable of mapping a wider range of salinity symptoms including soils with saline mineralogy other than gypsum, crop stress and different species of halophytic vegetation. Further studies need to evaluate hyperspectral imagery for mapping a wider range of salinity symptoms over different salt affected landscapes. However, the most vital extension to this research would be evaluation of hyperspectral imagery spanning the 450-2500 nm wavelength range for mapping later senescing halophytic grasses. Even with imagery containing this expanded spectral range, the timing of image acquisition would still be important for optimising discrimination, in terms of maximising differences in rates of senescence. The ability to map sea barley grass would provide improved mapping of emerging salinity and moderately salt affected areas. Future research could also involve data integration to improve the accuracy of salinity maps, in particular integration with high-resolution terrain models to limit salinity mapping to depressions and lowlying areas.

This study has demonstrated that readily available software and image analysis techniques are capable of mapping indicators of varying levels of salinity. With the ability to map symptoms across multiple image strips, hyperspectral imagery has the potential for mapping larger areas covering sizeable dryland agriculture catchments, closer in extent to single satellite images. For farm scale mapping, hyperspectral airborne imagery is superior to aerial photography and multispectral satellite imagery for mapping the spatial variability of salinity within soil units, particularly in previously difficult to map areas with a high cover of vegetation. With the ability to produce maps across multiple airborne swaths, unmixing of high spatial and high spectral resolution imagery has a significant advantage of fine scale mapping over smaller catchments. Catchment managers could employ image analyst experts to directly apply hyperspectral imagery to baseline salinity mapping and monitoring.

Hyperspectral salinity maps are capable of enhancing currently available soil maps. The samphire and saltpan maps would provide suitable raster based input data to the more

recent digital soil mapping approaches that are using raster data to improve soil mapping. The ability to map the spatial variability of salinity, in particular emerging saline areas and moderately affected areas with a good cover of vegetation would provide valuable data for digital soil modellers attempting to improve the resolution of soil mapping units.

Even though airborne hyperspectral imagery and available processing methods are sufficient for broader scale salinity mapping, uptake of airborne technology may continue to be hindered by two factors identified by Spies and Woodgate (2004) including the perceived high cost of airborne image acquisition and the requirement for specialist in image interpretation. Indeed, uptake of hyperspectral salinity mapping is constrained by the need for 1) groundbased knowledge regarding potentially mappable salinity symptoms 2) expert knowledge of spectral properties of soil and plants to determine the scope for spectral mapping 3) high level hyperspectral image processing skills and 4) the cost of airborne surveys. Perhaps at this time, catchment managers may be most likely to commission airborne hyperspectral salinity mapping for targeted high value agricultural areas.

With the advent of hyperspectral satellite-borne sensors, hyperspectral salinity mapping may provide an improved cost effective method for mapping and monitoring dryland salinity at regional or catchment scales. Because satellite imagery covers larger areas and has the advantage of regularly passing over the same area, hyperspectral satellites are best suited to monitoring salinity over medium sized catchments. If future high spectral resolution satellites have significantly improved SNR performance over Hyperion, then the salinity mapping has enormous potential. The European based EnMAP satellite equipped with the Hyper-spectral Imaging (HSI) system is currently proposed for launch in 2009 and 2012 (Stuffler *et al*, 2004). Future hyperspectral satellite scanners would be suited to partial unmixing and mapping of important salinity symptoms with distinguishing features in the SWIR, such as soils and vegetation with scleromorphic characteristics and symptoms that cover homogenous zones encompassing several image ground resolution elements. Hyperspectral satellite sensors would therefore be ideal imagery broad-scale salinity mapping and monitoring.

9 REFERENCES

Asner, G.P. and Heidebrecht, K.B., 2003. Imaging Spectroscopy for desertification Studies: Comparing AVIRIS and EO-1 Hyperion in Argentina Drylands. *IEEE Transactions on Geoscience and Remote Sensing*, 41: 1283-1296.

Barnett, S., 2000. *National Land and Water Resources Audit: Extent and Impacts of Dryland Salinity in South Australia*. PIRSA Report Book 2000/00045, National Land and Water Resources Unit, Adelaide.

Barrett-Lennard, E.G., 2003. *Saltland Pastures in Australia: A Practical Guide*. Land, Water and Wool Sustainable Grazing on Saline Lands Sub-program, Western Australia.

Baumgardner, M.F., Silva, L.F., Biehl, L.L. and Stoner, E.R., 1985. Reflectance properties of soil. *Advances in agronomy*, 38: 1-44.

Ben-Dor, E., 2002. Quantitative remote sensing of soil properties, *Advances in Agronomy*. Academic Press, pp. 173-243.

Ben-Dor, E. and Banin, A., 1994. Visible and near-infrared (0.4-1.1 μm) analysis of arid and semiarid soils. *Remote Sensing of Environment*, 48: 261-274.

Ben-Dor, E., Inbar, Y. and Chen, Y., 1997. The reflectance spectra of organic matter in the visible near-infrared and short wave infrared region (400-2500 nm) during a controlled decomposition process. *Remote Sensing of Environment*, 61: 1-15.

Ben-Dor, E., Irons, J.R. and Epema, G.F. (Editors), 1999. Soil Reflectance (Chapter 3). In *Manual of Remote Sensing*, 3. John Wiley and Sons in association with the American Society for Photogrammetry and Remote Sensing, New York.

Ben-Dor, E., Levin, N., Singer, A., Karnieli, A., Braun, O. and Kidron, G.J., In Press. Quantitative mapping of the soil rubification process on sand dunes using an airborne hyperspectral sensor. *Geoderma*, In Press.

Better Solutions Consulting, 1999. *ENVI User's Guide, the Environment for Visualizing Images, Version 3.2*. Research Systems, Inc., and Better Solutions Consulting, 1997.

Bhargava, R., Ribar, T. and Koenig, J.L., 1999. Towards Faster FT-IR Imaging by Reducing Noise. *Applied Spectroscopy*, 53: 1313-1322.

Blackburn, G.A. and Milton, E.J., 1997. An ecological survey of deciduous woodlands using airborne remote sensing and geographical information systems (GIS), *International Journal of Remote Sensing*, 18: 1919-1935.

Boardman, J.W., 1998. Leveraging the High Dimensionality of AVIRIS Data for Improved Sub – Pixel Target Unmixing and Rejection of False Positives: Mixture Tuned Matched Filtering. In *Summaries of the Ninth Annual JPL Airborne Earth Science Workshop*, Pasadena, CA.

Boardman, J.W., Kruse, F.A. and Green, R.O., 1995. Mapping target signatures via partial unmixing of AVIRIS data. In *Summaries, Fifth JPL Airborne Earth Science Workshop*, Pasadena, CA, 1: 23-26.

Caccetta, P.A., Allen, A. and Watson, I., 2000. The Land Monitor Project. In *Proceedings 10th Australasian Remote Sensing and Photogrammetry Conference*, 21-25 August 2000, Adelaide Australia, 10th Australasian Remote Sensing and Photogrammetry Conference Proceedings.

Campbell, J.B., 1996. *Introduction to Remote Sensing*. Taylor & Francis Ltd., London.

Carter, G.A. and Miller, R.L., 1994. Early detection of plant stress by digital imaging within narrow stress-sensitive wavebands. *Remote Sensing of Environment*, 50: 295-302.

Cetin, H., 2004. Comparison of spaceborne and airborne hyperspectral imaging systems for environmental mapping. In *Proceedings of XXth ISPRS Congress*, 12-23 July 2004, Istanbul, Turkey.

Chabrillat, S., Pinet, P.C. and Ceuleneer, G., 2000. Ronda peridotite massif: methodology for its geological mapping and lithological discrimination from airbourne hyperspectral data. *International Journal of Remote Sensing*, 21: 2363-2388.

Chabrillat, S., Goetz, A.F.H., Krosley, L. and Olsen, H.W., 2002. Use of hyperspectal images in the identification and mapping of expansive clay soils and the role of spatial resolution. *Remote Sensing of Environment*, 82: 431-445.

Chaturvedi, L., Carver, K.R., Harlan, J.C., Hancock, G.D., Small, F.V. and Dalstead, K.J., 1983. Multispectral remote sensing of saline seeps. *IEEE Transactions on Geoscience and Remote Sensing*, GE-21: 239-251.

Chen, Z., Elvidge, C.D. and Goenveld, D.P., 1998. Monitoring seasonal dynamics of arid land vegetation using AVIRIS data. *Remote Sensing of Environment*, 65: 255-266.

Chewings, V.H., Bastin, G.N., Crawford, M.M. and Kinloch, J.E., 2002. Characterisation of vegetation components in the Australian arid zone using EO-1 Hyperion imagery. In *Proceedings 11th Australasian Remote Sensing and Photogrammetry Conference*, 2-6 September, 2002, Brisbane, Australia.

Chewings, V.H., Pickup, G., Bastin, G.N. and Pearce, G., 2000. The Potential For Hyperspectral Data Mapping In Australian Arid-Zone Vegetation. *Proceedings 10th Australasian Remote Sensing and Photogrammetry Conference*, 21-25 August 2000, Adelaide, Australia.

Chhabra, R., 1996. *Soil salinity and water quality*. A. A. Balkema Publishers, Brookfield, VT, USA.

Chisholm, L., 2001. *Characterisation and evaluation of moisture stress in E. camaldulensis using hyperspectral remote sensing*, PhD Thesis, University of New South Wales, Sydney, Australia.

Clark, C.D., Ripley, H.T., Green, E.P., Edwards, A.J. and Mumby, P.J., 1997. Mapping and measurement of tropical coastal environments with hyperspectral and high spatial resolution data. *International Journal of Remote Sensing*, 18: 237-242.

Clarke, K.D., 2000. *The Utility of Multi Temporal Landsat 7 ETM+ imagery and digital Topographic Information for Detection of Dryland Salinity*. Honours Thesis, University of Adelaide, Adelaide, South Australia.

Cochrane, M.A., 2000. Using vegetation reflectance variability for species level classification of hyperspectral data. *International Journal of Remote Sensing*, 21: 2075-2087.

Cocks, T., Jenssen, R., Stewart, A., Wilson, I. and Shields, T., 1998. The HyMap^{TM} airborne hyperspectral sensor: The system, calibration and performance. Integrated Spectronics Pty Ltd, CSIRO Manufacturing Science and Technology.

Congalton, R.G., 1991. A Review of Assessing the Accuracy of Classifications of Remotely Sensed Data. *Remote Sensing of the Environment*, 37: 35-46.

Coram, J.E., Dyson, P.E., Houlder, P.A. and Evans, W.R., 2000. Australian Groundwater Flow Systems contributing to Dryalnd Salinity, A Bureau of Rural Sciences Project for the National Land and Water Resources Audit's Dryalnd Salinity Theme.

Crowley, J.K., 1993. Mapping playa evaporite minerals with AVIRIS data: a first report from Death Valley. *Remote Sensing of Environment*, 44: 337-356.

Crowley, J.K., Hubbard, B.E. and Mars, J.C., 2003. Analysis of potential debris flow source areas on Mount Shasta, California, by using airborne and satellite remote sensing data. *Remote Sensing of Environment*, 87: 345-358.

Csillag, F., Pastor, L. and Beihl, L.L., 1993. Spectral band selection of the characterisation of salinity status in soils. *Remote Sensing of Environment*, 43: 231-242.

Cudahy, T.J., Hewson, R., Huntington, J.F., Quigley, M.A. and Barry, P.S., 2001. The Performance of the Satellite-borne Hyperion Hyperspectral VNIR-SWIR Imaging System for Mineral Mapping at Mount Fitton, South Australia. In *Proceedings of International Geoscience and Remote Sensing Symposium (IGARSS)*, 9-13 July, 2001, Sydney, Australia.

Dehaan, R. and Taylor, G.R., 2002A. Image-derived spectral endmemders as indicators of salinisation. *International Journal of Remote Sensing*, 24: 775-794.

Dehaan, R.L. and Taylor, G.R., 2002B. Field-derived spectra of salinized soils and vegetation as indicators of irrigation-induced soil salinization. *Remote Sensing of Environment*, 80: 406-417.

Dekker, A.G. and Bukata, R.P., 2002. Remote Sensing of Inland and Coastal Waters (Chapter 23), In *Review of Radio Science,* Ross Stone (Book Editor), 1999-2002, IEEE Press, W. Piscataway, N.J., USA, pp. 519-534.

Department of Primary Industries, 2004. Salinity Indicator Plants. A guide to spotting soil salting. Department of Primary Industries, Victoria, Australia. Available at URL{http://www.dpi.vic.gov.au/dpi/vro/vrosite.nsf/pages/water_spotting_soil_salting}

Dooley, T. and Henschke, C., 1999. *Salinity Management within the Goolwa to Wellington LAP area*, PIRSA Rural Solutions.

Drake, N.A., 1995. Reflectance spectra of evaporite minerals (400-2500 nm): applications for remote sensing. *International Journal of Remote Sensing*, 16: 2555-2571.

Eckert, S. and Kneubuhler, M., 2001. Application of Hyperion data to agricultural land classification and vegetation properties estimation in Switzerland. *Proceedings of XXth ISPRS Congress*, 12-23 July 2004, Istanbul, Turkey.

Elvidge, C.D., 1990. Visible and near infrared reflectance characteristics of dry plant materials. *International Journal of Remote Sensing*, 11: 1775-1795.

Evans, F.H. and Caccetta, P.A., 2000. Salinity risk prediction using Landsat TM and DEM-derived data. In *Proceedings 10th Australasian Remote Sensing and Photogrammetry Conference*, 21-25 August 2000, Adelaide, South Australia.

Evans, F.H., Caccetta, P.A. and Ferdowsian, R., 1996. Integrating remotely sensed data with other spatial data sets to predict areas at risk from salinity. In *Proceedings 8th Australasian Remote Sensing Conference*, Canberra, Australia.

Faull, J. (Editor), 1981. *Alexandrina's Shore: a History of the Milang District*. Milang and District Historical Society, Adelaide, S.A.

Ferdowsian, R., 1994. *"Aerial Photographs for identifying saline discharges" in Remote Sensing Methods for identification of Dryland Salinity: Report on a Workshop, Albany, Western Australia*, Land and Water Resources Research and Development Corporation, Murray Darling Basin Commission, Department of Primary Industries and Energy and the States, Canberra.

Fernandes, R.A., Miller, J.R., Chen, J.M. and Rubinstein, I.G., 2004. Evaluating image-based estimates of leaf area index in boreal conifer stands over a range of scales using high-resolution CASI imagery. *Remote Sensing of Environment*, 89: 200-216.

Fitzpatrick, R.W., Merry, R.H., Cox, W., Rengasamy, P. and Davies, P.J., 2003. *Assessment of physio-chemical changes in dryland saline soils when drained or disturbed for developing management options. Technical Report 2/03*. Technical Report 2/03, CSIRO Land and Water and the National Dryalnd Salinity Program, Adelaide, South Australia.

Fraser, D. and Joseph, S., 1998. Mapping Soil Salinity In The Murray Valley (NSW) Using Satellite Imagery. *Proceedings 9th Australasian Remote Sensing and Photogrammetry Conference*, Volume 1, page (NA), paper no. 127.

Furby, S.L., Wallace, J.F., Caccetta, P. and Wheaton, G.A., 1995. *Detecting and monitoring salt-affected land: A report from the LWRRDC project detecting and monitoring changes in land condition through time using remotely sensed data*, Remote Sensing and Image Integration Group, CSIRO Division of Mathematics & Statistics, Perth, Western Australia. Availiable at URL {http://www.cmis.csiro.au/rsm/research/salmapmon/salmapmon_full.htm}

Furby, S.L., Flavel, R., Sherrah, M. and McFarlane, J., 1998. *Mapping Salinity in the Upper South East Catchment in South Australia: A report from the LWWRDC project Mapping Dryland Salinity (CDM2)*, Remote Sensing and Image Integration Group, CSIRO Mathematical and Information Sciences, Western Australia.

Gamon, J.A., Field, C.B., Roberts, D.A., Ustin, S.L. and Valentini, R., 1993. Functional patterns in an annual grassland during an AVIRIS overflight. *Remote Sensing of Environment*, 44: 239-253.

Gao, B and Goetz, A.F.H., 1990. Colum Atmospheric Water Vapor and Vegetation Liquid Water Retrievals from Airborne Imaging Spectrometer Data. *Journal of Geophysical Research*, 95: 3549-3564.

Gates, D.M., Keegan, H.J., Schelter, J.C. and Weidner, V.R., 1965. Spectral properties of plants. *Applied Optics*, 4: 11-20.

Gausman, H.W. and Allen, W.A., 1973. Optical parameters of leaves of 30 plant species. *Plant Physiology*, 52: 57-62.

George, R.J., Beasley, R., Gordon, I., Heislers, D., Speed, R., Brodie, R., McConnell, C. and Woodgate, P.W., 1998. *The National Airborne Geophysics Project National Report: Evaluation of airborne geophysics for catchment management*, Agriculture, Fisheries and Forestry Australia and The National Dryland Salinity Program, Australia, {http://www.lwa.gov.au/ndsp/orphan.asp?section=100}.

Ghassemi, F., Jakeman, A.J. and Nix, H.A., 1995. *Salinisation of Land and Water Resources: Human causes, extent, management and case studies*. University of NSW Press Ltd, Canberra.

Goetz, A.F.H., Kindel, B.C., Ferri, M. and Qu, Z., 2003. HATCH: Results from Simulated Radiances, AVIRIS and Hyperion. *IEEE Transactions on Geoscience and Remote Sensing*, 42: 1215-1222.

Goetz, A.F.H., Vane, G., Solomon, J.E. and Rock, B.N., 1985. Imaging spectrometry for earth remote sensing. *Science*, 228: 1147-1153.

Green, A.A., Berman, M., Switzer, P. and Craig, M.D., 1988. "A transformation for ordering multispectral data in terms of image quality with implications for noise removal. *IEEE Transactions on Geoscience and Remote Sensing*, 26: 65-74.

Green, E.P., Clark, C.D., Mumby, P.J., Edwards, A.J. and Ellis, A.C., 1998. Remote sensing techniques for mangrove mapping, *International Journal of Remote Sensing*, pp. 935-956.

Gunn, R.H., Beattie, J.A., Reid, R.E. and van der Graaff, R.H.M. (Editors), 1988. *Australian Soil and Land Survey Handbook: Guidelines for Conducting Surveys*. Inkata Press, Melbourne and Sydney, Australia.

Haboudane, D., Miller, J.R., Pattey, E., Zarco-Tejada, P.J. and Strachan, I.B., 2004. Hyperspectral vegetation indices and novel algorithms for predicting green LAI of crop canopies: Modeling and validation in the context of precision agriculture. *Remote Sensing of Environment*, 90: 337-352.

Harsanyi, J.C. and Chang, C.I., 1994. Hyperspectral image classification and dimensionality reduction: An orthogonal subspace projection approach. *IEEE Transactions on Geoscience and Remote Sensing*, 32: 779-785.

Henschke, C., 2000. *In "Point Sturt and Districts Landcare Group, Natural Heritage Trust Point Sturt and Districts Natural Resource Strategy. 1999 Project Officer's Report", Michalski, C.,*, Natural Heritage Trust funding for the Point Sturt and Districts Landcare Group, South Australia.

Herzeg, A.L., Dogramaci, S.S. and Leaney, F.W.J., 2001. Origin of dissolved salts in a large, semi-arid groundwater system: Murray Basin, Australia. Marine and Freshwater Research, 52(1): 41-52.

Hick, P.T. and Russell, W.G.R., 1988. *Remote sensing of agricultural salinity*, WA Remote Sensing Group, CSIRO Division of Exploration Geoscience, Western Australia.

Hick, P.T. and Russell, W.G.R., 1990. Some spectral considerations for remote sensing of soil salinity. *Australian Journal of Soil Research*, 28: 417-431.

Howari, F.M., 2003. The use of remote sensing data to extract information from agricultural land with emphasis on soil salinity. *Australian Journal of Soil Research*, 41: 1243-1253.

Hunt, G. R., J. W. Salisbury, *et al*. (1972). "Visible Rocks and Near-Infrared Spectra of Minerals and Rocks: V. Halides, Phosphates, Arsenates, Vanadates and Borates." *Modern Geology* 3: 121-132.

Isbell, R.F., Reeve, R. and Hutton, J.T., 1983. Salt and sodicity (Chapter 9), In *Soils: an Australian Viewpoint*. CSIRO Division of Soils, CSIRO, Melbourne, Autralia, pp. 107-117.

Jacobsen, A., 2000. *Analysing airborne optical remote sensing data from a hyperspectral scanner and implications for environmental mapping and monitoring—results from a case study of casi data and Danish semi natural, dry grasslands*. PhD thesis, University of Copenhagen, Copenhagen, Denmark.

ImSpec LLC, 2002. *ACORN 4.0 Users Guide*, Boulder, Colorado, USA.

Jensen, J.R., 2000. *Remote sensing of the environment: An earth resource perspective*. *Prentice-Hall Series in Geographic Information Science*. Prentice Hall, Upper Saddle River, N. J., USA.

Jupp, D.L.B. and Datt, B., 2004. *CSIRO Earth Observation Centre, CSIRO Atmospheric Research, Evaluation of the EO-1 Hyperion Hyperspectral Instrument & its Applications at Australian Validation Sites 2001-2003*, CSIRO Earth Observation Centre, Canberra, ACT, Australia.

Jupp, D.L.B., Datt, B., Lovell, J., Campbell, S., King, E. and others, Science Validation Team and others, 2002. *Discussions around Hyperion Data: Background Notes for the Hyperion Data Users Workshop*, CSIRO, Canberra, Australia.

Kiiveri, H.T. and Caccetta, P.A., 1998. Mapping salinity using decision trees and conditional probability networks. *Digital Signal Processing*, 8: 225-230.

Kirkby, S.D., Longmore, M.E. and Maslen, M.A., 1992. The integrated use of SPOT 1 imagery and geographic information systems to quantify spatial changes in saline discharge areas. In *Proceedings 6th Australasian Remote Sensing Conference*, Wellington, New Zealand, 2: 384-390.

Knipling, E.B., 1970. Physical and physiological basis for the reflectance of visible and near-infrared radiation from vegetation. *Remote Sensing of Environment*, 1: 155-159.

Kruse, F.A., 1998. Advances in Hyperspectral Remote Sensing for Geologic Mapping and Exploration. In *Proceedings 9th Australasian Remote Sensing and Photogrammetry Conference*, 20-24 July 1998, Sydney, Australia.

Kruse, F.A., 2004. Comparison of ATREM, ACORN, and FLAASH Atmospheric Corrections using Low-Altitude AVIRIS Data of Boulder, Colorado. In *Proceedings 13th JPL Airborne Geoscience Workshop, Jet Propulsion Laboratory*, 31 March – 2 April 2004, Pasadena, CA, USA.

Kruse, F.A. and Boardman, J.W., 2002. Evaluation and validation of EO-1 Hyperion for geological mapping. In *Proceedings of International Geoscience and Remote Sensing Symposium (IGARSS)*, 24-28 June, 2002, Toronto, Canada.

Kruse, F.A., Boardman, J.W. and Huntington, J.F., 1999. Fifteen Years of Hyperspectral Data: northern Grapevine Mountains, Nevada. In *Proceedings of the 8th JPL Airborne Earth Science Workshop*, Feb 8-11, Pasadena, CA, 99-17: 247 - 258.

Larcher, W., 1980. *Physiological plant ecology*. Springer Verlag, Berlin - Heidelberg, Germany.

Leckie, D.G., Gougeon, F.A., Tinis, S., Nelson, T., Burnett, C.N. and Paradine, D., 2005. Automated tree recognition in old growth conifer stands with high resolution digital imagery. *Remote Sensing of Environment*, 94: 311-326.

Lee, J.B., Woodyatt, A.S. and Berman, M., 1990. Enhancement of high spectral resolution remote-sensing data by a noise-adjusted principal components transform. *IEEE Transactions on Geoscience and Remote Sensing*, 28: 295-304.

Lewis, M., 2001. Discriminating vegetation with hyperspectral imagery - what is possible? *IEEE 2001 International Geoscience and Remote Sensing Symposium (IGARSS)*, University of NSW, Sydney, Australia.

Lewis, M., 2002. Spectral characterisation of Australian arid zone plants. *Canadian Journal Of Remote Sensing*, 28: 1-12.

Lewis, M. and Jooste, V., 1999. *Identification of vegetation signatures in AMS imagery.*, Unpublished report to the Anglo American Corporation.

Lewis, M.M., Jooste, V. and deGasparis, A.A., 2000. Discrimination of arid vegetation with hyperspectral imagery. In *Proceedings 10th Australasian Remote Sensing and Photogrammetry Conference*, 21-25 August 2000, Adelaide, Australia.

Lobell, D.B. and Asner, G.P., 2002. Moisture Effects on Soil Reflectance. *Soil Sci Soc Am J*, 66: 722-1034.

Maschmedt, D., 2000. *Assessing Agricultural Land: Agricultural land classification standards used in South Australia's land resource mapping program*, PIRSA, Adelaide, SA.

Maschmedt, D., 2001. *Analysing and Mapping Soil and Landscape Attribute Data*, PIRSA Land Information, South Australia.

Mason, P., 2002. *MMTG A-List Hyperspectral Data Processing Software*. 920C, CSIRO, Division of Exploration and Mining, Sydney, Australia.

McGwire, K., Minor, T. and Fenstermaker, L., 2000. Hyperspectral Mixture Modeling for Quantifying Sparse Vegetation Cover in Arid Environments. *Remote Sensing of Environment*, 72: 360-374.

Metternicht, G. and Gonzalez, S., 2000. Integrated remote sensing and fuzzy modelling for mapping and monitoring of salinity processes. In *Proceedings 10th Australasian Remote Sensing and Photogrammetry Conference*, 21-25 August 2000, Adelaide, South Australia.

Metternicht, G. and Zinck, J.A., 1997. Spatial discrimination of salt- and sodium affected soil surfaces. *International Journal of Remote Sensing*, 18: 2571-2586.

Metternicht, G. and Zinck, J.A., 2003. Remote sensing of soil salinity: potentials and constraints. *Remote Sensing of Environment*, 85: 1-20.

Michalski, C., 2000. *Point Sturt and Districts Landcare Group, Natural Heritage Trust Point Sturt and Districts Natural Resource Strategy. 1999 Project Officer's Report*, Natural Heritage Trust funding for the Point Sturt and Districts Landcare Group, South Australia.

Mougenot, B., Pouget, M. and Epema, G.F., 1993. Remote Sensing of Salt Affected Soils. *Remote Sensing Reviews*, 7: 241-259.

Mundt, J.T., Glenn, N.F., Weber, K.T., Prather, T.S., Lass, L.W. and Pettingill, J., 2005. Discrimination of hoary cress and determination of its detection limits via hyperspectral image processing and accuracy assessment techniques. *Remote Sensing of Environment*, 96: 509-517.

NDSP, 2000. National Dryland Salinity Program Phase I. National Dryland Salinity Program, {http://www.ndsp.gov.au/about.asp?section=7}.

Natural Resources and Mines, 2001. *Geophysical Manual: The Role of Geophysics in Understatnding Landscapes*. Queensland Government, Natural Resources and Mines, Australia

Palacios-Orueta, A. and Ustin, S.L., 1998. Remote Sensing of Soil Properties in the Santa Monica Mountains. *Remote Sensing of Environment*, 65: 170-183.

Pannel, D.J., 2001. Dryland Salinity: Economic, Scientific, Social and Policy Dimensions. *Australian Journal of Agriculture and Resource Economics*, 45: 1-22.

Pearlman, J., Carman, S., Segal, C., Jarecke, P. and Clancy, P., 2001. Overview of the Hyperion Imaging Spectrometer for the NASA EO-1 Mission. In *Proceedings of International Geoscience and Remote Sensing Symposium (IGARSS)*, 9 - 13 July 2001, Sydney, Australia.

PIMSEC, 1999. *Prime Ministers Science, Engineering and Innovation Council: Dryland Salinity and its impact on rural industries and the landscape: Occasional Paper Number 1*, Department of Industry, Science and Resources, Canberra, Australia.

PIRSA, 2001a. Soil Landscape Mapping (CD). Department of Primary Industries and Resources, South Australia.

PIRSA Land Information, 2001b. *Atlas of Key Soil and Landscape Attributes: Agricultural Districts of South Australia*. Department of Primary Industries and Resources, South Australia.

Post, D.F., Fimbres, A., Matthias, A.D., Sano, E.E., Accioly, L., Batchily, A.K. and Ferreira, L.G., 2000. Predicting Soil Albedo from Soil Color and Spectral Reflectance Data. *Soil Sci. Soc. Am. J.*, 64: 1027-1034.

Price, J.C., 1994. How unique are spectral signatures. *Remote Sensing of Environment*, 49: 181-186.

Quattrochi, D.A. and Goodchild, M.F., 1997. *Scale in Remote Sensing and GIS*. CRC Press LLC, Boca Raton, Florida.

Quigley, M.A., Mason, P. and Huntington, J., 2004. *Image Restoration and Atmospheric Correction of 'Hyperion' Hyperspectral EO-1 Satellite Data.* 1218F, CSIRO, Division of Exploration and Mining, Sydney, Australia.

Rao, B.R.M., Dwivedi, L., Venkataratnam, L., Ravishankar, T., Thammappa, L., Bhargawa, G.P. and Singh, A.N., 1991. Mapping the magnitude of sodicity in part of the Indo-Gangetic plains of Uttar Pradesh, Northern India using Landsat-TM data. *International Journal of Remote Sensing*, 12: 419-425.

Resmini, R.G., Kappus, M.E., Aldrich, W.S., Harsanyi, J.C. and Anderson, M., 1997. Mineral mapping with HYperspectral Digital Imagery Collection Experiment (HYDICE) sensor data at CUprite, Nevada, U.S.A. *International Journal of Remote Sensing*, 18.

Roberts, D.A., Smith, M.O. and Adams, J.B., 1993. Green vegetation, nonphotosynthetic vegetation and soils in AVIRIS data. *Remote Sensing of Environment*, 44: 255-269.

Ryan, S. and Lewis, M., 2001. Mapping soils using high resolution airborne imagery, Barossa Valley, SA. In *Proceedings of the Inaugural Australian Geospatial Information and Agriculture Conference Incorporating Precision Agriculture in Australasia 5th Annual Symposium*, 17-19 July 2001, Sydney, NSW: Paper 801, 12p.

Savitsky, A. and Golay, M.J.E., 1964. Smoothing and differentiation of data by simplified least squares procedures. *Analytical Chemistry*, 36: 1627-1639.

SCARM, 2000. *Management of dryland salinity: Future strategic directions in the context of developing a national policy for natural resource management*. Report No.78, The Standing Committee on Agriculture and Resource Management, Melbourne.

Schmidt, K.S. and Skidmore, A.K., 2001. Exploring spectral discrimination of grass species in African rangelands. *International Journal of Remote Sensing*, 22: 3421-3434.

Schmidt, K.S. and Skidmore, A.K., 2003. Spectral discrimination of vegetation types in a coastal wetland. *Remote Sensing of Environment*, 85: 92-108.

Silvestri, S., Marani, M., Settle, J., Benvenuto, F. and Marani, A., 2002. Salt marsh vegetation radiometry; Data analysis and scaling. *Remote Sensing of Environment*, 80: 473-482.

Skidmore, A.K., Varekamp, C., Wilson, L., Knowles, E. and Delaney, J., 1997. Remote sensing of soils in a eucalypt forest environment, *International Journal of Remote Sensing*, pp. 39-56.

Sommer, S., Hill, J. and Megier, J., 1998. The potential of remote sensing for monitoring rural land use changes and their effects on soil conditions. *Agriculture, Ecosystems and Environment*, 67: 197–209.

Spies, B. and Woodgate, P., 2004. *Technical Report: Salinity Mapping Methods in the Australian Context*, Prepared for the Programs Committee of the Natural Resource Management, Ministerial Council through Land and Water Australia and the National Dryland Salinity Program, Canberra, Australia.

Stuffler, T., Kaufmann, H., Hofer, S., Förster, K.P., R.Graue, Kampf, D., Mehl, H., Schreier, G., Mueller, A., Arnold, G., Bach, H., Benz, U., Jung-Rothenhäusler, F. and Haydn, R., 2005. The Advanced German Hyperspectral Mission EnMAP. *In Proceedings of 31st International Symposium on Remote Sensing of Environment*, Istanbul.

Sumner, M.E. (Editor), 2000. *Handbook of Soil Science*. CRC Press LLC, Boca Raton, Florida, USA.

Szabolcs, I., 1989. *Salt-affected soils*. CRC Press, Boca Raton, Florida, USA.

Taylor, G.R., Hempill, P., Currie, D., Broadfoot, T. and Dehaan, R. L., 2001. Mapping Dryland Salinity with Hyperspectral Imagery. *IEEE 2001 International Geoscience and Remote Sensing Symposium*, 9-14 July 2001, University of NSW, Sydney, Australia.

Thenkabail, P.S., Smith, R.B. and De Pauw, E., 2000. Hyperspectral Vegetation Indices and Their Relationships with Agricultural Crop Characteristics. *Remote Sensing of Environment*, 71: 158-182.

Thenkabail, P.S., Enclona, E.A., Ashton, M.S. and Van Der Meer, B., 2004. Accuracy assessments of hyperspectral waveband performance for vegetation analysis applications. *Remote Sensing of Environment*, 91: 354-376.

Thomas, M., 2001. *Remote Sensing in South Australia's Land Condition Monitoring Project*, Unpublished report, PIRSA Sustainable Resources, Land Information Group, Adelaide, Australia.

Thomson, A.G., Fuller, R.M. and Eastwood, J.A., 1998. Supervised versus unsupervised methods for classification of coasts and river corridors from airborne remote sensing. *International Journal of Remote Sensing*, 19: 3423-3431.

Thomson, A.G., Fuller, R.M., Yates, M.G., Brown, S.L., Cox, R. and Wadsworth, R.A., 2003. The use of airborne remote sensing for extensive mapping of intertidal sediments and saltmarshes in eastern England. *International Journal of Remote Sensing*, 24: 2717–2737.

Underwood, E., Ustin, S. and DiPietro, D., 2003. Mapping nonnative plants using hyperspectral imagery. *Remote Sensing of Environment*, 86: 150-161.

Ungar, S., 2002. Overview of The Earth Observing One (EO-1) Mission. In *Proceedings of International Geoscience and Remote Sensing Symposium (IGARSS)*, 24-28 June, 2002, Toronto, Canada.

van der Meer, F., 1998. Imaging spectrometry for geological remote sensing. *Geologie en Mijnbouw*, 77: 137-151.

van Gool, D. and Moore, G., 1998. *Land evaluation standards for land resource mapping. Guidelines for assessing land qualities and determining land capability in south-west Western Australia (2nd edition)*. Resource Management

Technical Report 181, Natural Resources Assessment Group, Agriculture Western Australia, Perth, Western Australia.

Van Niel, T., McVicar, T., Campbell, S., Liang, S., Kaul, M., Pearlman, J., Clancy, P. and Segal, C., 2001. The Coleambally agricultural component of Hyperion instrument validation. In *Proceedings of International Geoscience and Remote Sensing Symposium (IGARSS)*, Sydney, Australia.

Verma, K.S., Saxena, R.K., A.K., B. and Deshmukh, S.N., 1994. Remote sensing technique for mapping salt affected soils. *International Journal of Remote Sensing*, 15: 1901-1914.

Wang, D., Shannon, M.C. and Grieve, C.M., 2001. Salinity reduces radiation absorption and use efficiency in soybean. *Field Crops Research*, 69: 267-277.

Warren, J.K., 1982. The hydrological setting, occurrence and significance of gypsum in late Quaternary salt lakes in South Australia. *Sedimentology*, 29: 609-637.

Webb, A., 2000. *Australian Dryland Salinity Assessment 2000, Technical Report*, National Land and Water Resources Audit, Brookfield, Queensland, Australia.

Webb, A. and Price, R., 1994. *Remote Sensing Methods for identification of Dryland Salinity: Report on a Workshop, Albany, Western Australia*. Occasional Paper No 10/94, Land and Water Resources Research and Development Corporation, Murray Darling Basin Commission, Department of Primary Industries and Energy and the States, Canberra, Australia.

Wheaton, G.A., Wallace, J.F., McFarlane, D.J. and Campbell, N.A., 1992. Mapping salt-affected land in Western Australia. In *Proceedings 6th Australasian Remote Sensing Conference*, Wellington, New Zealand, 2: 369-377.

Whiting, M.L. and Ustin, S.L., 1999. Use of Low Altitude AVIRIS Data For Identifying Salt Affected Soil Surfaces in Western Fresno County, California. In *Proceedings of 8th JPL Airborne Visible Infrared Imaging Spectrometer (AVIRIS) Workshop,* Jet Propulsion Laboratory, California Institute of Technology, Pasadena, USA.

Williams, A.P. and Hunt Jr., E., R., 2002. Estimation of leafy spurge cover from hyperspectral imagery using mixture tuned matched filtering. *Remote Sensing of Environment*, 82: 446-456.

Yamano, H., Chen, J. and Tamura, M., 2003. Hyperspectral identification of grassland vegetation in Xilinhot, Inner Mongolia, China. *International Journal of Remote Sensing*, 24: 3171-3178.

Zarco-Tejada, P.J., Miller, J.R., Mohammed, G.H., Noland, T.L. and Sampson, P.H., 2000. Chlorophyll Fluorescence Effects on Vegetation Apparent Reflectance; II. Laboratory and Airborne Canopy-Level Measurements with Hyperspectral Data. *Remote Sensing of Environment*, 74: 596-608.

APPENDIX 1

"Bad Bands" removed before processing HyMap and Hyperion data

HyMap
446.6
1404.3
1418.7
1432.6
1803
1950.4
2470.39
2485.8

Hyperion
356.370
366.540
376.710
386.880
397.050
407.210
417.380
427.550
437.720
936.020
946.190
956.360
966.530
976.700
986.870
997.040
1007.200
1017.370
1027.540
1037.710
1047.880
1058.050
852.000
862.090
872.180
882.270
892.350
902.440
912.530
922.620
2365.240
2375.340
2385.430
2395.530
2405.630
2415.730
2425.830
2435.930
2446.020
2456.120
2466.120
2476.220
2486.320
2496.420

2506.510
2516.610
2526.710
2536.810
2546.910
2557.010
2567.000
2577.100
2577.100

APPENDIX 2

Atmospheric correction parameters

ACORN input parameters for one HyMap swath

Image format
1
Integer format
0
Bands, Samples, Lines, Offset
126 512 5306 0
latitude
-35.51082
longitude
138.9455
Day, Month, Year
14 3 2002
Day of year
73
Hour, minute, second
6.000000 12.00000 3.000000
Decimal hour
6.200833
Elevation
1.86E-03
Altitude
1.418
Model
1
Derive water vapor
3
Include path in water fit
0
Visibility
100
Estimate visibility
1
Artifact suppression
1 1 0

ACORN gain and offset values

Wavelength	FWHM	Offset	Gain
446.6	11.6	0	0.01
455.5	15.5	0	0.01
469.8	18.6	0	0.01
485.8	17.5	0	0.01
500.3	17.2	0	0.01
515.4	17.7	0	0.01
531.3	17.4	0	0.01
546.8	17.5	0	0.01
561.9	16.7	0	0.01
576.9	17	0	0.01
592.1	16.6	0	0.01
607.5	17.5	0	0.01
623.2	16.8	0	0.01
638.4	16.7	0	0.01
653.4	16.2	0	0.01
668.4	16.4	0	0.01
683.6	16.8	0	0.01
699.1	16.7	0	0.01
714.3	16.3	0	0.01
729.3	16.1	0	0.01
744.4	16.6	0	0.01
759.6	16.5	0	0.01
774.6	16.1	0	0.01
789.5	16.3	0	0.01
804.8	16.6	0	0.01
820.1	16.5	0	0.01
835.2	16.7	0	0.01
850.4	17.1	0	0.01
865.6	17.1	0	0.01
880.7	17	0	0.01
875.5	16.2	0	0.01
891.8	18.1	0	0.01
908.2	17.6	0	0.01
924.5	17.4	0	0.01
940.4	16.8	0	0.01
956.3	17.3	0	0.01
972.1	17	0	0.01
987.8	16.9	0	0.01
1003.6	16.6	0	0.01
1019.2	17	0	0.01
1034.9	16.6	0	0.01
1050.3	16.3	0	0.01
1065.6	16.4	0	0.01
1080.8	16.3	0	0.01
1095.9	16	0	0.01
1110.8	15.7	0	0.01
1125.9	16.4	0	0.01
1140.7	15.6	0	0.01
1155.3	15.6	0	0.01
1169.9	16	0	0.01

1184.7	16.3	0	0.01
1199.2	15.9	0	0.01
1213.4	15.6	0	0.01
1227.8	15.9	0	0.01
1242.2	16	0	0.01
1256.6	16	0	0.01
1270.6	15.5	0	0.01
1284.7	15.9	0	0.01
1298.8	15.9	0	0.01
1312.8	16	0	0.01
1326.9	15.8	0	0.01
1340.4	15.4	0	0.01
1404.3	15.9	0	0.0025
1418.7	16	0	0.0025
1432.6	16.4	0	0.0025
1446.7	16	0	0.0025
1460.6	16.1	0	0.0025
1474.6	15.9	0	0.0025
1488.4	16.1	0	0.0025
1502	16.2	0	0.0025
1515.4	15.9	0	0.0025
1528.7	16.1	0	0.0025
1542.3	16.6	0	0.0025
1555.6	16.5	0	0.0025
1568.7	16.2	0	0.0025
1581.6	16.2	0	0.0025
1594.5	16.7	0	0.0025
1607.5	16.3	0	0.0025
1620.3	16.2	0	0.0025
1633	16.5	0	0.0025
1645.7	16.5	0	0.0025
1658.2	16.3	0	0.0025
1670.6	16.1	0	0.0025
1682.9	16.3	0	0.0025
1695.3	16.3	0	0.0025
1707.7	16.1	0	0.0025
1719.7	16	0	0.0025
1731.8	16.3	0	0.0025
1743.9	16.2	0	0.0025
1755.9	15.9	0	0.0025
1767.8	15.6	0	0.0025
1779.5	16.1	0	0.0025
1791.3	15.8	0	0.0025
1803	15.2	0	0.0025
1950.4	20.2	0	0.0025
1969.4	21.2	0	0.0025
1988.6	21.2	0	0.0025
2007.5	21.3	0	0.0025
2026.5	21.6	0	0.0025
2045.5	21.9	0	0.0025
2064.4	21.5	0	0.0025
2082.8	21.1	0	0.0025

2101	20.7	0	0.0025
2118.9	21.2	0	0.0025
2136.8	21.9	0	0.0025
2155	21.9	0	0.0025
2172.7	21.4	0	0.0025
2189.6	20.9	0	0.0025
2207.2	23.1	0	0.0025
2225.5	21	0	0.0025
2242.4	21.9	0	0.0025
2260.1	22.5	0	0.0025
2277.3	21.5	0	0.0025
2294.1	21.9	0	0.0025
2310.7	21.8	0	0.0025
2327	21.8	0	0.0025
2343.4	22.6	0	0.0025
2360.2	22.6	0	0.0025
2376.2	22.3	0	0.0025
2392.4	21.8	0	0.0025
2408	22	0	0.0025
2423.9	21.5	0	0.0025
2439.3	21.6	0	0.0025
2455.2	22.4	0	0.0025
2470.4	22.7	0	0.0025
2485.8	22.4	0	0.0025

Hyperion input parameters for ACORN

Image format
1
Integer format
0
Bands, Samples, Lines, Offset
189 255 2532 0
latitude
-35.46667
longitude
138.95
Day, Month, Year
18 2 2002
Day of year
49
Hour, minute, second
0.0000000E+00 2.000000 38.00000
Decimal hour
4.39E-02
Elevation
0.1
Altitude
705
Model
1
Derive water vapor
2
Include path in water fit
1
Visibility
100
Estimate visibility
1
Artifact suppression
1 1 1

Hyperion gain and offset values for ACORN

Wavelength	FWHM	Offset	Gain
458.06	11.35	0	0.025
468.23	11.35	0	0.025
478.4	11.35	0	0.025
488.57	11.34	0	0.025
498.74	11.32	0	0.025
508.91	11.28	0	0.025
519.08	11.22	0	0.025
529.25	11.16	0	0.025
539.42	11.08	0	0.025
549.59	10.99	0	0.025
559.75	10.9	0	0.025
569.92	10.81	0	0.025
580.09	10.71	0	0.025
590.26	10.62	0	0.025
600.43	10.53	0	0.025
610.6	10.46	0	0.025
620.77	10.39	0	0.025
630.94	10.33	0	0.025
641.11	10.29	0	0.025
651.28	10.27	0	0.025
661.45	10.26	0	0.025
671.62	10.27	0	0.025
681.79	10.31	0	0.025
691.96	10.37	0	0.025
702.12	10.44	0	0.025
712.29	10.51	0	0.025
722.46	10.58	0	0.025
732.63	10.64	0	0.025
742.8	10.67	0	0.025
752.97	10.69	0	0.025
763.14	10.71	0	0.025
773.31	10.77	0	0.025
783.48	10.86	0	0.025
793.65	10.97	0	0.025
803.82	11.08	0	0.025
813.99	11.18	0	0.025
824.16	11.24	0	0.025
834.33	11.26	0	0.025
844.5	11.26	0	0.025
854.66	11.27	0	0.025
864.83	11.27	0	0.025
875	11.28	0	0.025
885.17	11.29	0	0.025
895.34	11.3	0	0.025
905.51	11.31	0	0.025
915.68	11.31	0	0.025
925.85	11.31	0	0.025
932.72	11.17	0	0.0125
942.81	11.17	0	0.0125
952.89	11.17	0	0.0125

962.98	11.17	0	0.0125
973.07	11.17	0	0.0125
983.16	11.17	0	0.0125
993.25	11.17	0	0.0125
1003.37	11.17	0	0.0125
1013.37	11.17	0	0.0125
1023.47	11.17	0	0.0125
1033.57	11.17	0	0.0125
1043.67	11.17	0	0.0125
1053.77	11.16	0	0.0125
1063.86	11.15	0	0.0125
1073.96	11.14	0	0.0125
1084.06	11.13	0	0.0125
1094.16	11.12	0	0.0125
1104.26	11.1	0	0.0125
1114.26	11.09	0	0.0125
1124.35	11.07	0	0.0125
1134.45	11.05	0	0.0125
1144.55	11.03	0	0.0125
1154.65	11.02	0	0.0125
1164.75	11	0	0.0125
1174.84	10.98	0	0.0125
1184.94	10.96	0	0.0125
1195.04	10.94	0	0.0125
1205.14	10.93	0	0.0125
1215.24	10.91	0	0.0125
1225.24	10.89	0	0.0125
1235.33	10.88	0	0.0125
1245.43	10.87	0	0.0125
1255.53	10.86	0	0.0125
1265.63	10.85	0	0.0125
1275.73	10.84	0	0.0125
1285.83	10.83	0	0.0125
1295.92	10.83	0	0.0125
1306.02	10.82	0	0.0125
1316.12	10.82	0	0.0125
1326.12	10.82	0	0.0125
1336.22	10.83	0	0.0125
1346.32	10.84	0	0.0125
1356.41	10.85	0	0.0125
1366.51	10.86	0	0.0125
1376.61	10.88	0	0.0125
1386.71	10.9	0	0.0125
1396.81	10.92	0	0.0125
1406.9	10.95	0	0.0125
1417	10.98	0	0.0125
1427	11.01	0	0.0125
1437.1	11.04	0	0.0125
1447.2	11.07	0	0.0125
1457.3	11.11	0	0.0125
1467.39	11.14	0	0.0125
1477.49	11.18	0	0.0125

1487.59	11.22	0	0.0125
1497.69	11.26	0	0.0125
1507.79	11.3	0	0.0125
1517.89	11.34	0	0.0125
1527.98	11.38	0	0.0125
1537.98	11.42	0	0.0125
1548.08	11.46	0	0.0125
1558.18	11.5	0	0.0125
1568.28	11.54	0	0.0125
1578.37	11.57	0	0.0125
1588.47	11.61	0	0.0125
1598.57	11.64	0	0.0125
1608.67	11.67	0	0.0125
1618.77	11.7	0	0.0125
1628.87	11.72	0	0.0125
1638.86	11.75	0	0.0125
1648.96	11.77	0	0.0125
1659.06	11.78	0	0.0125
1669.16	11.8	0	0.0125
1679.26	11.81	0	0.0125
1689.36	11.82	0	0.0125
1699.45	11.82	0	0.0125
1709.55	11.82	0	0.0125
1719.65	11.82	0	0.0125
1729.75	11.81	0	0.0125
1739.75	11.8	0	0.0125
1749.85	11.78	0	0.0125
1759.94	11.76	0	0.0125
1770.04	11.74	0	0.0125
1780.14	11.71	0	0.0125
1790.24	11.68	0	0.0125
1800.34	11.64	0	0.0125
1810.43	11.6	0	0.0125
1820.53	11.56	0	0.0125
1830.63	11.51	0	0.0125
1840.63	11.47	0	0.0125
1850.73	11.42	0	0.0125
1860.83	11.37	0	0.0125
1870.92	11.33	0	0.0125
1881.02	11.28	0	0.0125
1891.12	11.24	0	0.0125
1901.22	11.19	0	0.0125
1911.32	11.15	0	0.0125
1921.42	11.11	0	0.0125
1931.51	11.07	0	0.0125
1941.61	11.04	0	0.0125
1951.61	11.01	0	0.0125
1961.71	10.99	0	0.0125
1971.81	10.96	0	0.0125
1981.9	10.95	0	0.0125
1992	10.93	0	0.0125
2002.1	10.93	0	0.0125

2012.2	10.92	0	0.0125
2022.3	10.92	0	0.0125
2032.4	10.92	0	0.0125
2042.49	10.91	0	0.0125
2052.49	10.9	0	0.0125
2062.59	10.89	0	0.0125
2072.69	10.88	0	0.0125
2082.79	10.86	0	0.0125
2092.89	10.84	0	0.0125
2102.98	10.82	0	0.0125
2113.08	10.8	0	0.0125
2123.18	10.78	0	0.0125
2133.28	10.75	0	0.0125
2143.38	10.73	0	0.0125
2153.38	10.7	0	0.0125
2163.47	10.67	0	0.0125
2173.57	10.65	0	0.0125
2183.67	10.62	0	0.0125
2193.77	10.6	0	0.0125
2203.87	10.57	0	0.0125
2213.96	10.55	0	0.0125
2224.06	10.52	0	0.0125
2234.16	10.5	0	0.0125
2244.26	10.49	0	0.0125
2254.26	10.47	0	0.0125
2264.36	10.45	0	0.0125
2274.45	10.44	0	0.0125
2284.55	10.43	0	0.0125
2294.65	10.43	0	0.0125
2304.75	10.42	0	0.0125
2314.85	10.42	0	0.0125
2324.95	10.42	0	0.0125
2335.04	10.42	0	0.0125
2345.14	10.42	0	0.0125
2355.24	10.42	0	0.0125

FLAASH input parameters for CASI

MODTRAN Parameters

enviacc.modtran.visvalue = 40.0000
enviacc.modtran.f_resolution = 15.0000
enviacc.modtran.day = 25
enviacc.modtran.month = 11
enviacc.modtran.year = 2003
enviacc.modtran.gmt = 5.1506
enviacc.modtran.latitude = -35.4935
enviacc.modtran.longitude = 138.9746
enviacc.modtran.sensor_altitude = 2.2900
enviacc.modtran.ground_elevation = 0.0010
enviacc.modtran.view_zenith_angle = 180.0000
enviacc.modtran.view_azimuth = 0.0000
enviacc.modtran.atmosphere_model = 2
enviacc.modtran.aerosol_model = 1
enviacc.modtran.multiscatter_model = 0
enviacc.modtran.disort_streams = 8
enviacc.modtran.co2mix = 390.0000

Image Parameters

enviacc.img.nspatial = 6087
enviacc.img.nlines = 1035
enviacc.img.margin1 = 0
enviacc.img.margin2 = 0
enviacc.img.nskip = 0
enviacc.img.ifov = 1.3439
enviacc.img.sensor_name = CASI_82

Analysis Parameters

enviacc.ana.aerosol_scaleht = 2.0000
enviacc.ana.output_scale = 10000.0000
enviacc.ana.polishing_res = 9
enviacc.ana.aerosol_retrieval = 0
enviacc.ana.reuse_modtran_calcs = 0

CASI gain and offset values for FLAASH

Wavelength	FWHM	Offset	Gain
418.1	11.4	0	0.01
429.1	11.4	0	0.01
440.2	11.4	0	0.01
451.3	11.4	0	0.01
462.4	11.4	0	0.01
473.5	11.4	0	0.01
484.6	11.4	0	0.01
495.8	11.6	0	0.01
507	11.6	0	0.01
518.2	11.6	0	0.01
529.4	11.6	0	0.01
540.7	11.6	0	0.01
552	11.6	0	0.01
563.2	11.6	0	0.01
574.6	11.6	0	0.01
585.9	11.6	0	0.01
597.2	11.6	0	0.01
608.6	11.6	0	0.01
620	11.6	0	0.01
631.3	11.6	0	0.01
642.7	11.8	0	0.01
654.2	11.8	0	0.01
665.6	11.8	0	0.01
677	11.8	0	0.01
688.5	11.8	0	0.01
699.9	11.8	0	0.01
711.4	11.8	0	0.01
722.9	11.8	0	0.01
734.4	11.8	0	0.01
745.9	11.8	0	0.01
757.4	11.8	0	0.01
768.9	11.8	0	0.01
780.4	11.8	0	0.01
791.9	11.8	0	0.01
803.4	11.8	0	0.01
815	11.8	0	0.01
826.5	11.8	0	0.01
838	11.8	0	0.01
849.6	11.8	0	0.01
861.1	11.8	0	0.01
872.6	11.8	0	0.01
884.2	11.8	0	0.01
895.7	11.8	0	0.01
907.2	11.8	0	0.01
918.7	11.8	0	0.01
930.3	11.8	0	0.01
941.8	11.8	0	0.01
953.3	11.8	0	0.01

APPENDIX 3

Groundtruthing field data used to compile error matrices

HyMap saltpan (P=saltpan present)

Field Site ID	Easting	Northing	Field Cover	Image Map
000	313066.42702	6075465.09656		
002	312456.66596	6071561.29565		
003	315081.71303	6071033.24763		
004	314304.00455	6073801.04102	**P**	
005	314863.30268	6071786.45888		
006	311261.35118	6075760.18189		
008	312111.32531	6070527.47856		
009	322316.69332	6069541.19391		
010	308654.26815	6073895.26906		
011	322371.54197	6069639.83116		
012	313732.74124	6075826.17585		
013	316140.71815	6070589.57341	**P**	**P**
017	320553.14556	6069013.17698		
020	313833.92456	6072608.61321		
021	321930.93246	6068863.37246		
022	310444.84300	6074344.21188		
023	318537.08270	6070609.40052		
024	309084.39952	6073235.99777		
025	309521.34292	6072645.33666		
026	313493.15389	6074995.25346		
027	317892.53862	6070589.62183		
028	321740.76990	6068566.41282		
029	310666.96228	6075231.25042		
030	314396.48888	6074680.52687		
031	314102.63798	6071467.76756		
034	310799.95167	6075282.32546		
035	320020.54283	6069815.80923		
036	310552.01084	6073082.57726		
037	313937.40102	6073800.09912	**P**	
038	318610.95136	6070396.08150		
039	308940.44234	6074282.42394		
040	311750.21244	6076040.33255		
041	320609.16121	6069100.21675		
042	313593.67278	6075173.15201		
044	308147.34823	6075939.63940		
048	322194.47124	6069563.08724		
049	310084.25657	6072661.19426		
050	315137.21903	6071608.40844	**P**	**P**
051	309270.66233	6074626.80715		
052	320494.00205	6069590.06268		
054	322055.28491	6069748.67563		
055	311339.61932	6074997.40101		
056	313925.59647	6070883.84827		
057	314469.09272	6073732.38979		
058	307499.88655	6075148.40138		

059	320190.91565	6069575.38604		
060	309406.03068	6073298.94855		
061	320097.44145	6070221.56686		
062	313325.98921	6075493.66778		
064	310366.83986	6073173.27429		
065	313983.80902	6075435.98484		
066	310946.20124	6072874.86908		
067	313211.86274	6075799.12364		
068	314523.88908	6072439.65018		
069	314854.90346	6070792.93861		
071	319409.10410	6070321.68476		
072	314370.12490	6073190.51059	**P**	
073	312479.90041	6075438.92884		
076	313729.27580	6076412.41938		
078	311660.48093	6075254.29609		
079	312060.13617	6070551.48152		
080	310612.66359	6072559.18749		
081	320827.68226	6069121.45257		
084	308552.14167	6074890.99851		
085	313990.58488	6073168.30681		
087	311188.23466	6072760.80421		
088	319498.60705	6070533.58911		
089	315583.43231	6071104.89642		
096	310512.67006	6074319.02763		
097	314800.88444	6074001.99344		
099	308965.64853	6073633.44112		
100	313393.00000	6072021.00000		
101	313937.00000	6073040.00000		
103	313212.00000	6071360.00000	**P**	
104	314387.00000	6073982.00000		
107	314415.00000	6074559.00000		
108	313587.00000	6072512.00000		
109	314640.00000	6073257.00000		
110	316561.00000	6070413.00000	**P**	**P**
111	315454.00000	6071556.00000	**P**	**P**
112	314107.00000	6073143.00000	**P**	
113	314580.00000	6072746.00000	**P**	
114	313755.00000	6074901.00000	**P**	
116	314850.00000	6071725.00000	**P**	**P**
118	315273.00000	6071304.00000	**P**	**P**
119	314469.00000	6073027.00000		
120	314233.00000	6074823.00000		
121	314328.00000	6073764.00000	**P**	**P**
123	312768.00000	6072288.00000		
124	313649.00000	6074926.00000		
127	315145.00000	6071514.00000	**P**	
128	313288.00000	6071425.00000	**P**	
129	314446.00000	6074670.00000	**P**	**P**
130	314608.00000	6072534.00000		
131	316158.00000	6070697.00000		
134	312871.00000	6072165.00000		
135	314003.00000	6074759.00000		

136	313920.00000	6073243.00000		
137	313910.00000	6072027.00000		
138	314439.00000	6072446.00000		
139	314366.00000	6073109.00000		
141	314321.00000	6074418.00000		
143	312701.00000	6071209.00000		
144	314408.60651	6073561.00000		
145	316491.00000	6070485.00000	**P**	**P**
146	315010.00000	6071731.00000	**P**	**P**
147	314520.00000	6074361.00000	**P**	
149	314590.00000	6072760.00000	**P**	
151	313143.67180	6074786.15400		
155	311765.67505	6076484.94316		
156	318130.47150	6070547.50600		
158	315000.67380	6071665.34300	**P**	
159	315371.15230	6071519.71700	**P**	**P**
161	311342.12220	6072923.13400		
162	313997.25680	6073673.31100	**P**	
168	314305.36490	6073829.04200		
169	313982.21320	6071924.85200	**P**	**P**
170	313152.53010	6071358.26000		
171	313167.72630	6075637.50700		**P**
173	309672.83310	6072920.07500		**P**
174	313232.54300	6075674.43700		
176	312477.83380	6071741.52300	**P**	**P**
179	311739.39750	6070693.57100		
180	313800.49600	6073124.13500	**P**	
181	314853.26480	6071695.61400		
183	314648.38230	6074224.77400		
185	314594.59160	6074247.63900		
186	314348.15180	6071621.57400		
187	312369.85100	6071760.03800	**P**	
188	315233.70440	6071501.54300	**P**	**P**
189	314418.87090	6074728.12900	**P**	**P**
190	311695.63340	6070547.27100		
191	312511.06610	6071660.64600	**P**	
192	314193.11650	6073919.49200	**P**	**P**
193	311691.43085	6076716.59856		
197	315313.68150	6071609.80000	**P**	**P**
198	314488.53080	6071580.18300		

HyMap samphire (S=samphire present)

Field Site ID	Easting	Northing	Field Cover	Image Map
002	312456.66596	6071561.29565		
003	315081.71303	6071033.24763		
004	314304.00455	6073801.04102		
005	314863.30268	6071786.45888	**S**	
006	311261.35118	6075760.18189		
008	312111.32531	6070527.47856		
009	322316.69332	6069541.19391		
010	308654.26815	6073895.26906		
011	322371.54197	6069639.83116		
013	316140.71815	6070589.57341		
017	320553.14556	6069013.17698		
020	313833.92456	6072608.61321		
021	321930.93246	6068863.37246		
022	310444.84300	6074344.21188		
023	318537.08270	6070609.40052		
024	309084.39952	6073235.99777		
025	309521.34292	6072645.33666		
026	313493.15389	6074995.25346		
027	317892.53862	6070589.62183		**S**
028	321740.76990	6068566.41282		
029	310666.96228	6075231.25042		
030	314396.48888	6074680.52687		
031	314102.63798	6071467.76756		
034	310799.95167	6075282.32546		
035	320020.54283	6069815.80923		
036	310552.01084	6073082.57726		
037	313937.40102	6073800.09912	**S**	**S**
038	318610.95136	6070396.08150		
039	308940.44234	6074282.42394		
041	320609.16121	6069100.21675		
042	313593.67278	6075173.15201		
044	308147.34823	6075939.63940		
048	322194.47124	6069563.08724		
049	310084.25657	6072661.19426		
050	315137.21903	6071608.40844		
051	309270.66233	6074626.80715		
052	320494.00205	6069590.06268		
053	311507.87279	6074895.80723		
054	322055.28491	6069748.67563		
055	311339.61932	6074997.40101		
056	313925.59647	6070883.84827		
057	314469.09272	6073732.38979		
058	307499.88655	6075148.40138		
059	320190.91565	6069575.38604		
060	309406.03068	6073298.94855		
061	320097.44145	6070221.56686		
064	310366.83986	6073173.27429		

066	310946.20124	6072874.86908		
067	313211.86274	6075799.12364		
068	314523.88908	6072439.65018	**S**	
069	314854.90346	6070792.93861		
071	319409.10410	6070321.68476		
072	314370.12490	6073190.51059	**S**	**S**
073	312479.90041	6075438.92884		
074	311149.38762	6074759.85973		
6				
079	312060.13617	6070551.48152		
080	310612.66359	6072559.18749		
081	320827.68226	6069121.45257		
084	308552.14167	6074890.99851		
085	313990.58488	6073168.30681		
087	311188.23466	6072760.80421		
088	319498.60705	6070533.58911		
089	315583.43231	6071104.89642		
096	310512.67006	6074319.02763		
097	314800.88444	6074001.99344		
099	308965.64853	6073633.44112		
100	313393.00000	6072021.00000		
101	313937.00000	6073040.00000		
103	313212.00000	6071360.00000	**S**	
104	314387.00000	6073982.00000		**S**
107	314415.00000	6074559.00000		
108	313587.00000	6072512.00000	**S**	
109	314640.00000	6073257.00000	**S**	**S**
110	316561.00000	6070413.00000	**S**	**S**
111	315454.00000	6071556.00000		
112	314107.00000	6073143.00000	**S**	**S**
113	314580.00000	6072746.00000	**S**	**S**
114	313755.00000	6074901.00000	**S**	
116	314850.00000	6071725.00000	**S**	**S**
118	315273.00000	6071304.00000		
119	314469.00000	6073027.00000	**S**	
120	314233.00000	6074823.00000		
121	314328.00000	6073764.00000	**S**	**S**
123	312768.00000	6072288.00000		
124	313649.00000	6074926.00000		
127	315145.00000	6071514.00000	**S**	
128	313288.00000	6071425.00000	**S**	
129	314446.00000	6074670.00000		
130	314608.00000	6072534.00000	**S**	**S**
131	316158.00000	6070697.00000	**S**	**S**
134	312871.00000	6072165.00000		
136	313920.00000	6073243.00000	**S**	**S**
137	313910.00000	6072027.00000		
138	314439.00000	6072446.00000	**S**	**S**
139	314366.00000	6073109.00000		
141	314321.00000	6074418.00000		**S**
143	312701.00000	6071209.00000		
144	314408.60651	6073561.00000	**S**	**S**

145	316491.00000	6070485.00000		
146	315010.00000	6071731.00000		
147	314520.00000	6074361.00000	**S**	**S**
149	314590.00000	6072760.00000	**S**	**S**
151	313143.67180	6074786.15400		
156	318130.47150	6070547.50600		
158	315000.67380	6071665.34300		
159	315371.15230	6071519.71700		
161	311342.12220	6072923.13400		
162	313997.25680	6073673.31100		
168	314305.36490	6073829.04200		
169	313982.21320	6071924.85200		
170	313152.53010	6071358.26000		
173	309672.83310	6072920.07500		
175	312643.01700	6072443.83500	**S**	**S**
176	312477.83380	6071741.52300	**S**	
179	311739.39750	6070693.57100		
180	313800.49600	6073124.13500	**S**	
181	314853.26480	6071695.61400	**S**	**S**
183	314648.38230	6074224.77400		
185	314594.59160	6074247.63900		
186	314348.15180	6071621.57400		
187	312369.85100	6071760.03800	**S**	
188	315233.70440	6071501.54300		
189	314418.87090	6074728.12900		**S**
190	311695.63340	6070547.27100		
191	312511.06610	6071660.64600		
192	314193.11650	6073919.49200	**S**	
197	315313.68150	6071609.80000		
198	314488.53080	6071580.18300		

Hyperion saltpan (P=saltpan present)

Field Site ID	Easting	Northing	Field Cover	Image Map
000	313066.42702	6075465.09656		
002	312456.66596	6071561.29565		
003	315081.71303	6071033.24763		
004	314304.00455	6073801.04102	**P**	**P**
005	314863.30268	6071786.45888		
006	311261.35118	6075760.18189		
008	312111.32531	6070527.47856		
012	313732.74124	6075826.17585		
020	313833.92456	6072608.61321		**P**
022	310444.84300	6074344.21188		
024	309084.39952	6073235.99777		
025	309521.34292	6072645.33666		
026	313493.15389	6074995.25346		
029	310666.96228	6075231.25042		
030	314396.48888	6074680.52687		
031	314102.63798	6071467.76756		**P**
032	309894.12210	6074987.97396		
034	310799.95167	6075282.32546		
036	310552.01084	6073082.57726		
037	313937.40102	6073800.09912	**P**	
040	311750.21244	6076040.33255		
042	313593.67278	6075173.15201		
043	311476.37992	6076757.08774		
049	310084.25657	6072661.19426		
050	315137.21903	6071608.40844	**P**	**P**
051	309270.66233	6074626.80715		
053	311507.87279	6074895.80723		
055	311339.61932	6074997.40101		
056	313925.59647	6070883.84827		
057	314469.09272	6073732.38979		
060	309406.03068	6073298.94855		
062	313325.98921	6075493.66778		
064	310366.83986	6073173.27429		
065	313983.80902	6075435.98484		
066	310946.20124	6072874.86908		
067	313211.86274	6075799.12364		
068	314523.88908	6072439.65018		
069	314854.90346	6070792.93861		
072	314370.12490	6073190.51059	**P**	
073	312479.90041	6075438.92884		
074	311149.38762	6074759.85973		
076	313729.27580	6076412.41938		
078	311660.48093	6075254.29609		
079	312060.13617	6070551.48152		
080	310612.66359	6072559.18749		
085	313990.58488	6073168.30681		
087	311188.23466	6072760.80421		

089	315583.43231	6071104.89642		
096	310512.67006	6074319.02763		
097	314800.88444	6074001.99344		
099	308965.64853	6073633.44112		
100	313393.00000	6072021.00000		
101	313937.00000	6073040.00000		
103	313212.00000	6071360.00000	**P**	
104	314387.00000	6073982.00000		
107	314415.00000	6074559.00000		
108	313587.00000	6072512.00000		**P**
109	314640.00000	6073257.00000		
111	315454.00000	6071556.00000	**P**	**P**
112	314107.00000	6073143.00000	**P**	
113	314580.00000	6072746.00000	**P**	
114	313755.00000	6074901.00000	**P**	
116	314850.00000	6071725.00000	**P**	
118	315273.00000	6071304.00000	**P**	
119	314469.00000	6073027.00000		
120	314233.00000	6074823.00000		
121	314328.00000	6073764.00000	**P**	
123	312768.00000	6072288.00000		
124	313649.00000	6074926.00000		
127	315145.00000	6071514.00000	**P**	
128	313288.00000	6071425.00000	**P**	**P**
129	314446.00000	6074670.00000	**P**	
130	314608.00000	6072534.00000		
134	312871.00000	6072165.00000		
135	314003.00000	6074759.00000		
136	313920.00000	6073243.00000		
137	313910.00000	6072027.00000		
138	314439.00000	6072446.00000		
139	314366.00000	6073109.00000		
141	314321.00000	6074418.00000		
143	312701.00000	6071209.00000		
144	314408.60651	6073561.00000		
146	315010.00000	6071731.00000	**P**	
147	314520.00000	6074361.00000	**P**	
149	314590.00000	6072760.00000	**P**	
151	313143.67180	6074786.15400		
155	311765.67505	6076484.94316		
158	315000.67380	6071665.34300	**P**	**P**
159	315371.15230	6071519.71700	**P**	**P**
161	311342.12220	6072923.13400		
162	313997.25680	6073673.31100	**P**	**P**
168	314305.36490	6073829.04200		**P**
169	313982.21320	6071924.85200	**P**	**P**
170	313152.53010	6071358.26000		
171	313167.72630	6075637.50700		
173	309672.83310	6072920.07500		
174	313232.54300	6075674.43700		
175	312477.83380	6071741.52300		
176	312477.83380	6071741.52300	**P**	**P**

179	311739.39750	6070693.57100		
180	313800.49600	6073124.13500	**P**	
181	314853.26480	6071695.61400		
183	314648.38230	6074224.77400		
185	314594.59160	6074247.63900		
186	314348.15180	6071621.57400		
187	312369.85100	6071760.03800	**P**	
188	315233.70440	6071501.54300	**P**	**P**
189	314418.87090	6074728.12900	**P**	
190	311695.63340	6070547.27100		**P**
191	312511.06610	6071660.64600	**P**	**P**
192	314193.11650	6073919.49200	**P**	**P**
193	311691.43085	6076716.59856		
197	315313.68150	6071609.80000	**P**	
198	314488.53080	6071580.18300		**P**

Hyperion samphire (S=samphire present)

Field Site ID	Easting	Northing	Field Cover	Image Map
000	313066.42702	6075465.09656		
002	312456.66596	6071561.29565		
003	315081.71303	6071033.24763		
004	314304.00455	6073801.04102		**S**
005	314863.30268	6071786.45888	**S**	
006	311261.35118	6075760.18189		
008	312111.32531	6070527.47856		
012	313732.74124	6075826.17585		
020	313833.92456	6072608.61321		
022	310444.84300	6074344.21188		
024	309084.39952	6073235.99777		
025	309521.34292	6072645.33666		
026	313493.15389	6074995.25346		
029	310666.96228	6075231.25042		
030	314396.48888	6074680.52687		
031	314102.63798	6071467.76756		
032	309894.12210	6074987.97396		
034	310799.95167	6075282.32546		
036	310552.01084	6073082.57726		
037	313937.40102	6073800.09912	**S**	
040	311750.21244	6076040.33255		
042	313593.67278	6075173.15201		
043	311476.37992	6076757.08774		
049	310084.25657	6072661.19426		
050	315137.21903	6071608.40844		
051	309270.66233	6074626.80715		
053	311507.87279	6074895.80723		
055	311339.61932	6074997.40101		
056	313925.59647	6070883.84827		
057	314469.09272	6073732.38979		
060	309406.03068	6073298.94855		
062	313325.98921	6075493.66778		
064	310366.83986	6073173.27429		
065	313983.80902	6075435.98484		
066	310946.20124	6072874.86908		
067	313211.86274	6075799.12364		
068	314523.88908	6072439.65018	**S**	
069	314854.90346	6070792.93861		
072	314370.12490	6073190.51059	**S**	**S**
073	312479.90041	6075438.92884		
074	311149.38762	6074759.85973		
076	313729.27580	6076412.41938		
078	311660.48093	6075254.29609		
079	312060.13617	6070551.48152		
080	310612.66359	6072559.18749		
085	313990.58488	6073168.30681		
087	311188.23466	6072760.80421		

089	315583.43231	6071104.89642		
096	310512.67006	6074319.02763		
097	314800.88444	6074001.99344		
099	308965.64853	6073633.44112		
100	313393.00000	6072021.00000		
101	313937.00000	6073040.00000		
103	313212.00000	6071360.00000	**S**	
104	314387.00000	6073982.00000		
107	314415.00000	6074559.00000		
108	313587.00000	6072512.00000	**S**	**S**
109	314640.00000	6073257.00000	**S**	**S**
111	315454.00000	6071556.00000		**S**
112	314107.00000	6073143.00000	**S**	**S**
113	314580.00000	6072746.00000	**S**	**S**
114	313755.00000	6074901.00000	**S**	
116	314850.00000	6071725.00000	**S**	
118	315273.00000	6071304.00000		
119	314469.00000	6073027.00000	**S**	
120	314233.00000	6074823.00000		
121	314328.00000	6073764.00000	**S**	**S**
123	312768.00000	6072288.00000		
124	313649.00000	6074926.00000		**S**
127	315145.00000	6071514.00000	**S**	
128	313288.00000	6071425.00000	**S**	
129	314446.00000	6074670.00000		
130	314608.00000	6072534.00000	**S**	**S**
134	312871.00000	6072165.00000		
135	314003.00000	6074759.00000		
136	313920.00000	6073243.00000	**S**	**S**
137	313910.00000	6072027.00000		
138	314439.00000	6072446.00000	**S**	**S**
139	314366.00000	6073109.00000		
141	314321.00000	6074418.00000		
143	312701.00000	6071209.00000		
144	314408.60651	6073561.00000	**S**	**S**
146	315010.00000	6071731.00000		**S**
147	314520.00000	6074361.00000	**S**	**S**
149	314590.00000	6072760.00000	**S**	**S**
151	313143.67180	6074786.15400		
155	311765.67505	6076484.94316		
158	315000.67380	6071665.34300		
159	315371.15230	6071519.71700		
161	311342.12220	6072923.13400		
162	313997.25680	6073673.31100		
168	314305.36490	6073829.04200		**S**
169	313982.21320	6071924.85200		
170	313152.53010	6071358.26000		
171	313167.72630	6075637.50700		
173	309672.83310	6072920.07500		
174	313232.54300	6075674.43700	**S**	**S**
175	312477.83380	6071741.52300	**S**	**S**
176	312477.83380	6071741.52300	**S**	

179	311739.39750	6070693.57100		
180	313800.49600	6073124.13500	**S**	**S**
181	314853.26480	6071695.61400	**S**	**S**
183	314648.38230	6074224.77400		**S**
185	314594.59160	6074247.63900		**S**
186	314348.15180	6071621.57400		
187	312369.85100	6071760.03800	**S**	
188	315233.70440	6071501.54300		**S**
189	314418.87090	6074728.12900		
190	311695.63340	6070547.27100		
191	312511.06610	6071660.64600		
192	314193.11650	6073919.49200	**S**	
193	311691.43085	6076716.59856		
197	315313.68150	6071609.80000		
198	314488.53080	6071580.18300		

CASI saltpan (P=saltpan present)

Field Site ID	Easting	Northing	Field Cover	Image Map
000	313066.42702	6075465.09656		
002	312456.66596	6071561.29565		
003	315081.71303	6071033.24763		
004	314304.00455	6073801.04102	**P**	
005	314863.30268	6071786.45888		
006	311261.35118	6075760.18189		
008	312111.32531	6070527.47856		**P**
009	322316.69332	6069541.19391		
010	308654.26815	6073895.26906		
011	322371.54197	6069639.83116		
012	313732.74124	6075826.17585		
013	316140.71815	6070589.57341	**P**	**P**
017	320553.14556	6069013.17698		
020	313833.92456	6072608.61321		
021	321930.93246	6068863.37246		
022	310444.84300	6074344.21188		
023	318537.08270	6070609.40052		
024	309084.39952	6073235.99777		
025	309521.34292	6072645.33666		
026	313493.15389	6074995.25346		
027	317892.53862	6070589.62183		
028	321740.76990	6068566.41282		
029	310666.96228	6075231.25042		
030	314396.48888	6074680.52687		**P**
031	314102.63798	6071467.76756		
034	310799.95167	6075282.32546		
035	320020.54283	6069815.80923		
036	310552.01084	6073082.57726		
037	313937.40102	6073800.09912	**P**	
038	318610.95136	6070396.08150		
039	308940.44234	6074282.42394		
040	311750.21244	6076040.33255		
041	320609.16121	6069100.21675		
042	313593.67278	6075173.15201		
044	308147.34823	6075939.63940		
048	322194.47124	6069563.08724		
049	310084.25657	6072661.19426		
050	315137.21903	6071608.40844	**P**	**P**
051	309270.66233	6074626.80715		
052	320494.00205	6069590.06268		
054	322055.28491	6069748.67563		
055	311339.61932	6074997.40101		
056	313925.59647	6070883.84827		
057	314469.09272	6073732.38979		
058	307499.88655	6075148.40138		
059	320190.91565	6069575.38604		
060	309406.03068	6073298.94855		

061	320097.44145	6070221.56686		
062	313325.98921	6075493.66778		
064	310366.83986	6073173.27429		
065	313983.80902	6075435.98484		
066	310946.20124	6072874.86908		
067	313211.86274	6075799.12364		
068	314523.88908	6072439.65018		
069	314854.90346	6070792.93861		
071	319409.10410	6070321.68476		
072	314370.12490	6073190.51059	**P**	**P**
073	312479.90041	6075438.92884		
076	313729.27580	6076412.41938		
078	311660.48093	6075254.29609		
079	312060.13617	6070551.48152		
080	310612.66359	6072559.18749		
081	320827.68226	6069121.45257		
084	308552.14167	6074890.99851		
085	313990.58488	6073168.30681		**P**
087	311188.23466	6072760.80421		
088	319498.60705	6070533.58911		
089	315583.43231	6071104.89642		
096	310512.67006	6074319.02763		
097	314800.88444	6074001.99344		
099	308965.64853	6073633.44112		
100	313393.00000	6072021.00000		
101	313937.00000	6073040.00000		
103	313212.00000	6071360.00000	**P**	
104	314387.00000	6073982.00000		
107	314415.00000	6074559.00000		
108	313587.00000	6072512.00000		**P**
109	314640.00000	6073257.00000		
110	316561.00000	6070413.00000	**P**	
111	315454.00000	6071556.00000	**P**	**P**
112	314107.00000	6073143.00000	**P**	
113	314580.00000	6072746.00000	**P**	
114	313755.00000	6074901.00000	**P**	**P**
116	314850.00000	6071725.00000	**P**	**P**
118	315273.00000	6071304.00000	**P**	**P**
119	314469.00000	6073027.00000		
120	314233.00000	6074823.00000		
121	314328.00000	6073764.00000	**P**	
123	312768.00000	6072288.00000		
124	313649.00000	6074926.00000		
127	315145.00000	6071514.00000	**P**	**P**
128	313288.00000	6071425.00000	**P**	**P**
129	314446.00000	6074670.00000	**P**	
130	314608.00000	6072534.00000		
131	316158.00000	6070697.00000		
134	312871.00000	6072165.00000		
135	314003.00000	6074759.00000		
136	313920.00000	6073243.00000		
137	313910.00000	6072027.00000		

138	314439.00000	6072446.00000		
139	314366.00000	6073109.00000		
141	314321.00000	6074418.00000		
143	312701.00000	6071209.00000		
144	314408.60651	6073561.00000		
145	316491.00000	6070485.00000	**P**	**P**
146	315010.00000	6071731.00000	**P**	**P**
147	314520.00000	6074361.00000	**P**	**P**
149	314590.00000	6072760.00000	**P**	
151	313143.67180	6074786.15400		
155	311765.67505	6076484.94316		
156	318130.47150	6070547.50600		
158	315000.67380	6071665.34300	**P**	
159	315371.15230	6071519.71700	**P**	**P**
161	311342.12220	6072923.13400		
162	313997.25680	6073673.31100	**P**	
168	314305.36490	6073829.04200		
169	313982.21320	6071924.85200	**P**	**P**
170	313152.53010	6071358.26000		
171	313167.72630	6075637.50700		**P**
173	309672.83310	6072920.07500		
174	313232.54300	6075674.43700		**P**
176	312477.83380	6071741.52300	**P**	**P**
179	311739.39750	6070693.57100		
180	313800.49600	6073124.13500	**P**	
181	314853.26480	6071695.61400		
183	314648.38230	6074224.77400		
185	314594.59160	6074247.63900		
186	314348.15180	6071621.57400		
187	312369.85100	6071760.03800	**P**	
188	315233.70440	6071501.54300	**P**	**P**
189	314418.87090	6074728.12900	**P**	
190	311695.63340	6070547.27100		
191	312511.06610	6071660.64600	**P**	**P**
192	314193.11650	6073919.49200	**P**	
193	311691.43085	6076716.59856		
197	315313.68150	6071609.80000	**P**	
198	314488.53080	6071580.18300		

CASI samphire (S=samphire present)

Field Site ID	Easting	Northing	Field Cover	Image Map
000	313066.42702	6075465.09656		
002	312456.66596	6071561.29565		
003	315081.71303	6071033.24763		
004	314304.00455	6073801.04102		
005	314863.30268	6071786.45888	**S**	**S**
006	311261.35118	6075760.18189		
008	312111.32531	6070527.47856		
009	322316.69332	6069541.19391		
010	308654.26815	6073895.26906		
011	322371.54197	6069639.83116		
013	316140.71815	6070589.57341		
017	320553.14556	6069013.17698		
020	313833.92456	6072608.61321		
021	321930.93246	6068863.37246		
022	310444.84300	6074344.21188		
023	318537.08270	6070609.40052		
024	309084.39952	6073235.99777		
025	309521.34292	6072645.33666		
026	313493.15389	6074995.25346		**S**
027	317892.53862	6070589.62183		
028	321740.76990	6068566.41282		
029	310666.96228	6075231.25042		**S**
030	314396.48888	6074680.52687		
031	314102.63798	6071467.76756		
034	310799.95167	6075282.32546		**S**
035	320020.54283	6069815.80923		
036	310552.01084	6073082.57726		
037	313937.40102	6073800.09912	**S**	**S**
038	318610.95136	6070396.08150		
039	308940.44234	6074282.42394		
041	320609.16121	6069100.21675		
042	313593.67278	6075173.15201		
044	308147.34823	6075939.63940		
048	322194.47124	6069563.08724		
049	310084.25657	6072661.19426		
050	315137.21903	6071608.40844		
051	309270.66233	6074626.80715		
052	320494.00205	6069590.06268		
053	311507.87279	6074895.80723		
054	322055.28491	6069748.67563		
055	311339.61932	6074997.40101		
056	313925.59647	6070883.84827		
057	314469.09272	6073732.38979		
058	307499.88655	6075148.40138		
059	320190.91565	6069575.38604		
060	309406.03068	6073298.94855		
061	320097.44145	6070221.56686		

062	309406.03068	6073298.94855		
064	310366.83986	6073173.27429		
065	320097.44145	6070221.56686		
066	310946.20124	6072874.86908		
068	314523.88908	6072439.65018	**S**	
069	314854.90346	6070792.93861		
071	319409.10410	6070321.68476		
072	314370.12490	6073190.51059	**S**	
073	312479.90041	6075438.92884		
078	311660.48093	6075254.29609		
079	312060.13617	6070551.48152		
080	310612.66359	6072559.18749		
081	320827.68226	6069121.45257		
084	308552.14167	6074890.99851		
085	313990.58488	6073168.30681		
087	311188.23466	6072760.80421		
088	319498.60705	6070533.58911		
089	315583.43231	6071104.89642		
096	310512.67006	6074319.02763		
097	314800.88444	6074001.99344		
099	308965.64853	6073633.44112		
100	313393.00000	6072021.00000		**S**
101	313937.00000	6073040.00000		
103	313212.00000	6071360.00000	**S**	
104	314387.00000	6073982.00000		
107	314415.00000	6074559.00000		
108	313587.00000	6072512.00000	**S**	**S**
109	314640.00000	6073257.00000	**S**	
110	316561.00000	6070413.00000	**S**	
111	315454.00000	6071556.00000		
112	314107.00000	6073143.00000	**S**	**S**
113	314580.00000	6072746.00000	**S**	**S**
114	313755.00000	6074901.00000	**S**	
116	314850.00000	6071725.00000	**S**	
118	315273.00000	6071304.00000		
119	314469.00000	6073027.00000	**S**	**S**
120	314233.00000	6074823.00000		
121	314328.00000	6073764.00000	**S**	**S**
123	312768.00000	6072288.00000		
124	313649.00000	6074926.00000		
127	315145.00000	6071514.00000	**S**	**S**
128	313288.00000	6071425.00000	**S**	
129	314446.00000	6074670.00000		
130	314608.00000	6072534.00000	**S**	
131	316158.00000	6070697.00000	**S**	**S**
134	312871.00000	6072165.00000		
135	314003.00000	6074759.00000		
136	313920.00000	6073243.00000	**S**	**S**
137	313910.00000	6072027.00000		**S**
138	314439.00000	6072446.00000	**S**	**S**
139	314366.00000	6073109.00000		
141	314321.00000	6074418.00000		

143	312701.00000	6071209.00000		
144	314408.60651	6073561.00000	**S**	**S**
145	316491.00000	6070485.00000		
146	315010.00000	6071731.00000		
147	314520.00000	6074361.00000	**S**	
149	314590.00000	6072760.00000	**S**	**S**
151	313143.67180	6074786.15400		
156	318130.47150	6070547.50600		
158	315000.67380	6071665.34300		
159	315371.15230	6071519.71700		
161	311342.12220	6072923.13400		
162	313997.25680	6073673.31100		
168	314305.36490	6073829.04200		
169	313982.21320	6071924.85200		
170	313152.53010	6071358.26000		
171	312550.18860	6071039.50300		
173	309672.83310	6072920.07500		
174	309672.83310	6072920.07500		
175	312643.01700	6072443.83500	**S**	**S**
176	312477.83380	6071741.52300	**S**	
179	311739.39750	6070693.57100		**S**
180	313800.49600	6073124.13500	**S**	
181	314853.26480	6071695.61400	**S**	
183	314648.38230	6074224.77400		
185	314594.59160	6074247.63900		
186	314348.15180	6071621.57400		
187	312369.85100	6071760.03800	**S**	
188	315233.70440	6071501.54300		
189	314418.87090	6074728.12900		
190	311695.63340	6070547.27100		
191	312511.06610	6071660.64600		
192	314193.11650	6073919.49200	**S**	
197	315313.68150	6071609.80000		
198	314488.53080	6071580.18300		